THE IMPACT OF mRNA MODIFICATIONS ON RIBOSOMAL DECODING: A MOLECULAR DYNAMICS SIMULATION STUDY

MARK JORDAN LEA
Bachelor of Science, University of Lethbridge, 2022

A thesis submitted
in partial fulfilment of the requirements for the degree of

MASTER OF SCIENCE

in

CHEMISTRY

Department of Chemistry and Biochemistry
University of Lethbridge
LETHBRIDGE, ALBERTA, CANADA

THE IMPACT OF mRNA MODIFICATIONS ON RIBOSOMAL DECODING: A MOLECULAR DYNAMICS SIMULATION STUDY

MARK JORDAN LEA

Date of Defence: May 28, 2025

Dr. Stacey Wetmore Supervisor	Professor	Ph.D.
Dr. Marc Roussel Thesis Examination Committee Member	Professor	Ph.D.
Dr. Michael Gerken Thesis Examination Committee Member	Professor	Ph.D.
Dr. Evan Mercier External Examiner Université de Sherbrooke	Assistant Professor	Ph.D.
Dr. Jean-Denys Hamel Chair, Thesis Examination Committee	Assistant Professor	Ph.D.

ABSTRACT

Post-transcriptional RNA modifications are key regulators of translational accuracy and efficiency. While ribosomal RNA (rRNA) and transfer RNA (tRNA) modifications have well-characterized roles in protein synthesis, the functions of messenger RNA (mRNA) codon modifications are less understood. However, growing evidence suggests that mRNA codon modifications can modulate translation. Naturally occurring mRNA modifications can be enzymatically added, such as inosine (I), which is incorporated into mRNA codons to expand decoding capacity and remodel the proteome. Alternatively, modifications can result from damage to mRNA codons, such as the alkylative lesions 1-methylguanosine (m^1G) and 2-methylguanosine (m^2G), which can have potentially unpredictable and harmful consequences. This thesis developed a large-scale computational model of the ribosomal A-site (>370,000 atoms) and performed molecular dynamics (MD) simulations to understand the position-dependent structural effects of the inosine, m^1G, and m^2G codon modifications. These investigations revealed that modified codons associated with experimentally-observed reduced peptide formation rates exhibit tRNA dissociation or distorted decoding center geometries. In contrast, modified codons with negligible effects on experimental rates maintain A-site conformations that promote productive decoding. Thus, this thesis provides mechanistic insight into how mRNA modifications can regulate translation at the atomic level and establishes a robust computational method for future studies that strive to understand the roles of numerous additional RNA modifications during translation.

ACKNOWLEDGEMENTS

I would first like to thank my committee members, Dr. Michael Gerken and Dr. Marc Roussel, for their support throughout both my undergraduate and graduate studies, and for your much-needed insight, questions, and feedback. Thank you to Dr. Evan Mercier for making time in your schedule to be my external examiner and Dr. Jean-Denys Hamel for chairing my defence.

To my incredible supervisor, Dr. Wetmore, thank you for your constant enthusiasm for science, for encouraging me to branch out into challenging new ventures, and for guiding me when I felt stuck. Your unwavering support has allowed me to develop a project I am truly proud of and I feel honoured to have had the opportunity to work with such a brilliant and inspirational scientist all throughout my undergraduate and graduate studies.

To my colleagues in the Wetmore lab, thank you for the shared laughs, advice and feedback, coffee breaks, Tetris, and chess games. Briana Boychuk, thank you for overseeing my first computational chemistry project. Angela Frederickson, Ridwan Tajudeen, Rebecca Jeong, Indu Negi, and Briana, thank you for your kindness, friendship, advice, feedback, and never-ending support since day one. Dylan Nikkel, Makay Murray, Austin Pounder, and Basel Mansour, thank you for your willingness to lend your extensive knowledge and expertise.

To my piano teacher, Dr. Brad Parker, thank you for always accommodating my hectic schedule and supporting me through hundreds of lessons, performances, studio classes, and competitions. Thank you to my friends and family. To Clarence, thank you for your daily support, reassurance, and patience. Thank you to my cat, Paimon, for the daily cuddles. Thank you to my mom and dad for being my greatest supporters, celebrating my successes, helping me through challenging times, and always encouraging me to pursue my goals.

TABLE OF CONTENTS

LIST OF FIGURES

LIST OF ABBREVIATIONS

aaMD	All-Atom Molecular Dynamics
aa-tRNA	Aminoacylated Transfer RNA
A-site	Aminoacyl Site
A-to-I	Adenosine-to-Inosine
AC	Accommodated
ACS	Acceptor Stem
ADAR	Adenosine Deaminase Acting on mRNA
ADAT	Adenosine Deaminase Acting on tRNA
AMBER	Assisted Model Building with Energy Refinement
ANM	Anisotropic Network Model
ASL	Anticodon Stem Loop
Acpype	AnteChamber PYthon Parser interfacE
AlkB	Alkylated DNA Repair Protein B
aa-tRNA$^{aa}_{BBB}$	Amino-acyl-tRNA with anticodon B34, B35, B36
CDS	Coding Sequence
CG	Coarse Graining
cgMD	Coarse-Grained Molecular Dynamics
COM	Center of Mass
CPPTRAJ	C++ Trajectory Analysis
CPU	Central Processing Unit
CR	Codon Recognition
Cryo-EM	Cryogenic Electron Microscopy
CV	Coefficient of Variation
DBSCAN	Density-Based Spatial Clustering of Applications with Noise
DC	Decoding Center
DHU	Dihydrouridine
DNA	Deoxyribonucleic Acid
E. coli	*Escherichia coli*
eEF1A	Eukaryotic Elongation Factor 1A
eEF2	Eukaryotic Elongation Factor 2
EF-G	Elongation Factor G
EF-Tu	Elongation Factor Thermo Unstable
ENM	Elastic Network Model
eRMSD	Root-Mean-Squared Deviation (computed by Barnaba)
FEL	Free Energy Landscape
FENE	Finite Extension Nonlinear Elastic
FEP	Free Energy Perturbation
GA	GTPase-Activated
GAFF	General AMBER Force Field
GDP	Guanosine Diphosphate
GENION	GROMACS Ion Addition Utility
GPU	Graphics Processing Unit
GROMACS	GROningen MAchine for Chemical Simulations
GTP	Guanosine Triphosphate
H89	LSU rRNA Helix 89
H95	LSU rRNA Helix 95

h18	SSU rRNA helix-18
h44	SSU rRNA helix-44
hESCs	Human Embryonic Stem Cells
HPC	High-Performance Computing
IC	Initiation Complex
IF	Initiation Factor
LFER	Linear Free Energy Relationship
LINCS	Linear Constraint Solver
LJ	Lennard-Jones
LSU	Large Subunit
MD	Molecular Dynamics
MDAnalysis	Molecular Dynamics Analysis Toolkit
MDTraj	Molecular Dynamics Trajectory Analysis Library
mRNA	Messenger RNA
METTL3	N6-adenosine-methyltransferase 70 kDa subunit
MGD	Minor Groove Distance
miRNA	microRNA
microMg	Microsecond Magnesium Ion Parameters
MPI	Message Passing Interface
N	Non-Rotated; General nucleobase
NAST	Nucleic Acid Simulation Tool
NAT10	N-Acetyltransferase 10
NGD	No-Go Decay
NMR	Nuclear Magnetic Resonance
ncRNA	Non-coding RNA
NPR1	Nonexpresser of Pathogenesis-Related Genes 1
NPT	Isothermal-Isobaric Ensemble (Constant Number, Pressure, Temperature)
NSXLID	Non-Syndromic X-Linked Intellectual Disability
NVT	Canonical Ensemble (Constant Number, Volume, Temperature)
ORF	Open Reading Frame
Occ	Occupancy
OpenMP	Open Multi-Processing
P-site	Peptidyl Site
pep-tRNA	Peptidyl-tRNA
PCA	Principal Component Analysis
PDB	Protein Data Bank
PKR	Protein Kinase R
PME	Particle Mesh Ewald
PMF	Potential of Mean Force
PTC	Peptidyl Transferase Center
Pi	Inorganic Phosphate
R	Rotated; Ribose
RESP	Restrained ElectroStatic Potential
RF2	Release Factor 2
RF	Release Factor
rRNA	Ribosomal RNA
RIG-I	Retinoic Acid-Inducible Gene 1
RIP-seq	RNA Immunoprecipitation Sequencing

RMSD	Root-Mean-Squared Deviation
RMSF	Root-Mean-Squared Fluctuation
RNA	Ribonucleic Acid
ROS	Reactive Oxygen Species
SBM	Structure-Based Model
smFRET	Single-Molecule Förster Resonance Energy Transfer
snoRNA	Small Nucleolar RNA
SPC/E	Simple Point Charge Extended model for water
SRL	Sarcin-Ricin Loop
SSU	Small Subunit
TBE	Translation Bypass Efficiency
TC	Ternary Complex
tRNA	Transfer RNA
trEM	Time-Resolved Cryogenic Electron Microscopy
TLR	Toll-like Receptor
UV	Ultraviolet
VemP	Vibrio Export Monitoring Peptide
WCF	Watson-Crick-Franklin
WT	Wild-Type
YTHDF	YTH Domain Family Protein
YUP	Yammp Under Python

Abbreviations for RNA Modifications

8-oxoG	8-oxoguanine
ac^4C	N4-acetylcytidine
Bm	2'-O-methylated ribonucleotide with nucleobase (B = A, C, G, or U)
cmo^5U	5-carboxymethoxyuridine
m^1A	1-methyladenosine
m^1G	1-methylguanosine
$m^1acp^3\Psi$	1-methyl-3-α-amino-α-carboxyl-propyl pseudouridine
$m^1\Psi$	1-methylpseudouridine
m^2G	2-methylguanosine
m^3C	3-methylcytidine
m^5C	5-methylcytosine
$m^6{}_2A$	N6,N6-dimethyladenosine
m^6A	N6-methyladenosine
m^6A	N6-methyladenosine
m^6G	N6-methylguanosine
mcm^5U	5-methoxycarbonylmethyluridine
mcm^5s^2U	5-methoxycarbonylmethyl-2-thiouridine
ms^2t^6A	2-methylthio-N6-threonylcarbamoyladenosine
$nchm^5U$	5-carbamoylmethyluridine
o^2yW	Peroxywybutosine
s^2U	2-thiouridine
s^2C	2-thiocytidine
t^6A	N6-threonylcarbamoyladenosine
τm^5U	5-taurinomethyluridine

Single- and Triple-Letter Abbreviations for the Amino Acids

A	Ala	Alanine
C	Cys	Cysteine
D	Asp	Aspartate, aspartic acid
E	Glu	Glutamate, glutamic acid
F	Phe	Phenylalanine
G	Gly	Glycine
H	His	Histidine
I	Ile	Isoleucine
K	Lys	Lysine
L	Leu	Leucine
M	Met	Methionine
N	Asn	Asparagine
P	Pro	Proline
Q	Gln	Glutamine
R	Arg	Arginine
S	Ser	Serine
T	Thr	Threonine
V	Val	Valine
W	Trp	Tryptophan
Y	Tyr	Tyrosine

Mathematical Symbols

Φ	A1492–3 Monitoring Angle
θ	tRNA-mRNA Alignment Angle
λ	Perturbation Parameter
Δ^{ACS}	ACS-tRNA Junction Angle Deviation

CHAPTER 1: INTRODUCTION

1.1 Thesis overview

To meet cellular demands, proteins must be synthesized accurately and efficiently by the ribosome. Accurate translation depends on coordinated conformational changes and interactions between three RNA molecules: messenger RNA (mRNA), which carries the genetic code; transfer RNA (tRNA), which decodes mRNA; and ribosomal RNA (rRNA), which catalyzes peptide bond formation. All cells employ regulatory mechanisms to fine-tune protein synthesis, among which RNA modification plays a central role. To date, over 170 modifications have been identified that expand the chemical diversity and function of RNA.[1] Dysregulation of RNA modifications has been linked to human disease,[2] making both mechanistic and systems-level investigations important for understanding how these chemical changes alter translation dynamics. Many rRNA and tRNA modifications have established structural or functional roles in translation, including promoting rRNA folding and ribosome assembly,[3] ensuring translational fidelity,[2, 4-7] and enabling precise kinetic control of decoding.[8, 9] In contrast, the effects of mRNA modifications on the kinetics and fidelity of translation remain incompletely characterized, with relatively few studies directly examining their influence on protein synthesis rates and accuracy.[10-14] This thesis uses molecular dynamics (MD) simulations to investigate how select mRNA modifications influence the structural dynamics of ribosomal decoding. The following sections review the molecular mechanisms of translation and how the ribosome modulates tRNA–mRNA recognition. The known impacts of RNA modifications in translation are then examined, focusing on emerging evidence for roles of mRNA modifications that are introduced by enzymes, damage, or artificial means. Finally, the utility of computational biochemistry in complementing experimental approaches is discussed in the context of decoding.

1.2 Protein synthesis is controlled by RNA

Proteins are biological polymers composed of 20 chemically distinct amino acids and perform highly specialized cellular functions, from catalyzing chemical reactions to regulating membrane permeability to direct cellular transport processes. In contrast, RNA is built from just 4 standard ribonucleosides (adenosine (A), guanosine (G), cytidine (C), and uridine (U)), and is often characterized as a molecule used for the storage and transmission of genetic information. However, RNA molecules exhibit immense functional versatility, carrying out tasks in biomolecular catalysis,[15, 16] molecular recognition,[17] and feedback regulation.[18] In fact, accurate translation of the genetic code into functional proteins relies on the coordinated effort of three classes of RNA: rRNA, tRNA, and mRNA. Translation is carried out by the ribosome, a ribonucleoprotein complex conserved across all domains of life (Figure 1.1A). Although proteins are essential for the complexity and efficiency of translation by modern ribosomes, rudimentary functions of the ribosome (e.g., codon recognition and peptide bond formation) are thought to have occurred in primordial ribosomes before proteinization evolved.[19] RNA is therefore indispensable for translating the genetic code and maintaining protein balance essential to cellular homeostasis.

The expression of genetic information is made possible by specific molecular interactions between the codon of mRNA and anticodon of tRNA. During translation, the ribosome binds to an mRNA strand containing numerous three-nucleotide codons that specify the amino acid sequence for a protein. As the ribosome advances codon by codon, aminoacyl-tRNA (aa-tRNA) molecules enter the aminoacyl (A) site of the ribosome and attempt to bind to the mRNA codon (Figure 1.1B). Base pairing involves hydrogen-bonding interactions between mRNA codon bases B1, B2, and B3 (5′ to 3′ direction) and tRNA anticodon bases B36, B35, and B34 (3′ to 5′; Figure. 1.1B).

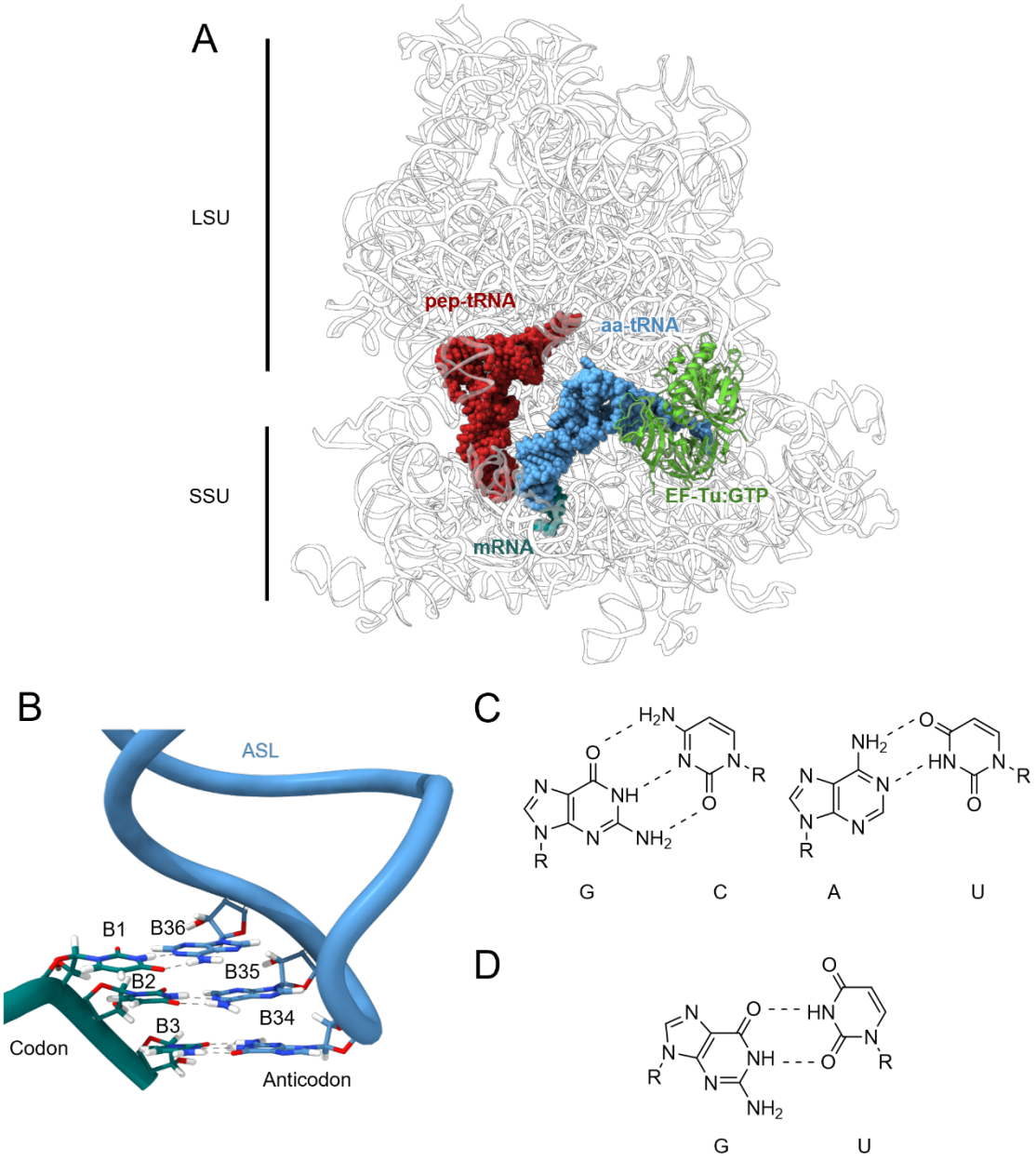

Figure 1.1. The structure of the RNA components of the ribosome. (A) Diagram of the 70S ribosome RNA in the A/T state with aminoacyl- (blue) and peptidyl- (red) tRNAs bound to the mRNA codons in the A- and P-sites of the ribosome, respectively. The rRNA (white) is shown in ribbon style with the large subunit (LSU) and small subunit (SSU) indicated. Elongation factor thermo-unstable (EF-Tu; green) is bound to the A-site tRNA (blue) and GTP (not shown). (B) Codon-anticodon base-pairing interactions in the A-site decoding center. The anticodon stem loop (ASL; blue) of tRNA is shown as ribbon with B34–36 shown as sticks. The mRNA codon (teal; B1–3) is shown as sticks with the phosphate backbone as a ribbon. Hydrogen-bonding interactions are depicted as dotted lines. (C) Watson-Crick-Franklin (WCF) and non-WCF (D) nucleobase-nucleobase hydrogen-bonding interactions between RNA nucleosides (R=ribose). Coordinates for ribosome structures used in the figure were extracted from PDB ID 8G5Z.

The first two positions (B1:B36 and B2:B35) generally form Watson-Crick-Franklin (WCF) base pairs, with A opposite U and G opposite C (Figure 1.1C). The third position (B3:B34), referred to as the "wobble" position, permits non-WCF pairings, such as G opposite U (Figure 1.1D). Codon-anticodon complementarity ensures that only the correct aa-tRNA is selected by the ribosome, and consequently, the corresponding amino acid is added to the growing polypeptide chain. This process repeats iteratively to build a polypeptide that ultimately folds into a functional protein.

The following section (1.2.1) discusses the overall stages of translation to appreciate the evolved interplay in functions between rRNA, tRNA, mRNA, and protein factors. Subsequently, Section 1.2.2 covers the process of elongation and the early models of how accuracy is preserved during tRNA selection. Section 1.2.3 discusses recent advancements revealing that structural dynamics play a more central role in tRNA selection than previously appreciated.

1.2.1 The three stages of protein synthesis: initiation, elongation, and termination, are regulated by distinct mechanisms

To translate an mRNA sequence into proteins, the ribosome undergoes three stages: initiation, elongation, and termination. While the detailed mechanism for initiation differs between prokaryotes and eukaryotes,[20, 21] the primary objective is for the ribosome to assemble into an elongation-competent form. At the end of initiation, the small subunit (SSU) and large subunit (LSU) assemble to form what is denoted as the 70S (80S) ribosomal complex (Figure 1.1A). The 70S ribosome contains initiator fMet-tRNA^{fMet} (Met-tRNA$_i^{Met}$ in eukaryotes) bound to the AUG codon in the peptidyl (P)-site with the aminoacyl (A)-site codon free for elongator aa-tRNAs to bind (Figure 1.1A). The mechanism of elongation is highly conserved between prokaryotes and eukaryotes and involves the iterative decoding of mRNA codons by aa-tRNAs, as assisted by several elongation factors (EFs).[22] Elongation continues until the ribosome

encounters a stop codon (UAA, UAG, or UGA) in the A-site, which is recognized by release factors (RFs) that trigger termination by catalyzing hydrolysis of the polypeptide from the peptidyl-tRNA (pep-tRNA; Figure 1.1A) in the P-site.[20] Ribosome recycling separates the LSU and SSU and prepares the ribosome for a new round of translation, with mRNA and deacylated tRNA released from the small subunit during or after subunit splitting.[20]

Protein synthesis must be controlled by the cell for a balance of protein levels (proteostasis) to be maintained. Regulatory control of initiation and termination relies on discrete molecular checkpoints. During initiation, discrete regulatory mechanisms include initiation factors (IFs), start codon recognition, and additional processes that differ between prokaryotes and eukaryotes. In prokaryotes, initiation often depends on Shine-Dalgarno recognition and IF-mediated control.[20] In eukaryotes, regulatory features include cap-dependent scanning, start codon selection, phosphorylation-dependent checkpoints, and microRNA-mediated inhibition.[23] During termination, stop codon recognition at the end of the open reading frame (ORF) and RF binding ensure that translation stops correctly. [24] However, the continuous, cyclic process of elongation presents challenges for regulation. Given that polypeptides typically contain hundreds of amino acids (median length of ~361 and ~267 amino acids in eukaryotes and prokaryotes, respectively),[25] the ribosome must maintain accuracy over many repeated elongation cycles. Errors in individual cycles of elongation can accumulate to compromise the function of protein products,[26] cause mRNA frameshifting,[27] and pause or stall the ribosome.[28, 29] Indeed, elongation utilizes significantly more energy than initiation or termination and compromised elongation is increasingly linked to various human cancers and neurodegenerative diseases.[30-34] Substantial research effort has therefore been dedicated to understanding elongation at the detailed mechanistic level. Section 1.2.2 discusses the current understanding of the elongation cycle and its regulatory features.

1.2.2 Elongation requires continuous accuracy and efficiency.

Each elongation cycle includes three phases that are conserved across all domains of life. In the first phase, the aa-tRNA binds to the ribosome at the A-site as part of a ternary complex (TC) with a GTP-bound EF-Tu.[20] Next, peptide bond formation occurs between the A- and P-site tRNAs.[20] Finally, translocation of the A- and P-site tRNAs to the P- and E-sites, respectively, occurs, leaving the A-site vacant for the next codon in the ORF to be decoded by a new elongator aa-tRNA.[20]

As discussed in Section 1.2.1, fidelity during elongation (i.e., accurate synthesis of proteins according to the amino acid sequence encoded in the mRNA) is crucial. This fidelity depends in part on base-pairing between the aa-tRNA anticodon and the A-site mRNA codon. However, the free energy differences between cognate and mismatch-containing (near- or non-cognate) base pairs are too small to account for how the ribosome achieves high fidelity aa-tRNA selection.[35] Near-cognate aa-tRNAs (i.e., containing a single mismatch with the codon) must be efficiently rejected from the ribosome despite forming base pairs often only 2–3 kcal/mol less stable than cognate pairs.[35] In trinucleotide RNA duplexes, the free energy difference (ΔG) of duplex formation can be as small as 2–3 kcal/mol for duplexes containing a G:U mispair relative to G:C.[35] The frequency of G:U mispair formation is proportional to $\exp(-\Delta G/RT)$, corresponding to incorrect base pairs forming approximately 1–2% of the time. Yet, the error frequency *in vivo* occurs at frequencies of 10^{-3} or less in prokaryotes.[36, 37] This discrepancy between the estimated error frequency due to aberrant near-cognate selection and the true *in vivo* error frequency suggests that additional mechanisms are at play to preserve elongation fidelity.

Early mechanistic frameworks were described to explain the selectivity of the ribosome towards cognate aa-tRNAs by invoking a 'proofreading' step.[38-41] In the kinetic-proofreading

model, discrimination between cognate and near-cognate aa-tRNAs occurs in a multistep pathway. The first (initial) selection stage is separated from the second (proofreading) stage by irreversible GTP hydrolysis. Irreversible hydrolysis allows correct aa-tRNAs to be rapidly accommodated, while near-cognate tRNAs fall are preferentially rejected either before or after GTP hydrolysis. Indeed, poly(U)-programmed *in vitro* translation experiments demonstrated that near-cognate ternary complexes hydrolyzed ~48 GTP molecules per peptide bond formed, compared to ~1 GTP per peptide bond for cognate Phe-tRNA^{Phe}, confirming the presence of a kinetic proofreading mechanism.[42] While the kinetic-discrimination framework was a crucial development in understanding how accuracy of elongation is maintained, it did not provide thorough insight into the elementary kinetic steps. Moreover, the role of structural changes in the ribosome were not well-understood from these early kinetic models. More recent developments in experimental methodologies, including fluorescence kinetic assays and three-dimensional structural characterization have built significantly on this initial mechanistic model. The detailed mechanism of elongation based on more recent insights will be detailed in the following section.

1.2.3 Recent insights reveal that elongation relies on dynamic conformational rearrangements in rRNA, tRNA, and mRNA

Improvements in experimental techniques, particularly fluorescence-based kinetics studies, have advanced the mechanistic understanding of initial selection and proofreading, culminating in the induced-fit kinetic model (Figure 1.2A-B).[43-50] According to this model, intrinsic differences in binding free energies play a minimal role during tRNA selection.[52] Instead, the codon-anticodon pairing for cognate tRNAs induces conformational changes in the decoding center that promote acceleration of the forward selection pathway towards eventual peptide bond formation.[51] Recent work has also provided a wealth of insight into the structural dynamics during peptide bond formation and translocation.[53, 54] Moreover, advancements in 3D

structural determination techniques, such as X-ray crystallography and cryogenic electron microscopy (cryo-EM), have generated high-resolution structures of elongation intermediates.[45, 55-75] These structures provide insight into the driving interactions between ribosomal proteins, rRNA, tRNA, and mRNA, and strategies used by the ribosome to preferentially select cognate over near-cognate aa-tRNAs.

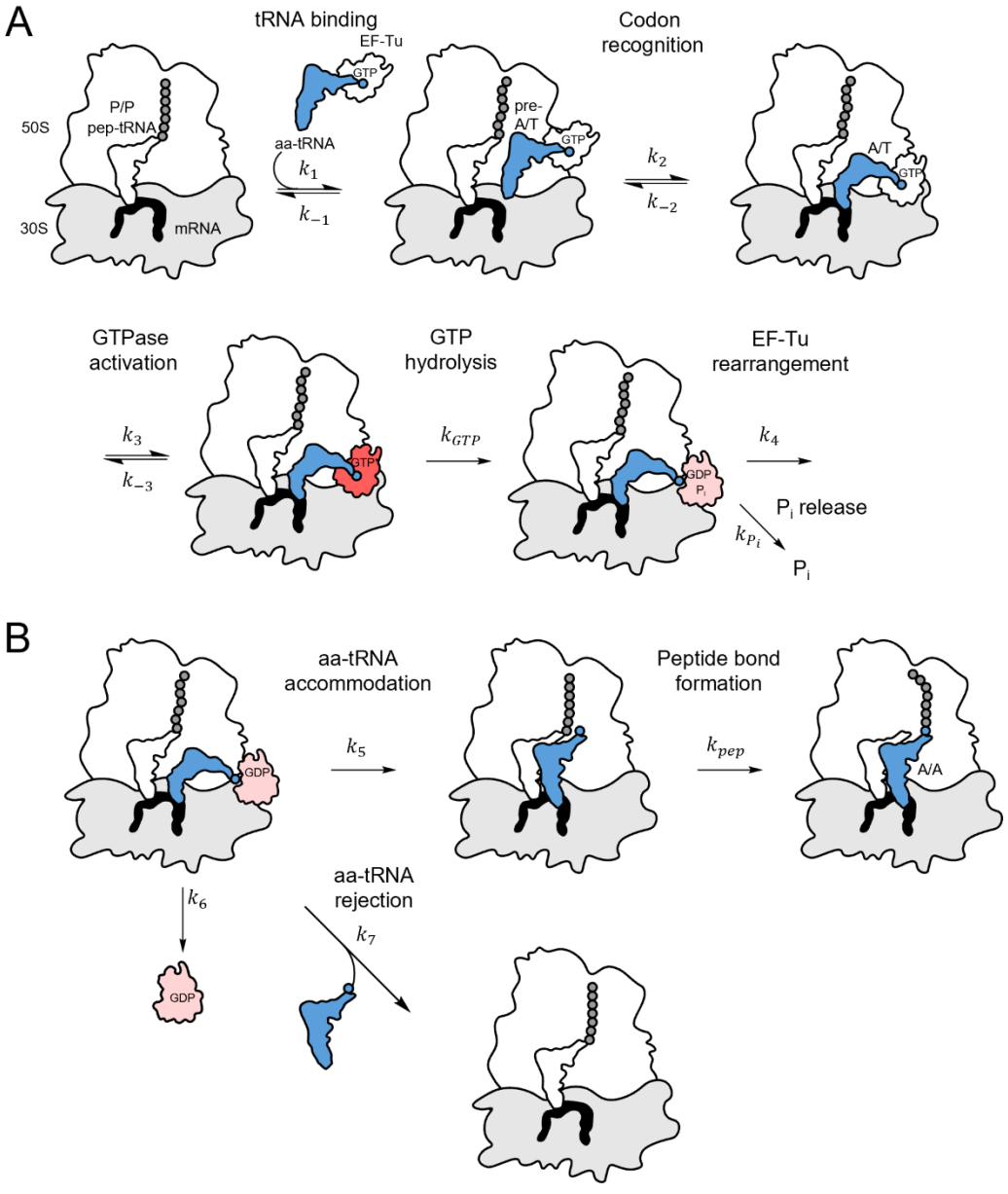

Figure 1.2. The kinetic discrimination mechanism of tRNA selection. (A) Sequence of elementary steps taking place during initial selection (A) and proofreading (B) based on ensemble kinetics and smFRET experiments.[20, 51]

In the first step of the induced-fit kinetic model, aa-tRNA enters the ribosomal A-site in a TC with the GTP-bound elongation factor thermo unstable (EF-Tu; eEF1A in eukaryotes; Figure 1.1A), and adopts the 'T' or 'pre-A/T' state,[44, 50, 56, 59] where the aa-tRNA anticodon is oriented towards the A-site and the acceptor domain is associated with EF-Tu (Figure 1.3A). [20, 22] Importantly, the first step is codon-independent, meaning that k_1 is identical for near-cognate, non-cognate, and cognate aa-tRNAs.[76] In step 2, the tRNA anticodon attempts to bind to the mRNA codon, eventually forming a minihelix with the mRNA codon and adopting the 'A/T', or codon recognition (CR) state (Figure 1.2A and 1.3B).[62, 63, 73] The forward rate constant for codon recognition (k_2) is comparable for cognate aa-tRNAs and near-cognate aa-tRNAs (180-190 s^{-1}), [52] but is essentially zero for non-cognate aa-tRNAs. [43] Selectivity at step 2 is instead controlled by the reverse rate constant (k_{-2}), which is increased for near-cognate (80–140 s^{-1}) compared to cognate (0.2 s^{-1}) aa-tRNAs.[51, 52]

During step 3, the 16S rRNA residues in the SSU decoding center (DC), A1492 and A1493 (A1824 and A1825 in eukaryotes) flip out of helix-44 (h44) to contact the minor groove of the codon-anticodon minihelix. In addition, G530 (G626 in eukaryotes) from h18 latches onto the minihelix.[56, 63, 77] The engagement of these so-called 'monitoring' residues initiates domain closure, where the SSU shoulder compresses against the body domain.[56, 63, 77] Domain closure promotes docking of the G domain of EF-Tu onto the sarcin ricin loop (SRL) located within Helix-95 (H95) of the 23S rRNA (28S in eukaryotes), in the large ribosomal subunit (LSU), forming the GTPase-activated (GA) state, while the aa-tRNA remains in the A/T state bound to the GTP-active EF-Tu (Figure 1.2A and 1.3B).[51] k_3 is preferentially sped up for the cognate aa-tRNAs (~120–500 s^{-1}) relative to the near-cognate aa-tRNAs (~0.06–1.3 s^{-1}).[52, 78]

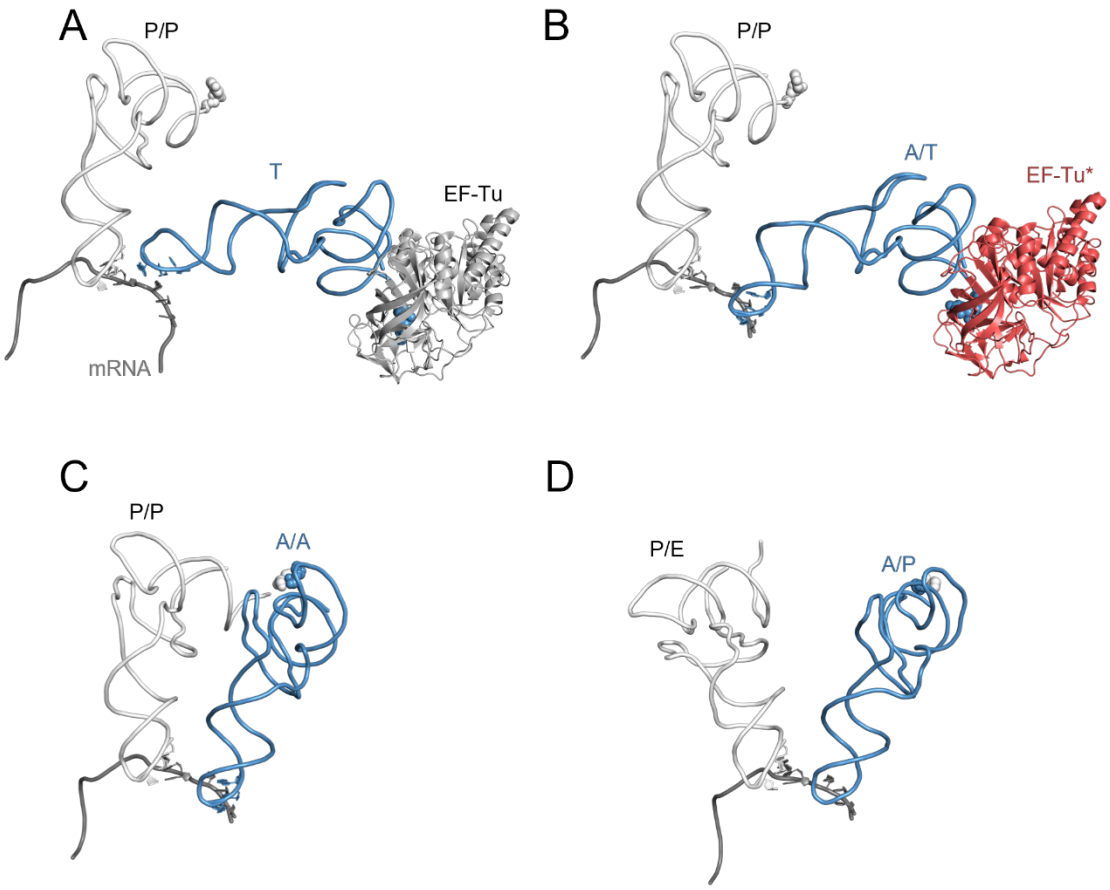

Figure 1.3. Conformations of aa-tRNA (blue) and pep-tRNA (white) during tRNA selection. (A) The T conformation of the aa-tRNA (blue) before establishing the codon-anticodon minihelix (PDB ID: 5UYK).[56] The mRNA is shown in gray. (B) The A/T conformation after the anticodon establishes base-pairing interactions. EF-Tu adopts the GTP-active form (EF-Tu*) if domain closure occurred successfully (PDB ID: 5UYM).[56] (C) Classically positioned A/A and P/P tRNAs after accommodation is complete (PDB ID: 6WDD).[58] (D) Hybrid A/P and P/E conformations of the tRNAs when the ribosome is in the rotated (R) state (PDB ID: 6WDF).[58]

In Step 4, GTP hydrolysis occurs when the catalytic histidine-84 (H84) in switch II of EF-Tu cleaves the γ-phosphate from GTP to form GDP and Pi.[79] EF-Tu then rearranges into its GDP-bound form in step 4, which is more loosely associated with the aa-tRNA, and Pi is released (Figure 1.2A).[80] Overall, during initial selection, mismatches between the codon and anticodon can cause structural deviations in the minihelix, prevent full engagement of the monitoring nucleotides, and increase the likelihood of early TC dissociation from the ribosome.[81, 82]

Proofreading occurs after initial selection, where two different paths are possible. In step 6, EF-Tu(GDP) dissociates from the ribosome, allowing the aa-tRNA to either be rejected or fully accommodated (Figure 1.2B). In the rejection pathway (step 7; Figure 1.2B), GDP-bound EF-Tu and aa-tRNA are removed from the A-site. Proofreading is preferentially sped up by a factor of 20 for near-cognate aa-tRNA over cognate aa-tRNA.[51] In step 5, (aa-tRNA accommodation), GDP-bound EF-Tu dissociation allows aa-tRNA to diffuse along the accommodation corridor from the 'A/T' orientation towards the peptidyl-tRNA (pep-tRNA), adopting the 'A/A' or accommodated (AC) state (Figure 1.2B and Figure 1.3C).[20, 51, 83] Finally, peptide bond formation rapidly occurs, and the nascent polypeptide chain is transferred to the aa-tRNA (Figure 1.2B). The peptide bond reaction is catalyzed by the rRNA peptidyl transferase center (PTC), which involves nucleophilic attack of the pep-tRNA carbonyl C by the α-amino group of the amino acid at the 3'-end of the aa-tRNA.[84-86] After peptide bond formation, the former aa-tRNA becomes the pep-tRNA and the former pep-tRNA is deacylated.

The third stage of elongation involves the translocation of pep-tRNA and deacylated tRNA into the P-site and E-site, respectively. Immediately following peptide bond formation, the ribosome undergoes intrinsic thermal rotation between the non-rotated (N) and rotated (R) states.[87, 88] In the N state, the pep-tRNA and deacylated tRNA adopt the classical A/A and P/P orientations (Figure 1.3C), respectively, whereas in the R state, they adopt hybrid 'A/P' and 'P/E' orientations (Figure 1.3D).[53, 55] GTP-bound EF-G (eEF2 in eukaryotes) preferentially binds to and stabilizes the R-state, promotes SSU domain rearrangements,[89, 90] loosens rRNA contacts with both pep- and deacylated tRNAs to unlock them for movement,[91] weakens rRNA bridges to allow the SSU head to undergo rapid (microsecond timescale) swivelling,[92, 93] to translocate deacylated tRNA to the E-site and pep-tRNA to the P-site.[51, 53, 91, 93-95] EF-G:GDP and the E-site tRNA are then released from the ribosome, completing translocation and opening the A-site for

the next aa-tRNA to bind. Importantly, when pep-tRNA and deacylated tRNA move between distinct binding sites during translocation, the mRNA reading frame can become misaligned, causing a frameshift. Although frameshifting can be due to aberrant translocation,[96-98] it can also be exploited as a viable 'recoding' strategy for certain mRNA sequences.[96, 99, 100]

The choreographed structural motions occurring during elongation are pivotal for maintenance of translational fidelity. However, these coordinated functions would not occur with high efficiency if RNA contained only the limited chemical diversity afforded by the canonical nucleotides (A, C, G, or U). In fact, the canonical nucleotides of tRNA, mRNA, and rRNA are often modified in a manner that can drastically alter their chemical properties, structural dynamics, and functional capabilities during translation.

1.3 The RNA components of translational machinery (rRNA, tRNA, and mRNA) are chemically modified

Naturally occurring modifications are introduced to RNA substrates by enzymes or as a result of damage, ranging from isomerization to complex bulky additions.[1] The most well-studied modifications occur in tRNA and rRNA, which both contain abundant and diverse modifications,[101-104] with crucial roles such as stability, decoding accuracy,[105] ribosome-tRNA interactions, and translational fidelity.[106] As more modifications are discovered due to advancements in detection techniques,[107] it becomes increasingly important to elucidate their roles in altering the structural dynamics of decoding. This section explores how a variety of modifications to tRNA, rRNA, and mRNA impact decoding.

1.3.1 rRNA modifications are highly species-specific, but are clustered in functionally important regions of the ribosome

In *Escherichia coli*, the 16S and 23S rRNA collectively contain 36 modification sites comprising 17 unique chemical structures.[108] These modifications are clustered in functionally important regions of the ribosome, including the PTC,[109] A-site (decoding center), P-,[110] and E-

sites, the peptide exit tunnel and interface regions between the SSU and LSU.[109] For example, two adjacent N6,N6-dimethyladenosine (m^6_2A; Figure 1.4A) modifications are incorporated at the A1518 and A1519 residues found in a stem-loop at the 3'-end of the 16S rRNA.[111] The m^6_2A1518–9 motif is highly conserved across nearly all organisms as essential modifications for ribosome assembly during initiation.[112-115] Another functionally relevant adenosine methylation is m^6A1500,[116, 117] which is positioned at h44 near the decoding site, is proposed to stabilize ribosomal interactions with aa-tRNA.[116]

In eukaryotes, rRNA modifications are generally more abundant than in prokaryotes. For example, in humans there are approximately 14 unique chemical modifications found at over 200 sites.[104] Functional roles have been ascribed to numerous rRNA modifications in eukaryotes, including ribosome biogenesis and maintaining the fidelity and speed of translation.[104, 109, 118, 119] The absence of rRNA modifications is tied to various human diseases.[120] For example, the m^6A4220 (Figure 1.4A) modification in the 28S rRNA, incorporated by ZCCHC4 in humans, has crucial impacts on global translation and may play a role in tumorigenesis.[120-122] Absence of the 1-methyl-3-α-amino-α-carboxyl-propyl pseudouridine ($m^1acp^3\Psi$), 2'-O-methylcytosine(Cm)-1703, and pseudouridine(Ψ)-1243 modifications (Figure 1.4A) have been shown to lead to bacterial resistance to the neomycin antibiotic and incorrect amino acid incorporation.[118, 123] 2'-O-methylations (Bm, where B can be either A, C, G, or U nucleobases; Figure 1.4A) are abundant in the rRNA and have roles in maintaining the efficiency of translation.[109, 124-126] Ψ is an C5-glycoside isomer of U (Figure 1.4B) that is abundantly introduced to rRNA modification with crucial functions in maintaining tRNA positioning and driving ribosome conformational changes (such as Ψ2919 and Ψ826 in yeast),[127, 128] altering rates of translation by ensuring proper H69 dynamics and stabilizing the interaction between h44 and eEF2 in translocation (such as of Ψ2258, Ψ2260, Ψ2264, and Ψ2266 in yeast),[119, 129, 130] and many other functions of the

ribosome.[131, 132] The absence of Ψ609 and Ψ863 in humans was found to interfere with aa-tRNA selection and increase miscoding and stop codon readthrough.[133, 134] Modifications to rRNA suggest a directed evolution towards enhanced function in the core regions of the translational machinery, especially in tRNA and mRNA binding sites where decoding occurs.

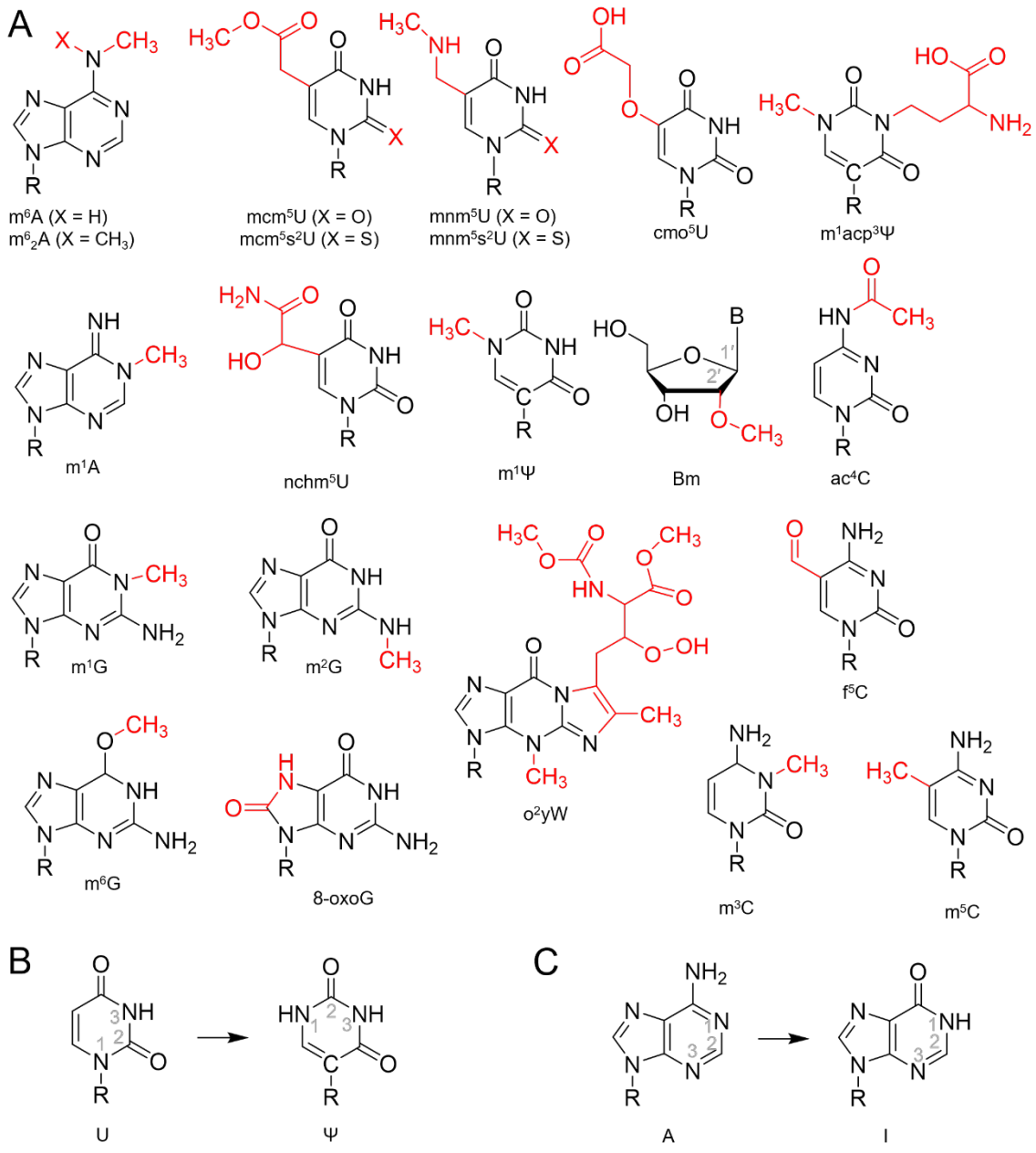

Figure 1.4. Post-transcriptional modifications to RNA. (A) Chemical structures of modified RNA nucleosides (R=ribose and B=nucleobase, which is either A, C, G, or U). (B) Modification of the U nucleobase to pseudouridine (Ψ). (C) Modification of the A nucleobase to inosine (I).

1.3.2 tRNA is heavily modified in the ASL and dysregulated modifications are tied to disease

Just as rRNA modifications cluster in functionally important regions of the ribosome, tRNA modifications are concentrated in key structural domains that enable precise codon recognition. In fact, tRNA is the most highly-modified class of RNA and contains numerous conserved modification sites.[135] The majority of the tRNA modifications appear in the ASL (Figure 1.1B).[135] Experimental work has revealed that ASL modifications are precisely organized and formed in conserved sequence positions *in vivo*, prompting further investigations into the consequences of disrupting tRNA modifications on translation.[136-138] Modifications that are known to impact decoding are predominantly found at the B34 and B37 positions of tRNA and many have well-characterized functions.[137, 139-145] As discussed in Section 1.2, the wobble B34 forms base-pairing interactions with the third codon position B3 and is often afforded additional flexibility in hydrogen-bonding interactions. Modifications to B34 can tune the flexibility in wobble base-pairing.[5, 8, 9, 141, 142, 146-149] For example, the C5 atom of U34 in $tRNA^{Gln}$, $tRNA^{Lys}$, and $tRNA^{Glu}$ is often decorated with a family of complex adducts (hypermodifications) differing by organism (e.g., cmo^5U in bacteria, $nchm^5U$ in archaea, and mcm^5U in eukarya; Figure 1.4A), whereas a thio group can be incorporated at C2 in place of the carbonyl (s^2; Figure 1.4A).[150] Decoding capacity can be altered due to an interplay between functional groups arising from modification.[7, 151] For example, when a bulky moiety is present at C5 of U, but the thio group is absent at C2, the U-turn of the ASL conformation is stabilized and codon reading is restricted to just A or G;[7, 151] however, if both the bulky moiety and the thio substitution are present, the 3'-endo sugar pucker is stabilized,[152] which permits a unique wobble hydrogen-bonding pattern with G that strengthens B3:B34 hydrogen-bonding interactions.[144, 147]

The loss of U34 modifications can impair the efficient translation of AAA, CAA, and GAA codons.[9, 153] For example, the influence of the yeast mcm^5s^2U34 (Figure 1.4A) modification on ribosomal A-site binding and peptide bond formation was studied by comparing A-site binding, dissociation (k_{off}) and association (k_{on}) rate constants, and peptide bond formation rate constants (k_{pep}) between wild-type (WT) fully-modified U34, urm1Δ (lacking s^2) and elp3Δ (lacking mcm^5).[9] In the knockout strains, the A-site binding was reduced, k_{on} was reduced, k_{off} constants were increased, and k_{pep} was reduced.[9] A later study further investigated the influence of uridine modifications in both yeast and nematodes (*Caenorhabditis elegans)*, finding that loss of U34 modifications in tRNA significantly slowed translation of CAA and AAA codons by causing the ribosome to pause.[153] Moreover, impaired U34 modification lead to accumulation of misfolded proteins and aggregates in both yeast and nematodes, indicating that the U34 modifications are crucial for maintaining efficient protein translation across eukaryotes.[153] Ribosome pausing effects were also investigated for the s^2U34 modification during the key kinetic steps of elongation (decoding, peptide bond formation, A- and P- tRNA translocation).[8] The lack of s^2 modifications was found to cause lower codon affinity of Lys-$tRNA^{Lys}$(UUU) towards AAA codons, delayed rearrangements following GTP hydrolysis and slower translocation. Recently, the loss of the s^2 group was found to compromise immune responses in plants, such as impeding translation of the immune regulator NPR1 important for salicylic acid signaling.[154] Therefore, the altered kinetics of decoding caused by hypermodified wobble nucleotide modifications can ultimately impact gene expression and phenotype.

Dysregulated tRNA modifications are associated with the development of several human diseases, known as RNA "modopathies".[155-157] For example, clinical and *in vitro* investigations have shown that impairment of the FTSJ1 enzyme responsible for methylation of the 2'–oxygen at the wobble G34 (Gm34; Figure 1.4A) of $tRNA^{Phe}$ is linked to the development of non-

syndromic X-linked disability (NSXLID) in humans.[158, 159] In the proposed pathogenic mechanism, aberrant Gm34 disrupts the ability of the ribosome to select wobble (UUU) compatible $tRNA^{Phe}$ with the same efficiency as the cognate (UUC) codon.[159, 160] Proper translocation of tRNAs in ribosomal binding sites also depends on modifications, in particular at B37.[96, 161, 162] For instance, the epigenetic silencing of the TYW writer enzymes responsible for the stepwise formation of the hypermodified peroxywybutosine (o^2yW; Figure 1.4A) at B37 in human $tRNA^{Phe}$ was found to disrupt translocation.[163] In particular, the lack of o^2yW37 causes reading frame shifts along the mRNA codon in the ORF for tumor-suppressor gene *ROBO1*, providing a growth advantage to colorectal tumor cells.[163, 164]

In several tRNAs, the wobble adenosine base can be converted into inosine (Figure 1.4C) via A-to-I editing by tRNA-adenosine deaminases (ADATs).[165] This modification confers a substantial effect to mRNA decoding by allowing a single tRNA to translate 3 codons in eukaryotes.[165] In most eukaryotes, 7-8 tRNAs contain I34 and its loss can cause defects in translation, potentially leading to the development of disease.[165, 166] For example, mutations to ADAT3 in humans causes autosomal recessive rare disorders that lead to intellectual disability.[165, 166] I34 was found to influence translation in human embryonic stem cells (hESCs), where in self-renewing cells, ADAT2/3 levels were higher (83-86%) compared to fully differentiated cells (60-79%), resulting in increasing A34I modification.[167] Thus, I34 was found to have a key role in cell fate decisions by managing the translational efficiency in pluripotent stem cells.[167] The impact of I34 on codon usage bias was examined in another study that found removal of I34 by silencing ADAT in *N. crassa* led to more optimal NNT codon translation with respect to NNC codons.[168] Another study examined the role of I34 in tRNAs, particularly focusing on how it enables efficient translation of low-complexity protein domains (rich in TAPSLIVR amino acid sequences) found abundantly in human cells and required for cell adhesion.[169]

Overall, this study found that low-complexity protein translation efficiency was compromised when I34-containing tRNA levels were reduced for only codons requiring I34-tRNAs.[169]

This section has established that modifications to tRNA are abundant, chemically diverse, and well-characterized, with B34 and B37 modifications having proven crucial relevance to decoding. Indeed, the entire set of tRNA modifications are known for *E. coli*, and these modifications have been integrated into the standard genetic code table to reveal how specific modifications at B34 and B37 contribute to accurate and efficient decoding.[170, 171] The increasing understanding of tRNA modifications has exciting implications, such as in expansion of the genetic code to develop protein-based therapeutics via tRNA engineering.[172-174] Although tRNA modifications at or near the anticodon, such as at B34 and B37, have been well recognized for their importance in decoding, the codon carried by the mRNA is equally critical to this interaction. Section 1.3.3 discusses how mRNA modifications within the codon itself are now emerging as important contributors to translational control.

1.3.3 mRNA modifications are crucial for proteostasis but have elusive localized mechanistic impacts to ribosomal decoding

Despite being historically less studied due to their low known chemical diversity and abundance, [175, 176] mRNA modifications have gained attention in recent years due to the highly influential roles they hold in translational regulation and potential in preventative and therapeutic modalities. [11] As the origin of mRNA modifications (enzymatic, damage, or artificial) crucially relates to their cellular roles, the next three subsections detail how mRNA modifications introduced by different means influence protein synthesis. In Section 1.3.3.1, mRNA modifications introduced by enzymes are discussed, with an emphasis on their capabilities in protein regulation. Section 1.3.3.2 discusses various mRNA modifications that occur due to oxidative and alkylative damage, which are increasingly being associated with

pathological states. Lastly, Section 1.3.3.3 covers artificial mRNA modifications, which are scarce, but are emerging for potential use in clinical preventative platforms (e.g., RNA vaccines).

1.3.3.1 Modifications introduced to mRNA by enzymes

N6-methyladenosine (m^6A; Figure 1.4A) is the most extensively studied mRNA modification and one of the few with identified writer enzymes (which install the modification), readers (which recognize and bind to the modification), and erasers (which remove the modification).[177] m^6A controls protein output by stabilizing transcripts or acting as a recognition element for targeted degradation of mRNA.[177] Imbalanced m^6A levels can promote tumorigenesis and cause various cancers.[178, 179] Despite no clearly established pathogenic mechanism, *in vitro* studies revealed that m^6A modification to bacterial mRNA codons decreases the rate of peptide elongation during translation.[180] *In vivo*, m^6A is incorporated in thousands of mRNA sites,[181] and has a known role in modulating mRNA stability.[182] Ribosome profiling, RIP-seq, and reporter assays suggest that the m^6A binding proteins YTHDF1/3 and METTL3 improve translation efficiency for mRNAs containing m^6A modifications.[183] *In vitro* studies with purified ribosome systems showed that elongation rates, as measured by the rate of peptide formation (k_{pep}), are the slowest when m^6A is present in the first position of the codon, while its presence in the third position has a minimal impact,[13, 184-186] likely due to the more permissive nature of wobble pairing. The m^6A modification has been shown to disrupt GTP hydrolysis by EF-Tu,[13] possibly due to destabilization of optimal A:U base-pairing geometry.[187] Interestingly, while the m^6A modification interferes with tRNA binding and accommodation, it does not increase errors in tRNA selection.[13, 184-186] The *in vitro* results can be reconciled by *in vivo* findings, and m^6A likely acts to preserve translational accuracy while regulating translation speed during processes such as co-translational folding.[183,186]

There are several other mRNA modifications that are introduced by enzymes that have been studied to understand their mechanisms in disease treatment or progression. Some notable naturally occurring enzymatic modifications include 5-methylcytosine (m^5C; Figure 1.4A), 2'-O-methylation (Nm; Figure 1.4A), and N4-acetylcytidine (ac^4C; Figure 1.4A). m^5C is widespread in mRNA and was found to suppress full-length protein yield by ~40% when introduced to the middle of the coding sequence at any codon position (B1, B2, or B3) in bacterial mRNAs.[188] m^5C also had context-dependent effects: when introduced to the second codon position m^5C caused miscoding (incorporation of leucine or isoleucine instead of proline at a CCC codon) in a small portion (4%) of elongation events, but no miscoding occurred when in the first and third positions.[188] On the other hand, the Bm modification did not cause miscoding but slightly reduced (10-15%) full-length peptide translation when in the first codon position, but significantly reduced translation by 90% and 50% in the second and third positions, respectively.[188] This effect was attributed to Bm interfering with tRNA accommodation in the A-site. [188] ac^4C enhances translation as determined by *in vivo* experiments when NAT10 (the modification enzyme responsible for ac^4C) was depleted which reduced translation efficiency.[189] Moreover, *in vitro* experiments using reconstituted translation systems showed that ac^4C improved ribosome engagement in mRNA translation in ribosome profiling experiments.[189] The effect of ac^4C was also context-dependent as it was enriched in the third codon positions to stabilize wobble base pairing.[189]

As discussed in Section 1.3.2, inosine is a prevalent modification introduced to tRNA. In mRNA, adenosine nucleosides are also modified by A-to-I editing by enzymes called adenosine deaminases acting on mRNA (ADARs) in eukaryotes.[190, 191] While inosine is incorporated in multiple classes of RNA (miRNA, viral RNA, rRNA, and tRNA) as well as the non-coding regions of mRNA (untranslated regions or introns),[192] it can be found in the coding sequence (CDS) of

mRNA.[193] Inosine has considerable flexibility in base-pairing interactions (e.g., I:C, I:U, and I:A; Figure 1.5A) and experimental studies have attempted to elucidate how inosine can regulate protein expression.[193] In mammals, CDS A-to-I editing regulates protein synthesis for several genes and significantly changes protein function.[194] A-to-I editing sites can recode protein sequences and are often found in exons encoding neurotransmitter receptors and ion channels. Inosine modifications to mRNA can therefore alter functional properties of proteins such as G-protein coupling activity in receptors and ion permeability of ion channels.[193, 195, 196] Due to the importance of these genes in cellular processes, deficiencies or aberrant excesses of A-to-I editing in CDS are linked to human diseases such as neurological disorders,[196-199] cancers,[200-202] and immune-related diseases.[203, 204] Additionally, pathological consequences of dysregulated inosine modification are being identified for the > 1000 sites known for inosine incorporation in the human CDS.[205]

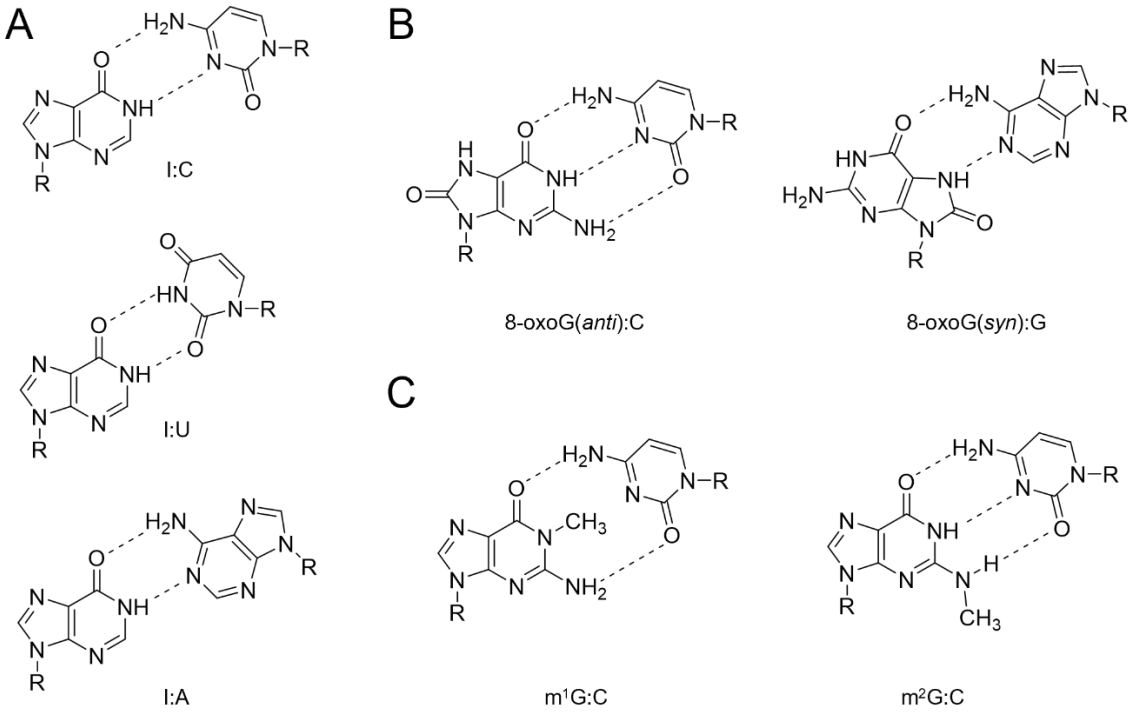

Figure 1.5. Representative base-pairing interactions between unmodified and modified RNA nucleobases. (R=ribose).

The biological impacts of inosine prompted *in vitro* mechanistic studies carried out with reconstituted translation systems.[206] TCs decoding a GGG codon with inosine in the first position (forming IGG) dissociate more readily, reducing translation rates (~30% reduction) in bacteria.[206] Preliminary experiments with *E. coli* reconstituted translation systems performed by the Koutmou lab (Chapter 3) have revealed that inosine insertion into the first position of GUG codons (IUG) causes reduction in the observed rate constant of dipeptide formation, k_{obs}.[207] While k_{obs} reflects an accumulation of fMet-Val dipeptides over time and cannot be directly assigned to a single elementary step, it likely corresponds to the kinetics of the rate-limiting step of aa-tRNA accommodation (k_5; Figure 1.2B).[207] Moreover, in agreement with the experiments for GGG codons, both second and third position modified codons (CIU and GUI, cognate for $tRNA^{Arg}$ and $tRNA^{Val}$, respectively) did not reduce k_{obs} significantly for fMet-Val or fMet-Arg. Inosine is one of the modifications selected for study in this thesis, with the goal to uncover how it modulates the structural dynamics of decoding depending on codon position.

1.3.3.2 mRNA modifications due to damage

mRNA modifications can also arise from alkylative or oxidative damage.[208-215] Such damage is often compared to analogous lesions in DNA, where reactive oxygen species (ROS) or UV light can generate harmful adducts on canonical nucleobases.[216, 217] To counteract the deleterious impacts of DNA damage (e.g., development of cancer or genetic disease), extensive repair mechanisms have evolved across all domains of life.[216, 217] In contrast to DNA, mRNA is more susceptible to the effects of damage.[213] Firstly, mature mRNA transcripts have less well-preserved secondary structures than non-coding RNAs (ncRNAs) such as tRNA and rRNA, and are exposed to the surrounding cytosolic environment that may contain noxious chemical agents. Secondly, direct enzymatic repair pathways have only been hypothesized for a small number of RNA damage modifications (e.g., AlkB repair of m^1A or m^3C lesions).[209, 218-220] Most damaged

nucleotides are retained on the mRNA transcript and serve as a marker to degrade the mRNA before being translated.[209, 211] For example, in eukaryotes, the no-go-decay (NGD) mechanism is typically activated when the ribosome stalls due to encountering an impediment on the mRNA (e.g., transcripts lacking a stop codon or containing a premature stop codon).[221] Recently, NGD mechanisms have been found to also be activated in the presence of mRNA nucleobase oxidation or alkylation damage.[212, 215, 222, 223] Considering that the typical targets of NGD can severely disrupt translation by stalling multiple ribosomes during elongation,[209] these findings suggest that mRNA damage can have particularly harmful outcomes in eukaryotes.[212, 224] While bacteria do not undergo NGD, similar ribosome-rescue mechanisms (e.g., *trans* translation) have been observed to activate when mRNA damage is present.[210]

mRNA damage has been suggested to interfere with the early stages of tRNA selection by disrupting the base-pairing interactions in the codon-anticodon minihelix for the cognate aa-tRNA.[12, 184, 185, 208-210, 214] This also means that mRNA can impair tRNA selection accuracy by slowing the forward selection steps for cognate aa-tRNAs to rates lower than those for near- or non-cognate aa-tRNAs, leading to miscoding. mRNA damage modifications cause ribosome stalling or miscoding in a position-dependent manner, as examined *in vitro* for a number of mRNA modifications.[208-210, 214]

Val-tRNA$^{Val}_{cmo^5UAC}$ recognizes the GUG codon under normal circumstances, but when the first position codon nucleobase contained the O6-methylguanosine (m^6G; Figure 1.4A) alkylative lesion, the bacterial ribosome only accepted near-cognate Met-tRNA$^{Met}_{CAU}$.[208] Moreover, m^6GAA and m^6GCC codons, for which the unmodified codons are decoded by cognate Glu-tRNA$^{Glu}_{UUC}$ and Gly-tRNA$^{Gly}_{GCC}$, led to miscoding of near-cognate Lys-tRNA$^{Lys}_{UUU}$ and Ser-tRNA$^{Ser}_{GCU}$, respectively, in *E. coli*.[185, 208] To test the impact on the second position m^6G, the CGC and AGU codons, decoded by cognate Arg-tRNA$^{Arg}_{ICG}$, and Ser-tRNA$^{Ser}_{GCU}$, respectively, were replaced by

Cm^{6}GC and Am^{6}GU codons, which did not lead to miscoding, but instead caused a significant reduction (>1000-fold) in k_{pep} for cognate tRNAs.[208] However, in another study on m^{6}G-modified mRNA, for Gly-tRNA$^{Gly}_{GCC}$, miscoding of Asp-tRNA$^{Asp}_{GUC}$ was increased in both *E. coli* and wheat germ extract systems encountering the Gm^{6}GC A-site codon.[185] When m^{6}G was incorporated in the third codon position of AUG to form AUm^{6}G, peptide-bond formation was efficient for both the cognate (Met-tRNA$^{Met}_{CAU}$) and near-cognate (Ile-tRNA$^{Ilek2}_{CAU}$) tRNA.[208] Moreover, for the UGm^{6}G codon, both Trp-tRNA^{Trp} and the release factor 2 (RF2) were efficiently selected by the ribosome, suggesting little influence of stalling, but potential premature translation termination induced by the m^{6}G damage in the wobble position.[208]

Damage modifications need not have such nuanced codon position dependency and can instead non-specifically disrupt decoding for any aa-tRNAs attempting to bind in the ribosomal A-site. For example, the oxidative lesion, 8-oxoG (Figure 1.4A), caused a 3-4 orders of magnitude decrease in efficiency of peptide bond formation for modified compared to unmodified codons in all three codon positions with only a moderate increase in miscoding.[213] Specifically, the Arg-tRNA$^{Arg}_{ICG}$ and Val-tRNA$^{Val}_{GAC}$ cognate tRNA for CGC and GUU, both led to poor efficiency of peptide bond formation when encountering the $^{8\text{-oxo}}$CGC and $^{8\text{-oxo}}$GUU codons, respectively.[213] While the corresponding near-cognate Leu-tRNA$^{Leu}_{GAG}$ and Phe-tRNA$^{Phe}_{GAA}$ reacted slightly more favourably than the cognate counterparts, peptide bond formation was still inefficient.[213] The trend of overall decreased peptide bond formation efficiency also held true for the incorporation of 8-oxoG damage in the second and third positions of the codon.[213] A follow-up study confirmed that 8-oxoG significantly perturbs tRNA selection regardless of cognate, near- or non-cognate base-pairing in the A-site.[214] These results were unexpected considering that the 8-oxoG adduct can base pair with A when in the *syn* conformation and C when in the *anti* conformation (Figure 1.5B).[214] Therefore, for cases in which 8-oxoG:A base-pairing interactions

could form, it was suggested to interfere with monitoring by A1492 and G530 with the codon-anticodon minihelix to prevent codon recognition.[214]

Among other alkylation-induced lesions, 1-methylguanosine (m^1G) and 2-methylguanosine (m^2G) have been recently identified in *Saccharomyces cerevisiae* mRNA transcripts (Figure 1.4A).[12, 176, 185] Although present in a low abundance, two studies have reported that both m^1G and m^2G impact translation elongation in a position-dependent fashion.[12, 185] Notably, the experimental methods differ between the two cited studies. The first study used *E. coli*-based cell-free translation kits that included the entire pool of native tRNAs.[185] Semi-quantitative mass spectrometry intensities were used to measure the formation of full-length, mistranslated, or truncated peptides resulting from a damaged nucleotide introduced at the first, second, or third position of the sixth codon in a nine-residue polypeptide chain. Translation bypass efficiency (TBE) was estimated by comparing the peptide signal ratio (modified mRNA vs. competitor) to an unmodified control (i.e., cognate tRNA encountering the unmodified codon represents 100% TBE). The second study was carried out by the Koutmou lab and utilized a fully reconstituted *E. coli* translation system with 70S initiation complexes (ICs) containing P-site $tRNA^{fMet}$.[12] The percent of dipeptides formed (fMet-Val or fMet-Arg) at the endpoint of the assay was precisely quantified for the complexes with m^1G or m^2G inserted into the three codon positions.[12] Despite the methodological differences in the studies, both studies assessed how m^1G and m^2G impact translational efficiency relative to unmodified codons. Moreover, while the second paper did not measure the observed rate constant, k_{obs}, of dipeptide formation, the Koutmou group has since measured them for m^1G and m^2G in all three codon positions.[207]

The m^1G modification disrupts the WCF base-pairing capacity in C:m^1G pairs (Figure 1.5C). In the first study, the first and second position m^1G-modified codons (m^1GCC and Gm^1GC,

respectively) caused negligible TBE measures, suggesting complete disruption of protein product formation.[185] These findings were highly consistent with the study by the Koutmou group and recent kinetics measurements,[12, 207] where the Val-tRNA$^{Val}_{cmo^5UAC}$ and Arg-tRNA$^{Arg}_{ICG}$ encountering the m^{1}GUG and Cm^{1}GU codons, respectively, caused a dramatic reduction in the extent of amino acid addition. Both studies were also in agreement with regard to the effects of the third position m^{1}G, where the presence of the GGm^{1}G codon had little influence on TBE in the first study, and the k_{obs} of Val-tRNA$^{Val}_{cmo^5UAC}$ were similar for GUG and GUm^{1}G in the Koutmou lab data.[12,185,207]

In contrast to m^{1}G, the m^{2}G methyl group is incorporated at the exocyclic amine which can allow it to continue participating directly in WCF hydrogen-bonding interactions in G:C base pairs (Figure 1.5C). In the first study, the m^{2}G modification moderately impeded translation for first (m^{2}GCC; TBE∼42%) and second (Cm^{2}GC; TBE∼48%) position-modified codons, with the largest reduction occurring for the third (GGm^{2}G; TBE∼36%) position. In good agreement, the Koutmou lab data shows that the m^{2}G modification modestly reduced k_{obs} when present in the first (Val-tRNA$^{Val}_{cmo^5UAC}$ decoding m^{2}GUG) and second position (Arg-tRNA$^{Arg}_{ICG}$ decoding Cm^{2}GU) but had a more substantial impact when in the third (Val-tRNA$^{Val}_{cmo^5UAC}$ decoding GUm^{2}G) position.[12, 207] These interesting trends in modulation of translation efficiency by m^{1}G and m^{2}G damage modifications prompted further investigations of these modifications in this thesis.

1.3.3.3 Synthetic mRNA modifications have potential therapeutic applications

Another well-studied modification, Ψ, which was discussed in Section 1.3.1 as an rRNA modification, is also found in thousands of locations in human mRNA sequences.[177, 225-227] Ψ has been proposed to enhance mRNA transcript stability to maintain gene expression during cellular stress responses.[177, 182, 228] Interestingly, Ψ and 1-methylpseudouridine (m^{1}Ψ; Figure 1.4A) are crucial modifications in synthetic mRNA therapeutics that improve clinical effectiveness of

mRNA vaccines by suppressing the innate immune response and increasing target protein production.[229, 230] Immunosuppression is accomplished by Ψ and $m^1Ψ$-enriched transcripts evading Toll-like receptor (TLR) recognition processes and subsequent downregulation of protein factors that detect exogenous RNAs; retinoic acid-inducible gene I (RIG-I) and protein kinase R (PKR).[231, 232] The immunosuppression improves ribosome loading (the proportion of ribosomes bound to mRNA) during initiation.[233]

Ψ and $m^1Ψ$ slow elongation by stabilizing secondary mRNA structural motifs, making it more difficult for advancing ribosomes to unwind the rapidly refolded mRNA structure left behind by the downstream ribosome.[234, 235] This is suggested to reduce collisions with adjacent ribosomes on the same mRNA strand and suppress mRNA degradation pathways to improve protein output.[234] However, such a hypothesis gives little regard to how Ψ and $m^1Ψ$ influence local processes during elongation (i.e., translocation and tRNA selection). For example, single-turnover assays of *E. coli in vitro* translation systems show that both EF-Tu GTPase activation and peptide bond formation were slowed when codons contained Ψ in any position.[10] The study further found that Ψ-containing codons promote miscoding by selecting near-cognate tRNAs *in vitro* and *in vivo*, with a ∼1.5% rise in incorrect amino acid substitutions in human cells.[10] In a separate study, ribosome stalling induced by $m^1Ψ$ was also found to cause +1 ribosomal frameshifting events, leading to mistranslated proteins *in vivo* and *in vitro*, and activating off-target T-cell immune responses.[236] The assumption of a global, sequence-independent mechanism in the ribosome collision hypothesis ignores these local context-dependent effects that may have important roles and off-target effects in development of mRNA modification-based medicines. The off-target effects observed for $m^1Ψ$ indicate that before synthetic mRNA modifications are widely applied in clinical settings, a clear understanding of their mechanistic roles in translation is needed. As new candidates with therapeutic potential are identified, the

need to study their impact on decoding will become increasingly important, including through biophysical and computational investigations. Section 1.4 focuses on experimental techniques used to investigate decoding and on the growing integration of computer simulations into this research workflow.

1.4 Methods to study the impact of mRNA modifications on decoding structural dynamics

Given the discovery of the role of induced-fit kinetics and structural dynamical changes that drive mRNA decoding in the ribosome over the last quarter century, a considerable effort has been put forth to use experimental techniques to establish the fundamental structural motions of the ribosomal complex during decoding,[45, 51, 83, 237] peptidyl transfer,[46, 83] and translocation.[54, 88, 90, 91, 93, 238-243] Since each of these processes involves structural dynamics on different spatial and temporal scales, a variety of experimental techniques have been effectively applied in different contexts. However, elongation dynamics are challenging to study experimentally, requiring many conformational changes that are too rapid (hundreds of microseconds to tens of milliseconds) to be captured by many current biophysical methods without artificially slowing down reaction speeds.[244, 245] However, some experimental techniques have been used to study longer time scale movements of the ribosome. Ribosome processes have been studied using time-resolved cryo-EM (trEM) using voltage-assisted sprays,[246] microfluidic mixing,[247] and Inkjet-based sample application.[248] trEM is limited to time resolutions of seconds to minutes.[55, 88, 242, 249-254] To generate data in the milliseconds range, microfluidic mixing has been used on ribosome complexes.[252, 255-265] While useful for understanding large scale directed processes, these time scales do not capture structural fluctuations on relevant time scales for many rapid molecular changes during decoding.

The precise roles of site-specific mRNA modifications are also difficult or impossible to capture experimentally *in vivo*. At any given instant, mRNA can contain different combinations

of multiple modified nucleotides. Despite the abundance of ribosome structures generated using methods like X-ray crystallography and cryo-EM, it is infeasible to determine structures for many different RNAs with distinct permutations of modifications in specific intermediate kinetic states at high resolution. Moreover, to obtain partially unmodified substrates *in vivo*, experiments rely on interrupting the function of modification enzymes, many of which have unknown alternate roles or may modify other translationally relevant RNA substrates, making it difficult to isolate individual or combined effects of various modification states on the kinetics of translation. Unless the modification of interest has a high-specificity eraser enzyme, this pursuit becomes virtually impossible for the most conventionally used approach where natively modified RNAs are purified from lysate and assembled into programmed ribosomes *in vitro*. Lastly, the central mRNA codon and tRNA anticodon interaction in decoding relies on minute changes to local structure and binding affinities, which are inaccessible within current spatiotemporal constraints of experimental methods. While there are many studies that have given some global insight into how mRNA modifications impact decoding,[10,12] they typically do not measure rate constants of elementary steps that are central to the tRNA selection mechanism, including the rate constants which are selectively increased (k_{-2}, k_{-3}, and k_7; Figure 1.2A) or decreased (k_5; Figure 1.2B) for near-cognate tRNAs relative to cognate. These challenges make it difficult to establish how modification-induced changes to base pairing can cause rapid rejection or perturbation to the codon-anticodon minihelix in the ribosome.

Computational chemistry provides a powerful set of tools to bridge the gaps in our understanding of RNA modifications during protein synthesis left from biochemical and structural experiments. For example, MD simulations use starting coordinates determined from experimental techniques such as X-ray crystallography or cryo-EM and describe the time-dependent atomistic motion of molecules using Newtonian mechanics and interatomic

potentials derived from quantum mechanical calculations and/or experimental data. In light of the "resolution revolution" of cryo-EM techniques producing high resolution models of massive ribosomal complexes including tRNA, mRNA and ribosomal RNA (rRNA),[266] MD simulations using starting models built from these structures are an attractive approach for studying the conformational and energetic changes occurring in the tRNA and mRNA-bound ribosomal complex during translation. Indeed, MD studies have provided crucial insights into the precise structural rearrangements and energetic pathways during the selection of cognate tRNAs over near-cognate tRNAs,[57, 83, 267-269] complementing experimental kinetics data,[270-272] NMR,[273, 274] and fluorescence experiments.[268, 275-278] However, only a small selection of mRNA modifications have been studied using MD simulations,[81, 140, 146, 148, 149, 279] leaving a gap in the literature. This thesis will utilize MD simulations on models built for intermediates during decoding to gain crucial insight into the structural dynamical changes induced by mRNA modifications. As a significant number of MD studies have been completed with the objective of understanding translation, Section 2.2 in Chapter 2 is dedicated to exploring these studies and developing a robust and accurate computational model to be used in this thesis.

1.5 Thesis objectives

The central aim of this thesis is to determine how introducing select mRNA codon modifications influences the structural dynamics of decoding in the ribosome. To accomplish this, all-atom MD (aaMD) simulations will be performed on models of ribosomes containing unmodified and modified codons with the cognate aa-tRNA bound at the A-site. Initially, Chapter 2 provides the groundwork for developing an effective computational model of the ribosome. Chapter 2 is crucial as the A-site model used in this thesis is still new to the literature and is relatively challenging to set up compared to simulations of simple systems. In line with ongoing efforts to promote transparency and reproducibility in MD simulations,[280-282] Section 2.3

of Chapter 2 provides full details of the model and methods used in Chapters 3 and 4, including how each model was built and parameterized, equilibration and production protocols, a computational cost assessment, and details of the trajectory analysis.

This introductory chapter discussed a number of naturally occurring modifications that occur in the mRNA, including those introduced by enzymes (e.g., inosine) or damage (e.g., m^1G and m^2G adducts to G). The goal of the first results chapter (Chapter 3) is to use MD simulations to understand how inosine mRNA modifications influence the structural dynamics of decoding in the ribosomal A-site and provide a structural explanation for the experimental results collected by the Koutmou lab.[207] Subsequently, Chapter 4 uses MD simulations to explore the roles of recently discovered damage modifications, m^1G and m^2G, which were also studied by the Koutmou lab.[207] Chapter 5 summarizes the importance of the present work as a first step to understanding mRNA modifications and their fundamental roles in protein regulation, and provides suggestions for future work in the Wetmore lab.

1.6 References

(1) Cappannini, A.; Ray, A.; Purta, E.; Mukherjee, S.; Boccaletto, P.; Moafinejad, S. N.; Lechner, A.; Barchet, C.; Klaholz, Bruno P.; Stefaniak, F.; et al. MODOMICS: a database of RNA modifications and related information. 2023 update. *Nucleic Acids Res.* **2023**, *52* (D1), D239-D244. DOI: 10.1093/nar/gkad1083 (acccessed 4/14/2025).

(2) Wang, L.; Lin, S. Emerging functions of tRNA modifications in mRNA translation and diseases. *J. Genet. Genom.* **2023**, *50* (4), 223-232. DOI: https://doi.org/10.1016/j.jgg.2022.10.002.

(3) Sloan, K. E.; S., W. A.; Sunny, S.; Karl-Dieter, E.; J., L. D. L.; and Bohnsack, M. T. Tuning the ribosome: The influence of rRNA modification on eukaryotic ribosome biogenesis and function. *RNA Biol.* **2017**, *14* (9), 1138-1152. DOI: 10.1080/15476286.2016.1259781.

(4) Schultz, S. K.; Katanski, C. D.; Halucha, M.; Peña, N.; Fahlman, R. P.; Pan, T.; Kothe, U. Modifications in the T arm of tRNA globally determine tRNA maturation, function, and cellular fitness. *Proc. Natl. Acad. Sci. U.S.A.* **2024**, *121* (26), e2401154121. DOI: doi:10.1073/pnas.2401154121.

(5) Kurata, S.; Weixlbaumer, A.; Ohtsuki, T.; Shimazaki, T.; Wada, T.; Kirino, Y.; Takai, K.; Watanabe, K.; Ramakrishnan, V.; Suzuki, T. Modified uridines with C5-methylene substituents at the first position of the tRNA anticodon stabilize U·G wobble pairing during decoding. *J. Biol. Chem.* **2008**, *283* (27), 18801-18811.

(6) Weixlbaumer, A.; Murphy IV, F. V.; Dziergowska, A.; Malkiewicz, A.; Vendeix, F. A.; Agris, P. F.; Ramakrishnan, V. Mechanism for expanding the decoding capacity of transfer RNAs by modification of uridines. *Nat. Struct. Mol. Biol.* **2007**, *14* (6), 498-502.

(7) Murphy, F. V.; Ramakrishnan, V.; Malkiewicz, A.; Agris, P. F. The role of modifications in codon discrimination by tRNALysUUU. *Nat. Struct. Mol. Biol.* **2004**, *11* (12), 1186-1191. DOI: 10.1038/nsmb861.

(8) Ranjan, N.; Rodnina, M. V. Thio-Modification of tRNA at the Wobble Position as Regulator of the Kinetics of Decoding and Translocation on the Ribosome. *J. Am. Chem. Soc.* **2017**, *139* (16), 5857-5864. DOI: 10.1021/jacs.7b00727.

(9) Rezgui, V. A. N.; Tyagi, K.; Ranjan, N.; Konevega, A. L.; Mittelstaet, J.; Rodnina, M. V.; Peter, M.; Pedrioli, P. G. A. tRNA tK^{UUU}, tQ^{UUG}, and tE^{UUC} wobble position modifications fine-tune protein translation by promoting ribosome A-site binding. *Proc. Natl. Acad. Sci. U.S.A.* **2013**, *110* (30), 12289-12294. DOI: doi:10.1073/pnas.1300781110.

(10) Eyler, D. E.; Franco, M. K.; Batool, Z.; Wu, M. Z.; Dubuke, M. L.; Dobosz-Bartoszek, M.; Jones, J. D.; Polikanov, Y. S.; Roy, B.; Koutmou, K. S. Pseudouridinylation of mRNA coding sequences alters translation. *Proc. Natl. Acad. Sci. U.S.A.* **2019**, *116* (46), 23068-23074. DOI: doi:10.1073/pnas.1821754116.

(11) Franco, M. K.; Koutmou, K. S. Chemical modifications to mRNA nucleobases impact translation elongation and termination. *Biophys. Chem.* **2022**, *285*, 106780. DOI: 10.1016/j.bpc.2022.106780.

(12) Jones, J. D.; Franco, M. K.; Smith, T. J.; Snyder, L. R.; Anders, A. G.; Ruotolo, B. T.; Kennedy, R. T.; Koutmou, K. S. Methylated guanosine and uridine modifications in S. cerevisiae mRNAs modulate translation elongation. *RSC Chem. Biol.* **2023**, *4* (5), 363-378. DOI: 10.1039/d2cb00229a.

(13) Choi, J.; Ieong, K.-W.; Demirci, H.; Chen, J.; Petrov, A.; Prabhakar, A.; O'Leary, S. E.; Dominissini, D.; Rechavi, G.; Soltis, S. M.; et al. N6-methyladenosine in mRNA disrupts tRNA selection and translation-elongation dynamics. *Nat. Struct. Mol. Biol.* **2016**, *23* (2), 110-115. DOI: 10.1038/nsmb.3148.

(14) Choi, J.; Indrisiunaite, G.; DeMirci, H.; Ieong, K.-W.; Wang, J.; Petrov, A.; Prabhakar, A.; Rechavi, G.; Dominissini, D.; He, C.; et al. 2'-O-methylation in mRNA disrupts tRNA decoding during translation elongation. *Nat. Struct. Mol. Biol.* **2018**, *25* (3), 208-216. DOI: 10.1038/s41594-018-0030-z.

(15) Fedor, M. J.; Westhof, E. Ribozymes: The First 20 Years. *Mol. Cell.* **2002**, *10* (4), 703-704. DOI: https://doi.org/10.1016/S1097-2765(02)00700-1.

(16) Walter, N. G.; Engelke, D. R. Ribozymes: catalytic RNAs that cut things, make things, and do odd and useful jobs. *Biologist (London)* **2002**, *49* (5), 199-203.

(17) Maris, C.; Dominguez, C.; Allain, F. H. The RNA recognition motif, a plastic RNA-binding platform to regulate post-transcriptional gene expression. *FEBS J* **2005**, *272* (9), 2118-2131. DOI: 10.1111/j.1742-4658.2005.04653.x.

(18) Li, B.; Vilardell, J.; Warner, J. R. An RNA structure involved in feedback regulation of splicing and of translation is critical for biological fitness. *Proc. Natl. Acad. Sci. U.S.A.* **1996**, *93* (4), 1596-1600. DOI: doi:10.1073/pnas.93.4.1596.

(19) Petrov, A. S.; Gulen, B.; Norris, A. M.; Kovacs, N. A.; Bernier, C. R.; Lanier, K. A.; Fox, G. E.; Harvey, S. C.; Wartell, R. M.; Hud, N. V.; et al. History of the ribosome and the origin of translation. *Proc. Natl. Acad. Sci. U.S.A.* **2015**, *112* (50), 15396-15401. DOI: doi:10.1073/pnas.1509761112.

(20) Rodnina, M. V. Translation in Prokaryotes. *Cold. Spring. Harb. Perspect. Biol.* **2018**, *10* (9). DOI: 10.1101/cshperspect.a032664.

(21) Blanchet, S.; Ranjan, N. Translation Phases in Eukaryotes. In *Ribosome Biogenesis: Methods and Protocols*, Entian, K.-D. Ed.; Springer US, 2022; pp 217-228.

(22) Dever, T. E.; Dinman, J. D.; Green, R. Translation Elongation and Recoding in Eukaryotes. *Cold. Spring. Harb. Perspect. Biol.* **2018**, *10* (8). DOI: 10.1101/cshperspect.a032649.

(23) Sonenberg, N.; Hinnebusch, A. G. Regulation of translation initiation in eukaryotes: mechanisms and biological targets. *Cell* **2009**, *136* (4), 731-745. DOI: 10.1016/j.cell.2009.01.042.

(24) Hellen, C. U. T. Translation Termination and Ribosome Recycling in Eukaryotes. *Cold. Spring. Harb. Perspect. Biol.* **2018**, *10* (10). DOI: 10.1101/cshperspect.a032656.

(25) Brocchieri, L.; Karlin, S. Protein length in eukaryotic and prokaryotic proteomes. *Nucleic Acids Res.* **2005**, *33* (10), 3390-3400. DOI: 10.1093/nar/gki615.

(26) Jia, X.; He, X.; Huang, C.; Li, J.; Dong, Z.; Liu, K. Protein translation: biological processes and therapeutic strategies for human diseases. *Signal Transduct. Target. Ther.* **2024**, *9* (1), 44. DOI: 10.1038/s41392-024-01749-9.

(27) Klassen, R.; Bruch, A.; Schaffrath, R. Independent suppression of ribosomal+ 1 frameshifts by different tRNA anticodon loop modifications. *RNA Biol.* **2017**, *14* (9), 1252-1259.

(28) Chandrasekaran, V.; Juszkiewicz, S.; Choi, J.; Puglisi, J. D.; Brown, A.; Shao, S.; Ramakrishnan, V.; Hegde, R. S. Mechanism of ribosome stalling during translation of a poly(A) tail. *Nat. Struct. Mol. Biol.* **2019**, *26* (12), 1132-1140. DOI: 10.1038/s41594-019-0331-x.

(29) Chyżyńska, K.; Labun, K.; Jones, C.; Grellscheid, S. N.; Valen, E. Deep conservation of ribosome stall sites across RNA processing genes. *NAR Genom. Bioform.* **2021**, *3* (2). DOI: 10.1093/nargab/lqab038 (acccessed 4/18/2025).

(30) Kapur, M.; Ackerman, S. L. mRNA Translation Gone Awry: Translation Fidelity and Neurological Disease. *Trends Genet.* **2018**, *34* (3), 218-231. DOI: 10.1016/j.tig.2017.12.007.

(31) Knight, J. R. P.; Garland, G.; Pöyry, T.; Mead, E.; Vlahov, N.; Sfakianos, A.; Grosso, S.; De-Lima-Hedayioglu, F.; Mallucci, G. R.; von der Haar, T.; et al. Control of translation elongation in health and disease. *Dis Model Mech* **2020**, *13* (3). DOI: 10.1242/dmm.043208.

(32) Faller, W. J.; Jackson, T. J.; Knight, J. R.; Ridgway, R. A.; Jamieson, T.; Karim, S. A.; Jones, C.; Radulescu, S.; Huels, D. J.; Myant, K. B. mTORC1-mediated translational elongation limits intestinal tumour initiation and growth. *Nature* **2015**, *517* (7535), 497-500.

(33) Jan, A.; Jansonius, B.; Delaidelli, A.; Bhanshali, F.; An, Y. A.; Ferreira, N.; Smits, L. M.; Negri, G. L.; Schwamborn, J. C.; Jensen, P. H. Activity of translation regulator eukaryotic elongation factor-2 kinase is increased in Parkinson disease brain and its inhibition reduces alpha synuclein toxicity. *Acta Neuropathol. Commun.* **2018**, *6*, 1-17.

(34) Beckelman, B. C.; Yang, W.; Kasica, N. P.; Zimmermann, H. R.; Zhou, X.; Keene, C. D.; Ryazanov, A. G.; Ma, T. Genetic reduction of eEF2 kinase alleviates pathophysiology in Alzheimer's disease model mice. *J. Clin. Invest.* **2019**, *129* (2), 820-833.

(35) Thompson, R. C.; Stone, P. J. Proofreading of the codon-anticodon interaction on ribosomes. *Proc. Natl. Acad. Sci. U.S.A.* **1977**, *74* (1), 198-202. DOI: doi:10.1073/pnas.74.1.198.

(36) Drummond, D. A. Claus O Wilke The evolutionary consequences of erroneous protein synthesis. *Nat. Rev. Genet.* **2009**, *10* (10), 715-724.

(37) Edelmann, P.; Gallant, J. Mistranslation in E. coli. *Cell* **1977**, *10* (1), 131-137.

(38) Hopfield, J. J. Kinetic Proofreading: A New Mechanism for Reducing Errors in Biosynthetic Processes Requiring High Specificity. *Proc. Natl. Acad. Sci. U.S.A.* **1974**, *71* (10), 4135-4139. DOI: doi:10.1073/pnas.71.10.4135.

(39) Ninio, J. Kinetic amplification of enzyme discrimination. *Biochimie* **1975**, *57* (5), 587-595.

(40) Ehrenberg, M.; Blomberg, C. Thermodynamic constraints on kinetic proofreading in biosynthetic pathways. *Biophys. J.* **1980**, *31* (3), 333-358. DOI: 10.1016/S0006-3495(80)85063-6 (acccessed 2025/04/13).

(41) Thompson, R. C. EFTu provides an internal kinetic standard for translational accuracy. *Trends Biochem. Sci* **1988**, *13* (3), 91-93.

(42) Ruusala, T.; Ehrenberg, M.; Kurland, C. Is there proofreading during polypeptide synthesis? *EMBO J* **1982**, *1* (6), 741-745.

(43) Pape, T.; Wintermeyer, W.; Rodnina, M. Induced-fit in initial selection and proofreading of aminoacyl-tRNA on the ribosome. *EMBO J* **1999**, *18* (13), 3800-3807. DOI: https://doi.org/10.1093/emboj/18.13.3800.

(44) Geggier, P.; Dave, R.; Feldman, M. B.; Terry, D. S.; Altman, R. B.; Munro, J. B.; Blanchard, S. C. Conformational Sampling of Aminoacyl-tRNA during Selection on the Bacterial Ribosome. *J. Mol. Biol.* **2010**, *399* (4), 576-595. DOI: https://doi.org/10.1016/j.jmb.2010.04.038.

(45) Holm, M.; Natchiar, S. K.; Rundlet, E. J.; Myasnikov, A. G.; Watson, Z. L.; Altman, R. B.; Wang, H.-Y.; Taunton, J.; Blanchard, S. C. mRNA decoding in human is kinetically and structurally distinct from bacteria. *Nature* **2023**, *617* (7959), 200-207. DOI: 10.1038/s41586-023-05908-w.

(46) Polikanov, Yury S.; Starosta, Agata L.; Juette, Manuel F.; Altman, Roger B.; Terry, Daniel S.; Lu, W.; Burnett, Benjamin J.; Dinos, G.; Reynolds, Kevin A.; Blanchard, Scott C.; et al. Distinct tRNA Accommodation Intermediates Observed on the Ribosome with the Antibiotics Hygromycin A and A201A. *Mol. Cell.* **2015**, *58* (5), 832-844. DOI: 10.1016/j.molcel.2015.04.014 (acccessed 2025/03/19).

(47) Liu, W.; Chen, C.; Kavaliauskas, D.; Knudsen, C. R.; Goldman, Y. E.; Cooperman, B. S. EF-Tu dynamics during pre-translocation complex formation: EF-Tu· GDP exits the ribosome via two different pathways. *Nucleic Acids Res.* **2015**, *43* (19), 9519-9528.

(48) Schuette, J. C.; Murphy IV, F. V.; Kelley, A. C.; Weir, J. R.; Giesebrecht, J.; Connell, S. R.; Loerke, J.; Mielke, T.; Zhang, W.; Penczek, P. A. GTPase activation of elongation factor EF-Tu by the ribosome during decoding. *EMBO J* **2009**, *28* (6), 755-765.

(49) Lee, T.-H.; Blanchard, S. C.; Kim, H. D.; Puglisi, J. D.; Chu, S. The role of fluctuations in tRNA selection by the ribosome. *Proc. Natl. Acad. Sci. U.S.A.* **2007**, *104* (34), 13661-13665.

(50) Blanchard, S. C.; Gonzalez Jr, R. L.; Kim, H. D.; Chu, S.; Puglisi, J. D. tRNA selection and kinetic proofreading in translation. *Nat. Struct. Mol. Biol.* **2004**, *11* (10), 1008-1014.

(51) Rodnina, M. V.; Fischer, N.; Maracci, C.; Stark, H. Ribosome dynamics during decoding. *Philos. Trans. R. Soc. B, Biol. Sci.* **2017**, *372* (1716), 20160182. DOI: doi:10.1098/rstb.2016.0182.

(52) Gromadski, K. B.; Rodnina, M. V. Kinetic Determinants of High-Fidelity tRNA Discrimination on the Ribosome. *Mol. Cell.* **2004**, *13* (2), 191-200. DOI: 10.1016/S1097-2765(04)00005-X (acccessed 2025/03/19).

(53) Belardinelli, R.; Heena, S.; Frank, P.; Wolfgang, W.; and Rodnina, M. V. Translocation as continuous movement through the ribosome. *RNA Biol.* **2016**, *13* (12), 1197-1203. DOI: 10.1080/15476286.2016.1240140.

(54) Belardinelli, R.; Sharma, H.; Caliskan, N.; Cunha, C. E.; Peske, F.; Wintermeyer, W.; Rodnina, M. V. Choreography of molecular movements during ribosome progression along mRNA. *Nat. Struct. Mol. Biol.* **2016**, *23* (4), 342-348.

(55) Carbone, C. E.; Loveland, A. B.; Gamper Jr, H. B.; Hou, Y.-M.; Demo, G.; Korostelev, A. A. Time-resolved cryo-EM visualizes ribosomal translocation with EF-G and GTP. *Nat. Commun.* **2021**, *12* (1), 7236.

(56) Loveland, A. B.; Demo, G.; Grigorieff, N.; Korostelev, A. A. Ensemble cryo-EM elucidates the mechanism of translation fidelity. *Nature* **2017**, *546* (7656), 113-117. DOI: 10.1038/nature22397.

(57) Girodat, D.; Blanchard, S. C.; Wieden, H.-J.; Sanbonmatsu, K. Y. Elongation Factor Tu Switch I Element is a Gate for Aminoacyl-tRNA Selection. *J. Mol. Biol.* **2020**, *432* (9), 3064-3077. DOI: https://doi.org/10.1016/j.jmb.2020.01.038.

(58) Loveland, A. B.; Demo, G.; Korostelev, A. A. Cryo-EM of elongating ribosome with EF-Tu•GTP elucidates tRNA proofreading. *Nature* **2020**, *584* (7822), 640-645. DOI: 10.1038/s41586-020-2447-x.

(59) Fislage, M.; Zhang, J.; Brown, Z. P.; Mandava, C. S.; Sanyal, S.; Ehrenberg, M.; Frank, J. Cryo-EM shows stages of initial codon selection on the ribosome by aa-tRNA in ternary complex with GTP and the GTPase-deficient EF-Tu^{H84A}. *Nucleic Acids Res.* **2018**, *46* (11), 5861-5874. DOI: 10.1093/nar/gky346 (acccessed 4/21/2025).

(60) Fischer, N.; Neumann, P.; Konevega, A. L.; Bock, L. V.; Ficner, R.; Rodnina, M. V.; Stark, H. Structure of the E. coli ribosome–EF-Tu complex at< 3 Å resolution by Cs-corrected cryo-EM. *Nature* **2015**, *520* (7548), 567-570.

(61) Schmeing, T. M.; Voorhees, R. M.; Kelley, A. C.; Gao, Y.-G.; Murphy IV, F. V.; Weir, J. R.; Ramakrishnan, V. The crystal structure of the ribosome bound to EF-Tu and aminoacyl-tRNA. *Science* **2009**, *326* (5953), 688-694.

(62) Ogle, J. M.; Brodersen, D. E.; Clemons Jr, W. M.; Tarry, M. J.; Carter, A. P.; Ramakrishnan, V. Recognition of cognate transfer RNA by the 30 S ribosomal subunit. *Science* **2001**, *292* (5518), 897-902.

(63) Ogle, J. M.; Murphy, F. V.; Tarry, M. J.; Ramakrishnan, V. Selection of tRNA by the ribosome requires a transition from an open to a closed form. *Cell* **2002**, *111* (5), 721-732.

(64) Jenner, L.; Demeshkina, N.; Yusupova, G.; Yusupov, M. Structural rearrangements of the ribosome at the tRNA proofreading step. *Nat. Struct. Mol. Biol.* **2010**, *17* (9), 1072-1078.

(65) Rozov, A.; Demeshkina, N.; Westhof, E.; Yusupov, M.; Yusupova, G. Structural insights into the translational infidelity mechanism. *Nat. Commun.* **2015**, *6* (1), 7251.

(66) Voorhees, R. M.; Schmeing, T. M.; Kelley, A. C.; Ramakrishnan, V. The mechanism for activation of GTP hydrolysis on the ribosome. *Science* **2010**, *330* (6005), 835-838.

(67) Schmeing, T. M.; Voorhees, R. M.; Kelley, A. C.; Ramakrishnan, V. How mutations in tRNA distant from the anticodon affect the fidelity of decoding. *Nat. Struct. Mol. Biol.* **2011**, *18* (4), 432-436.

(68) Voorhees, R. M.; Mandal, D.; Neubauer, C.; Köhrer, C.; RajBhandary, U. L.; Ramakrishnan, V. The structural basis for specific decoding of AUA by isoleucine tRNA on the ribosome. *Nat. Struct. Mol. Biol.* **2013**, *20* (5), 641-643.

(69) Agirrezabala, X.; Schreiner, E.; Trabuco, L. G.; Lei, J.; Ortiz-Meoz, R. F.; Schulten, K.; Green, R.; Frank, J. Structural insights into cognate versus near-cognate discrimination during decoding. *EMBO Jl* **2011**, *30* (8), 1497-1507. DOI: https://doi.org/10.1038/emboj.2011.58.

(70) Valle, M.; Sengupta, J.; Swami, N. K.; Grassucci, R. A.; Burkhardt, N.; Nierhaus, K. H.; Agrawal, R. K.; Frank, J. Cryo-EM reveals an active role for aminoacyl-tRNA in the accommodation process. *EMBO J* **2002**.

(71) Valle, M.; Zavialov, A.; Li, W.; Stagg, S. M.; Sengupta, J.; Nielsen, R. C.; Nissen, P.; Harvey, S. C.; Ehrenberg, M.; Frank, J. Incorporation of aminoacyl-tRNA into the ribosome as seen by cryo-electron microscopy. *Nat. Struct. Biol.* **2003**, *10* (11), 899-906.

(72) Shao, S.; Murray, J.; Brown, A.; Taunton, J.; Ramakrishnan, V.; Hegde, R. S. Decoding mammalian ribosome-mRNA states by translational GTPase complexes. *Cell* **2016**, *167* (5), 1229-1240. e1215.

(73) Stark, H.; Rodnina, M. V.; Wieden, H.-J.; Zemlin, F.; Wintermeyer, W.; Van Heel, M. Ribosome interactions of aminoacyl-tRNA and elongation factor Tu in the codon-recognition complex. *Nat. Struct. Biol.* **2002**, *9* (11), 849-854.

(74) Tsai, A.; Uemura, S.; Johansson, M.; Puglisi, E. V.; Marshall, R. A.; Aitken, C. E.; Korlach, J.; Ehrenberg, M.; Puglisi, J. D. The impact of aminoglycosides on the dynamics of translation elongation. *Cell Rep.* **2013**, *3* (2), 497-508.

(75) Villa, E.; Sengupta, J.; Trabuco, L. G.; LeBarron, J.; Baxter, W. T.; Shaikh, T. R.; Grassucci, R. A.; Nissen, P.; Ehrenberg, M.; Schulten, K. Ribosome-induced changes in elongation factor Tu conformation control GTP hydrolysis. *Proc. Natl. Acad. Sci. U.S.A.* **2009**, *106* (4), 1063-1068.

(76) Zaher, H. S.; Green, R. Fidelity at the Molecular Level: Lessons from Protein Synthesis. *Cell* **2009**, *136* (4), 746-762. DOI: https://doi.org/10.1016/j.cell.2009.01.036.

(77) Pavlov, M. Y.; Ehrenberg, M. Substrate-Induced Formation of Ribosomal Decoding Center for Accurate and Rapid Genetic Code Translation. *Anu.l Rev. Biophys.* **2018**, *47* (Volume 47, 2018), 525-548. DOI: https://doi.org/10.1146/annurev-biophys-060414-034148.

(78) Gromadski, K. B.; Daviter, T.; Rodnina, M. V. A uniform response to mismatches in codon-anticodon complexes ensures ribosomal fidelity. *Mol. Cell.* **2006**, *21* (3), 369-377.

(79) Daviter, T.; Wieden, H.-J.; Rodnina, M. V. Essential role of histidine 84 in elongation factor Tu for the chemical step of GTP hydrolysis on the ribosome. *J. Mol. Biol.* **2003**, *332* (3), 689-699.

(80) Frank, J.; Sengupta, J.; Gao, H.; Li, W.; Valle, M.; Zavialov, A.; Ehrenberg, M. The role of tRNA as a molecular spring in decoding, accommodation, and peptidyl transfer. *FEBS Lett.* **2005**, *579* (4), 959-962.

(81) Satpati, P.; Sund, J.; Åqvist, J. Structure-Based Energetics of mRNA Decoding on the Ribosome. *Biochem.* **2014**, *53* (10), 1714-1722. DOI: 10.1021/bi5000355.

(82) Daviter, T.; Gromadski, K. B.; Rodnina, M. V. The ribosome's response to codon–anticodon mismatches. *Biochimie* **2006**, *88* (8), 1001-1011. DOI: https://doi.org/10.1016/j.biochi.2006.04.013.

(83) Morse, J. C.; Girodat, D.; Burnett, B. J.; Holm, M.; Altman, R. B.; Sanbonmatsu, K. Y.; Wieden, H.-J.; Blanchard, S. C. Elongation factor-Tu can repetitively engage aminoacyl-tRNA within the ribosome during the proofreading stage of tRNA selection. *Proc. Natl. Acad. Sci. U.S.A.* **2020**, *117* (7), 3610-3620. DOI: doi:10.1073/pnas.1904469117.

(84) Wallin, G.; Åqvist, J. The transition state for peptide bond formation reveals the ribosome as a water trap. *Proc. Natl. Acad. Sci. U.S.A.* **2010**, *107* (5), 1888-1893.

(85) Kuhlenkoetter, S.; Wintermeyer, W.; Rodnina, M. V. Different substrate-dependent transition states in the active site of the ribosome. *Nature* **2011**, *476* (7360), 351-354.

(86) Hiller, D. A.; Singh, V.; Zhong, M.; Strobel, S. A. A two-step chemical mechanism for ribosome-catalysed peptide bond formation. *Nature* **2011**, *476* (7359), 236-239.

(87) Rodnina, M. V.; Wintermeyer, W. The ribosome as a molecular machine: the mechanism of tRNA-mRNA movement in translocation. *Biochem. Soc. Trans.* **2011**, *39* (2), 658-662. DOI: 10.1042/bst0390658.

(88) Petrychenko, V.; Peng, B.-Z.; de AP Schwarzer, A. C.; Peske, F.; Rodnina, M. V.; Fischer, N. Structural mechanism of GTPase-powered ribosome-tRNA movement. *Nat. Commun.* **2021**, *12* (1), 5933.

(89) Savelsbergh, A.; Katunin, V. I.; Mohr, D.; Peske, F.; Rodnina, M. V.; Wintermeyer, W. An elongation factor G-induced ribosome rearrangement precedes tRNA-mRNA translocation. *Mol. Cell.* **2003**, *11* (6), 1517-1523.

(90) Liu, G.; Song, G.; Zhang, D.; Zhang, D.; Li, Z.; Lyu, Z.; Dong, J.; Achenbach, J.; Gong, W.; Zhao, X. S. EF-G catalyzes tRNA translocation by disrupting interactions between decoding center and codon–anticodon duplex. *Nat. Struct. Mol. Biol.* **2014**, *21* (9), 817-824.

(91) Wasserman, M. R.; Alejo, J. L.; Altman, R. B.; Blanchard, S. C. Multiperspective smFRET reveals rate-determining late intermediates of ribosomal translocation. *Nat. Struct. Mol. Biol.* **2016**, *23* (4), 333-341. DOI: 10.1038/nsmb.3177.

(92) Liu, Q.; Fredrick, K. Contribution of intersubunit bridges to the energy barrier of ribosomal translocation. *Nucleic Acids Res.* **2013**, *41* (1), 565-574. DOI: 10.1093/nar/gks1074.

(93) Bock, L. V.; Blau, C.; Schröder, G. F.; Davydov, I. I.; Fischer, N.; Stark, H.; Rodnina, M. V.; Vaiana, A. C.; Grubmüller, H. Energy barriers and driving forces in tRNA translocation through the ribosome. *Nat. Struct. Mol. Biol.* **2013**, *20* (12), 1390-1396.

(94) Frank, J.; Gonzalez Jr, R. L. Structure and dynamics of a processive Brownian motor: the translating ribosome. *Annu. Rev. Biochem* **2010**, *79* (1), 381-412.

(95) Adio, S.; Senyushkina, T.; Peske, F.; Fischer, N.; Wintermeyer, W.; Rodnina, M. V. Fluctuations between multiple EF-G-induced chimeric tRNA states during translocation on the ribosome. *Nat. Commun.* **2015**, *6* (1), 7442.

(96) Hong, S.; Sunita, S.; Maehigashi, T.; Hoffer, E. D.; Dunkle, J. A.; Dunham, C. M. Mechanism of tRNA-mediated +1 ribosomal frameshifting. *Proc. Natl. Acad. Sci. U.S.A.* **2018**, *115* (44), 11226-11231. DOI: doi:10.1073/pnas.1809319115.

(97) Poulis, P.; Patel, A.; Rodnina, M. V.; Adio, S. Altered tRNA dynamics during translocation on slippery mRNA as determinant of spontaneous ribosome frameshifting. *Nat. Commun.* **2022**, *13* (1), 4231. DOI: 10.1038/s41467-022-31852-w.

(98) Dunkle, J. A.; Dunham, C. M. Mechanisms of mRNA frame maintenance and its subversion during translation of the genetic code. *Biochimie* **2015**, *114*, 90-96. DOI: 10.1016/j.biochi.2015.02.007.

(99) Demo, G.; Gamper, H. B.; Loveland, A. B.; Masuda, I.; Carbone, C. E.; Svidritskiy, E.; Hou, Y.-M.; Korostelev, A. A. Structural basis for +1 ribosomal frameshifting during EF-G-catalyzed translocation. *Nat. Commun.* **2021**, *12* (1), 4644. DOI: 10.1038/s41467-021-24911-1.

(100) Yan, S.; Wen, J. D.; Bustamante, C.; Tinoco, I., Jr. Ribosome excursions during mRNA translocation mediate broad branching of frameshift pathways. *Cell* **2015**, *160* (5), 870-881. DOI: 10.1016/j.cell.2015.02.003.

(101) Pan, T. Modifications and functional genomics of human transfer RNA. *Cell Res.* **2018**, *28* (4), 395-404. DOI: 10.1038/s41422-018-0013-y.

(102) Zhang, W.; Foo, M.; Eren, A. M.; Pan, T. tRNA modification dynamics from individual organisms to metaepitranscriptomics of microbiomes. *Mol Cell* **2022**, *82* (5), 891-906. DOI: 10.1016/j.molcel.2021.12.007.

(103) Suzuki, T. The expanding world of tRNA modifications and their disease relevance. *Nat. Rev. Mol. Cell. Biol.* **2021**, *22* (6), 375-392. DOI: 10.1038/s41580-021-00342-0.

(104) Taoka, M.; Nobe, Y.; Yamaki, Y.; Sato, K.; Ishikawa, H.; Izumikawa, K.; Yamauchi, Y.; Hirota, K.; Nakayama, H.; Takahashi, N.; et al. Landscape of the complete RNA chemical modifications in the human 80S ribosome. *Nucleic Acids Res.* **2018**, *46* (18), 9289-9298. DOI: 10.1093/nar/gky811 (acccessed 2/3/2025).

(105) Gustilo, E. M.; Vendeix, F. A.; Agris, P. F. tRNA's modifications bring order to gene expression. *Curr. Opin. Microbiol.* **2008**, *11* (2), 134-140. DOI: 10.1016/j.mib.2008.02.003.

(106) Ontiveros, R. J.; Stoute, J.; Liu, K. F. The chemical diversity of RNA modifications. *Biochem. J* **2019**, *476* (8), 1227-1245. DOI: 10.1042/bcj20180445.

(107) Zhang, Y.; Lu, L.; Li, X. Detection technologies for RNA modifications. *Exp. Mol. Med.* **2022**, *54* (10), 1601-1616. DOI: 10.1038/s12276-022-00821-0.

(108) Fleming, A. M.; Bommisetti, P.; Xiao, S.; Bandarian, V.; Burrows, C. J. Direct Nanopore Sequencing for the 17 RNA Modification Types in 36 Locations in the E. coli Ribosome Enables Monitoring of Stress-Dependent Changes. *ACS Chem. Bio.* **2023**, *18* (10), 2211-2223. DOI: 10.1021/acschembio.3c00166.

(109) Decatur, W. A.; Fournier, M. J. rRNA modifications and ribosome function. *Trends Biochem. Sci.* **2002**, *27* (7), 344-351.

(110) Kimura, S.; Suzuki, T. Fine-tuning of the ribosomal decoding center by conserved methyl-modifications in the Escherichia coli 16S rRNA. *Nucleic Acids Res.* **2009**, *38* (4), 1341-1352. DOI: 10.1093/nar/gkp1073 (acccessed 4/20/2025).

(111) Formenoy, L. J.; Cunningham, P. R.; Nurse, K.; Pleij, C. W. A.; Ofengand, J. Methylation of the conserved A1518-A1519 in Escherichia coli 16S ribosomal RNA by the ksgA methyltransferase is influenced by methylations around the similarly conserved U1512-G1523 base pair in the 3' terminal hairpin. *Biochimie* **1994**, *76* (12), 1123-1128. DOI: https://doi.org/10.1016/0300-9084(94)90040-X.

(112) Natchiar, S. K.; Myasnikov, A. G.; Kratzat, H.; Hazemann, I.; Klaholz, B. P. Visualization of chemical modifications in the human 80S ribosome structure. *Nature* **2017**, *551* (7681), 472-477. DOI: 10.1038/nature24482.

(113) van Buul, C. P. J. J.; van Knippenberg, P. H. Nucleotide sequence of the ksgA gene of Escherichia coli: comparison of methyltransferases effecting dimethylation of adenosine in ribosomal RNA. *Gene* **1985**, *38* (1), 65-72. DOI: https://doi.org/10.1016/0378-1119(85)90204-5.

(114) O'Farrell, H. C.; Scarsdale, J. N.; Rife, J. P. Crystal Structure of KsgA, a Universally Conserved rRNA Adenine Dimethyltransferase in Escherichia coli. *J. Mol. Biol.* **2004**, *339* (2), 337-353. DOI: https://doi.org/10.1016/j.jmb.2004.02.068.

(115) Zorbas, C.; Nicolas, E.; Wacheul, L.; Huvelle, E.; Heurgué-Hamard, V.; Lafontaine, D. L. J. The human 18S rRNA base methyltransferases DIMT1L and WBSCR22-TRMT112 but not rRNA modification are required for ribosome biogenesis. *Mol. Biol. Cell.* **2015**, *26* (11), 2080-2095. DOI: 10.1091/mbc.E15-02-0073.

(116) Rong, B.; Zhang, Q.; Wan, J.; Xing, S.; Dai, R.; Li, Y.; Cai, J.; Xie, J.; Song, Y.; Chen, J.; et al. Ribosome 18S m6A Methyltransferase METTL5 Promotes Translation Initiation and Breast Cancer Cell Growth. *Cell Rep.* **2020**, *33* (12), 108544. DOI: https://doi.org/10.1016/j.celrep.2020.108544.

(117) López, J.; Blanco, S. Exploring the role of ribosomal RNA modifications in cancer. *Curr. Opin. Genet. Dev.* **2024**, *86*, 102204. DOI: https://doi.org/10.1016/j.gde.2024.102204.

(118) Baudin-Baillieu, A.; Fabret, C.; Liang, X.-h.; Piekna-Przybylska, D.; Fournier, M. J.; Rousset, J.-P. Nucleotide modifications in three functionally important regions of the Saccharomyces cerevisiae ribosome affect translation accuracy. *Nucleic Acids Res.* **2009**, *37* (22), 7665-7677.

(119) Liang, X.-h.; Liu, Q.; Fournier, M. J. rRNA modifications in an intersubunit bridge of the ribosome strongly affect both ribosome biogenesis and activity. *Mol. Cell.* **2007**, *28* (6), 965-977.

(120) Cui, L.; Zheng, J.; Lin, Y.; Lin, P.; Lu, Y.; Zheng, Y.; Guo, B.; Zhao, X. Decoding the ribosome's hidden language: rRNA modifications as key players in cancer dynamics and targeted therapies. *Clin. Transl. Med.* **2024**, *14* (5), e1705. DOI: 10.1002/ctm2.1705.

(121) Ma, H.; Wang, X.; Cai, J.; Dai, Q.; Natchiar, S. K.; Lv, R.; Chen, K.; Lu, Z.; Chen, H.; Shi, Y. G. N 6-Methyladenosine methyltransferase ZCCHC4 mediates ribosomal RNA methylation. *Nat. Chem. Biol.* **2019**, *15* (1), 88-94.

(122) Pinto, R.; Vågbø, C. B.; Jakobsson, M. E.; Kim, Y.; Baltissen, M. P.; O'Donohue, M.-F.; Guzmán, U. H.; Małecki, J. M.; Wu, J.; Kirpekar, F. The human methyltransferase ZCCHC4 catalyses N 6-methyladenosine modification of 28S ribosomal RNA. *Nucleic Acids Res.* **2020**, *48* (2), 830-846.

(123) Liang, X.-h.; Liu, Q.; Fournier, M. J. Loss of rRNA modifications in the decoding center of the ribosome impairs translation and strongly delays pre-rRNA processing. *RNA* **2009**, *15* (9), 1716-1728.

(124) Wiechert, F.; Unbehaun, A.; Sprink, T.; Seibel, H.; Bürger, J.; Loerke, J.; Mielke, T.; Diebolder, Christoph A.; Schacherl, M.; Spahn, Christian M. T. Visualizing the modification landscape of the human 60S ribosomal subunit at close to atomic resolution. *Nucleic Acids Res.* **2024**, *53* (1). DOI: 10.1093/nar/gkae1191 (acccessed 2/18/2025).

(125) Lin, J.; Lai, S.; Jia, R.; Xu, A.; Zhang, L.; Lu, J.; Ye, K. Structural basis for site-specific ribose methylation by box C/D RNA protein complexes. *Nature* **2011**, *469* (7331), 559-563.

(126) Marcel, V.; Ghayad, S. E.; Belin, S.; Therizols, G.; Morel, A.-P.; Solano-Gonzàlez, E.; Vendrell, J. A.; Hacot, S.; Mertani, H. C.; Albaret, M. A. p53 acts as a safeguard of translational control by regulating fibrillarin and rRNA methylation in cancer. *Cancer Cell* **2013**, *24* (3), 318-330.

(127) Zhao, Y.; Rai, J.; Yu, H.; Li, H. CryoEM structures of pseudouridine-free ribosome suggest impacts of chemical modifications on ribosome conformations. *Structure* **2022**, *30* (7), 983-992.e985. DOI: https://doi.org/10.1016/j.str.2022.04.002.

(128) King, T. H.; Liu, B.; McCully, R. R.; Fournier, M. J. Ribosome structure and activity are altered in cells lacking snoRNPs that form pseudouridines in the peptidyl transferase center. *Mol. Cell.* **2003**, *11* (2), 425-435.

(129) Sumita, M.; Desaulniers, J.-P.; Chang, Y.-C.; Chui, H. M.-P.; CLOS, L.; Chow, C. S. Effects of nucleotide substitution and modification on the stability and structure of helix 69 from 28S rRNA. *RNA* **2005**, *11* (9), 1420-1429.

(130) Zhao, Y.; Rai, J.; Li, H. Regulation of translation by ribosomal RNA pseudouridylation. *Sci. Adv.* **2023**, *9* (33), eadg8190. DOI: doi:10.1126/sciadv.adg8190.

(131) Jia, S.; Yu, X.; Deng, N.; Zheng, C.; Ju, M.; Wang, F.; Zhang, Y.; Gao, Z.; Li, Y.; Zhou, H.; et al. Deciphering the pseudouridine nucleobase modification in human diseases: From molecular mechanisms to clinical perspectives. *Clin. Trans. Med.* **2025**, *15* (1), e70190. DOI: https://doi.org/10.1002/ctm2.70190.

(132) Barozzi, C.; Zacchini, F.; Corradini, A. G.; Morara, M.; Serra, M.; De Sanctis, V.; Bertorelli, R.; Dassi, E.; Montanaro, L. Alterations of ribosomal RNA pseudouridylation in human breast cancer. *NAR Cancer* **2023**, *5* (2). DOI: 10.1093/narcan/zcad026 (acccessed 2/18/2025).

(133) McMahon, M.; Contreras, A.; Holm, M.; Uechi, T.; Forester, C. M.; Pang, X.; Jackson, C.; Calvert, M. E.; Chen, B.; Quigley, D. A. A single H/ACA small nucleolar RNA mediates tumor suppression downstream of oncogenic RAS. *Elife* **2019**, *8*, e48847.

(134) Milenkovic, I.; Novoa, E. M. Dynamic rRNA modifications as a source of ribosome heterogeneity. *Trends Cell Biol.* **2024**. DOI: https://doi.org/10.1016/j.tcb.2024.10.001.

(135) Machnicka, M. A.; Olchowik, A.; Grosjean, H.; Bujnicki, J. M. Distribution and frequencies of post-transcriptional modifications in tRNAs. *RNA Biol.* **2014**, *11* (12), 1619-1629. DOI: 10.4161/15476286.2014.992273.

(136) Li, J.; Zhu, W. Y.; Yang, W. Q.; Li, C. T.; Liu, R. J. The occurrence order and cross-talk of different tRNA modifications. *Sci. China Life Sci.* **2021**, *64* (9), 1423-1436. DOI: 10.1007/s11427-020-1906-4.

(137) Smith, T. J.; Giles, R. N.; Koutmou, K. S. Anticodon stem-loop tRNA modifications influence codon decoding and frame maintenance during translation. *Semin. Cell Dev. Biol.* **2024**, *154* (Pt B), 105-113. DOI: 10.1016/j.semcdb.2023.06.003.

(138) Han, L.; Phizicky, E. M. A rationale for tRNA modification circuits in the anticodon loop. *RNA* **2018**, *24* (10), 1277-1284. DOI: 10.1261/rna.067736.118.

(139) Lea, M. J.; Fonderson, C.; Prabhakar, P. S.; Pandya, B.; Yee, K.; Takyi, N.; Wetmore, S. D. Chemical Composition, Sequence Context, and Base-Pairing Potential of Posttranscriptional Modifications at the Wobble Position of the tRNA Anticodon Loop. *Can. J. Chem.* **2025**, *103* (5), 17. DOI: 10.1139/cjc-2024-0276.

(140) Allnér, O.; Nilsson, L. Nucleotide modifications and tRNA anticodon-mRNA codon interactions on the ribosome. *RNA* **2011**, *17* (12), 2177-2188. DOI: 10.1261/rna.029231.111.

(141) Nilsson, E. M.; Alexander, R. W. Bacterial wobble modifications of NNA-decoding tRNAs. *IUBMB Life* **2019**, *71* (8), 1158-1166. DOI: 10.1002/iub.2120.

(142) Agris, P. F.; Vendeix, F. A. P.; Graham, W. D. tRNA's Wobble Decoding of the Genome: 40 Years of Modification. *J. Mol. Biol.* **2007**, *366* (1), 1-13. DOI: https://doi.org/10.1016/j.jmb.2006.11.046.

(143) Kompatscher, M.; Bartosik, K.; Erharter, K.; Plangger, R.; Juen, Fabian S.; Kreutz, C.; Micura, R.; Westhof, E.; Erlacher, Matthias D. Contribution of tRNA sequence and modifications to the decoding preferences of *E. coli* and *M. mycoides* $tRNA_{Gly}^{UCC}$ for synonymous glycine codons. *Nucleic Acids Res.* **2023**, *52* (3), 1374-1386. DOI: 10.1093/nar/gkad1136 (acccessed 4/20/2025).

(144) Rozov, A.; Demeshkina, N.; Khusainov, I.; Westhof, E.; Yusupov, M.; Yusupova, G. Novel base-pairing interactions at the tRNA wobble position crucial for accurate reading of the genetic code. *Nat. Commun.* **2016**, *7* (1), 10457. DOI: 10.1038/ncomms10457.

(145) Agris, P. F.; R., E. E.; Amithi, N.; P., V. V. Y.; Sweta, V.; and Ranganathan, S. V. Celebrating wobble decoding: Half a century and still much is new. *RNA Biol.* **2018**, *15* (4-5), 537-553. DOI: 10.1080/15476286.2017.1356562.

(146) Kamble, A. S.; Fandilolu, P. M.; Sambhare, S. B.; Sonawane, K. D. Idiosyncratic recognition of UUG/UUA codons by modified nucleoside 5-taurinomethyluridine, $taum^5U$ present at 'wobble' position in anticodon loop of tRNALeu: A molecular modeling approach. *PLoS One* **2017**, *12* (4), e0176756. DOI: 10.1371/journal.pone.0176756.

(147) Sochacka, E.; Lodyga-Chruscinska, E.; Pawlak, J.; Cypryk, M.; Bartos, P.; Ebenryter-Olbinska, K.; Leszczynska, G.; Nawrot, B. C5-substituents of uridines and 2-thiouridines present at the wobble position of tRNA determine the formation of their keto-enol or zwitterionic forms-a factor important for accuracy of reading of guanosine at the 3′-end of the mRNA codons. *Nucleic Acids Res.* **2017**, *45* (8), 4825-4836.

(148) Vangaveti, S.; Cantara, W. A.; Spears, J. L.; DeMirci, H.; Murphy, F. V. t.; Ranganathan, S. V.; Sarachan, K. L.; Agris, P. F. A Structural Basis for Restricted Codon Recognition Mediated by 2-thiocytidine in tRNA Containing a Wobble Position Inosine. *J. Mol. Biol.* **2020**, *432* (4), 913-929. DOI: 10.1016/j.jmb.2019.12.016.

(149) Vangaveti, S.; Ranganathan, S. V.; Agris, P. F. Physical Chemistry of a Single tRNA-Modified Nucleoside Regulates Decoding of the Synonymous Lysine Wobble Codon and Affects Type 2 Diabetes. *J. Phys. Chem. B* **2022**, *126* (6), 1168-1177. DOI: 10.1021/acs.jpcb.1c09053.

(150) Bimai, O.; Legrand, P.; Ravanat, J.-L.; Touati, N.; Zhou, J.; He, N.; Lénon, M.; Barras, F.; Fontecave, M.; Golinelli-Pimpaneau, B. The thiolation of uridine 34 in tRNA, which controls protein translation, depends on a [4Fe-4S] cluster in the archaeum *Methanococcus maripaludis*. *Sci. Rep.* **2023**, *13* (1), 5351. DOI: 10.1038/s41598-023-32423-9.

(151) Durant, P. C.; Bajji, A. C.; Sundaram, M.; Kumar, R. K.; Davis, D. R. Structural Effects of Hypermodified Nucleosides in the *Escherichia coli* and Human $tRNA^{Lys}$ Anticodon Loop: The Effect of Nucleosides s^2U, mcm^5U, mcm^5s^2U, mnm^5s^2U, t^6A, and ms^2t^6A. *Biochem.* **2005**, *44* (22), 8078-8089. DOI: 10.1021/bi050343f.

(152) Kumar, R. K.; Davis, D. R. Synthesis and Studies on the Effect of 2-Thiouridine and 4-Thiouridine on Sugar Conformation and RNA Duplex Stability. *Nucleic Acids Res.* **1997**, *25* (6), 1272-1280. DOI: 10.1093/nar/25.6.1272.

(153) Nedialkova, Danny D.; Leidel, Sebastian A. Optimization of Codon Translation Rates via tRNA Modifications Maintains Proteome Integrity. *Cell* **2015**, *161* (7), 1606-1618. DOI: 10.1016/j.cell.2015.05.022.

(154) Zheng, X.; Chen, H.; Deng, Z.; Wu, Y.; Zhong, L.; Wu, C.; Yu, X.; Chen, Q.; Yan, S. The tRNA thiolation-mediated translational control is essential for plant immunity. *Elife* **2024**, *13*. DOI: 10.7554/eLife.93517.

(155) Cui, W.; Zhao, D.; Jiang, J.; Tang, F.; Zhang, C.; Duan, C. tRNA Modifications and Modifying Enzymes in Disease, the Potential Therapeutic Targets. *Int. J Biol. Sci.* **2023**, *19* (4), 1146-1162. DOI: 10.7150/ijbs.80233.

(156) Chujo, T.; Tomizawa, K. Human transfer RNA modopathies: diseases caused by aberrations in transfer RNA modifications. *FEBS J* **2021**, *288* (24), 7096-7122. DOI: 10.1111/febs.15736.

(157) Zhou, J. B.; Wang, E. D.; Zhou, X. L. Modifications of the human tRNA anticodon loop and their associations with genetic diseases. *Cell Mol. Life Sci.* **2021**, *78* (23), 7087-7105. DOI: 10.1007/s00018-021-03948-x.

(158) Guy, M. P.; Shaw, M.; Weiner, C. L.; Hobson, L.; Stark, Z.; Rose, K.; Kalscheuer, V. M.; Gecz, J.; Phizicky, E. M. Defects in tRNA Anticodon Loop 2'-O-Methylation Are Implicated in Nonsyndromic X-Linked Intellectual Disability due to Mutations in FTSJ1. *Hum. Mutat.* **2015**, *36* (12), 1176-1187. DOI: 10.1002/humu.22897.

(159) Li, J.; Wang, Y. N.; Xu, B. S.; Liu, Y. P.; Zhou, M.; Long, T.; Li, H.; Dong, H.; Nie, Y.; Chen, P. R.; et al. Intellectual disability-associated gene ftsj1 is responsible for 2'-O-methylation of specific tRNAs. *EMBO Rep.* **2020**, *21* (8), e50095. DOI: 10.15252/embr.202050095.

(160) Nagayoshi, Y.; Chujo, T.; Hirata, S.; Nakatsuka, H.; Chen, C. W.; Takakura, M.; Miyauchi, K.; Ikeuchi, Y.; Carlyle, B. C.; Kitchen, R. R.; et al. Loss of Ftsj1 perturbs codon-specific translation efficiency in the brain and is associated with X-linked intellectual disability. *Sci. Adv.* **2021**, *7* (13). DOI: 10.1126/sciadv.abf3072.

(161) Hoffer, E. D.; Hong, S.; Sunita, S.; Maehigashi, T.; Gonzalez, R. L. J.; Whitford, P. C.; Dunham, C. M. Structural insights into mRNA reading frame regulation by tRNA modification and slippery codon-anticodon pairing. *Elife* **2020**, *9*. DOI: 10.7554/eLife.51898.

(162) Nguyen, H. A.; Hoffer, E. D.; Dunham, C. M. Importance of a tRNA anticodon loop modification and a conserved, noncanonical anticodon stem pairing in tRNACGGPro for decoding. *J. Biol. Chem.* **2019**, *294* (14), 5281-5291. DOI: https://doi.org/10.1074/jbc.RA119.007410.

(163) Rosselló-Tortella, M.; Llinàs-Arias, P.; Sakaguchi, Y.; Miyauchi, K.; Davalos, V.; Setien, F.; Calleja-Cervantes, M. E.; Piñeyro, D.; Martínez-Gómez, J.; Guil, S.; et al. Epigenetic loss of the

transfer RNA-modifying enzyme TYW2 induces ribosome frameshifts in colon cancer. *Proc. Natl. Acad. Sci. U.S.A.* **2020**, *117* (34), 20785-20793. DOI: doi:10.1073/pnas.2003358117.

(164) Pan, Y.; Yan, T. M.; Wang, J. R.; Jiang, Z. H. The nature of the modification at position 37 of tRNAPhe correlates with acquired taxol resistance. *Nucleic Acids Res.* **2021**, *49* (1), 38-52. DOI: 10.1093/nar/gkaa1164.

(165) Dolce, L. G.; Zimmer, A. A.; Tengo, L.; Weis, F.; Rubio, M. A. T.; Alfonzo, J. D.; Kowalinski, E. Structural basis for sequence-independent substrate selection by eukaryotic wobble base tRNA deaminase ADAT2/3. *Nat. Commun.* **2022**, *13* (1), 6737. DOI: 10.1038/s41467-022-34441-z.

(166) Sharkia, R.; Zalan, A.; Jabareen-Masri, A.; Zahalka, H.; Mahajnah, M. A new case confirming and expanding the phenotype spectrum of ADAT3-related intellectual disability syndrome. *Eur. J. Med. Genet.* **2019**, *62* (11), 103549. DOI: https://doi.org/10.1016/j.ejmg.2018.10.001.

(167) Bornelöv, S.; Selmi, T.; Flad, S.; Dietmann, S.; Frye, M. Codon usage optimization in pluripotent embryonic stem cells. *Genome Biol.* **2019**, *20* (1), 119. DOI: 10.1186/s13059-019-1726-z.

(168) Lyu, X.; Yang, Q.; Li, L.; Dang, Y.; Zhou, Z.; Chen, S.; Liu, Y. Adaptation of codon usage to tRNA I34 modification controls translation kinetics and proteome landscape. *PLOS Genetics* **2020**, *16* (6), e1008836. DOI: 10.1371/journal.pgen.1008836.

(169) Torres, A. G.; Rodríguez-Escribà, M.; Marcet-Houben, M.; Santos Vieira, H. G.; Camacho, N.; Catena, H.; Murillo Recio, M.; Rafels-Ybern, À.; Reina, O.; Torres, F. M.; et al. Human tRNAs with inosine 34 are essential to efficiently translate eukarya-specific low-complexity proteins. *Nucleic Acids Res.* **2021**, *49* (12), 7011-7034. DOI: 10.1093/nar/gkab461.

(170) Masuda, I.; Hou, Y.-M. A tRNA modification pattern that facilitates interpretation of the genetic code. *Front. Mol. Biosci.* **2024**, *Volume 15 - 2024*, Perspective. DOI: 10.3389/fmicb.2024.1415100.

(171) de Crécy-Lagard, V.; Jaroch, M. Functions of Bacterial tRNA Modifications: From Ubiquity to Diversity. *Trends Microbiol.* **2021**, *29* (1), 41-53. DOI: 10.1016/j.tim.2020.06.010.

(172) Shandell, M. A.; Tan, Z.; Cornish, V. W. Genetic Code Expansion: A Brief History and Perspective. *Biochem.* **2021**, *60* (46), 3455-3469. DOI: 10.1021/acs.biochem.1c00286.

(173) Gamper, H.; Masuda, I.; Hou, Y.-M. Genome Expansion by tRNA +1 Frameshifting at Quadruplet Codons. *J. Mol. Biol.* **2022**, *434* (8), 167440. DOI: https://doi.org/10.1016/j.jmb.2021.167440.

(174) Kim, Y.; Cho, S.; Kim, J.-C.; Park, H.-S. tRNA engineering strategies for genetic code expansion. *Front. Genet.* **2024**, *Volume 15 - 2024*, Review. DOI: 10.3389/fgene.2024.1373250.

(175) Anreiter, I.; Mir, Q.; Simpson, J. T.; Janga, S. C.; Soller, M. New Twists in Detecting mRNA Modification Dynamics. *Trends Biotechnol.* **2021**, *39* (1), 72-89. DOI: https://doi.org/10.1016/j.tibtech.2020.06.002.

(176) Tardu, M.; Jones, J. D.; Kennedy, R. T.; Lin, Q.; Koutmou, K. S. Identification and Quantification of Modified Nucleosides in *Saccharomyces cerevisiae* mRNAs. *ACS Chem. Biol.* **2019**, *14* (7), 1403-1409. DOI: 10.1021/acschembio.9b00369.

(177) Boo, S. H.; Kim, Y. K. The emerging role of RNA modifications in the regulation of mRNA stability. *Exp. Mol. Med.* **2020**, *52* (3), 400-408. DOI: 10.1038/s12276-020-0407-z.

(178) Chen, X.-Y.; Zhang, J.; Zhu, J.-S. The role of m6A RNA methylation in human cancer. *Mol. Cancer* **2019**, *18* (1), 103. DOI: 10.1186/s12943-019-1033-z.

(179) Huang, H.; Weng, H.; Chen, J. The biogenesis and precise control of RNA m6A methylation. *Trends Genet.* **2020**, *36* (1), 44-52.

(180) Jain, S.; Koziej, L.; Poulis, P.; Kaczmarczyk, I.; Gaik, M.; Rawski, M.; Ranjan, N.; Glatt, S.; Rodnina, M. V. Modulation of translational decoding by m^6A modification of mRNA. *Nat. Commun.* **2023**, *14* (1), 4784. DOI: 10.1038/s41467-023-40422-7.

(181) Linder, B.; Grozhik, A. V.; Olarerin-George, A. O.; Meydan, C.; Mason, C. E.; Jaffrey, S. R. Single-nucleotide-resolution mapping of m^6A and m^6Am throughout the transcriptome. *Nat. Methods.* **2015**, *12* (8), 767-772. DOI: 10.1038/nmeth.3453.

(182) Nachtergaele, S.; He, C. Chemical Modifications in the Life of an mRNA Transcript. *Annu. Rev. Genet.* **2018**, *52* (Volume 52, 2018), 349-372. DOI: https://doi.org/10.1146/annurev-genet-120417-031522.

(183) Franco, M. K.; Koutmou, K. S. Chemical modifications to mRNA nucleobases impact translation elongation and termination. *Biophys. Chem.* **2022**, *285*, 106780. DOI: https://doi.org/10.1016/j.bpc.2022.106780.

(184) Hoernes, Thomas P.; Clementi, N.; Faserl, K.; Glasner, H.; Breuker, K.; Lindner, H.; Hüttenhofer, A.; Erlacher, Matthias D. Nucleotide modifications within bacterial messenger RNAs regulate their translation and are able to rewire the genetic code. *Nucleic Acids Res.* **2015**, *44* (2), 852-862. DOI: 10.1093/nar/gkv1182.

(185) You, C.; Dai, X.; Wang, Y. Position-dependent effects of regioisomeric methylated adenine and guanine ribonucleosides on translation. *Nucleic Acids Res.* **2017**, *45* (15), 9059-9067. DOI: 10.1093/nar/gkx515.

(186) Hoernes, T. P.; Heimdörfer, D.; Köstner, D.; Faserl, K.; Nußbaumer, F.; Plangger, R.; Kreutz, C.; Lindner, H.; Erlacher, M. D. Eukaryotic Translation Elongation is Modulated by Single Natural Nucleotide Derivatives in the Coding Sequences of mRNAs. *Genes* **2019**, *10* (2), 84.

(187) Liu, B.; Merriman, D. K.; Choi, S. H.; Schumacher, M. A.; Plangger, R.; Kreutz, C.; Horner, S. M.; Meyer, K. D.; Al-Hashimi, H. M. A potentially abundant junctional RNA motif stabilized by m^6A and Mg^{2+}. *Nat. Commun.* **2018**, *9* (1), 2761. DOI: 10.1038/s41467-018-05243-z.

(188) Hoernes, T.; Clementi, N.; Faserl, K.; Glasner, H.; Breuker, K.; Lindner, H.; Hu ttenhofer, A.; Erlacher, M. Nucleotide modifications within bacterial messenger RNAs regulate their translation and are able to rewire the genetic code. *Nucleic Acids Res.* **2015**, *44*. DOI: 10.1093/nar/gkv1182.

(189) Arango, D.; Sturgill, D.; Alhusaini, N.; Dillman, A. A.; Sweet, T. J.; Hanson, G.; Hosogane, M.; Sinclair, W. R.; Nanan, K. K.; Mandler, M. D.; et al. Acetylation of Cytidine in mRNA Promotes Translation Efficiency. *Cell* **2018**, *175* (7), 1872-1886.e1824. DOI: https://doi.org/10.1016/j.cell.2018.10.030.

(190) Sun, H.; Li, K.; Liu, C.; Yi, C. Regulation and functions of non-m6A mRNA modifications. *Nature Reviews Mol. Cell Biol.* **2023**, *24* (10), 714-731. DOI: 10.1038/s41580-023-00622-x.

(191) Keegan, L. P.; Hajji, K.; O'Connell, M. A. Adenosine Deaminase Acting on RNA (ADAR) Enzymes: A Journey from Weird to Wondrous. *Acc. Chem. Res.* **2023**, *56* (22), 3165-3174. DOI: 10.1021/acs.accounts.3c00433.

(192) Srinivasan, S.; Torres, A. G.; Ribas de Pouplana, L. Inosine in Biology and Disease. *Genes (Basel)* **2021**, *12* (4). DOI: 10.3390/genes12040600.

(193) Licht, K.; Hartl, M.; Amman, F.; Anrather, D.; Janisiw, M. P.; Jantsch, M. F. Inosine induces context-dependent recoding and translational stalling. *Nucleic Acids Res.* **2019**, *47* (1), 3-14. DOI: 10.1093/nar/gky1163.

(194) Nishikura, K. A-to-I editing of coding and non-coding RNAs by ADARs. *Nature Reviews Mol. Cell Biol.* **2016**, *17* (2), 83-96. DOI: 10.1038/nrm.2015.4.

(195) Mendoza, H. G.; Beal, P. A. Structural and functional effects of inosine modification in mRNA. *RNA* **2024**, *30* (5), 512-520. DOI: 10.1261/rna.079977.124.

(196) Hosaka, T.; Tsuji, H.; Kwak, S. RNA Editing: A New Therapeutic Target in Amyotrophic Lateral Sclerosis and Other Neurological Diseases. *Int. J. Mol. Sci.* **2021**, *22* (20). DOI: 10.3390/ijms222010958.

(197) Singh, M. Dysregulated A to I RNA editing and non-coding RNAs in neurodegeneration. *Front. Genet.* **2013**, *3*, 326.

(198) Costa Cruz, P. H.; Kawahara, Y. RNA editing in neurological and neurodegenerative disorders. *RNA Editing: Methods and Protocols* **2021**, 309-330.

(199) Zhu, X.; Zhang, Y.; Yang, X.; Hao, C.; Duan, H. Gene therapy for neurodegenerative disease: clinical potential and directions. *Frontiers in Molecular Neuroscience* **2021**, *14*, 618171.

(200) Chan, T. H. M.; Lin, C. H.; Qi, L.; Fei, J.; Li, Y.; Yong, K. J.; Liu, M.; Song, Y.; Chow, R. K. K.; Ng, V. H. E. A disrupted RNA editing balance mediated by ADARs (Adenosine DeAminases that act on RNA) in human hepatocellular carcinoma. *Gut* **2014**, *63* (5), 832-843.

(201) Qin, Y.-R.; Qiao, J.-J.; Chan, T. H. M.; Zhu, Y.-H.; Li, F.-F.; Liu, H.; Fei, J.; Li, Y.; Guan, X.-Y.; Chen, L. Adenosine-to-inosine RNA editing mediated by ADARs in esophageal squamous cell carcinoma. *Cancer Res.* **2014**, *74* (3), 840-851.

(202) Chan, T. H.; Qamra, A.; Tan, K. T.; Guo, J.; Yang, H.; Qi, L.; Lin, J. S.; Ng, V. H.; Song, Y.; Hong, H.; et al. ADAR-Mediated RNA Editing Predicts Progression and Prognosis of Gastric Cancer. *Gastroenterol.* **2016**, *151* (4), 637-650.e610. DOI: 10.1053/j.gastro.2016.06.043.

(203) Giraulo, C.; De Palma, G.; Plaitano, P.; Cicala, C.; Morello, S. Insight into adenosine pathway in psoriasis: Elucidating its role and the potential therapeutical applications. *Life Sci.* **2024**, *357*, 123071. DOI: https://doi.org/10.1016/j.lfs.2024.123071.

(204) Guo, X.; Wiley, C. A.; Steinman, R. A.; Sheng, Y.; Ji, B.; Wang, J.; Zhang, L.; Wang, T.; Zenatai, M.; Billiar, T. R.; et al. Aicardi-Goutières syndrome-associated mutation at ADAR1 gene locus activates innate immune response in mouse brain. *J. Neuroinflammation* **2021**, *18* (1), 169. DOI: 10.1186/s12974-021-02217-9.

(205) Picardi, E.; Manzari, C.; Mastropasqua, F.; Aiello, I.; D'Erchia, A. M.; Pesole, G. Profiling RNA editing in human tissues: towards the inosinome Atlas. *Sci. Rep.* **2015**, *5* (1), 14941.

(206) Hoernes, T. P.; Faserl, K.; Juen, M. A.; Kremser, J.; Gasser, C.; Fuchs, E.; Shi, X.; Siewert, A.; Lindner, H.; Kreutz, C.; et al. Translation of non-standard codon nucleotides reveals minimal requirements for codon-anticodon interactions. *Nat. Commun.* **2018**, *9* (1), 4865. DOI: 10.1038/s41467-018-07321-8.

(207) Koutmou, K.; Giles, R. Private Communication. 2025.

(208) Hudson, B. H.; Zaher, H. S. O6-Methylguanosine leads to position-dependent effects on ribosome speed and fidelity. *RNA* **2015**, *21* (9), 1648-1659. DOI: 10.1261/rna.052464.115.

(209) Simms, C. L.; Zaher, H. S. Quality control of chemically damaged RNA. *CMLS.* **2016**, *73* (19), 3639-3653. DOI: 10.1007/s00018-016-2261-7.

(210) Thomas, E. N.; Kim, K. Q.; McHugh, E. P.; Marcinkiewicz, T.; Zaher, H. S. Alkylative damage of mRNA leads to ribosome stalling and rescue by trans translation in bacteria. *eLife* **2020**, *9*, e61984. DOI: 10.7554/eLife.61984.

(211) Wurtmann, E. J.; and Wolin, S. L. RNA under attack: Cellular handling of RNA damage. *Crit. Rev. Biochem. Mol. Biol.* **2009**, *44* (1), 34-49. DOI: 10.1080/10409230802594043.

(212) Zaher, H. S.; Mosammaparast, N. RNA Damage Responses in Cellular Homeostasis, Genome Stability, and Disease. *Annu. Re. Pathol.* **2025**, *20* (Volume 20, 2025), 433-457. DOI: https://doi.org/10.1146/annurev-pathmechdis-111523-023516.

(213) Simms, C. L.; Hudson, B. H.; Mosior, J. W.; Rangwala, A. S.; Zaher, H. S. An active role for the ribosome in determining the fate of oxidized mRNA. *Cell Rep.* **2014**, *9* (4), 1256-1264. DOI: 10.1016/j.celrep.2014.10.042.

(214) Thomas, E. N.; Simms, C. L.; Keedy, H. E.; Zaher, H. S. Insights into the base-pairing preferences of 8-oxoguanosine on the ribosome. *Nucleic Acids Res.* **2019**, *47* (18), 9857-9870. DOI: 10.1093/nar/gkz701.

(215) Yan, L.; Simms, C.; McLoughlin, F.; Vierstra, R.; Zaher, H. Oxidation and alkylation stresses activate ribosome-quality control. *Nat. Commun.* **2019**, *10*, 5611. DOI: 10.1038/s41467-019-13579-3.

(216) Huang, R.; Zhou, P.-K. DNA damage repair: historical perspectives, mechanistic pathways and clinical translation for targeted cancer therapy. *Sinal Transduct. Target. Ther.* **2021**, *6* (1), 254. DOI: 10.1038/s41392-021-00648-7.

(217) Wozniak, K. J.; Simmons, L. A. Bacterial DNA excision repair pathways. *Nat. Rev. Microbiol.* **2022**, *20* (8), 465-477. DOI: 10.1038/s41579-022-00694-0.

(218) Aas, P. A.; Otterlei, M.; Falnes, P. Ø.; Vågbø, C. B.; Skorpen, F.; Akbari, M.; Sundheim, O.; Bjørås, M.; Slupphaug, G.; Seeberg, E.; et al. Human and bacterial oxidative demethylases repair alkylation damage in both RNA and DNA. *Nature* **2003**, *421* (6925), 859-863. DOI: 10.1038/nature01363.

(219) Ougland, R.; Zhang, C.-M.; Liiv, A.; Johansen, R. F.; Seeberg, E.; Hou, Y.-M.; Remme, J.; Falnes, P. Ø. AlkB Restores the Biological Function of mRNA and tRNA Inactivated by Chemical Methylation. *Mol. Cell.* **2004**, *16* (1), 107-116. DOI: 10.1016/j.molcel.2004.09.002.

(220) van den Born, E.; Omelchenko, M. V.; Bekkelund, A.; Leihne, V.; Koonin, E. V.; Dolja, V. V.; Falnes, P. Ø. Viral AlkB proteins repair RNA damage by oxidative demethylation. *Nucleic Acids Res.* **2008**, *36* (17), 5451-5461. DOI: 10.1093/nar/gkn519.

(221) Simms, C. L.; Thomas, E. N.; Zaher, H. S. Ribosome-based quality control of mRNA and nascent peptides. *WIREs RNA* **2017**, *8* (1), e1366. DOI: https://doi.org/10.1002/wrna.1366.

(222) Simms, C.; Yan, L.; Qiu, J.; Zaher, H. Ribosome Collisions Result in +1 Frameshifting in the Absence of No-Go Decay. *Cell Reports* **2019**, *28*, 1679-1689.e1674. DOI: 10.1016/j.celrep.2019.07.046.

(223) Yan, L. L.; Zaher, H. S. Ribosome quality control antagonizes the activation of the integrated stress response on colliding ribosomes. *Mol. Cell.* **2021**, *81* (3), 614-628.e614. DOI: https://doi.org/10.1016/j.molcel.2020.11.033.

(224) Doma, M. K.; Parker, R. Endonucleolytic cleavage of eukaryotic mRNAs with stalls in translation elongation. *Nature* **2006**, *440* (7083), 561-564. DOI: 10.1038/nature04530.

(225) Li, X.; Zhu, P.; Ma, S.; Song, J.; Bai, J.; Sun, F.; Yi, C. Chemical pulldown reveals dynamic pseudouridylation of the mammalian transcriptome. *Nat. Chem. Biol.* **2015**, *11* (8), 592-597.

(226) Carlile, T. M.; Rojas-Duran, M. F.; Zinshteyn, B.; Shin, H.; Bartoli, K. M.; Gilbert, W. V. Pseudouridine profiling reveals regulated mRNA pseudouridylation in yeast and human cells. *Nature* **2014**, *515* (7525), 143-146. DOI: 10.1038/nature13802.

(227) Hoernes, T. P.; Hüttenhofer, A.; Erlacher, M. D. mRNA modifications: Dynamic regulators of gene expression? *RNA Biol.* **2016**, *13* (9), 760-765. DOI: 10.1080/15476286.2016.1203504.

(228) Schwartz, S.; Bernstein, D. A.; Mumbach, M. R.; Jovanovic, M.; Herbst, R. H.; León-Ricardo, B. X.; Engreitz, J. M.; Guttman, M.; Satija, R.; Lander, E. S. Transcriptome-wide mapping reveals widespread dynamic-regulated pseudouridylation of ncRNA and mRNA. *Cell* **2014**, *159* (1), 148-162.

(229) Nance, K. D.; Meier, J. L. Modifications in an Emergency: The Role of N1-Methylpseudouridine in COVID-19 Vaccines. *ACS Cent. Sci.* **2021**, *7* (5), 748-756. DOI: 10.1021/acscentsci.1c00197.

(230) Karikó, K.; Muramatsu, H.; Welsh, F. A.; Ludwig, J.; Kato, H.; Akira, S.; Weissman, D. Incorporation of pseudouridine into mRNA yields superior nonimmunogenic vector with increased translational capacity and biological stability. *Mol. Ther.* **2008**, *16* (11), 1833-1840. DOI: 10.1038/mt.2008.200.

(231) Liu, A.; Wang, X. The Pivotal Role of Chemical Modifications in mRNA Therapeutics. *Front. Cell. Dev. Biol.* **2022**, *10*, Review. DOI: 10.3389/fcell.2022.901510.

(232) Anderson, B. R.; Muramatsu, H.; Nallagatla, S. R.; Bevilacqua, P. C.; Sansing, L. H.; Weissman, D.; Karikó, K. Incorporation of pseudouridine into mRNA enhances translation by diminishing PKR activation. *Nucleic Acids Res.* **2010**, *38* (17), 5884-5892. DOI: 10.1093/nar/gkq347.

(233) Svitkin, Y. V.; Gingras, A.-C.; Sonenberg, N. Membrane-dependent relief of translation elongation arrest on pseudouridine- and N1-methyl-pseudouridine-modified mRNAs. *Nucleic Acids Res.* **2021**, *50* (13), 7202-7215. DOI: 10.1093/nar/gkab1241.

(234) Mauger, D. M.; Cabral, B. J.; Presnyak, V.; Su, S. V.; Reid, D. W.; Goodman, B.; Link, K.; Khatwani, N.; Reynders, J.; Moore, M. J.; et al. mRNA structure regulates protein expression through changes in functional half-life. *Proc. Natl. Acad. Sci. U.S.A.* **2019**, *116* (48), 24075-24083. DOI: 10.1073/pnas.1908052116.

(235) Mustoe, A. M.; Busan, S.; Rice, G. M.; Hajdin, C. E.; Peterson, B. K.; Ruda, V. M.; Kubica, N.; Nutiu, R.; Baryza, J. L.; Weeks, K. M. Pervasive regulatory functions of mRNA structure revealed by high-resolution SHAPE probing. *Cell* **2018**, *173* (1), 181-195. e118.

(236) Mulroney, T. E.; Pöyry, T.; Yam-Puc, J. C.; Rust, M.; Harvey, R. F.; Kalmar, L.; Horner, E.; Booth, L.; Ferreira, A. P.; Stoneley, M.; et al. N1-methylpseudouridylation of mRNA causes +1 ribosomal frameshifting. *Nature* **2024**, *625* (7993), 189-194. DOI: 10.1038/s41586-023-06800-3.

(237) Ieong, K.-W.; Uzun, Ü.; Selmer, M.; Ehrenberg, M. Two proofreading steps amplify the accuracy of genetic code translation. *Proc. Natl. Acad. Sci. U.S.A.* **2016**, *113* (48), 13744-13749. DOI: doi:10.1073/pnas.1610917113.

(238) Sharma, H.; Adio, S.; Senyushkina, T.; Belardinelli, R.; Peske, F.; Rodnina, M. V. Kinetics of spontaneous and EF-G-accelerated rotation of ribosomal subunits. *Cell Rep.* **2016**, *16* (8), 2187-2196.

(239) Peske, F.; Savelsbergh, A.; Katunin, V. I.; Rodnina, M. V.; Wintermeyer, W. Conformational changes of the small ribosomal subunit during elongation factor G-dependent tRNA–mRNA translocation. *J. Mol. Biol.* **2004**, *343* (5), 1183-1194.

(240) Zhou, J.; Lancaster, L.; Donohue, J. P.; Noller, H. F. How the ribosome hands the A-site tRNA to the P site during EF-G–catalyzed translocation. *Science* **2014**, *345* (6201), 1188-1191.

(241) Girodat, D. J.; Nishima, W.; Holm, M.; Rundlet, E. J.; Prajapati, J. D.; Amaya, J. L. A.; Fischer, K.; Blanchard, S. C.; Sanbonmatsu, K. Y. Ribosome hyper-swivel head domain motions are required for translocation and resetting. *Biophys. J.* **2023**, *122* (3), 360a. DOI: 10.1016/j.bpj.2022.11.1990.

(242) Rundlet, E. J.; Holm, M.; Schacherl, M.; Natchiar, S. K.; Altman, R. B.; Spahn, C. M.; Myasnikov, A. G.; Blanchard, S. C. Structural basis of early translocation events on the ribosome. *Nature* **2021**, *595* (7869), 741-745.

(243) Wang, L.; Altman, R. B.; Blanchard, S. C. Insights Into the Molecular Determinants of EF-G Catalyzed Translocation. *Biophys. J.* **2012**, *102* (3), 68a. DOI: 10.1016/j.bpj.2011.11.401.

(244) Amann, S. J.; Keihsler, D.; Bodrug, T.; Brown, N. G.; Haselbach, D. Frozen in time: analyzing molecular dynamics with time-resolved cryo-EM. *Structure* **2023**, *31* (1), 4-19. DOI: https://doi.org/10.1016/j.str.2022.11.014.

(245) Sharma, A. K.; Sormanni, P.; Ahmed, N.; Ciryam, P.; Friedrich, U. A.; Kramer, G.; O'Brien, E. P. A chemical kinetic basis for measuring translation initiation and elongation rates from ribosome profiling data. *PLoS Comput. Biol.* **2019**, *15* (5), e1007070. DOI: 10.1371/journal.pcbi.1007070.

(246) Kontziampasis, D.; Klebl, D. P.; Iadanza, M. G.; Scarff, C. A.; Kopf, F.; Sobott, F.; Monteiro, D. C.; Trebbin, M.; Muench, S. P.; White, H. D. A cryo-EM grid preparation device for time-resolved structural studies. *IUCrJ* **2019**, *6* (6), 1024-1031.

(247) Lu, Z.; Shaikh, T. R.; Barnard, D.; Meng, X.; Mohamed, H.; Yassin, A.; Mannella, C. A.; Agrawal, R. K.; Lu, T.-M.; Wagenknecht, T. Monolithic microfluidic mixing–spraying devices for time-resolved cryo-electron microscopy. *J. Struct. Biol.* **2009**, *168* (3), 388-395.

(248) Dandey, V. P.; Budell, W. C.; Wei, H.; Bobe, D.; Maruthi, K.; Kopylov, M.; Eng, E. T.; Kahn, P. A.; Hinshaw, J. E.; Kundu, N.; et al. Time-resolved cryo-EM using Spotiton. *Nat. Methods.* **2020**, *17* (9), 897-900. DOI: 10.1038/s41592-020-0925-6.

(249) Halfon, Y.; Matzov, D.; Eyal, Z.; Bashan, A.; Zimmerman, E.; Kjeldgaard, J.; Ingmer, H.; Yonath, A. Exit tunnel modulation as resistance mechanism of S. aureus erythromycin resistant mutant. *Sci. Rep.* **2019**, *9* (1), 11460.

(250) Watson, Z. L.; Ward, F. R.; Méheust, R.; Ad, O.; Schepartz, A.; Banfield, J. F.; Cate, J. H. Structure of the bacterial ribosome at 2 Å resolution. *elife* **2020**, *9*, e60482.

(251) Frank, J.; Agrawal, R. K. A ratchet-like inter-subunit reorganization of the ribosome during translocation. *Nature* **2000**, *406* (6793), 318-322.

(252) Valle, M.; Zavialov, A.; Sengupta, J.; Rawat, U.; Ehrenberg, M.; Frank, J. Locking and unlocking of ribosomal motions. *Cell* **2003**, *114* (1), 123-134.

(253) Konevega, A. L.; Fischer, N.; Semenkov, Y. P.; Stark, H.; Wintermeyer, W.; Rodnina, M. V. Spontaneous reverse movement of mRNA-bound tRNA through the ribosome. *Nat. Struct. Mol. Biol.* **2007**, *14* (4), 318-324.

(254) Rodnina, M. V.; Savelsbergh, A.; Katunin, V. I.; Wintermeyer, W. Hydrolysis of GTP by elongation factor G drives tRNA movement on the ribosome. *Nature* **1997**, *385* (6611), 37-41.

(255) Mäeots, M.-E.; Lee, B.; Nans, A.; Jeong, S.-G.; Esfahani, M. M.; Ding, S.; Smith, D. J.; Lee, C.-S.; Lee, S. S.; Peter, M. Modular microfluidics enables kinetic insight from time-resolved cryo-EM. *Nat. Commun.* **2020**, *11* (1), 3465.

(256) Shaikh, T. R.; Yassin, A. S.; Lu, Z.; Barnard, D.; Meng, X.; Lu, T.-M.; Wagenknecht, T.; Agrawal, R. K. Initial bridges between two ribosomal subunits are formed within 9.4 milliseconds, as studied by time-resolved cryo-EM. *Proc. Natl. Acad. Sci. U.S.A.* **2014**, *111* (27), 9822-9827.

(257) Hennelly, S. P.; Antoun, A.; Ehrenberg, M.; Gualerzi, C. O.; Knight, W.; Lodmell, J. S.; Hill, W. E. A time-resolved investigation of ribosomal subunit association. *J. Mol. Biol.* **2005**, *346* (5), 1243-1258.

(258) Chen, B.; Kaledhonkar, S.; Sun, M.; Shen, B.; Lu, Z.; Barnard, D.; Lu, T.-M.; Gonzalez, R. L.; Frank, J. Structural dynamics of ribosome subunit association studied by mixing-spraying time-resolved cryogenic electron microscopy. *Structure* **2015**, *23* (6), 1097-1105.

(259) Antoun, A.; Pavlov, M. Y.; Andersson, K.; Tenson, T.; Ehrenberg, M. The roles of initiation factor 2 and guanosine triphosphate in initiation of protein synthesis. *EMBO J.* **2003**.

(260) Kaledhonkar, S.; Fu, Z.; Caban, K.; Li, W.; Chen, B.; Sun, M.; Gonzalez Jr, R. L.; Frank, J. Late steps in bacterial translation initiation visualized using time-resolved cryo-EM. *Nature* **2019**, *570* (7761), 400-404.

(261) Goyal, A.; Belardinelli, R.; Maracci, C.; Milon, P.; Rodnina, M. V. Directional transition from initiation to elongation in bacterial translation. *Nucleic Acids Res.* **2015**, *43* (22), 10700-10712.

(262) Klaholz, B. P.; Pape, T.; Zavialov, A. V.; Myasnikov, A. G.; Orlova, E. V.; Vestergaard, B.; Ehrenberg, M.; van Heel, M. Structure of the Escherichia coli ribosomal termination complex with release factor 2. *Nature* **2003**, *421* (6918), 90-94.

(263) Shin, D. H.; Brandsen, J.; Jancarik, J.; Yokota, H.; Kim, R.; Kim, S.-H. Structural analyses of peptide release factor 1 from Thermotoga maritima reveal domain flexibility required for its interaction with the ribosome. *J. Mol. Biol.* **2004**, *341* (1), 227-239.

(264) Song, H.; Mugnier, P.; Das, A. K.; Webb, H. M.; Evans, D. R.; Tuite, M. F.; Hemmings, B. A.; Barford, D. The crystal structure of human eukaryotic release factor eRF1—mechanism of stop codon recognition and peptidyl-tRNA hydrolysis. *Cell* **2000**, *100* (3), 311-321.

(265) Vestergaard, B.; Van, L. B.; Andersen, G. R.; Nyborg, J.; Buckingham, R. H.; Kjeldgaard, M. Bacterial polypeptide release factor RF2 is structurally distinct from eukaryotic eRF1. *Mol. Cell.* **2001**, *8* (6), 1375-1382.

(266) Kühlbrandt, W. The Resolution Revolution. *Science* **2014**, *343* (6178), 1443-1444. DOI: doi:10.1126/science.1251652.

(267) Girodat, D.; Wieden, H.-J.; Blanchard, S. C.; Sanbonmatsu, K. Y. Geometric alignment of aminoacyl-tRNA relative to catalytic centers of the ribosome underpins accurate mRNA decoding. *Nat. Commun.* **2023**, *14* (1), 5582. DOI: 10.1038/s41467-023-40404-9.

(268) Bock, L. V.; Gabrielli, S.; Kolar, M. H.; Grubmüller, H. Simulation of Complex Biomolecular Systems: The Ribosome Challenge. *Annu. Rev. Biophys.* **2023**, *52*, 361-390, Review. DOI: 10.1146/annurev-biophys-111622-091147.

(269) Yang, H.; Bandarkar, P.; Horne, R.; Leite, V. B. P.; Chahine, J.; Whitford, P. C. Diffusion of tRNA inside the ribosome is position-dependent. *J. Chem. Phys.* **2019**, *151* (8), 085102. DOI: 10.1063/1.5113814.

(270) Leininger, S. E.; Rodriguez, J.; Vu, Q. V.; Jiang, Y.; Li, M. S.; Deutsch, C.; O'Brien, E. P. Ribosome Elongation Kinetics of Consecutively Charged Residues Are Coupled to Electrostatic Force. *Biochem.* **2021**, *60* (43), 3223-3235. DOI: 10.1021/acs.biochem.1c00507.

(271) Noel, J. K.; Chahine, J.; Leite, V. B. P.; Whitford, P. C. Capturing transition paths and transition states for conformational rearrangements in the ribosome. *Biophys. J.* **2014**, *107* (12), 2881-2890. DOI: 10.1016/j.bpj.2014.10.022.

(272) Sonawane, K. D.; Sambhare, S. B. The influence of hypermodified nucleosides lysidine and t(6)A to recognize the AUA codon instead of AUG: a molecular dynamics simulation study. *Integr. Biol. (Camb).* **2015**, *7* (11), 1387-1395. DOI: 10.1039/c5ib00058k.

(273) Zeng, X.; Chugh, J.; Casiano-Negroni, A.; Al-Hashimi, H. M.; Brooks, C. L., 3rd. Flipping of the ribosomal A-site adenines provides a basis for tRNA selection. *J. Mol. Biol.* **2014**, *426* (19), 3201-3213. DOI: 10.1016/j.jmb.2014.04.029.

(274) Wang, X.; Kirkpatrick, J. P.; Launay, H. M. M.; de Simone, A.; Häussinger, D.; Dobson, C. M.; Vendruscolo, M.; Cabrita, L. D.; Waudby, C. A.; Christodoulou, J. Probing the dynamic stalk region of the ribosome using solution NMR. *Sci. Rep.* **2019**, *9* (1), 13528. DOI: 10.1038/s41598-019-49190-1.

(275) Aqvist, J.; Lind, C.; Sund, J.; Wallin, G. Bridging the gap between ribosome structure and biochemistry by mechanistic computations. *Curr. Opin. Struct. Biol.* **2012**, *22* (6), 815-823. DOI: 10.1016/j.sbi.2012.07.008.

(276) Sanbonmatsu, K. Y. Computational studies of molecular machines: the ribosome. *Curr. Opin. Struct. Biol.* **2012**, *22* (2), 168-174.

(277) Sanbonmatsu, K. Y.; Blanchard, S. C.; Whitford, P. C. Molecular Dynamics Simulations of the Ribosome. In *Biophysical approaches to translational control of gene expression*, 2012; pp 51-68.

(278) Sanbonmatsu, K. Y.; Joseph, S. Understanding Discrimination by the Ribosome: Stability Testing and Groove Measurement of Codon–Anticodon Pairs. *J. Mol. Biol.* **2003**, *328* (1), 33-47. DOI: 10.1016/s0022-2836(03)00236-5.

(279) Elliott, B. A.; Ho, H.-T.; Ranganathan, S. V.; Vangaveti, S.; Ilkayeva, O.; Abou Assi, H.; Choi, A. K.; Agris, P. F.; Holley, C. L. Modification of messenger RNA by 2'-O-methylation regulates gene expression in vivo. *Nat. Commun.* **2019**, *10* (1), 3401. DOI: 10.1038/s41467-019-11375-7.

(280) Reliability and reproducibility checklist for molecular dynamics simulations. *Communications Biology* **2023**, *6* (1), 268. DOI: 10.1038/s42003-023-04653-0.

(281) Ormeño, F.; General, I. J. Convergence and equilibrium in molecular dynamics simulations. *Commun. Chem.* **2024**, *7* (1), 26. DOI: 10.1038/s42004-024-01114-5.

(282) Bonomi, M.; Bussi, G.; Camilloni, C.; Tribello, G. A.; Banáš, P.; Barducci, A.; Bernetti, M.; Bolhuis, P. G.; Bottaro, S.; Branduardi, D.; et al. Promoting transparency and reproducibility in enhanced molecular simulations. *Nat. Methods.* **2019**, *16* (8), 670-673. DOI: 10.1038/s41592-019-0506-8.

CHAPTER 2: DEVELOPING A COMPUTATIONAL METHOD FOR SIMULATING THE INFLUENCE OF mRNA MODIFICATIONS ON DECODING IN THE RIBOSOME

2.1 Objectives

As discussed in Chapter 1, experimental techniques lack the spatiotemporal resolution to directly observe rapid atomistic motions (i.e., timescales on the order of ns–μs) in the ribosome. Furthermore, preparation of ribosomal complexes with a wide variety of site-specific RNA modifications is time-consuming and laborious. These challenges leave a noticeable gap in the understanding of the molecular mechanisms that drive tRNA selection. MD simulations provide an essential tool for studying biomolecular processes in fine detail, and can, in principle, be used to understand how RNA modifications modulate the rapid local conformational changes in the actively elongating ribosomal A-site. However, routine simulations of large heterogeneous macromolecular systems (i.e., containing millions to billions of atoms) like the ribosome remain computationally demanding. Nonetheless, the number of MD simulation studies of ribosomal processes, such as elongation, has steadily increased over the past 25 years,[1-5] giving crucial insights into various ribosomal processes ranging from co-translational folding of nascent polypeptides in the exit tunnel to fast allosteric signal transduction over the entire ribosome.[6, 7] For computational studies to provide reliable insight into biological processes, they must strike a balance between the model size, accuracy of the underlying force field, and extent of sampling required to investigate specific motions within the ribosome.

The goals of this Chapter are first to review computational studies on ribosomal processes and then to establish a methodology to examine the impact of mRNA modifications on ribosomal decoding. In Section 2.2, the relevant literature spanning the approaches that have been used to study elongation will be discussed, including the small selection of studies that investigated the roles of RNA modifications on ribosomal decoding. Following this review, the detailed computational methodology employed in this thesis (Chapters 3 and 4) will be

discussed in Section 2.3. Specifically, this section will provide a thorough description of how the models were built and minimized, the force field parameters used, and the trajectory protocols used for equilibration and production simulations. Additionally, data analysis techniques, including establishing trajectory convergence, generation of free energy landscapes (FELs), and conformational analysis, and more will be detailed.

2.2 Computational background

The first class of simulation techniques to be discussed is coarse graining (CG), where system conformational sampling is greatly improved at the expense of spatial detail. For ribosomal processes that take a significant amount of time (milliseconds to seconds), aaMD is prohibitively computationally expensive and cgMD is a commonly used technique. cgMD techniques treat groups of atoms as "beads" to reduce the number of degrees of freedom in the system and access larger timescales. For example, the resolution in cgMD approaches for describing RNA nucleotides can range from extremely coarse (e.g., 1–3 beads per nucleotide in the YUP and NAST force fields),[8, 9] to moderate (e.g., 6–7 beads in the MARTINI force fields).[10, 11] cgMD simulations also tend to use simpler functional forms for their potential energy functions compared to those used in traditional aaMD force fields.[10, 11] For example, in a study of the dynamics of polypeptides in the exit tunnel, each residue was represented by three identical beads, with nonbonded interactions modeled using a simple Lennard-Jones (LJ) potential (no Coulombic potential) and bonded interactions described by stiff harmonic terms, omitting angle and dihedral potentials.[12] cgMD has also been used to develop a sequence-sensitive model of protein translocation, using a potential energy function that combines finite extension nonlinear elastic (FENE) bonds, repulsive Lennard-Jones interactions, Debye–Hückel electrostatics, and sequence-specific interactions with both the membrane and translocon.[13, 14] cgMD approaches can be complemented by network models, which divide biomolecules into "nodes" connected

by harmonic springs with spring constants.[15] The potential energy function in anisotropic network models (ANMs) and elastic network models (ENMs) is harmonic and centered around the native cryo-EM or X-ray structure and dynamics are not sampled (i.e., normal mode analysis yields directions and amplitudes of motions, but not real time evolution).[15] ENMs and ANMs are therefore heavily reliant on experimental structures and have been used to examine global 70S ribosomal dynamics during ribosome assembly,[16] translocation,[17-19] and other processes.[20]

Another often-used simulation method is structure-based modeling (SBM).[6, 21-25] SBMs, also called Gō models, operate on the principle of minimal frustration, meaning that the native-state interactions are assumed to be strongly stabilizing, while non-native interactions are largely ignored or treated as repulsive.[26, 27] These models encode native contacts from an experimentally-determined structure (e.g., a crystal structure or NMR ensemble) into a simplified potential energy function, allowing the system to naturally evolve along a static energy landscape.[26] While SBMs often use CG, "all heavy-atom" force fields exist and are typically used for simulations of the ribosome, such as in the SMOG force field.[27] SBMs typically do not include any explicit solvent model and treat the system with some coarse-graining (treating entire residues as beads or omitting hydrogens).[23, 28]

Simplifications to the treatment of RNA nucleotides and protein amino acids in the ribosome provide an immense payoff in computational efficiency.[29] For example, in SBM simulations that use an all-heavy atom force field, ribosome simulations could be as fast as 10-100 μs/day on a single GPU (149,587 particles in total).[27] Indeed, SBMs have been able to uncover the pathways of large-scale motions that take place on the order of milliseconds to seconds, such as ribosome subunit internal dynamics and rotation,[30-31] tRNA diffusion into the accommodation corridor during proofreading,[21, 32-35] and translocation of A- and P-site tRNAs. However, the computational efficiency is drastically reduced (to 1-10 μs/day) for these

simulations when solvent and ionic environments are taken into account (186,929 particles in total).[29] Explicit waters are typically not used in the SBM simulations of ribosomes, which instead use an implicit solvent continuum model.[29] However, if explicit waters were included, it would reduce the efficiency of the calculations by additional orders of magnitude as it is common for the number of particles to exceed 2 million atoms in fully-solvated ribosome simulations.[36]

cgMD techniques are suitable for sampling slow motions such as large internal conformational changes in the ribosome.[30,31] However, smaller motions often occur on shorter time scales, such as the formation or loss of individual hydrogen bonds between the codon and anticodon or decoding center residues in the ribosome. The simplifications in even the most detailed cgMD force fields are problematic for studying codon recognition, regardless of the number of beads used to represent each nucleotide or amino acid. For example, the lack of explicit solvation poses issues for modeling the solvent shielding accomplished by the ribosomal monitoring residues.[37,38] Moreover, monovalent (K^+ and Cl^-) and divalent (Mg^{2+}) ions have long-established roles in maintaining ribosome structure and function.[39-44] High-resolution experimental structures show tight binding of Mg^{2+} at functional ribosome sites,[45, 46] and kinetics studies have found that Mg^{2+} ions influence the stability of B37 of tRNA and the mRNA in the decoding center.[47, 48] Despite recent efforts to include ions in SBMs,[49] the ion parameters for K^+, Cl^-, and Mg^{2+} neglect long-range screening and pairwise Coulomb or Lennard-Jones (LJ) terms are oversimplified (i.e., by using harmonic or minimal LJ potentials).[39] Moreover, structures of ribosome complexes indicate that a significant portion of Mg^{2+} ions coordinate into octahedral water complexes, $Mg(H_2O)_6^{2+}$, which interact with the rRNA phosphate backbone via indirect coordination.[39, 50] The lack of explicit solvation in SBMs neglects the different coordination modes of Mg^{2+} ions or ion-water interactions. For these reasons, the cgMD or SBM approaches were not ideal methods for the problems addressed in this thesis.

Decoding relies on short-time-scale fluctuations such as changes to solvent and ion distributions in the decoding center, hydrogen bonding between the codon and anticodon minihelix or interactions between the tRNA and/or mRNA and the ribosomal A-site monitoring nucleotides. A technique most suited to sample these relevant dynamics is explicit solvent, all-atom (including hydrogens) equilibrium aaMD simulations. aaMD simulations come in many different flavors, but all use Newtonian mechanics to compute the time-dependent motion of each particle in the system. The typical potential energy function for aaMD includes the less-expensive bonded interactions (bonds, angles and dihedral angles) and the more expensive non-bonded interactions (short-range van der Waals and long-range electrostatic interactions). From an initial set of atomic coordinates typically extracted from available experimental structures and initial velocities selected randomly from a Maxwell-Boltzmann distribution, the motion of each atom is computed for each time step (~0.5–4 fs) until the desired total simulation time is reached. The atomistic treatment in aaMD can often present a computational bottleneck. Even with GPU acceleration and multi-core CPU parallelization, most MD studies require access to high-performance computing (HPC) resources or special-purpose hardware to achieve statistically-relevant sampling. However, fully solvated aaMD simulations of the entire ribosome (2–2.5 million atoms) have been reported in the literature to study translational processes including translation arrest by the monitoring peptide VemP or antibiotics,[51] ribosome surface-binding enzyme peptide deformylase,[52] translocation of tRNAs,[36, 53, 54] and other processes.[55-63] While these simulations are detailed given the system size, they often take additional liberties compared to conventional all-atom MD, such as using a 4-fs time step. This longer time step is enabled by techniques like hydrogen mass repartitioning,[64] in which mass is shifted from heavy atoms to their bonded hydrogens to lower the vibrational frequencies of bonds involving hydrogen atoms. Despite these cost-saving alterations, even speeds for multi-node simulations

conducted on supercomputers are slow (~10 ns/day), limiting the scope and quantity of these studies in the literature.[1, 65]

Given that MD simulations can provide an ensemble of structures and corresponding potential energy states, it is possible to calculate relative or absolute free energies using specialized simulation methods such as free energy perturbation (FEP).[66] FEP is an attractive approach for gaining quantitative energetic insights into tRNA selection in the ribosome, as binding free energies can be related to experimental measurements of rate or equilibrium constants by the linear free energy relationship (LFER).[67] FEP simulations introduce a parameter, λ, into the standard aaMD force field, which forces the system from an initial and final state through a non-physical path. This allows one to avoid needing to simulate slow and rare (high energy barrier) physical processes such as the diffusion of tRNA through the intersubunit space following EF-Tu mediated GTP hydrolysis.[67] FEP and umbrella sampling simulations have been used in the context of tRNA selection to study the impact of base-substitutions in the mRNA codon or tRNA anticodon on the free energy of binding to the ribosomal A-site.[37, 68, 69] For example, previous work studied the free energy changes for the cognate $tRNA^{Phe}$ codon-anticodon pairing interaction upon mutation that produced near- and non-cognate interactions, providing free energy estimates in excellent agreement to experiment (deviations of < 0.3 kcal/mol).[68, 70, 71] This study also examined the energetic impacts of post-transcriptional modifications, cmo^5U34 and m^6A37 to $tRNA^{Val}$, which collectively allow reading of all redundant cognate $tRNA^{Val}$ codons [5'-GU(A/G/U/C)-3'].[68]

The subsequent rise in available ribosome X-ray and cryo-EM structures showed that the tRNA adopts distinct conformations during selection, moving from a bent (A/T) conformation to a straight (A/A) conformation after GTP hydrolysis.[72, 73] These considerations were included in FEP models to establish a more comprehensive selection model, where first and second position

substitutions in the mRNA codon were found to cause higher discrimination of tRNAs than those in the third (wobble) position.[68] A similar study used umbrella sampling to generate the potential of mean force (PMF) along the free energy landscape according to a progress variable that measures the flipping of monitoring adenine nucleobases A1492 and A1493 in the 16S rRNA.[74]

While FEP simulations are a tempting choice, they have limitations. Typically, FEP requires using a truncated model (tens of thousands of atoms), short time-steps (0.5–1 fs), and extensive sampling of both initial and final states to achieve convergence.[75] Moreover, FEP requires sampling along an unphysical path because it involves an alchemical transformation rather than a real, time-dependent transition. Thus, the dynamics observed during the FEP process are not physically meaningful at any intermediate λ window. FEP is therefore not well-suited for studying real-time decoding dynamics. Given the importance of sampling physically meaningful induced-fit kinetics to understand codon recognition,[76, 77] FEP is not an ideal model choice for the present work.

Perhaps the most common use of explicit solvent aaMD simulations for studying the ribosome involves "subsystem" models that extract the ribosome region of interest or include only a single ribosome subunit from an experimental structure.[7, 38, 59-63, 78-90] For example, subsystems of ribosomes in atomistic MD simulations have included regions around the PTC,[55, 81, 82, 91] exit tunnel,[61, 83, 85, 86] or A- and P-sites.[59-63] This strategy has been used in studies to elucidate decoding principles for tRNA selection within the context of selecting cognate tRNAs over near cognate.[38, 68, 69] Early studies that used aaMD ribosome subsystems explored how the ribosome distinguishes between near-cognate and cognate tRNAs using a combination of shape measuring and stability testing, steric hindrance, and hydrogen bond reorganization.[38]

Beyond studying mismatches in canonical nucleotides, the subsystem model approach has also been the primary approach for aaMD simulations examining how tRNA and mRNA modifications affect ribosomal decoding.[92-95] While aaMD studies of tRNA selection in the ribosome typically use large segments or even entire subunits during long simulations with multiple independent replicas,[7, 38, 59-63, 78-90] studies focusing solely on codon recognition tend to use smaller models (hundreds of rRNA or amino acid residues), short time scales (<100 ns), and lack replicas.[92-94, 96] For example, the influence of $tRNA^{Leu}$ modification τm^5U34 on decoding UUG/UUA codons was explored with models containing the ASL bound to each mRNA codon and 55S mammalian mitochondrial ribosome residues A916-C917-A918-A919-G920-U921 and C254-G255-G256-U257-C258 (A918-919 and G256 are equivalent to monitoring residues A1492-1493 and G530 in the *E. coli* ribosome).[95] These simulations were carried out for 50 ns, an order of magnitude shorter than the typical microsecond-timescale simulations achieved for even larger subsystem or whole-ribosome models.[2] Moreover, conclusions were based on only single simulations (no replicas), which brings into question the reliability and reproducibility of the results.[95] Importantly, even in 50 ns, the minihelix integrity was visually compromised in half of the models studied, which was more likely an artefact of insufficient stabilization of the codon-anticodon minihelix rather than representative of a real, physical tRNA rejection process.[95]

Another study used MD simulations to examine how the s^2C32 modification present in the *E. coli* $tRNA^{Arg1}$, but absent in $tRNA^{Arg2}$, contributes to decoding discrimination between three synonymous cognate arginine codons (CGU, CGC, and CGA).[94] Specifically, s^2C32 of $tRNA^{Arg1}$ blocks recognition of the rarest arginine codon, CGA, while still permitting decoding of CGU and CGC. While a substantial number of water molecules (~43,000) and ions (~997 K^+ and ~884 Cl^-) were included, the models of the ribosomal subsystem contained only the ASL, mRNA, and surrounding rRNA that was in direct contact to the ASL or mRNA (the specific residues or cut-off

distance for inclusion in the model were not provided in the computational details). Additionally, only a single-replica 50 ns production simulation was performed, and the surrounding rRNA and ASL heavy atoms were held fixed, only allowing the mRNA codon to move.

Across two later studies,[92, 96] a slightly more rigorous approach was used to study the influence of the t^6A37 and ms^2t^6A37 modifications on $tRNA^{Lys3}$, which is postulated to promote adequate stability of the minihelix when bound to the AAG codon in insulin mRNA. In these studies, the model included the anticodon loop and surrounding rRNA and ribosomal proteins within 25 Å of the codon-anticodon minihelix. However, in the first study, the simulation length was elongated to 100 ns and trajectories were run in quintuplicate.[92] In the second study, simulation length was decreased to 25 ns and no replicas were considered.[96] In both studies, restraints were applied to all heavy atoms in the rRNA, proteins, and mRNA (excluding the codon). A similar study examining the influence of different modification patterns present in the ASL of $tRNA^{Lys,3}$ in the context of the ribosome A-site also suffered from inadequate sampling, generating only 4 ns in a single simulation for each model.[97]

While tRNA modifications have received some attention in MD simulation studies of translation, attention to mRNA modifications has been minimal by comparison. In a study on the influence of 2'-O-methylation of mRNA codons and cognate $tRNA^{Lys3}$ binding in the ribosomal A-site, MD simulations were performed on a model consisting of the ASL bound to mRNA and surrounding rRNA (total of 150 nucleotides).[93] Simulations were conducted for unmodified codons (AAA) and codons with 2'O-methylations introduced into either the first or second codon position (AmAA and AAmA). In this case, a longer 500 ns simulation was carried out for each model, but no replicas. It was unclear whether the backbone atoms were restrained as done in the work described above with the same primary computational author.[92, 94, 96]

It is apparent that methodological issues are common in the computational literature using aaMD to study the influence of RNA modifications on decoding. The most pertinent issues are the likely inadequate model sizes or limited sampling of conformational dynamics either by intentionally enforced restraints on motion (in the region of interest rather than just the periphery of a truncated model) during production simulations, short timescales, and/or lack of replicas. It is unclear why the available computational literature studying RNA modifications have such methodological inconsistencies compared to the studies on selection of near-cognate and cognate tRNAs using aaMD. Both model types typically use the same cryo-EM or crystal structure starting points and should only differ in that tRNA selection studies typically involve canonical nucleoside substitutions (e.g., $tRNA^{Phe}$ recognition of UUC vs. UUU codons) rather than modified nucleosides (e.g., $tRNA^{Phe}$ recognition of UUΨ vs. UUU codons). Regardless, this absence of rigorous modeling leaves a noticeable lack of understanding of the structural dynamic influences of tRNA and/or mRNA modifications on decoding.

2.3 Methodology

2.3.1 A-site ribosome subsystem model building

In this thesis, an A-site ribosomal subsystem model was constructed that includes the ternary complex of tRNA:EF-Tu:GTP bound to the mRNA codon and surrounding rRNA and protein residues. Initial coordinates were extracted from the full 70S *E. coli* ribosome cryo-EM structure that contains a cognate ternary complex in the A-site (PDB ID: 5UYL). In this structure, the tRNA adopts a bent conformation such that the anticodon is bound in the A-site, while the acceptor domain is bound to EF-Tu (denoted A/T) and makes contact with the 23S rRNA. The ribosomal region of the model included all residues within 30 Å of any atoms in the tRNA, which generated a model of ~31,200 atoms (Figure 2.1). Specifically, the full tRNA was included because progression of translation is highly dependent on its conformational changes during

initial selection. From the SSU, the ribosomal protein s12 and disparate regions of 16S rRNA from helices 1, 2, 18, 28, 29, 30, 31, 32, 34, 35, 44 and 45 were included. From the LSU, regions from the ribosomal proteins L6, L11, L36, and rRNA helices 69, 89, 90, 91, and 95 were included. As the 5UYL structure did not contain resolved magnesium ions bound to the phosphate oxygens of rRNA, the 43 magnesium ions were introduced by aligning the 2.0 Å resolution *E. coli* ribosome backbone atoms (PDB ID: 7K00) to the model. Known modifications in the 16S rRNA that were not resolved in PDB ID: 5UYL were included by aligning 16S rRNA from PDB ID: 7K00 and replacing the relevant nucleotides in the model,[98] while maintaining the original backbone conformation of PDB ID: 5UYL.

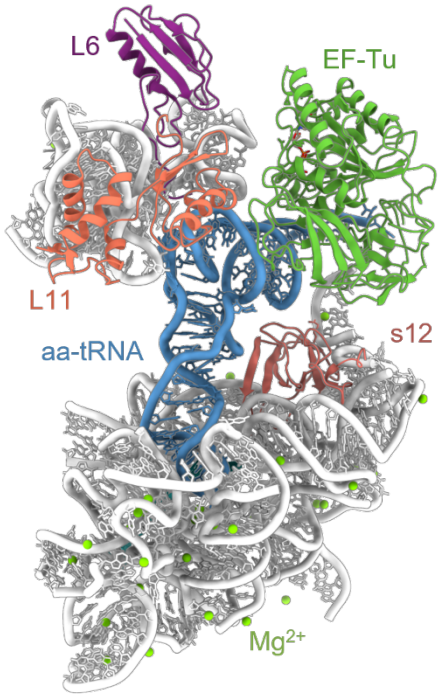

Figure 2.1. The ribosomal A-site subsystem model. The modeled region includes the rRNA (white) of the LSU and SSU surrounding the A-site aa-tRNA (blue), magnesium ions (green), and mRNA (obscured by the SSU rRNA), and ribosomal proteins. The ribosomal proteins are labeled according to the *E. coli* nomenclature (L36 is also included in the model but is not visible from this orientation). Solvent and monoatomic ions were also included in the model but are not shown for clarity.

The monitoring residues A1492 and A1493 both flip out of the 16S rRNA helix 44 to contact the first and second base pairs in the codon–anticodon minihelix through the minor groove during codon recognition.[77] Numerous cryo-EM structures provide evidence of this state occurring for both cognate and near-cognate tRNAs bound in the A-site.[72, 73, 84, 98-127] In the cryo-EM structure (PDB ID: 5UYL), the monitoring adenines adopt a conformation where A1492 is not flipped out of helix 44 and A1493 is not fully engaged with the minihelix. However, there is little to no map density for nucleotides A1492–3, preventing confident modeling of their positions (Figure A.1G). The coordinates of residues 1491–1494 in PDB ID: 5UYL were replaced with those from PDB ID: 7K00 by aligning the corresponding backbone atoms.

Once the template A-site model was built, new models were created by changing the full $tRNA^{Phe}$(GAA) to $tRNA^{Val}$(mcm^5UAC), $tRNA^{Arg}$(ICG), and mRNA to GUG and CGU codons, respectively, and $tRNA^{Met}$(CAU) to be used as a near-cognate tRNA for GUG and IUG mRNA codons. $tRNA^{Met}$(CAU) contains an additional nucleotide in the tRNA D-loop compared to $tRNA^{Phe}$(GAA). Therefore, the $tRNA^{Met}$(CAU) D-loop from an *E. coli* ribosomal complex (PDB: 4V7B) [128] was superimposed to replace the D-loop coordinates in $tRNA^{Phe}$(GAA). For each tRNA, the parent nucleotides contained in $tRNA^{Phe}$ were first changed to the unmodified forms of the sequence corresponding to $tRNA^{Val}$, $tRNA^{Arg}$, and $tRNA^{Met}$ using the swapna function in ChimeraX,[129] with the preserve keyword specified so that the cryo-EM backbone conformation was unaltered. Next, all native modifications were "grown" into the structures according to a fragment residue library using tLEaP in Amber23,[130] which does not alter the backbone coordinates. A similar procedure was followed for the mRNA sequence, where the A-site nucleotides of the 5UYL structure were changed to either GUG, CGU, IUG, CIU, GUI, m^1GUG, Cm^1GU, GUm^1G, m^2GUG, Cm^2GU, or GUm^2G. Note that, as previously mentioned for the near-cognate system with $tRNA^{Met}$, only the GUG and IUG codons were considered.

Before minimization of the entire near-cognate system, the D-loop of the fully modified $tRNA^{Met}$ was energy minimized in the absence of the ribosome, solvent, and ions to remove atomic clashes using the steepest descent and conjugate gradient procedure described in 'System preparation' with all atoms except the D-loop nucleobases restrained across 5 stages of decreasing force constants from 20,000 $kJ \cdot mol^{-1} \cdot nm^{-2}$ to 1,000 $kJ \cdot mol^{-1} \cdot nm^{-2}$. The $tRNA^{Val}$ containing GUG or IUG were then replaced with the $tRNA^{Met}$ coordinates to complete the initial near-cognate models. The amino acids attached to the 3'-end of each tRNA were built by forming a covalent link between the carboxyl carbon of the amino acid and the O3' atom of the terminal adenosine, while maintaining the amide backbone conformation of the phenylalanine present in PDB ID: 5UYL. While the valine moiety fit well in the rRNA pocket, the larger arginine (present in the CGU, CIU, Cm^1GU and Cm^2GU models) clashed with surrounding residues. Therefore, the sculpt tool in PyMol was used to manually remove atomic clashes in the CGU model.[131] Using an energy minimization procedure described in 'System preparation', 20,000 minimization steps were performed with restraints of k=2,500 $kJ \cdot mol^{-1} \cdot nm^{-2}$ applied to all atoms except the 3' adenine and arginine moiety, a 5.0 Å region surrounding the 3' adenine and arginine moiety, and all hydrogen atoms, water molecules, and ions. These minimized coordinates for the CGU model were copied and the G was swapped to an I, m^1G, or m^2G for CIU, Cm^1GU, and Cm^2GU, respectively.

The Amber-formatted topology and coordinate files generated for each A-site ribosome model were converted into a GROMACS-compatible format using Acpype.[132] GROMACS 2024 was then used for all system preparation and simulation steps.[133] All systems were solvated in a periodic truncated octahedral water box with a distance of at least 12 Å from the solute to the nearest box face in all directions. The negative charge remaining after the addition of the experimental magnesium ions was neutralized by replacing solvent water molecules with K^+

ions, and then the salt concentration was set to 150 mM KCl by adding K^+ and Cl^- ions in randomized positions in the solvent with the GROMACS GENION program.[133] The number of particles in each system are summarized in Table A.1.

2.3.2 System preparation

All simulations were performed using the AMBER force field (ff99bsc0χOL3 for RNA),[134, 135] ff14SB for ribosomal proteins,[136] SPC/E for waters,[137] microMg parameters for magnesium ions, [138] and previously developed parameters for modified RNA). [139] The partial charges for aminoacyl terminal nucleotides were calculated using the RESP-fitting procedure in PyRED.[140, 141] Parameters were assigned using Antechamber for the corresponding GAFF atom types.[142]

For all minimization steps, GROMACS index files were generated using selection exporters available in MDAnalysis.[133, 143] The energy of each system was minimized using steepest descent (until convergence criteria were met to a maximum of 10,000 steps) followed by conjugate gradient (up to 10,000 steps) minimization. The systems were minimized with restraints removed on the minihelix for 20,000 steps and finally with all restraints removed for 20,000 steps. Minimization was followed by solvent temperature and pressure equilibration, where 1,000 $kJ \cdot mol^{-1} \cdot nm^{-2}$ positional restraints were applied to all heavy atoms. The system temperature was equilibrated to 300 K under an NVT ensemble within 50,000 steps using a 2 fs time-step and the velocity rescaling thermostat. Following temperature equilibration, the pressure was stabilized under an NPT ensemble with the isotropic pressure coupling using the C-rescale barostat to bring the system pressure to 1 bar over 50,000 steps using a 2 fs time-step. For both NVT and NPT equilibrations, the Verlet cutoff scheme was used for neighbor searching and nonbonded interactions. The Particle Mesh Ewald (PME) method was used for the long-range electrostatic interactions, with a Coulomb cutoff of 10 Å. The van der Waals interactions were modeled using a force-switching modifier, with a 10 Å cutoff and a switching region

starting at 8 Å. All bonds to hydrogen atoms were constrained using LINCS configured with a fourth-order expansion and 2 iterations per time step.

2.3.3 MD production simulation protocol

1 μs production MD simulations were performed in quadruplicate for each model under an NPT ensemble, with the temperature held at 300 K using the velocity rescaling thermostat and pressure fixed to 1 bar using the C-rescale barostat. The microsecond time scale allowed for system convergence, as evidenced by a plateau in the backbone RMSDs of the flexible region within the timescale. Moreover, the system sampled local structural changes of interest, including the flipping of monitoring bases in the 16S rRNA helix, dissociation of the tRNA from mRNA, and large internal conformational changes in the tRNA upon unbinding. Each of the four replicas started with a set of unique initial atomic velocities taken randomly from a Maxwell-Boltzmann distribution at T = 300 K. Previous simulation studies of large ribonucleoprotein complexes used hydrogen mass repartitioning and virtual site constraints to allow for a longer integration time step of 4 fs, which afforded a significant increase in performance.[107, 144] However, due to the central importance of hydrogen-bonding interactions to the underlying dynamics of ribosomal decoding, hydrogen atoms were explicitly modeled in the present work and a 2 fs integration time step was implemented. The long-range interactions were computed using the particle mesh Ewald algorithm with a real-space cutoff of 10 Å. All Cα and C1’ atoms in the P-site mRNA, rRNA, and ribosomal protein exceeding a distance of 20 Å from any atoms of the aa-tRNA were restrained to the initial positions throughout production simulations (k = 1,000 $kJ \cdot mol^{-1} \cdot nm^{-2}$), a procedure used commonly in literature for ribosome subsystem simulations.[36, 51, 59, 61, 63, 107, 144] The size and time scale chosen for the model allowed sampling of conformational changes and interactions known to occur during codon recognition in the A-site, including the 16S rRNA monitoring residue dynamics (e.g., base flipping or interactions with the

minor groove of the codon–anticodon minihelix) and rapid dissociation of tRNA from mRNA. Simulations were performed using an MPI-enabled build of the GROMACS 5 engine with GPU acceleration and GPU–GPU interconnect switched on.[145] All simulations used a single multi-GPU node with 2–8 CPU cores and 2–4 GPUs, with an entire GPU dedicated to the PME summation and the rest assigned to particle–particle interactions. During production runs, the nonbonded, bonded, and PME calculations were offloaded to the GPU to obtain maximal performance. The simulation performance varied depending on the number of GPUs, CPUs, and OpenMP threads (Table A.2).

2.3.4 Analysis of simulations

The programs used for analysis of MD trajectories included CPPTRAJ,[146] Pymol,[131] ChimeraX,[129] Barnaba,[147] and MDTraj.[148]

Root-mean-squared deviation (RMSD) was calculated for each system using equation 1.

$$RMSD = \sqrt{\frac{1}{N}\sum(x_i - y_i)^2} \quad (1)$$

where N is the number of data points, x_i is the position of the ith atom in the reference cryo-EM structure coordinates, and y_i is the position of the ith atom in the simulation frame. The RMSD was computed for backbone atoms of the whole system including the outer 10 Å restrained shell region, whole system, A-site tRNA, mRNA, EF-Tu, h18, h45, H69, GAC, SRL, H89, H91, s12, L6, L11, and L36.

Due to the large size of the flexible region of the model, clustering was not used to generate representative structures. Clustering algorithms face computational bottlenecks when applied to global (large) selections of atoms due to the high dimensionality of the data in the pre-clustering step (i.e., for N atoms and M frames, O(N) operations are needed to compute RMSD between two frames, and combined with the M x M pairwise distance matrix, cost scales as $O(NM^2)$). Therefore, the last frame was extracted from each simulation replica as a

representative structure. Representative structures for the tRNA and G530 interactions with the codon-anticodon minihelix were generated using the hierarchical agglomerative clustering with average-linkage and RMSD as a distance metric. For tRNA, the atoms considered included phosphate (P), oxygen (O3', O5'), and carbon (C3', C4', C5') atoms from residues 1-76, focusing on the backbone to capture global conformational shifts while ignoring base pair fluctuations. For G530 conformations, the clustering routine included all nucleotide atoms from positions 34-36, 83-85, and G530, excluding hydrogen atoms.

The root-mean-squared fluctuation (RMSF) was computed according to the equation:

$$RMSF = \sqrt{\frac{1}{N}\sum(x_i(t) - \langle x_i \rangle)^2} \quad (2)$$

where N is the number of frames, $x_i(t)$ is the position of the ith atom at time t, and $\langle x_i \rangle$ is the quadruplicate ensemble-averaged position of the ith atom. The RMSF was averaged across the quadruplicate ensemble and standard deviations computed to measure how RMSF varied across independent simulations.

The flipping of the two 16S rRNA adenines in helix 44 towards the minor groove of the minihelix was measured using a dihedral angle denoted Φ, the monitoring angle. The four points of the dihedral angle were designated according to the centers of mass (COM) of four atom masks as done in a previous simulation study.[74] Specifically, the points were defined based on the center of mass of C1407, C1409, G1491, and G1494 nucleobase atoms in the 16S rRNA (COM1), the phosphate group of the 3' adjacent nucleobase to the flipping adenine (COM2), the nucleobase phosphate group for A1492 or A1493 (COM3), and the nucleobase atoms of either A1492 or A1493 (COM4). First, Φ angles were measured from an experimental suite of 126 X-ray and cryo-EM ribosomal complexes (Table A.1) to compare with the simulation data (Chapter 3).[60, 72, 73, 84, 99, 105, 119, 121, 123-126, 149-172] The suite included ribosome structures with near-cognate or cognate A-site tRNA or without A-site tRNA. The map-model fit tends to be poor for A1492–3

with flexible conformations as the map density may be absent or at a poor local resolution. The 16S A1492–3 map-model fit was assessed using ChimeraX for structures with empty A-site, or in the off-on conformation (Figure A.1). The map-model fit was concluded to be poor for PDB IDs 5KCR, 5MDY, 5MDZ, 5UYK, 5UYN, 5UYL, and 8G7S, and therefore these structures were excluded from the dataset (Figure A.1A,C-H), leaving 116 ribosome structures in the final dataset.

The Φ angles were collected for both A1492 and A1493 and plotted over the simulation time. A joint probability distribution was generated using the 2D histogram function (of Φ for A1492 on the x-axis and A1493 on the y-axis) in NumPy set to 80 bins. The 2D histogram counts were converted into a joint probability density, $P(i,j)$:

$$P(i,j) = \frac{H(i,j)}{\sum_{i,j} H(i,j)} \quad (3)$$

with the normalization condition:

$$\sum_{i,j} P(i,j) = 1 \quad (4)$$

where i and j represent the bin index of A1492 and A1493, respectively. $H(i,j)$ is the array of all possible bins where data is partitioned and $\sum H$ is the total number of data points across all bins. The free energy, $G(i,j)$, was then computed according to equation 5:

$$G(i,j) = -RT \cdot ln\left(\frac{P(i,j)}{P_{max}}\right) \quad (5)$$

where $T = 300\ K$, R = 1.987 x 10^{-3} kcal·K^{-1}·mol^{-1} and $P_{max} = 1$. Since zero probabilities occur in MD simulations because of finite sampling limitations despite density-related quantities in true physical systems always being nonzero, zero probabilities were substituted by a small value, $P = 1 \times 10^{-7}$, to keep $ln\big(P(i,j)\big)$ defined and finite. Local minima were chosen using the scipy.ndimage.minimum_filter, with a size of 10 and a threshold of <0.25 kcal/mol. The COM

distance between the monitoring residues (A1492, A1493, and G530) C1′ atom and the center of mass of all minihelix atoms were calculated using the distance function in cpptraj.

To analyze the local solvent distribution in the minihelix minor groove, the watershell function from CPPTRAJ was utilized. The number of water molecules within 5 Å of the COM of the minihelix minor groove of the first, second, and third base-pairing positions of the codon were computed separately. For the GUG systems and modified variants, the COMs included the N2 and N3 of G1 and O2 of C36 in the first base pair, the O2 of U2 and N3 of A35 in the second base pair, and the N2 and N3 of G3 and O2 of cmo^{5}U34 in the third base pair. For the CGU systems and modified variants, the COMs included the O2 of C1 and the N3 and N2 of G36 in the first base pair, the N3 and N2 of G2 and O2 of C35 in the second base pair, and the O2 of U3 and N3 of I34 in the third base pair. As the first and second base-pairing positions are less prone to noise and actively monitored, the datasets for the B1:B36 and B2:B35 were concatenated and frequency histograms were generated to compare between models. The ensemble-average and standard deviation (S.D.) of the number of waters were tabulated for all three base-pairing positions.

To assess the proximity of A1492–3 to the minihelix minor groove, interatomic distances were computed for A1493 from the COM of the first base pair (B1:B36) and for A1492 from the COM of the second base pair (B2:B35) using the distance function in CPPTRAJ.

Minihelix nucleobase–nucleobase coplanar angles were computed by generating vectors orthogonal to the plane defined by nucleobase atoms using the corrplane and vectormath functions in cpptraj for each codon–anticodon base pair. The C1′–C1′ distances were computed using the distance function in cpptraj between opposing nucleotides in the minihelix. Hydrogen bonds were computed using the hbond function in cpptraj and defined using an angle cutoff of 120° and a distance cut-off of 3.4 Å.

The alignment of tRNA within the A-site was calculated by measuring the angle, θ, between vectors defining the mRNA codon, $\vec{m}$, and the tRNA body, $\vec{t}$, using equation 6.

$$\theta = arccos\left(\frac{\vec{m}\cdot\vec{t}}{||\vec{m}||\,||\vec{t}||}\right) \quad (6)$$

The absolute deviation of the angle formed between the center of the anticodon stem (ACS) and the central domain junction of the tRNA (Δ^{ACS}) was computed using cpptraj. To compute Δ^{ACS}, a reference vector formed between the COM of the central junction of the tRNA (base pair 10–25 of the D-arm and residue 44 of the variable loop) and the COM of the TΨC/acceptor arm (residues 1–8 and 58–76) was generated from the experimental structure coordinates. The analogous vector was subsequently generated for the structure in each simulation frame. The dot product between the (fixed) reference vector and the vector for the current frame was computed for each frame in an analogous manner to equation 6. Since the starting structure exhibits a bent conformation, larger Δ^{ACS} values indicate a higher degree of straightening. The distance between the COM of the ASL and the tRNA elbow was also expected to increase for straight tRNA (i.e., if the tRNA body is uncompressed). Therefore, the ASL–elbow distance was measured between the COM of the ASL (residues 27-43) and the elbow region on the acceptor domain (residues 55–57).

The Barnaba python library was used to cluster the trajectories into conformational states using the $\varepsilon RMSD$ metric with the DBSCAN algorithm.[147] Barnaba defines a vector, r, expressed in cylindrical coordinates ρ, θ, and z measured from the local COM coordinates defined by the C2, C4, and O6 atoms of each RNA nucleobase. The relative position and orientation between two nucleobases are defined in the cylindrical coordinate system. The scaled anisotropic position vector, $\tilde{r}$, is used to describe the relative coordinates of the nucleobases:

$$\tilde{r} = \left(\frac{r_x}{a}, \frac{r_y}{a}, \frac{r_z}{b}\right) = \left(\frac{\rho}{a}\cos\theta, \frac{\rho}{a}\sin\theta, \frac{z}{b}\right) \quad (7)$$

where a = 5.0 Å and b = 3.0 Å so that $1 < \tilde{r} < \sqrt{2.5}$, which defines an ellipsoidal region where over 99% of stacking and base pairing interactions occur.[147] The stacking can be distinguished from the pairing by determining the projection of the position vector, r, along the z-axis. Specifically, if the projection is less than 2.0 Å then the base–base contact is defined as pairing, while if it is greater than 2.0 Å, it is defined as stacking. With all the scaled vectors, $\tilde{r}$, the structural deviation between RNA structures (α and β) can be calculated by using a cut-off distance $\tilde{r}_{cutoff}$ and mapping the $\tilde{r}$ vectors using the 4-dimensional vectorial function G($\tilde{r}$):

$$\mathrm{G}(\tilde{r}) = \begin{pmatrix} \frac{\tilde{r_x}}{\tilde{r}}\sin(\gamma\tilde{r}) \\ \frac{\tilde{r_y}}{\tilde{r}}\sin(\gamma\tilde{r}) \\ \frac{\tilde{r_z}}{\tilde{r}}\sin(\gamma\tilde{r}) \\ 1+\cos(\gamma) \end{pmatrix} \times \frac{\Theta(\tilde{r}_{cutoff}-\tilde{r})}{\gamma} \quad (8)$$

where $\tilde{r}_{cutoff}$ = 2.4 Å and $\gamma = \frac{\pi}{\tilde{r}_{cutoff}}$.[147]

The metric eRMSD is then defined as:

$$\mathrm{eRMSD} = \sqrt{\frac{1}{N}\sum_{j,k}\left|G\left(\tilde{r}_{jk}^{\alpha}\right) - G\left(\tilde{r}_{jk}^{\beta}\right)\right|^2} \quad (9)$$

where α and β represent the two RNA structures being compared and N is the number of data points. The eRMSD metric depends on the distance between G vectors and allows for structural comparison using a continuous function with suitable cut-off distances. To generate conformational profiles for the MD trajectories, the eRMSD was used as a clustering metric with the DBSCAN algorithm.

2.4 Conclusions

This chapter discussed the strengths and weaknesses of various MD techniques for studying how mRNA modifications impact decoding. This knowledge was used to develop the model used in this thesis. Specifically, a ribosome subsystem model was developed that includes

the entire ternary complex of aa-tRNA:EF-Tu:GTP in the codon recognition configuration and all surrounding Mg^{2+} ions, rRNA, and proteins. The simulations utilized explicit solvent and aaMD to describe the detailed interactions in the decoding center and solvent shielding of the minihelix minor groove by A1492–3 and G530. Moreover, the model enables simulations to capture rapid local dynamics in the A-site that are inaccessible to experiment, such as fluctuations between intra- and extrahelical conformations for 16S monitoring residues, latching of G530 onto the minor groove, minihelix structural changes, and conformational changes in the aa-tRNA body. Indeed, Chapters 3 and 4 will show that the models developed in this thesis can be used to interpret kinetic studies of the impact of mRNA modifications on protein synthesis.

2.5 References

(1) Bock, L. V.; Gabrielli, S.; Kolář, M. H.; Grubmüller, H. Simulation of Complex Biomolecular Systems: The Ribosome Challenge. *Annu. Rev. Biophys.* **2023**, *52* (Volume 52, 2023), 361-390. DOI: https://doi.org/10.1146/annurev-biophys-111622-091147.

(2) Chowdhury, A. R.; Sapkota, D.; Girodat, D. Conformational changes of ribosomes during translation elongation resolved by molecular dynamics simulations. *Curr. Opin. Struct. Biol.* **2024**, *86*, 102804. DOI: https://doi.org/10.1016/j.sbi.2024.102804.

(3) Sanbonmatsu, K. Y. Computational studies of molecular machines: the ribosome. *Curr. Opin. Struct. Biol.* **2012**, *22* (2), 168-174.

(4) Makarov, G. I.; Makarova, T. M.; Sumbatyan, N. V.; Bogdanov, A. A. Investigation of ribosomes using molecular dynamics simulation methods. *Biochemistry (Moscow)* **2016**, *81* (13), 1579-1588. DOI: 10.1134/S0006297916130010.

(5) Trovato, F.; apos; Brien, E. P. Insights into Cotranslational Nascent Protein Behavior from Computer Simulations. *Annu. Rev. Biophys.* **2016**, *45* (Volume 45, 2016), 345-369. DOI: https://doi.org/10.1146/annurev-biophys-070915-094153.

(6) Nissley, D. A.; Vu, Q. V.; Trovato, F.; Ahmed, N.; Jiang, Y.; Li, M. S.; O'Brien, E. P. Electrostatic Interactions Govern Extreme Nascent Protein Ejection Times from Ribosomes and Can Delay Ribosome Recycling. *J. Am. Chem. Soc.* **2020**, *142* (13), 6103-6110. DOI: 10.1021/jacs.9b12264.

(7) Makarov, G. I.; Golovin, A. V.; Sumbatyan, N. V.; Bogdanov, A. A. Molecular dynamics investigation of a mechanism of allosteric signal transmission in ribosomes. *Biochemistry (Moscow)* **2015**, *80* (8), 1047-1056. DOI: 10.1134/S0006297915080106.

(8) Jonikas, M. A.; Radmer, R. J.; Laederach, A.; Das, R.; Pearlman, S.; Herschlag, D.; Altman, R. B. Coarse-grained modeling of large RNA molecules with knowledge-based potentials and structural filters. *RNA* **2009**, *15* (2), 189-199. DOI: 10.1261/rna.1270809.

(9) Tan, R. K. Z.; Petrov, A. S.; Harvey, S. C. YUP: A Molecular Simulation Program for Coarse-Grained and Multiscaled Models. *J. Chem. Theory Comput.* **2006**, *2* (3), 529-540. DOI: 10.1021/ct050323r.

(10) Marrink, S. J.; Risselada, H. J.; Yefimov, S.; Tieleman, D. P.; de Vries, A. H. The MARTINI Force Field: Coarse Grained Model for Biomolecular Simulations. *J. Phys. Chem. B.* **2007**, *111* (27), 7812-7824. DOI: 10.1021/jp071097f.

(11) Uusitalo, J. J.; Ingólfsson, H. I.; Marrink, S. J.; Faustino, I. Martini coarse-grained force field: extension to RNA. *Biophys. J.* **2017**, *113* (2), 246-256.

(12) Yu, S.; Srebnik, S.; Dao Duc, K. Geometric differences in the ribosome exit tunnel impact the escape of small nascent proteins. *Biophys. J.* **2023**, *122* (1), 20-29. DOI: https://doi.org/10.1016/j.bpj.2022.11.2945.

(13) Niesen, M. J. M.; Wang, C. Y.; Van Lehn, R. C.; Miller, T. F., III. Structurally detailed coarse-grained model for Sec-facilitated co-translational protein translocation and membrane integration. *PLOS Comput. Biol.* **2017**, *13* (3), e1005427. DOI: 10.1371/journal.pcbi.1005427.

(14) Niesen, M. J. M.; Müller-Lucks, A.; Hedman, R.; von Heijne, G.; Miller, T. F., III. Forces on Nascent Polypeptides during Membrane Insertion and Translocation via the Sec Translocon. *Biophys. J.* **2018**, *115* (10), 1885-1894. DOI: 10.1016/j.bpj.2018.10.002 (acccessed 2025/03/25).

(15) Kurkcuoglu, O.; Turgut, O. T.; Cansu, S.; Jernigan, R. L.; Doruker, P. Focused Functional Dynamics of Supramolecules by Use of a Mixed-Resolution Elastic Network Model. *Biophys. J.* **2009**, *97* (4), 1178-1187. DOI: https://doi.org/10.1016/j.bpj.2009.06.009.

(16) Wang, Y.; Rader, A. J.; Bahar, I.; Jernigan, R. L. Global ribosome motions revealed with elastic network model. *J. Struct. Biol.* **2004**, *147* (3), 302-314. DOI: https://doi.org/10.1016/j.jsb.2004.01.005.

(17) Tama, F.; Valle, M.; Frank, J.; Brooks, C. L. Dynamic reorganization of the functionally active ribosome explored by normal mode analysis and cryo-electron microscopy. *Proc. Natl. Acad. Sci. U.S.A.* **2003**, *100* (16), 9319-9323. DOI: doi:10.1073/pnas.1632476100.

(18) Trylska, J.; Konecny, R.; Tama, F.; Brooks III, C. L.; McCammon, J. A. Ribosome motions modulate electrostatic properties. *Biopolymers* **2004**, *74* (6), 423-431. DOI: https://doi.org/10.1002/bip.20093.

(19) Kurkcuoglu, O.; Doruker, P.; Sen, T. Z.; Kloczkowski, A.; Jernigan, R. L. The ribosome structure controls and directs mRNA entry, translocation and exit dynamics. *Phys Biol* **2008**, *5* (4), 046005. DOI: 10.1088/1478-3975/5/4/046005.

(20) Zhang, Z.; Sanbonmatsu, K. Y.; Voth, G. A. Key Intermolecular Interactions in the E. coli 70S Ribosome Revealed by Coarse-Grained Analysis. *J. Am. Chem. Soc.* **2011**, *133* (42), 16828-16838. DOI: 10.1021/ja2028487.

(21) Noel, J. K.; Whitford, P. C. How EF-Tu can contribute to efficient proofreading of aa-tRNA by the ribosome. *Nat. Commun.* **2016**, *7* (1), 13314. DOI: 10.1038/ncomms13314.

(22) Noel, Jeffrey K.; Chahine, J.; Leite, Vitor B. P.; Whitford, Paul C. Capturing Transition Paths and Transition States for Conformational Rearrangements in the Ribosome. *Biophys. J.* **2014**, *107* (12), 2881-2890. DOI: https://doi.org/10.1016/j.bpj.2014.10.022.

(23) Yang, H.; Noel, J. K.; Whitford, P. C. Anisotropic Fluctuations in the Ribosome Determine tRNA Kinetics. *J. Phys. Chem. B.* **2017**, *121* (47), 10593-10601. DOI: 10.1021/acs.jpcb.7b06828.

(24) Bui, P. T.; Hoang, T. X. Protein escape at the ribosomal exit tunnel: Effect of the tunnel shape. *J. Chem. Phys.* **2020**, *153* (4), 045105. DOI: 10.1063/5.0008292.

(25) Bui, P. T.; Hoang, T. X. Protein escape at the ribosomal exit tunnel: Effects of native interactions, tunnel length, and macromolecular crowding. *J. Chem. Phys.* **2018**, *149* (4).

(26) Takada, S. Gō model revisited. *Biophys. Physicobiol.* **2019**, *16*, 248-255. DOI: 10.2142/biophysico.16.0_248.

(27) de Oliveira, A. B., Jr.; Contessoto, V. G.; Hassan, A.; Byju, S.; Wang, A.; Wang, Y.; Dodero-Rojas, E.; Mohanty, U.; Noel, J. K.; Onuchic, J. N.; et al. SMOG 2 and OpenSMOG: Extending the limits of structure-based models. *Protein Sci.* **2022**, *31* (1), 158-172. DOI: 10.1002/pro.4209.

(28) Sanbonmatsu, K. Supercomputing in the biological sciences: Toward Zettascale and Yottascale simulations. *Curr. Opin. Struct. Biol.* **2024**, *88*, 102889. DOI: https://doi.org/10.1016/j.sbi.2024.102889.

(29) Levi, M.; Noel, J. K.; Whitford, P. C. Studying ribosome dynamics with simplified models. *Methods* **2019**, *162-163*, 128-140. DOI: 10.1016/j.ymeth.2019.03.023.

(30) Alejo, J. L.; Girodat, D.; Hammerling, M. J.; Willi, J. A.; Jewett, M. C.; Engelhart, A. E.; Adamala, K. P. Alternate conformational trajectories in ribosome translocation. *PLoS Comput. Biol.* **2024**, *20* (8), e1012319. DOI: 10.1371/journal.pcbi.1012319.

(31) Girodat, D. J.; Nishima, W.; Holm, M.; Rundlet, E. J.; Prajapati, J. D.; Amaya, J. L. A.; Fischer, K.; Blanchard, S. C.; Sanbonmatsu, K. Y. Ribosome hyper-swivel head domain motions are required for translocation and resetting. *Biophys. J.* **2023**, *122* (3), 360a. DOI: 10.1016/j.bpj.2022.11.1990 (acccessed 2025/03/19).

(32) Whitford, P. C.; Geggier, P.; Altman, R. B.; Blanchard, S. C.; Onuchic, J. N.; Sanbonmatsu, K. Y. Accommodation of aminoacyl-tRNA into the ribosome involves reversible excursions along multiple pathways. *RNA* **2010**, *16* (6), 1196-1204. DOI: 10.1261/rna.2035410.

(33) Girodat, D.; Wieden, H. J.; Blanchard, S. C.; Sanbonmatsu, K. Y. Geometric alignment of aminoacyl-tRNA relative to catalytic centers of the ribosome underpins accurate mRNA decoding. *Nat. Commun.* **2023**, *14* (1), 5582. DOI: 10.1038/s41467-023-40404-9.

(34) Sanbonmatsu, K. Y.; Girodat, D. BPS2025 - Human aminoacyl-tRNA pivots during accommodation. *Biophys. J.* **2025**, *124* (3), 82a. DOI: 10.1016/j.bpj.2024.11.505 (acccessed 2025/03/31).

(35) Wang, Y.; Wang, A. L.; Mohanty, U.; Whitford, P. C. Precise Steric Features Control Aminoacyl-tRNA Accommodation on the Ribosome. *J. Phys. Chem. B.* **2022**, *126* (42), 8447-8459, Article. DOI: 10.1021/acs.jpcb.2c05513.

(36) Bock, L. V.; Blau, C.; Schröder, G. F.; Davydov, I. I.; Fischer, N.; Stark, H.; Rodnina, M. V.; Vaiana, A. C.; Grubmüller, H. Energy barriers and driving forces in tRNA translocation through the ribosome. *Nat. Struct. Mol. Biol.* **2013**, *20* (12), 1390-1396. DOI: 10.1038/nsmb.2690.

(37) Satpati, P.; Sund, J.; Åqvist, J. Structure-Based Energetics of mRNA Decoding on the Ribosome. *Biochem.* **2014**, *53* (10), 1714-1722. DOI: 10.1021/bi5000355.

(38) Sanbonmatsu, K. Y.; Joseph, S. Understanding discrimination by the ribosome: stability testing and groove measurement of codon-anticodon pairs. *J. Mol. Biol.* **2003**, *328* (1), 33-47. DOI: 10.1016/s0022-2836(03)00236-5.

(39) Rozov, A.; Khusainov, I.; El Omari, K.; Duman, R.; Mykhaylyk, V.; Yusupov, M.; Westhof, E.; Wagner, A.; Yusupova, G. Importance of potassium ions for ribosome structure and function revealed by long-wavelength X-ray diffraction. *Nat. Commun.* **2019**, *10* (1), 2519. DOI: 10.1038/s41467-019-10409-4.

(40) McCarthy, B. J. The effects of magnesium starvation on the ribosome content of *Escherichia coli*. *Biochimica et Biophysica Acta (BBA) - Specialized Section on Nucleic Acids and Related Subjects* **1962**, *55* (6), 880-889. DOI: https://doi.org/10.1016/0926-6550(62)90345-6.

(41) Näslund, P. H.; Hultin, T. Effects of potassium deficiency on mammalian ribosomes. *Biochimica et Biophysica Acta (BBA) - Nucleic Acids and Protein Synthesis* **1970**, *204* (1), 237-247. DOI: https://doi.org/10.1016/0005-2787(70)90507-1.

(42) Rheinberger, H.-J.; and Nierhaus, K. H. The Ribosomal E Site at Low Mg2+: Coordinate Inactivation of Ribosomal Functions at Mg^{2+} Concentrations Below 10 mM and its Prevention by Polyamines. *J. Biomol. Struct. Dyn.* **1987**, *5* (2), 435-446. DOI: 10.1080/07391102.1987.10506403.

(43) Tal, M. Metal ions and ribosomal conformation. *Biochimica et Biophysica Acta (BBA) - Nucleic Acids and Protein Synthesis* **1969**, *195* (1), 76-86. DOI: https://doi.org/10.1016/0005-2787(69)90604-2.

(44) Nierhaus, K. H. Mg^{2+}, K^{+}, and the Ribosome. *J. Bacteriol.* **2014**, *196* (22), 3817-3819. DOI: doi:10.1128/jb.02297-14.

(45) Fromm, S. A.; O'Connor, K. M.; Purdy, M.; Bhatt, P. R.; Loughran, G.; Atkins, J. F.; Jomaa, A.; Mattei, S. The translating bacterial ribosome at 1.55 Å resolution generated by cryo-EM imaging services. *Nat. Commun.* **2023**, *14* (1), 1095. DOI: 10.1038/s41467-023-36742-3.

(46) Kišonaitė, M.; Wild, K.; Lapouge, K.; Ruppert, T.; Sinning, I. High-resolution structures of a thermophilic eukaryotic 80S ribosome reveal atomistic details of translocation. *Nat. Commun.* **2022**, *13* (1), 476. DOI: 10.1038/s41467-022-27967-9.

(47) Konevega, A. L.; Soboleva, N. G.; Makhno, V. I.; Semenkov, Y. P.; Wintermeyer, W.; Rodnina, M. V.; Katunin, V. I. Purine bases at position 37 of tRNA stabilize codon-anticodon interaction in the ribosomal A site by stacking and Mg^{2+}-dependent interactions. *RNA* **2004**, *10* (1), 90-101. DOI: 10.1261/rna.5142404.

(48) Keedy, H. E.; Thomas, E. N.; Zaher, H. S. Decoding on the ribosome depends on the structure of the mRNA phosphodiester backbone. *Proc. Natl. Acad. Sci. U.S.A.* **2018**, *115* (29), E6731-E6740. DOI: doi:10.1073/pnas.1721431115.

(49) Wang, A.; Levi, M.; Mohanty, U.; Whitford, P. C. Diffuse Ions Coordinate Dynamics in a Ribonucleoprotein Assembly. *J. Am. Chem. Soc.* **2022**, *144* (21), 9510-9522. DOI: 10.1021/jacs.2c04082.

(50) Holm, M.; Natchiar, S. K.; Rundlet, E. J.; Myasnikov, A. G.; Watson, Z. L.; Altman, R. B.; Wang, H.-Y.; Taunton, J.; Blanchard, S. C. mRNA decoding in human is kinetically and structurally distinct from bacteria. *Nature* **2023**, *617* (7959), 200-207. DOI: 10.1038/s41586-023-05908-w.

(51) Kolář, M. H.; Nagy, G.; Kunkel, J.; Vaiana, S. M.; Bock, L. V.; Grubmüller, H. Folding of VemP into translation-arresting secondary structure is driven by the ribosome exit tunnel. *Nucleic Acids Res.* **2022**, *50* (4), 2258-2269. DOI: 10.1093/nar/gkac038 (acccessed 2/6/2025).

(52) McGrath, H.; Černeková, M.; Kolář, M. H. Binding of the peptide deformylase on the ribosome surface modulates the exit tunnel interior. *Biophys. J.* **2022**, *121* (23), 4443-4451. DOI: https://doi.org/10.1016/j.bpj.2022.11.004.

(53) Bock, L. V.; Blau, C.; Vaiana, A. C.; Grubmüller, H. Dynamic contact network between ribosomal subunits enables rapid large-scale rotation during spontaneous translocation. *Nucleic Acids Res.* **2015**, *43* (14), 6747-6760. DOI: 10.1093/nar/gkv649.

(54) Ishida, H.; Matsumoto, A. Free-energy landscape of reverse tRNA translocation through the ribosome analyzed by electron microscopy density maps and molecular dynamics simulations. *PLoS One* **2014**, *9* (7), e101951. DOI: 10.1371/journal.pone.0101951.

(55) Brandman, R.; Brandman, Y.; Pande, V. S. A-site residues move independently from P-site residues in all-atom molecular dynamics simulations of the 70S bacterial ribosome. *PLoS One* **2012**, *7* (1), e29377. DOI: 10.1371/journal.pone.0029377.

(56) Whitford, P. C.; Blanchard, S. C.; Cate, J. H.; Sanbonmatsu, K. Y. Connecting the kinetics and energy landscape of tRNA translocation on the ribosome. *PLoS Comput. Biol.* **2013**, *9* (3), e1003003. DOI: 10.1371/journal.pcbi.1003003.

(57) Makarov, G. I.; Makarova, T. M. A noncanonical binding site of chloramphenicol revealed via molecular dynamics simulations. *Biochimica et Biophysica Acta (BBA) - General Subjects* **2018**, *1862* (12), 2940-2947. DOI: https://doi.org/10.1016/j.bbagen.2018.09.012.

(58) Ishida, H.; Hayward, S. Path of nascent polypeptide in exit tunnel revealed by molecular dynamics simulation of ribosome. *Biophys. J.* **2008**, *95* (12), 5962-5973. DOI: 10.1529/biophysj.108.134890.

(59) Beckert, B.; Leroy, E. C.; Sothiselvam, S.; Bock, L. V.; Svetlov, M. S.; Graf, M.; Arenz, S.; Abdelshahid, M.; Seip, B.; Grubmüller, H.; et al. Structural and mechanistic basis for translation inhibition by macrolide and ketolide antibiotics. *Nat. Commun.* **2021**, *12* (1), 4466. DOI: 10.1038/s41467-021-24674-9.

(60) Gersteuer, F.; Morici, M.; Gabrielli, S.; Fujiwara, K.; Safdari, H. A.; Paternoga, H.; Bock, L. V.; Chiba, S.; Wilson, D. N. The SecM arrest peptide traps a pre-peptide bond formation state of the ribosome. *Nat. Commun.* **2024**, *15* (1), 2431. DOI: 10.1038/s41467-024-46762-2.

(61) Huter, P.; Arenz, S.; Bock, L. V.; Graf, M.; Frister, J. O.; Heuer, A.; Peil, L.; Starosta, A. L.; Wohlgemuth, I.; Peske, F.; et al. Structural Basis for Polyproline-Mediated Ribosome Stalling and Rescue by the Translation Elongation Factor EF-P. *Mol. Cell.* **2017**, *68* (3), 515-527.e516. DOI: https://doi.org/10.1016/j.molcel.2017.10.014.

(62) Lauer, S. M.; Reepmeyer, M.; Berendes, O.; Klepacki, D.; Gasse, J.; Gabrielli, S.; Grubmüller, H.; Bock, L. V.; Krizsan, A.; Nikolay, R.; et al. Multimodal binding and inhibition of bacterial

ribosomes by the antimicrobial peptides Api137 and Api88. *Nat. Commun.* **2024**, *15* (1), 3945. DOI: 10.1038/s41467-024-48027-4.

(63) Morici, M.; Gabrielli, S.; Fujiwara, K.; Paternoga, H.; Beckert, B.; Bock, L. V.; Chiba, S.; Wilson, D. N. RAPP-containing arrest peptides induce translational stalling by short circuiting the ribosomal peptidyltransferase activity. *Nat. Commun.* **2024**, *15* (1), 2432. DOI: 10.1038/s41467-024-46761-3.

(64) Feenstra, K. A.; Hess, B.; Berendsen, H. J. C. Improving efficiency of large time-scale molecular dynamics simulations of hydrogen-rich systems. *J. Comput. Chem.* **1999**, *20* (8), 786-798. DOI: https://doi.org/10.1002/(SICI)1096-987X(199906)20:8<786::AID-JCC5>3.0.CO;2-B.

(65) Kutzner, C.; Páll, S.; Fechner, M.; Esztermann, A.; de Groot, B. L.; Grubmüller, H. More bang for your buck: Improved use of GPU nodes for GROMACS 2018. *J. Comput. Chem.* **2019**, *40* (27), 2418-2431. DOI: https://doi.org/10.1002/jcc.26011.

(66) Zwanzig, R. W. High-Temperature Equation of State by a Perturbation Method. I. Nonpolar Gases. *J. Chem. Phys.* **1954**, *22* (8), 1420-1426. DOI: 10.1063/1.1740409.

(67) Lind, C.; Esguerra, M.; Jespers, W.; Satpati, P.; Gutierrez-de-Terán, H.; Åqvist, J. Free energy calculations of RNA interactions. *Methods* **2019**, *162-163*, 85-95. DOI: https://doi.org/10.1016/j.ymeth.2019.02.014.

(68) Allnér, O.; Nilsson, L. Nucleotide modifications and tRNA anticodon-mRNA codon interactions on the ribosome. *RNA* **2011**, *17* (12), 2177-2188. DOI: 10.1261/rna.029231.111.

(69) Almlöf, M.; Andér, M.; Åqvist, J. Energetics of Codon−Anticodon Recognition on the Small Ribosomal Subunit. *Biochem.* **2007**, *46* (1), 200-209. DOI: 10.1021/bi061713i.

(70) Gromadski, K. B.; Daviter, T.; Rodnina, M. V. A Uniform Response to Mismatches in Codon-Anticodon Complexes Ensures Ribosomal Fidelity. *Mol. Cell.* **2006**, *21* (3), 369-377. DOI: https://doi.org/10.1016/j.molcel.2005.12.018.

(71) Johansson, M.; Zhang, J.; Ehrenberg, M. Genetic code translation displays a linear trade-off between efficiency and accuracy of tRNA selection. *Proc. Natl. Acad. Sci. U.S.A.* **2012**, *109* (1), 131-136. DOI: doi:10.1073/pnas.1116480109.

(72) Voorhees, R. M.; Schmeing, T. M.; Kelley, A. C.; Ramakrishnan, V. The Mechanism for Activation of GTP Hydrolysis on the Ribosome. *Science* **2010**, *330* (6005), 835-838. DOI: 10.1126/science.1194460.

(73) Demeshkina, N.; Jenner, L.; Westhof, E.; Yusupov, M.; Yusupova, G. A new understanding of the decoding principle on the ribosome. *Nature* **2012**, *484* (7393), 256-259. DOI: 10.1038/nature10913.

(74) Zeng, X.; Chugh, J.; Casiano-Negroni, A.; Al-Hashimi, H. M.; Brooks, C. L. Flipping of the Ribosomal A-Site Adenines Provides a Basis for tRNA Selection. *J. Mol. Biol.* **2014**, *426* (19), 3201-3213. DOI: https://doi.org/10.1016/j.jmb.2014.04.029.

(75) König, G.; Brooks, B. R.; Thiel, W.; York, D. M. On the convergence of multi-scale free energy simulations. *Mol. Simul.* **2018**, *44* (13-14), 1062-1081. DOI: 10.1080/08927022.2018.1475741.

(76) Pape, T.; Wintermeyer, W.; Rodnina, M. Induced-fit in initial selection and proofreading of aminoacyl-tRNA on the ribosome. *Embo j* **1999**, *18* (13), 3800-3807. DOI: 10.1093/emboj/18.13.3800.

(77) Rodnina, M. V.; Wintermeyer, W. Ribosome fidelity: tRNA discrimination, proofreading and induced-fit. *Trends Biochem. Sci* **2001**, *26* (2), 124-130. DOI: https://doi.org/10.1016/S0968-0004(00)01737-0.

(78) Caulfield, T.; Coban, M.; Tek, A.; Flores, S. C. Molecular Dynamics Simulations Suggest a Non-Doublet Decoding Model of −1 Frameshifting by $tRNA^{Ser3}$. *Biomolecules* **2019**, *9* (11), 745.

(79) Dalgarno, C.; Scopino, K.; Raval, M.; Nachmanoff, C.; Sakkas, E. D.; Krizanc, D.; Thayer, K. M.; Weir, M. P. The CAR–mRNA Interaction Surface Is a Zipper Extension of the Ribosome A Site. *Int. J. Mol. Sci.* **2022**, *23* (3), 1417.

(80) Scopino, K.; Dalgarno, C.; Nachmanoff, C.; Krizanc, D.; Thayer, K. M.; Weir, M. P. Arginine Methylation Regulates Ribosome CAR Function. *Int. J. Mol. Sci.* **2021**, *22* (3), 1335.

(81) Small, M. C.; Lopes, P.; Andrade, R. B.; Mackerell, A. D., Jr. Impact of ribosomal modification on the binding of the antibiotic telithromycin using a combined grand canonical monte carlo/molecular dynamics simulation approach. *PLoS Comput. Biol.* **2013**, *9* (6), e1003113. DOI: 10.1371/journal.pcbi.1003113.

(82) Englander, M. T.; Avins, J. L.; Fleisher, R. C.; Liu, B.; Effraim, P. R.; Wang, J.; Schulten, K.; Leyh, T. S.; Gonzalez, R. L.; Cornish, V. W. The ribosome can discriminate the chirality of amino acids within its peptidyl-transferase center. *Proc. Natl. Acad. Sci. U.S.A.* **2015**, *112* (19), 6038-6043. DOI: doi:10.1073/pnas.1424712112.

(83) Zimmer, M. H.; Niesen, M. J. M.; Miller, T. F., 3rd. Force transduction creates long-ranged coupling in ribosomes stalled by arrest peptides. *Biophys. J.* **2021**, *120* (12), 2425-2435. DOI: 10.1016/j.bpj.2021.03.041.

(84) Arenz, S.; Juette, M. F.; Graf, M.; Nguyen, F.; Huter, P.; Polikanov, Y. S.; Blanchard, S. C.; Wilson, D. N. Structures of the orthosomycin antibiotics avilamycin and evernimicin in complex with the bacterial 70S ribosome. *Proc. Natl. Acad. Sci. U.S.A.* **2016**, *113* (27), 7527-7532. DOI: doi:10.1073/pnas.1604790113.

(85) Lucent, D.; Snow, C. D.; Aitken, C. E.; Pande, V. S. Non-Bulk-Like Solvent Behavior in the Ribosome Exit Tunnel. *PLOS Comput. Biol.* **2010**, *6* (10), e1000963. DOI: 10.1371/journal.pcbi.1000963.

(86) Petrone, P. M.; Snow, C. D.; Lucent, D.; Pande, V. S. Side-chain recognition and gating in the ribosome exit tunnel. *Proc. Natl. Acad. Sci. U.S.A.* **2008**, *105* (43), 16549-16554. DOI: doi:10.1073/pnas.0801795105.

(87) Aleksandrov, A.; Simonson, T. Molecular Dynamics Simulations of the 30S Ribosomal Subunit Reveal a Preferred Tetracycline Binding Site. *J. Am. Chem. Soc.* **2008**, *130* (4), 1114-1115. DOI: 10.1021/ja0741933.

(88) Vaiana, A. C.; Sanbonmatsu, K. Y. Stochastic Gating and Drug–Ribosome Interactions. *J. Mol. Biol.* **2009**, *386* (3), 648-661. DOI: https://doi.org/10.1016/j.jmb.2008.12.035.

(89) Romanowska, J.; McCammon, J. A.; Trylska, J. Understanding the Origins of Bacterial Resistance to Aminoglycosides through Molecular Dynamics Mutational Study of the Ribosomal A-Site. *PLOS Comput. Biol.* **2011**, *7* (7), e1002099. DOI: 10.1371/journal.pcbi.1002099.

(90) Panecka, J.; Mura, C.; Trylska, J. Interplay of the Bacterial Ribosomal A-Site, S12 Protein Mutations and Paromomycin Binding: A Molecular Dynamics Study. *PLoS One* **2014**, *9* (11), e111811. DOI: 10.1371/journal.pone.0111811.

(91) Chirkova, A.; Erlacher, M. D.; Clementi, N.; Zywicki, M.; Aigner, M.; Polacek, N. The role of the universally conserved A2450-C2063 base pair in the ribosomal peptidyl transferase center. *Nucleic Acids Res.* **2010**, *38* (14), 4844-4855. DOI: 10.1093/nar/gkq213.

(92) Vangaveti, S.; Ranganathan, S. V.; Agris, P. F. Physical Chemistry of a Single tRNA-Modified Nucleoside Regulates Decoding of the Synonymous Lysine Wobble Codon and Affects Type 2 Diabetes. *J. Phys. Chem. B.* **2022**, *126* (6), 1168-1177. DOI: 10.1021/acs.jpcb.1c09053.

(93) Elliott, B. A.; Ho, H.-T.; Ranganathan, S. V.; Vangaveti, S.; Ilkayeva, O.; Abou Assi, H.; Choi, A. K.; Agris, P. F.; Holley, C. L. Modification of messenger RNA by 2'-O-methylation regulates gene expression in vivo. *Nat. Commun.* **2019**, *10* (1), 3401. DOI: 10.1038/s41467-019-11375-7.

(94) Vangaveti, S.; Cantara, W. A.; Spears, J. L.; DeMirci, H.; Murphy, F. V.; Ranganathan, S. V.; Sarachan, K. L.; Agris, P. F. A Structural Basis for Restricted Codon Recognition Mediated by 2-thiocytidine in tRNA Containing a Wobble Position Inosine. *J. Mol. Biol.* **2020**, *432* (4), 913-929. DOI: https://doi.org/10.1016/j.jmb.2019.12.016.

(95) Kamble, A. S.; Fandilolu, P. M.; Sambhare, S. B.; Sonawane, K. D. Idiosyncratic recognition of UUG/UUA codons by modified nucleoside 5-taurinomethyluridine, τm^5U present at 'wobble' position in anticodon loop of tRNALeu: A molecular modeling approach. *PLoS One* **2017**, *12* (4), e0176756. DOI: 10.1371/journal.pone.0176756.

(96) Narendran, A.; Vangaveti, S.; Ranganathan, S. V.; Eruysal, E.; Craft, M.; Alrifai, O.; Chua, F. Y.; Sarachan, K.; Litwa, B.; Ramachandran, S.; et al. Silencing of the tRNA Modification Enzyme Cdkal1 Effects Functional Insulin Synthesis in NIT-1 Cells: tRNALys3 Lacking ms^2- (ms^2t^6A37) is Unable to Establish Sufficient Anticodon:Codon Interactions to Decode the Wobble Codon AAG. *Front. Mol. Biosci.* **2021**, *7*, Brief Research Report. DOI: 10.3389/fmolb.2020.584228.

(97) McCrate, N. E.; Varner, M. E.; Kim, K. I.; Nagan, M. C. Molecular dynamics simulations of human $tRNA_{UUU}^{Lys}$: the role of modified bases in mRNA recognition. *Nucleic Acids Res.* **2006**, *34* (19), 5361-5368. DOI: 10.1093/nar/gkl580.

(98) Watson, Z. L.; Ward, F. R.; Méheust, R.; Ad, O.; Schepartz, A.; Banfield, J. F.; Cate, J. H. Structure of the bacterial ribosome at 2 Å resolution. *eLife* **2020**, *9*. DOI: 10.7554/elife.60482.

(99) Zhao, X.; Ma, D.; Ishiguro, K.; Saito, H.; Akichika, S.; Matsuzawa, I.; Mito, M.; Irie, T.; Ishibashi, K.; Wakabayashi, K.; et al. Glycosylated queuosines in tRNAs optimize translational rate and post-embryonic growth. *Cell* **2023**, *186* (25), 5517-5535.e5524. DOI: https://doi.org/10.1016/j.cell.2023.10.026.

(100) Tomono, J.; Asano, K.; Chiashi, T.; Suzuki, M.; Igarashi, M.; Takahashi, Y.; Tanaka, Y.; Yokoyama, T. Direct visualization of ribosomes in the cell-free system revealed the functional evolution of aminoglycoside. *J. Biochem.* **2024**, *175* (6), 587-598. DOI: 10.1093/jb/mvae002.

(101) McMullan, G.; Naydenova, K.; Mihaylov, D.; Yamashita, K.; Peet, M. J.; Wilson, H.; Dickerson, J. L.; Chen, S.; Cannone, G.; Lee, Y.; et al. Structure determination by cryoEM at 100 keV. *Proc. Natl. Acad. Sci. U.S.A.* **2023**, *120* (49). DOI: 10.1073/pnas.2312905120.

(102) Akiyama, N.; Ishiguro, K.; Yokoyama, T.; Miyauchi, K.; Nagao, A.; Shirouzu, M.; Suzuki, T. Structural insights into the decoding capability of isoleucine tRNAs with lysidine and agmatidine. *Nat. Struct. Mol. Biol.* **2024**, *31* (5), 817-825. DOI: 10.1038/s41594-024-01238-1.

(103) Watson, Z. L.; Knudson, I. J.; Ward, F. R.; Miller, S. J.; Cate, J. H.; Schepartz, A.; Abramyan, A. M. Atomistic simulations of the Escherichia coli ribosome provide selection criteria for translationally active substrates. *Nat. Chem.* **2023**, *15* (7), 913-921. DOI: 10.1038/s41557-023-01226-w.

(104) Agirrezabala, X.; Schreiner, E.; Trabuco, L. G.; Lei, J.; Ortiz-Meoz, R. F.; Schulten, K.; Green, R.; Frank, J. Structural insights into cognate versus near-cognate discrimination during decoding. *EMBO J.* **2011**, *30* (8), 1497-1507. DOI: 10.1038/emboj.2011.58.

(105) Loveland, A. B.; Demo, G.; Grigorieff, N.; Korostelev, A. A. Ensemble cryo-EM elucidates the mechanism of translation fidelity. *Nature* **2017**, *546* (7656), 113-117. DOI: 10.1038/nature22397.

(106) Nissley, A. J.; Penev, P. I.; Watson, Z. L.; Banfield, J. F.; Cate, J. H. Rare ribosomal RNA sequences from archaea stabilize the bacterial ribosome. *Nucleic Acids Res.* **2023**, *51* (4), 1880-1894. DOI: 10.1093/nar/gkac1273.

(107) Gersteuer, F.; Morici, M.; Gabrielli, S.; Fujiwara, K.; Safdari, H. A.; Paternoga, H.; Bock, L. V.; Chiba, S.; Wilson, D. N. The SecM arrest peptide traps a pre-peptide bond formation state of the ribosome. *Nat. Commun.* **2024**, *15* (1). DOI: 10.1038/s41467-024-46762-2.

(108) Majumdar, C.; Walker, J. A.; Francis, M. B.; Schepartz, A.; Cate, J. H. Aminobenzoic Acid Derivatives Obstruct Induced-fit in the Catalytic Center of the Ribosome. *ACS Cent. Sci.* **2023**, *9* (6), 1160-1169. DOI: 10.1021/acscentsci.3c00153.

(109) Rozov, A.; Demeshkina, N.; Khusainov, I.; Westhof, E.; Yusupov, M.; Yusupova, G. Novel base-pairing interactions at the tRNA wobble position crucial for accurate reading of the genetic code. *Nat. Commun.* **2016**, *7* (1). DOI: 10.1038/ncomms10457.

(110) Murphy, F. V.; Ramakrishnan, V.; Malkiewicz, A.; Agris, P. F. The role of modifications in codon discrimination by $tRNA_{Lys}^{UUU}$. *Nat. Struct. Mol. Biol.* **2004**, *11* (12), 1186-1191. DOI: 10.1038/nsmb861.

(111) Hoffer, E. D.; Hong, S.; Sunita, S.; Maehigashi, T.; Gonzalez, R. L.; Whitford, P. C.; Dunham, C. M. Structural insights into mRNA reading frame regulation by tRNA modification and slippery codon–anticodon pairing. *eLife* **2020**, *9*. DOI: 10.7554/elife.51898.

(112) Dunham, C. M.; Selmer, M.; Phelps, S. S.; Kelley, A. C.; Suzuki, T.; Joseph, S.; Ramakrishnan, V. Structures of tRNAs with an expanded anticodon loop in the decoding center of the 30S ribosomal subunit. *RNA* **2007**, *13* (6), 817-823. DOI: 10.1261/rna.367307.

(113) Ogle, J. M.; Brodersen, D. E.; Clemons, W. M.; Tarry, M. J.; Carter, A. P.; Ramakrishnan, V. Recognition of Cognate Transfer RNA by the 30S Ribosomal Subunit. *Science* **2001**, *292* (5518), 897-902. DOI: 10.1126/science.1060612.

(114) Schmeing, T. M.; Voorhees, R. M.; Kelley, A. C.; Ramakrishnan, V. How mutations in tRNA distant from the anticodon affect the fidelity of decoding. *Nat. Struct. Mol. Biol.* **2011**, *18* (4), 432-436. DOI: 10.1038/nsmb.2003.

(115) Rozov, A.; Westhof, E.; Yusupov, M.; Yusupova, G. The ribosome prohibits the G•U wobble geometry at the first position of the codon–anticodon helix. *Nucleic Acids Res.* **2016**, gkw431. DOI: 10.1093/nar/gkw431.

(116) Murphy, F. V.; Ramakrishnan, V. Structure of a purine-purine wobble base pair in the decoding center of the ribosome. *Nat. Struct. Mol. Biol.* **2004**, *11* (12), 1251-1252. DOI: 10.1038/nsmb866.

(117) Weixlbaumer, A.; Murphy, F. V.; Dziergowska, A.; Malkiewicz, A.; Vendeix, F. A.; Agris, P. F.; Ramakrishnan, V. Mechanism for expanding the decoding capacity of transfer RNAs by modification of uridines. *Nat. Struct. Mol. Biol.* **2007**, *14* (6), 498-502. DOI: 10.1038/nsmb1242.

(118) Voorhees, R. M.; Mandal, D.; Neubauer, C.; Köhrer, C.; RajBhandary, U. L.; Ramakrishnan, V. The structural basis for specific decoding of AUA by isoleucine tRNA on the ribosome. *Nat. Struct. Mol. Biol.* **2013**, *20* (5), 641-643. DOI: 10.1038/nsmb.2545.

(119) Fislage, M.; Zhang, J.; Brown, Z. P.; Mandava, C. S.; Sanyal, S.; Ehrenberg, M.; Frank, J. Cryo-EM shows stages of initial codon selection on the ribosome by aa-tRNA in ternary complex with GTP and the GTPase-deficient EF-TuH84A. *Nucleic Acids Res.* **2018**, *46* (11), 5861-5874. DOI: 10.1093/nar/gky346.

(120) Hoffer, E. D.; Maehigashi, T.; Fredrick, K.; Dunham, C. M. Ribosomal ambiguity (ram) mutations promote the open (off) to closed (on) transition and thereby increase miscoding. *Nucleic Acids Res.* **2018**, *47* (3), 1557-1563. DOI: 10.1093/nar/gky1178.

(121) Ogle, J. M.; Murphy, F. V.; Tarry, M. J.; Ramakrishnan, V. Selection of tRNA by the Ribosome Requires a Transition from an Open to a Closed Form. *Cell* **2002**, *111* (5), 721-732. DOI: https://doi.org/10.1016/S0092-8674(02)01086-3.

(122) Borovinskaya, M. A.; Pai, R. D.; Zhang, W.; Schuwirth, B. S.; Holton, J. M.; Hirokawa, G.; Kaji, H.; Kaji, A.; Cate, J. H. Structural basis for aminoglycoside inhibition of bacterial ribosome recycling. *Nat. Struct. Mol. Biol.* **2007**, *14* (8), 727-732. DOI: 10.1038/nsmb1271.

(123) Carter, A. P.; Clemons, W. M.; Brodersen, D. E.; Morgan-Warren, R. J.; Wimberly, B. T.; Ramakrishnan, V. Functional insights from the structure of the 30S ribosomal subunit and its interactions with antibiotics. *Nature* **2000**, *407* (6802), 340-348. DOI: 10.1038/35030019.

(124) Brodersen, D. E.; Clemons, W. M.; Carter, A. P.; Morgan-Warren, R. J.; Wimberly, B. T.; Ramakrishnan, V. The Structural Basis for the Action of the Antibiotics Tetracycline, Pactamycin, and Hygromycin B on the 30S Ribosomal Subunit. *Cell* **2000**, *103* (7), 1143-1154. DOI: https://doi.org/10.1016/S0092-8674(00)00216-6.

(125) Wimberly, B. T.; Brodersen, D. E.; Clemons, W. M.; Morgan-Warren, R. J.; Carter, A. P.; Vonrhein, C.; Hartsch, T.; Ramakrishnan, V. Structure of the 30S ribosomal subunit. *Nature* **2000**, *407* (6802), 327-339. DOI: 10.1038/35030006.

(126) Petry, S.; Brodersen, D. E.; Murphy, F. V.; Dunham, C. M.; Selmer, M.; Tarry, M. J.; Kelley, A. C.; Ramakrishnan, V. Crystal Structures of the Ribosome in Complex with Release Factors RF1 and RF2 Bound to a Cognate Stop Codon. *Cell* **2005**, *123* (7), 1255-1266. DOI: https://doi.org/10.1016/j.cell.2005.09.039.

(127) Rybak, M. Y.; Gagnon, M. G. Structures of the ribosome bound to EF-Tu–isoleucine tRNA elucidate the mechanism of AUG avoidance. *Nat. Struct. Mol. Biol.* **2024**, *31* (5), 810-816. DOI: 10.1038/s41594-024-01236-3.

(128) Ramrath, D. J. F.; Lancaster, L.; Sprink, T.; Mielke, T.; Loerke, J.; Noller, H. F.; Spahn, C. M. T. Visualization of two transfer RNAs trapped in transit during elongation factor G-mediated translocation. *Proc. Natl. Acad. Sci. U.S.A.* **2013**, *110* (52), 20964-20969. DOI: doi:10.1073/pnas.1320387110.

(129) Meng, E. C.; Goddard, T. D.; Pettersen, E. F.; Couch, G. S.; Pearson, Z. J.; Morris, J. H.; Ferrin, T. E. UCSF ChimeraX: Tools for structure building and analysis. *Protein Sci.* **2023**, *32* (11), e4792. DOI: https://doi.org/10.1002/pro.4792.

(130) Case, D. A.; Aktulga, H. M.; Belfon, K.; Ben-Shalom, I. Y.; Berryman, J. T.; Brozell, S. R.; Cerutti, D. S.; Cheatham, T. E., III; Cisneros, G. A.; Cruzeiro, V. W. D.; et al. Amber 2024. University of California, San Francisco: 2024.

(131) The PyMOL Molecular Graphics System, Version 3.1.6.1*; Schrödinger*, LLC: New York, NY, 2025. https://pymol.org (accessed May 26, 2025)

(132) Sousa da Silva, A. W.; Vranken, W. F. ACPYPE - AnteChamber PYthon Parser interfacE. *BMC Research Notes* **2012**, *5* (1), 367. DOI: 10.1186/1756-0500-5-367.

(133) Abraham, M.; Alekseenko, A.; Basov, V.; Bergh, C.; Briand, E.; Brown, A.; Doijade, M.; Fiorin, G.; Fleischmann, S.; Gorelov, S.; et al. GROMACS 2024.0 Source code. Zenodo: 2024.

(134) Zgarbová, M.; Otyepka, M.; Šponer, J.; Mládek, A.; Banáš, P.; Cheatham, T. E., III; Jurečka, P. Refinement of the Cornell et al. Nucleic Acids Force Field Based on Reference Quantum Chemical Calculations of Glycosidic Torsion Profiles. *J. Chem. Theory Comput.* **2011**, *7* (9), 2886-2902. DOI: 10.1021/ct200162x.

(135) Pérez, A.; Marchán, I.; Svozil, D.; Sponer, J.; Cheatham, T. E.; Laughton, C. A.; Orozco, M. Refinement of the AMBER Force Field for Nucleic Acids: Improving the Description of α/γ Conformers. *Biophys. J.* **2007**, *92* (11), 3817-3829. DOI: https://doi.org/10.1529/biophysj.106.097782.

(136) Maier, J. A.; Martinez, C.; Kasavajhala, K.; Wickstrom, L.; Hauser, K. E.; Simmerling, C. ff14SB: Improving the accuracy of protein side chain and backbone parameters from ff99SB. *J. Chem. Theory Comput.* **2015**, *11* (8), 3696-3713. DOI: 10.1021/acs.jctc.5b00255.

(137) Berendsen, H. J. C.; Grigera, J. R.; Straatsma, T. P. The missing term in effective pair potentials. *J. Phys. Chem.* **1987**, *91* (24), 6269-6271. DOI: 10.1021/j100308a038.

(138) Grotz, K. K.; Schwierz, N. Optimized Magnesium Force Field Parameters for Biomolecular Simulations with Accurate Solvation, Ion-Binding, and Water-Exchange Properties in SPC/E, TIP3P-fb, TIP4P/2005, TIP4P-Ew, and TIP4P-D. *J. Chem. Theory Comput.* **2022**, *18* (1), 526-537. DOI: 10.1021/acs.jctc.1c00791.

(139) Aduri, R.; Psciuk, B. T.; Saro, P.; Taniga, H.; Schlegel, H. B.; SantaLucia, J. AMBER Force Field Parameters for the Naturally Occurring Modified Nucleosides in RNA. *J. Chem. Theory Comput.* **2007**, *3* (4), 1464-1475. DOI: 10.1021/ct600329w.

(140) Vanquelef, E.; Simon, S.; Marquant, G.; Garcia, E.; Klimerak, G.; Delepine, J. C.; Cieplak, P.; Dupradeau, F.-Y. R.E.D. Server: a web service for deriving RESP and ESP charges and building force field libraries for new molecules and molecular fragments. *Nucleic Acids Res.* **2011**, *39* (suppl_2), W511-W517. DOI: 10.1093/nar/gkr288.

(141) Dupradeau, F.-Y.; Pigache, A.; Zaffran, T.; Savineau, C.; Lelong, R.; Grivel, N.; Lelong, D.; Rosanski, W.; Cieplak, P. The R.E.D. Tools: Advances in RESP and ESP charge derivation and force field library building. *Phys. Chem. Chem. Phys.* **2010**, *12* (28), 7821-7839.

(142) Wang, J.; Wang, W.; Kollman, P. A.; Case, D. A. Automatic atom type and bond type perception in molecular mechanical calculations. *J. Mol. Graph. Model.* **2006**, *25* (2), 247-260. DOI: https://doi.org/10.1016/j.jmgm.2005.12.005.

(143) Gowers, R. J.; Linke, M.; Barnoud, J.; Reddy, T. J. E.; Melo, M. N.; Seyler, S. L.; Domański, J.; Dotson, D. L.; Buchoux, S.; Kenney, I. M.; et al. MDAnalysis: A Python Package for the Rapid Analysis of Molecular Dynamics Simulations.

(144) McGrath, H.; Černeková, M.; Kolář, M. H. Binding of the peptide deformylase on the ribosome surface modulates the exit tunnel interior. *Biophys J* **2022**, *121* (23), 4443-4451. DOI: 10.1016/j.bpj.2022.11.004.

(145) Páll, S.; Zhmurov, A.; Bauer, P.; Abraham, M.; Lundborg, M.; Gray, A.; Hess, B.; Lindahl, E. Heterogeneous parallelization and acceleration of molecular dynamics simulations in GROMACS. *J. Chem. Phys.* **2020**, *153* (13). DOI: 10.1063/5.0018516.

(146) Roe, D. R.; Cheatham, T. E., III. PTRAJ and CPPTRAJ: Software for Processing and Analysis of Molecular Dynamics Trajectory Data. *J. Chem. Theory Comput.* **2013**, *9* (7), 3084-3095. DOI: 10.1021/ct400341p.

(147) Bottaro, S.; Bussi, G.; Pinamonti, G.; Reisser, S.; Boomsma, W.; Lindorff-Larsen, K. Barnaba: software for analysis of nucleic acid structures and trajectories. *RNA* **2019**, *25* (2), 219-231. DOI: 10.1261/rna.067678.118.

(148) McGibbon, R. T.; Beauchamp, K. A.; Harrigan, M. P.; Klein, C.; Swails, J. M.; Hernández, C. X.; Schwantes, C. R.; Wang, L.-P.; Lane, T. J.; Pande, V. S. MDTraj: A Modern Open Library for the Analysis of Molecular Dynamics Trajectories. *Biophys. J.* **2015**, *109* (8), 1528-1532. DOI: 10.1016/j.bpj.2015.08.015.

(149) Tomono, J.; Asano, K.; Chiashi, T.; Suzuki, M.; Igarashi, M.; Takahashi, Y.; Tanaka, Y.; Yokoyama, T. Direct visualization of ribosomes in the cell-free system revealed the functional evolution of aminoglycoside. *J Biochem* **2024**, *175* (6), 587-598. DOI: 10.1093/jb/mvae002.

(150) McMullan, G.; Naydenova, K.; Mihaylov, D.; Yamashita, K.; Peet, M. J.; Wilson, H.; Dickerson, J. L.; Chen, S.; Cannone, G.; Lee, Y.; et al. Structure determination by cryoEM at 100 keV. *Proc. Natl. Acad. Sci. U.S.A.* **2023**, *120* (49), e2312905120. DOI: doi:10.1073/pnas.2312905120.

(151) Akiyama, N.; Ishiguro, K.; Yokoyama, T.; Miyauchi, K.; Nagao, A.; Shirouzu, M.; Suzuki, T. Structural insights into the decoding capability of isoleucine tRNAs with lysidine and agmatidine. *Nat. Struct. Mol. Biol.* **2024**, *31* (5), 817-825. DOI: 10.1038/s41594-024-01238-1.

(152) Watson, Z. L.; Knudson, I. J.; Ward, F. R.; Miller, S. J.; Cate, J. H. D.; Schepartz, A.; Abramyan, A. M. Atomistic simulations of the Escherichia coli ribosome provide selection criteria for translationally active substrates. *Nat. Chem.* **2023**, *15* (7), 913-921. DOI: 10.1038/s41557-023-01226-w.

(153) Watson, Z. L.; Ward, F. R.; Méheust, R.; Ad, O.; Schepartz, A.; Banfield, J. F.; Cate, J. H. Structure of the bacterial ribosome at 2 Å resolution. *elife* **2020**, *9*, e60482.

(154) Agirrezabala, X.; Schreiner, E.; Trabuco, L. G.; Lei, J.; Ortiz-Meoz, R. F.; Schulten, K.; Green, R.; Frank, J. Structural insights into cognate versus near-cognate discrimination during decoding. *EMBO J.* **2011**, *30* (8), 1497-1507. DOI: https://doi.org/10.1038/emboj.2011.58.

(155) Nissley, Amos J.; Penev, Petar I.; Watson, Zoe L.; Banfield, Jillian F.; Cate, Jamie H. D. Rare ribosomal RNA sequences from archaea stabilize the bacterial ribosome. *Nucleic Acids Res.* **2023**, *51* (4), 1880-1894. DOI: 10.1093/nar/gkac1273.

(156) Majumdar, C.; Walker, J. A.; Francis, M. B.; Schepartz, A.; Cate, J. H. D. Aminobenzoic Acid Derivatives Obstruct Induced-fit in the Catalytic Center of the Ribosome. *ACS Cent. Sci.* **2023**, *9* (6), 1160-1169. DOI: 10.1021/acscentsci.3c00153.

(157) Rozov, A.; Demeshkina, N.; Khusainov, I.; Westhof, E.; Yusupov, M.; Yusupova, G. Novel base-pairing interactions at the tRNA wobble position crucial for accurate reading of the genetic code. *Nat. Commun.* **2016**, *7* (1), 10457. DOI: 10.1038/ncomms10457.

(158) Murphy, F. V.; Ramakrishnan, V.; Malkiewicz, A.; Agris, P. F. The role of modifications in codon discrimination by $tRNA^{Lys}_{UUU}$. *Nat. Struct. Mol. Biol.* **2004**, *11* (12), 1186-1191. DOI: 10.1038/nsmb861.

(159) Murphy, F. V.; Ramakrishnan, V. Structure of a purine-purine wobble base pair in the decoding center of the ribosome. *Nat. Struct. Mol. Biol.* **2004**, *11* (12), 1251-1252. DOI: 10.1038/nsmb866.

(160) DeMirci, H.; Destan, E. Crystal structure of the Thermus thermophilus (HB8) 30S ribosomal subunit with mRNA and cognate transfer RNA anticodon stem-loop and sisomicin derivative N1,3''Bz bound. **2022**. DOI: 10.2210/pdb7duj/pdb.

(161) Hoffer, E. D.; Hong, S.; Sunita, S.; Maehigashi, T.; Gonzalez, R. L. J.; Whitford, P. C.; Dunham, C. M. Structural insights into mRNA reading frame regulation by tRNA modification and slippery codon-anticodon pairing. *Elife* **2020**, *9*. DOI: 10.7554/eLife.51898.

(162) Dunham, C. M.; Selmer, M.; Phelps, S. S.; Kelley, A. C.; Suzuki, T.; Joseph, S.; Ramakrishnan, V. Structures of tRNAs with an expanded anticodon loop in the decoding center of the 30S ribosomal subunit. *RNA* **2007**, *13* (6), 817-823. DOI: 10.1261/rna.367307.

(163) Ogle, J. M.; Brodersen, D. E.; Clemons, W. M.; Tarry, M. J.; Carter, A. P.; Ramakrishnan, V. Recognition of Cognate Transfer RNA by the 30S Ribosomal Subunit. *Science* **2001**, *292* (5518), 897-902. DOI: doi:10.1126/science.1060612.

(164) Rozov, A.; Wolff, P.; Grosjean, H.; Yusupov, M.; Yusupova, G.; Westhof, E. Tautomeric G•U pairs within the molecular ribosomal grip and fidelity of decoding in bacteria. *Nucleic Acids Res.* **2018**, *46* (14), 7425-7435. DOI: 10.1093/nar/gky547.

(165) Rozov, A.; Westhof, E.; Yusupov, M.; Yusupova, G. The ribosome prohibits the G•U wobble geometry at the first position of the codon–anticodon helix. *Nucleic Acids Res.* **2016**, *44* (13), 6434-6441. DOI: 10.1093/nar/gkw431.

(166) Rybak, M. Y.; Gagnon, M. G. Structures of the ribosome bound to EF-Tu–isoleucine tRNA elucidate the mechanism of AUG avoidance. *Nat. Struct. Mol. Biol.* **2024**, *31* (5), 810-816. DOI: 10.1038/s41594-024-01236-3.

(167) Weixlbaumer, A.; Murphy, F. V.; Dziergowska, A.; Malkiewicz, A.; Vendeix, F. A. P.; Agris, P. F.; Ramakrishnan, V. Mechanism for expanding the decoding capacity of transfer RNAs by modification of uridines. *Nat. Struct. Mol. Biol.* **2007**, *14* (6), 498-502. DOI: 10.1038/nsmb1242.

(168) Kurata, S.; Weixlbaumer, A.; Ohtsuki, T.; Shimazaki, T.; Wada, T.; Kirino, Y.; Takai, K.; Watanabe, K.; Ramakrishnan, V.; Suzuki, T. Modified Uridines with C5-methylene Substituents at the First Position of the tRNA Anticodon Stabilize U·G Wobble Pairing during Decoding. *J. Biol. Chem.* **2008**, *283* (27), 18801-18811. DOI: https://doi.org/10.1074/jbc.M800233200.

(169) Voorhees, R. M.; Mandal, D.; Neubauer, C.; Köhrer, C.; RajBhandary, U. L.; Ramakrishnan, V. The structural basis for specific decoding of AUA by isoleucine tRNA on the ribosome. *Nat. Struct. Mol. Biol.* **2013**, *20* (5), 641-643. DOI: 10.1038/nsmb.2545.

(170) Borovinskaya, M. A.; Pai, R. D.; Zhang, W.; Schuwirth, B. S.; Holton, J. M.; Hirokawa, G.; Kaji, H.; Kaji, A.; Cate, J. H. D. Structural basis for aminoglycoside inhibition of bacterial ribosome recycling. *Nat. Struct. Mol. Biol.* **2007**, *14* (8), 727-732. DOI: 10.1038/nsmb1271.

(171) James, N. R.; Brown, A.; Gordiyenko, Y.; Ramakrishnan, V. Translational termination without a stop codon. *Science* **2016**, *354* (6318), 1437-1440. DOI: doi:10.1126/science.aai9127.

(172) Hoffer, E. D.; Maehigashi, T.; Fredrick, K.; Dunham, C. M. Ribosomal ambiguity (ram) mutations promote the open (off) to closed (on) transition and thereby increase miscoding. *Nucleic Acids Res.* **2019**, *47* (3), 1557-1563. DOI: 10.1093/nar/gky1178.

CHAPTER 3: THE INOSINE mRNA CODON MODIFICATIONS IMPACT THE STRUCTURAL DYNAMICS OF DECODING IN A POSITION-DEPENDENT MANNER

3.1 Objectives

Inosine is introduced to RNA through A-to-I editing by ADAR enzymes in eukaryotes.[1] A-to-I editing deaminates adenosine at the N6 position, altering the chemical structure of the nucleoside to resemble guanosine. In mammals, A-to-I editing within coding sequences regulates translation elongation and affects genes involved in neurotransmission, including those encoding neurotransmitter receptors and ion channels.[2-4] Dysregulated inosine modification is linked to neurological disorders,[4-7] cancers,[8-10] and immune diseases.[11, 12] Systems-level studies found that transcripts containing multiple inosines can lead to ribosome stalling *in vivo*, however the mechanisms underlying these effects are not presently understood.[13]

As discussed in Section 1.3.3.1, a mechanistic study found that inosine caused significant reductions in the efficiency of translation relative to the unmodified codon when it was placed in the first position.[14] In agreement, experiments conducted by the Koutmou lab indicated that first position inosine modification to the mRNA codon caused a severe reduction in the rate of dipeptide formation, whereas second and third position inosine modification did not.[15] It has been proposed that the I:C base pair, in addition to reducing the number of hydrogen-bonding interactions compared to G:C, also perturbs interactions with 16S rRNA monitoring bases in the ribosomal A-site.[14] However, these mechanistic effects have not been supported by structural or computational studies, making it unclear how inosine can drive these position-dependent effects on decoding.

Codon modifications that impair translational efficiency have been suggested to cause the ribosome to recognize aa-tRNA as near-cognate. For example, mechanistic studies of select mRNA modifications (e.g., m^6A, Ψ, or $m^1Ψ$) found that when modifications were inserted into

certain codon positions, cognate tRNAs performed as poorly as, or worse than, near-cognate tRNAs.[16, 17] While inosine has not been inserted into mRNA codons, it has been inserted into the tRNA anticodon, which caused the ribosome to treat tRNA as near-cognate when stop codons were encountered at the A-site. [18] It is well known that incorrect tRNAs are efficiently rejected during initial tRNA selection, but it is unclear whether the first position inosine codon modification causes cognate tRNA to be recognized as such.

Inosine is often decoded as G, but has also been found to be read as A or U (forming I:A or I:U base pairs).[13] The expanded decoding capacity of inosine suggests that it may cause miscoding (i.e., selection of near- or non-cognate tRNAs). Indeed, incorrect peptide products are formed at low levels when inosine was present in codons for both bacteria and eukaryotes.[14] However, it has not been established whether inosine codon modifications can allow near-cognate tRNAs to bypass selection mechanisms and induce miscoding.

To uncover the structural basis governing how inosine modifications drive changes to the kinetics of elongation, microsecond MD simulations were performed in quadruplicate on subsystem models of tRNA:EF-Tu:GTP ternary complex bound to the A-site of *E. coli* ribosome with and without inosine modifications in each codon position (see Chapter 2 for full details). To assess whether the inosine causes cognate $tRNA^{Val}$ to be recognized as near-cognate in the ribosomal A-site, a model containing near-cognate $tRNA^{Met}$ replacing cognate $tRNA^{Val}$ was built without altering the GUG codon (denoted GUG^{Met}). $tRNA^{Met}$ contains U36 instead of C36, and therefore introduces a U:G mismatch at the first codon position. The simulations of the mismatch-containing GUG^{Met} system were compared to those of cognate $tRNA^{Val}$ with the first position inosine modification. To determine if the first position inosine can alter selection of near-cognate tRNA, a model was built with near-cognate $tRNA^{Met}$ in the presence of an IUG codon (IUG^{Met}).

This chapter aims to determine how inosine mRNA modifications influence rapid structural changes during early codon recognition, including ribosomal monitoring nucleotide responses to modified codon-anticodon base pairs, minihelix geometry alterations, and aa-tRNA structural dynamics. These simulations provide a thorough mechanistic understanding to rationalize why only first, but not second or third, position inosine codon modifications reduced decoding efficiency.

3.2 Results and discussion

3.2.1 MD simulations of cognate tRNA

To rationalize the kinetics experiments conducted by the Koutmou lab, this section uses MD simulations to understand how inosine impacts the ribosomal recognition of cognate tRNA.

3.2.1.1 Structural convergence of the ribosome subsystem

To measure the global structural convergence of the ribosome subsystem model, backbone root-mean-squared deviation (RMSD) was computed for all residues included in the flexible region (i.e., residues not contained in the outer 30 Å restrained "shell") with respect to the starting structure coordinates. The RMSD signified convergence for most models and replicas by a plateau within 250 ns, but required a longer amount of time (~750 ns) to converge for IUG replicas 3 and 4 (Figure B.1). Variability in the RMSD distribution was quantified by the coefficient of variation ($CV = \frac{\sigma}{\overline{x}}$, where σ is the standard deviation and $\overline{x}$ is the mean RMSD over the quadruplicate ensembles for each system; Table B.1). The CV was lowest for CGU (0.121), higher for GUG (0.158) and CIU (0.154), and broadest for GUI (0.271) and IUG (0.221) (Table B.1; Figure 3.1A). The IUG and GUI systems each had individual replicas that sampled a high percentage of frames in the upper RMSD range (>6 Å), including replica 3 (66%) and 4 (19%) of IUG and replica 2 (84%) of GUI. In contrast, no replicas for any other system had >6% of frames with RMSDs exceeding 6 Å. All mean RMSDs fell within 3.73–6.50 Å (Table B.1), indicating an

expected minor global deviation from the experimental starting structures. Overlays of the representative structures from each replica indicate that the models maintain (1) the intactness of all complexes and (2) the tertiary fold of all RNA and protein components (Figure 3.1B). The deviations in structures between replicas indicate that no significant structural distortions occurred that would bias the dataset (i.e., the unrestrained central subsystem components do not diffuse away into solvent, the tRNA does not collapse, etc.). Overall, the analysis of the global structural features indicates that all models were stable over the trajectory and sampled global configurations resembling the experimental starting structure.

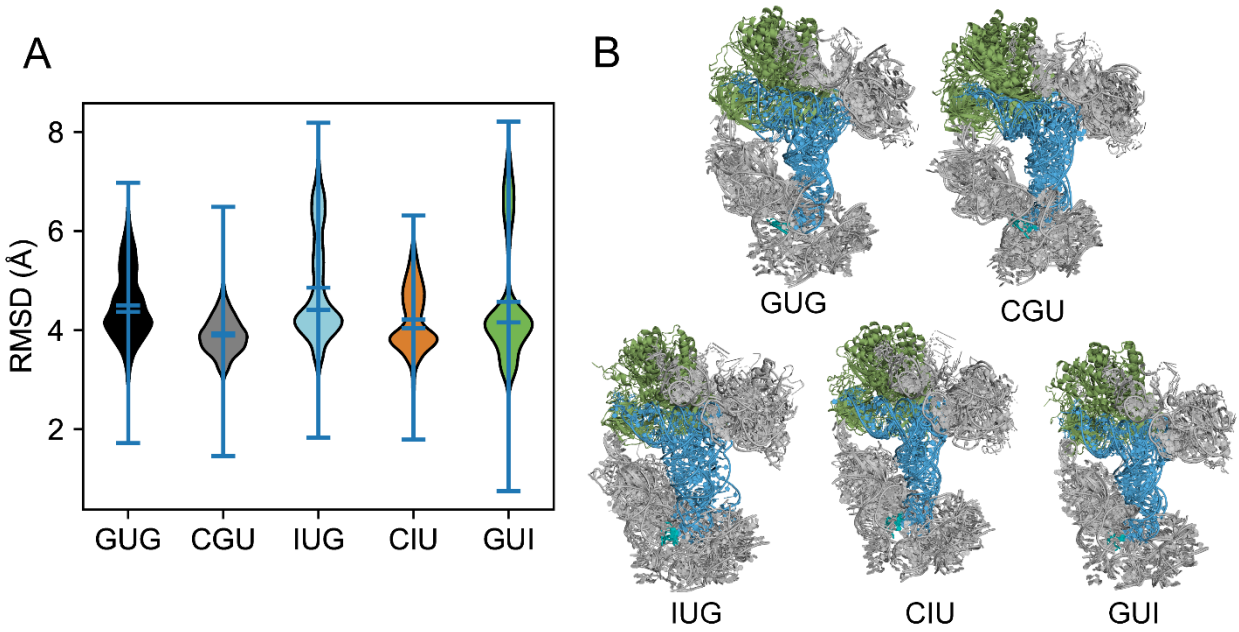

Figure 3.1. Structural convergence of MD simulations of the ribosomal A-site subsystem. (A) Violin plot of the backbone RMSD distributions with respect to the flexible region of the starting structure. (B) Overlays of the last frame of each replica simulation for systems containing containing cognate $tRNA^{Val}$ or $tRNA^{Arg}$.

Convergence of individual system components was assessed by measuring the backbone RMSD of each subcomponent with respect to the starting structure. The RMSD distributions of the selected model components from all five models overlapped substantially, with each distribution spanning approximately the same RMSD range and exhibiting peaks in similar regions (Figure B.2). The tRNA was chosen to examine and compare local convergence further

due to its pivotal role as a physical “adaptor” that spans the intersubunit cavity formed by the LSU and SSU near the A-site.

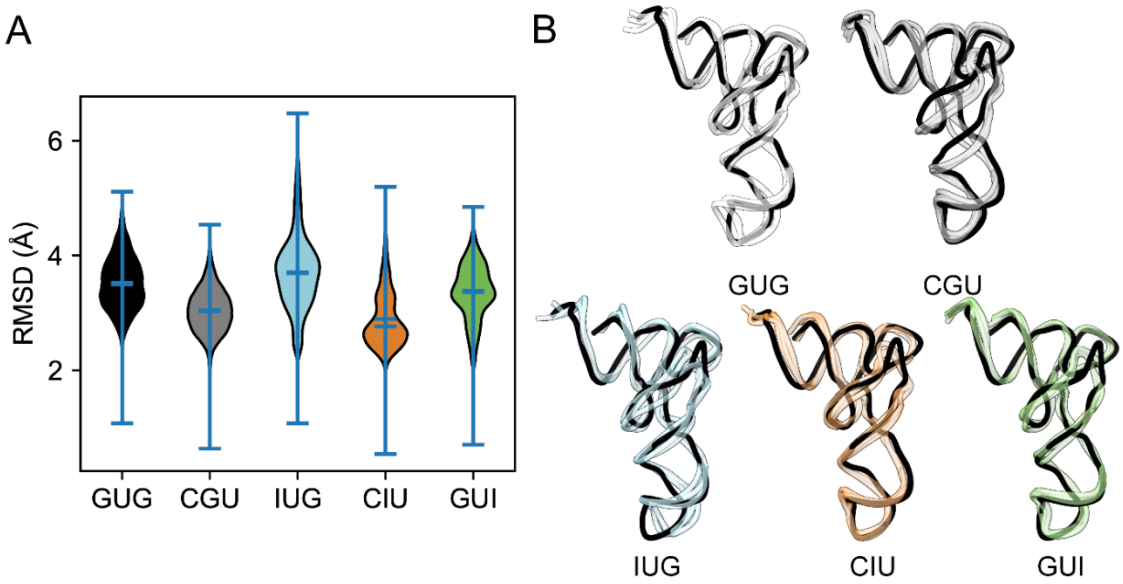

Figure 3.2. Structural convergence of MD simulations of the ribosomal A-site tRNA. (A) Violin plot of the RMSD distribution for systems containing cognate $tRNA^{Val}$ or $tRNA^{Arg}$. (B) Overlays of the three dominant conformations of the tRNA based on cluster analysis of RMSD with the initial coordinates from the cryo-EM structure (black).

The structure of tRNA is influenced by interactions with the LSU proximal to the acceptor stem region and the SSU proximal to the ASL. The convergence of the backbone RMSD tRNA itself was clear from the plateau in values across all models and replicas, generally after ~250 ns, but longer (~750 ns) for IUG replicas 3 and 4, and CIU replica 4 (Figure B.3). In the 99th percentile of the RMSD distribution, all models had RMSDs within 2.09–5.67 Å, with 95% of the data in the upper quartile (4.78–5.67 Å) contributed by replicas 3 (19%) and 4 (76%) of IUG (Figure 3.2A). Due to the independent behavior of its replicas, the IUG model exhibited a broader RMSD distribution in the quadruplicate ensemble, with a higher mean RMSD and a wider range spanning more extreme values (Figure 3.2A). The representative structures of tRNA were generated by cluster analysis (see Chapter 2), generating the three representative structures of each identified conformation for each system. The representative structures were

overlayed over the starting experimental structure coordinates (Figure 3.2B). The centroids of IUG adopted a slightly different conformation from the other systems, where the ASL pivots relative to the tRNA body. Moreover, a small shift in conformation was observed in the D-loop region for all models close to the elbow of the tRNA, suggesting steric crowding by the LSU moderately compresses the tRNA body (Figure 3.2B). However, the dominant structural conformations of each model were well-behaved over the simulations, maintaining the native tertiary structure of tRNA (Figure 3.2B).

3.2.1.2 The 16S rRNA nucleotides selectively reduce monitoring in the presence of the IUG mRNA codon

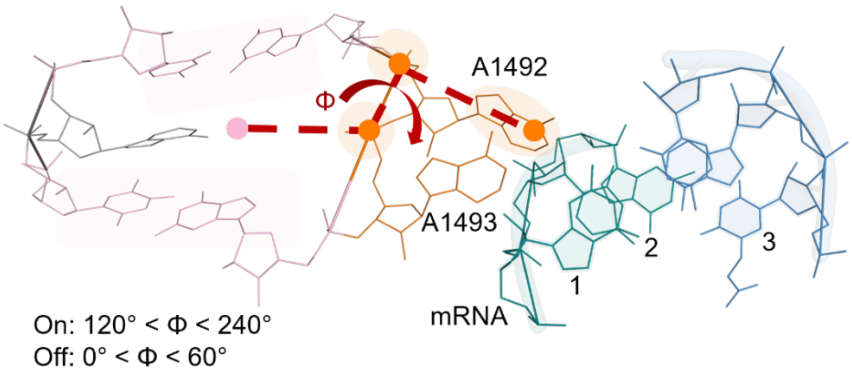

Figure 3.3. Definition of the monitoring angles (Φ). Center of masses (COMs) are represented by colored dots. COM1 (pink) includes C1407, C1409, G1491, and G1494 and is the same for both A1492 and A1493. COM2 is shown for A1492 includes the phosphate group of the 3'-adjacent residue (A1493). COM3 includes the 5'-phosphate group part of A1492 and COM4 is the nucleobase of A1492. COM2, COM3, and COM4 are shifted by 1 residue index in the 3'-direction for A1493 Φ. The mRNA (teal) and tRNA (blue) are shown from a top-down view.

Due to the known roles of three 16S rRNA nucleotides (A1492, A1493, and G530) in monitoring correct tRNA–mRNA base pairing to allow for progression of codon recognition,[19] the relative position of each nucleotide with respect to the minihelix was investigated. A1492 and A1493 are found in helix-44 (h44) of the 16S rRNA and have been reported to adopt an extrahelical ('flipped-out' or 'on') conformation during active monitoring or an intrahelical ('flipped-in' or 'off') conformation while inactive.[20] In the present work, the on and off states

were assessed according to the center-of-mass pseudo-dihedral angle for each adenine, denoted the monitoring angle, denoted Φ (Figure 3.3), where 120°< Φ < 240° corresponds to 'on' conformations and the ranges 0°< Φ < 60° or 300° < Φ < 360° correspond to 'off' conformations as defined in previous work.[21]

In 116 cryo-EM or X-ray structures of *E. coli* or *T. thermophilus* ribosomes containing cognate or near-cognate A-site tRNAs or an empty A-site, three distinct conformations were identified (Figure 3.4A-B). Specifically, both A1492 and A1493 adopt a flipped-out conformation (denoted 'on-on' in the present work), only A1493 is flipped out ('off-on'), or neither nucleotide is flipped out ('off-off'). While the on-on and off-on states are observed for ribosomal complexes containing cognate or near-cognate tRNAs, the off-off state was only observed for 30S ribosomal subunits with an empty A-site (PDB IDs: 1HNW, 1HNX, 1HNZ, 1J5E, 4V4S, and 4V4R),[22-24] or a 70S ribosome containing a non-cognate tRNA (PDB ID: 5WF0).[25] Intermediate states that do not fully satisfy the pre-defined angle requirements for on-on, off-on, or off-off were also present in experimental structures.

Each of the experimentally-reported monitoring conformations were sampled during the MD simulations (Figure 3.4B-G). The motions of A1492 and A1493 were often, but not always, correlated, with A1492 adopting the off state independently of A1493, but not vice versa (Figure 3.5). The motions between the on and off states for A1492 and A1493 comprise the large percentage of intermediate states in the simulations. For GUG, the on-on state was sampled for a large portion of the MD quadruplicate replica ensemble (62%), with the off-on state also present for 6% of the simulation time (Figure 3.4B). A significant portion of the conformations adopted represent an intermediate conformation between the states (33%), although off-off was never truly sampled (0.1%). Similarly, GUI, CGU, and CIU predominantly adopted on-on (18% GUI; 33% CGU; 55% CIU) and intermediate (81% GUI; 66% CGU; 39% CIU)

states (Figure 3.4C,E,F). In contrast, IUG only adopted the on-on state for 11% and off-on for 2% of the simulation ensemble, while the dominant conformation corresponded to the off-off state (25%) (Figure 3.4D). The off-off state being only significantly sampled in this system suggests reduced engagement of adenine monitoring bases for the IUG codon-containing ribosome.

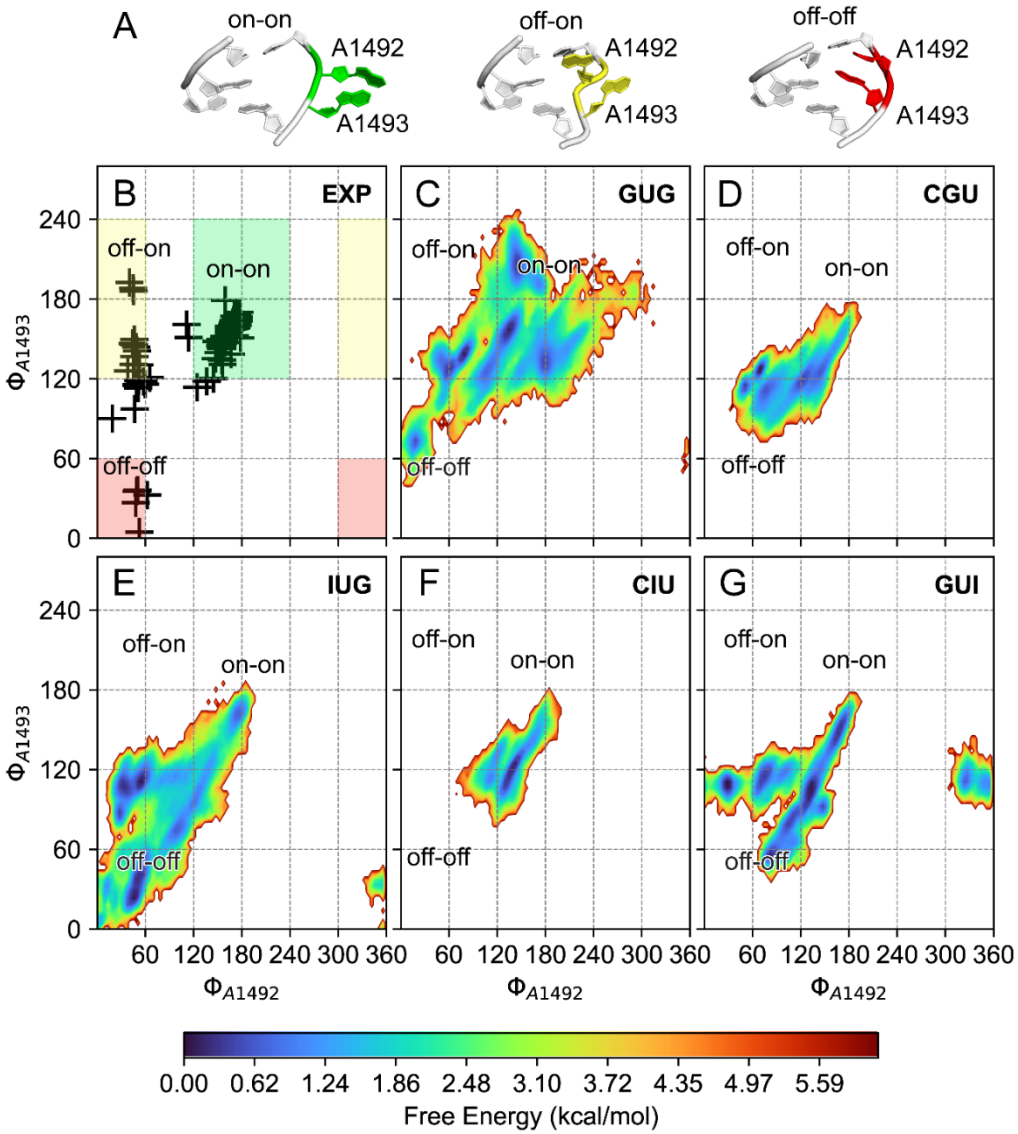

Figure 3.4. The experimental distribution and 2D FEL with respect to the monitoring angles (Φ). (A) The 'on-on' state (green) represents a conformation where A1492 and A1493 are flipped out of the 16S rRNA helix-44 (h44). The 'off-on' state (yellow) indicates A1492 is intrahelical and A1493 is flipped out, while 'off-off' (red) implies A1492 and A1493 are intrahelical. (B) Plot of Φ measured from experimental structures of the ribosome where the x and y axes measure Φ for A1492 and A1493, respectively. (C-D) FELs for quadruplicate ensemble MD simulations of each codon system containing cognate tRNA. The color bar at the bottom indicates the free energy scale used in the FELs (refer to section 2.3.4 for full details about the generation of the FEL plots).

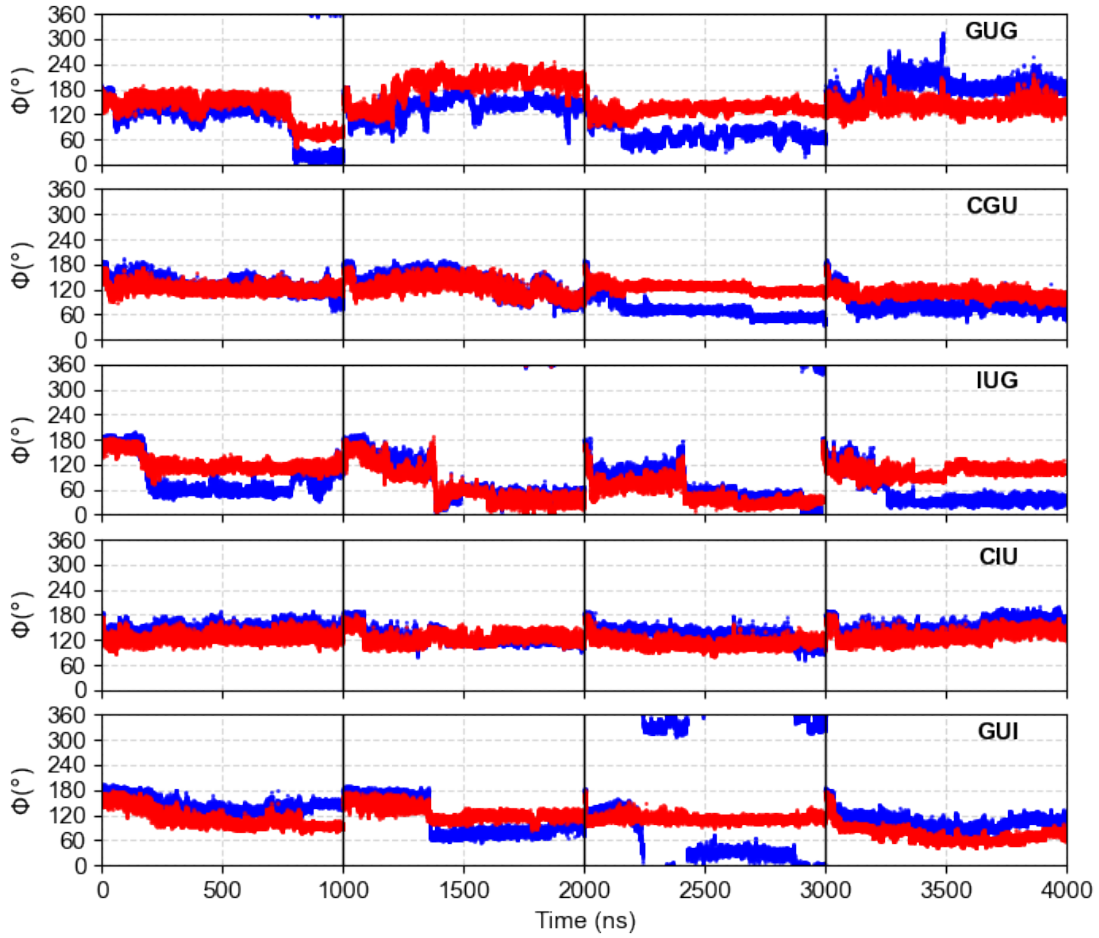

Figure 3.5. Time series plots for the monitoring angles of A1492 (blue) and A1493 (red) over the simulations of each ribosome subsystem model containing cognate $tRNA^{Val}$ or $tRNA^{Arg}$. The independent replica simulations are separated by black lines in the order of replica 1-4.

While Φ is useful for quantifying the preference for intra/extra-helical orientations of the 16S A1492–3 residues, Φ does not consider the intermolecular interactions between A1492–3 and the minihelix minor groove. To consider the intermolecular engagement of A1492–3 with the minihelix, the minor groove distances (MGDs) of A1492 from the second base pair and A1493 from the third base pair were measured. The MGDs showed that the second and third position inosine modification had little influence on the distance of each adenine from the minor groove regions in the first and second positions (Figure B.5B). However, for IUG a considerable

density was observed for high A1492 and A1493 MGDs, suggesting that the intermolecular monitoring was impaired (Figure B.5B).

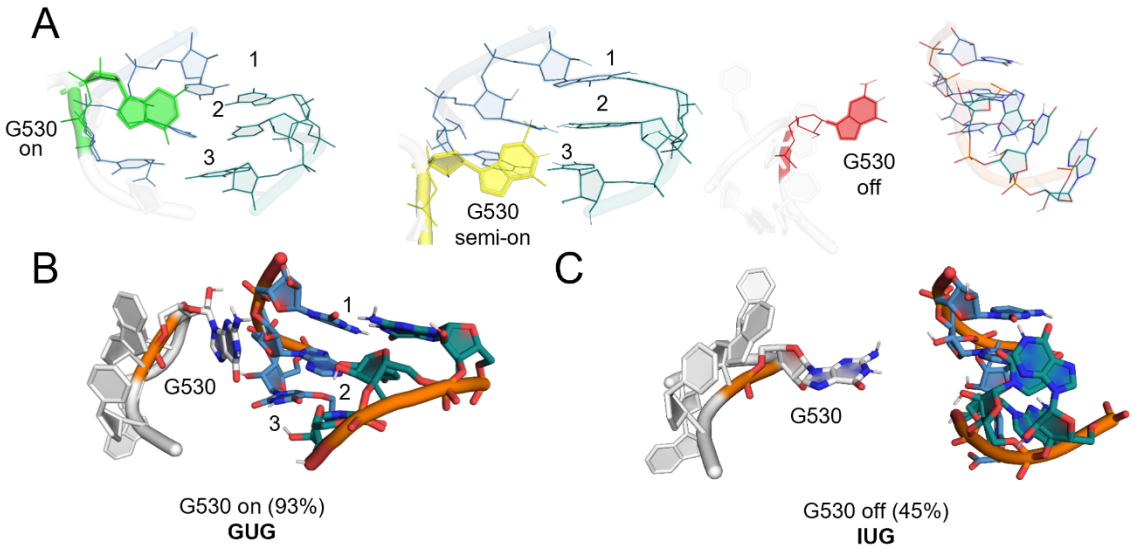

Figure 3.6. G530 conformations and occupancies during the MD simulations. (A) Diagrams of the conformation of G530 from helix-18 (h18) with respect to the minor groove of the mRNA-tRNA minihelix. In the 'on' state, G530 is centered between the position 1 and 2 of the minihelix minor groove. In the 'semi-on' state, G530 is centered between position 2 and 3. In the 'off' state, G530 is disengaged completely from the minihelix. (B-C) Conformational occupancies obtained by cluster analysis applied to the heavy atoms of G530, the tRNA anticodon (B34-36; colored in blue), and the A-site mRNA codon (B1-3; colored in teal) for the quadruplicate ensemble of the GUG and IUG systems. The conformations for inosine-modified codon systems containing cognate $tRNA^{Val}$ or $tRNA^{Arg}$ are shown in Figure B.4.

In addition to A1492 and A1493, G530 helps maintain the minihelix by latching onto the first (B1:B36) and second (B2:B35) base pairs through the minor groove, while a semi-on (partially latched) state involves interactions with the second and third (B3:B34) base pairs and an 'off' state implies a disengaged (unlatched) G530 nucleotide (Figure 3.6A).[26] For the GUG system, G530 was positioned near the 1st and 2nd residues ("on" conformation) for 93% of the simulation, indicating that it still provided stabilization by the hydrophobic effect (Figure 3.6B). G530 in the CGU and CIU systems interacted with all three base pairs of the minihelix, suggesting interchange between on and semi-on states regardless of the presence of inosine in the second position. However, the dominant observed conformation, semi-on, was identical for

CGU and CIU (Figure B.4B-D) and was sampled at similar occupancies (CGU: 92%, CIU: 91%), indicating little influence of second position inosine on G530 monitoring. The GUI system was in the semi-on conformation for the entirety of the simulations (100% occupancy; Figure B.4E) which was expected due to the additional hydrophobic stabilization required for the I3:cmo^{5}U34 base pair. [27, 28] While the G530 in the IUG system spent a significant amount of time in the semi-on state (55% occupancy; Figure B.4C), it was the only system to truly sample the off state of G530 (45% occupancy; Figure 3.6C) as a dominant conformation. The complete absence of G530 latching and occurrence of the off G530 state suggest reduced monitoring for IUG compared to all other codons.

As discussed in Chapters 1 and 2, part of the role of the monitoring nucleobases A1492–3 and G530 is to shield the minihelix minor groove from solvent. [19] The G530 conformational analysis is useful for understanding favoured orientations of G530 with respect to the minihelix, but does not convey how the solvent distribution is impacted by monitoring. To measure the degree of solvent shielding over the simulations, the number of waters within 5 Å of each base pair in the minihelix minor groove was measured (see Chapter 2 for full details). Values are reported as "mean(standard deviation)", where the standard deviation is computed across simulation replicas. The GUG system had 8(2) water molecules on average occupying the region within the first two base pairs of the minor groove, while GUI had 4(3), suggesting that the minor groove region was more solvent-shielded for GUI than for GUG. The distribution of water molecules was not significantly affected for CIU (4(3)) compared to CGU (5(2)). For the IUG system, the distribution of water molecules was significantly wider than for GUG (Figure B.5A), and the number of water molecules increased (10(5)) compared to GUG. These findings were in good alignment with the G530 and A1492–3 conformational analyses wherein IUG most significantly impaired the monitoring by all three monitoring bases.

3.2.1.3 The minihelix structural alignment is compromised in the presence of the IUG mRNA codon

The reduced ribosomal monitoring for IUG compared to other codons raises questions about the structures of the minihelix across models. For GUG, CGU, and CIU, the average glycosidic distances between opposing nucleotides of all three base pairs (10.3–11.1 Å; Figure 3.7A) were consistently near values in cryo-EM structures (e.g., 10.3–10.7 Å in PDB ID: 7K00). Furthermore, the nucleobase–nucleobase interplanar angles indicate each base pair maintains planarity (Figure 3.7B) and measurements of hydrogen-bonding interactions indicate persistent interactions between the WCF binding faces (Table B.2) across GUG, CGU, and CIU systems.

For GUI, due to the flexibility to the I3:cmo^{5}U34 base pair discussed previously, the 3rd base pair had a wider distribution of interplanar angles and hydrogen-bonding occupancies, while the 1st and 2nd base pairs maintained planarity and hydrogen bonding (Figure 3.7B, Table B.3). Nevertheless, the glycosidic distance was within the expected range for all three base pairs, suggesting the minihelix was not significantly disrupted for GUI (Figure 3.7B). Although the base pair distances and angles indicated that the minihelix remained intact for GUG, CGU, CIU, and GUI, IUG had a much higher average glycosidic distance and wider standard deviation for all three base pairs (12.8(3.6), 11.7(4.0), and 12.1(4.5) Å for position 1, 2, and 3, respectively; Figure 3.7B). Moreover, hydrogen-bonding occupancies between opposing nucleobases were decreased for all three base pairs from GUG to IUG, from 98% to 74% in the first position, 90% to 76% in the second position, and 47% to 23% in the third position (Table B.3). The structural variables indicate that the minihelix is significantly disrupted for only the IUG codon.

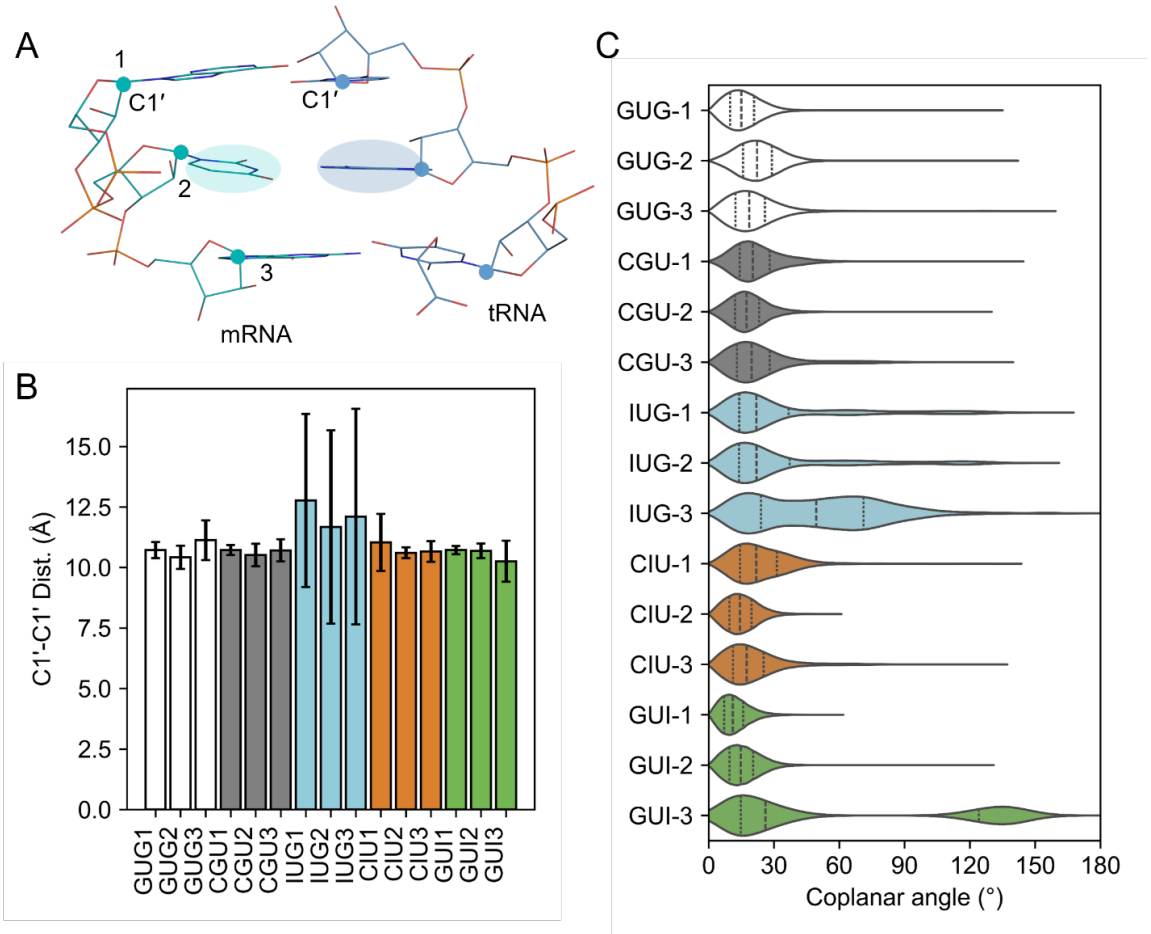

Figure 3.7. Geometric alignment of the codon–anticodon minihelix during the MD simulations. (A) Schematic diagram of the tRNA (blue) mRNA (teal) minihelix with base pair numbering (B1, B2, and B3) corresponding to the mRNA codon nucleotides from 5′–3′. The C1′ glycosidic carbons are shown as colored dots. The coplanar angles were computed using the dot product of the vectors perpendicular to the least-squares best fit plane defined by the nucleobase atoms enclosed in the shaded regions. (B) Glycosidic distances between opposing nucleobases in the minihelix. The error bars represent the standard deviation from the mean. (C) Coplanar angles between opposing nucleobase aromatic rings in the minihelix shown as a violin plot. The vertical dotted lines represent the interquartile range.

3.2.1.4 tRNA dynamics are compromised during recognition of the IUG codon

The conformational dynamics of tRNA also play an important role in initial selection. tRNA adopts a bent (A/T) conformation during codon recognition that is held in place by interactions with the A-site mRNA and EF-Tu:GTP. [29] After GTP hydrolysis, EF-Tu releases the cognate aa-tRNAs to allow for full accommodation and relaxation into a straight (A/A) conformation. Alternatively, near-cognate aa-tRNAs can misalign during initial selection and

dissociate from the A-site codon while still adhering to EF-Tu, causing premature relaxation into a straight conformation. [30] In a previous computational study, [30] the angle between the tRNA body and mRNA codon (θ, Figure 3.8A) was used to measure the position of the A-site tRNA with respect to the mRNA codon. Although the θ angle was measured only during accommodation, near-cognate tRNAs were not truly accommodated in 9% of simulations as they failed the codon recognition step. [30] This led to the near-cognate aa-tRNAs dissociating from the mRNA and caused distinct populations of θ to be measured as the aa-tRNA was oriented parallel to the ribosomal intersubunit tunnel axis. [30] Thus, θ was used to measure whether the tRNA straightens prematurely (when codon recognition fails) or remains in a bent state. In this work, the tRNA was accepted to adopt a bent conformation if θ was > 90° and a straight conformation if θ was < 90° (Figure 3.8A).

A bent conformation was well-maintained for GUG (occupancy of 100%; Figure 3.8B-C), CGU (100%; Figure B.6B), and GUI (100%; Figure B.6F), with an ensemble-averaged $\langle\theta\rangle$ of 129(11)°, 107(5)°, and 106(5)°, respectively (Figure 3.8A-C; Figure B.6B). CIU had a seemingly lower occupancy (93%) of the bent state and a subpopulation within the low range (< 90°) of θ (Figure 3.8B). The 1st base pair of the minihelix was disrupted in the second most dominant conformation of CIU (occupancy=6%), which shifted the COM of the 1st base pair and decreased the angle to fall within the "straight" range despite the conformation clearly being bent (Figure B.5E). Despite this disruption, the CIU model maintained a bent state for effectively the entire simulation time (99%). The dominant state for the IUG codon was also a bent conformation (78% and $\langle\theta\rangle$ was ~113(12)°; Figure B.6C). However, the IUG codon also sampled a distinct straightened conformation where $\langle\theta\rangle$ was ~59(11)° (Figure 3.8B-C), which occurred for approximately one-fifth (23%) of the simulation time (Figure 3.8D). The premature tRNA

straightening observed for IUG was associated with the tRNA moving away from the mRNA while maintaining association with EF-Tu.

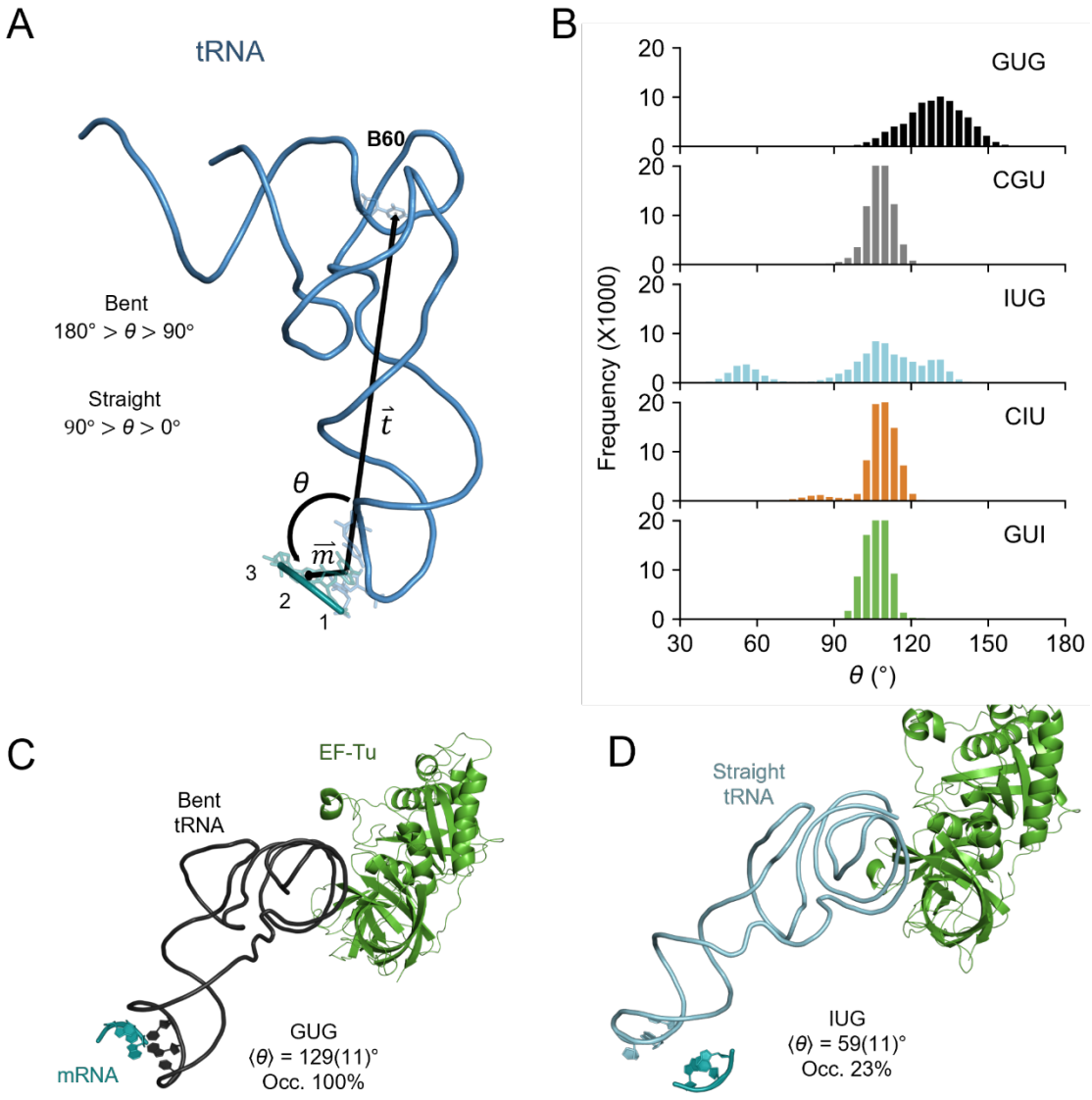

Figure 3.8. Alignment and conformation of tRNA in the A-site during MD simulations. (A) Definition of the alignment angle (θ) between the tRNA (blue) and mRNA (teal). The angle is measured as the angle between the tRNA vector ($\vec{t}$) along the center of mass of the anticodon nucleotides to the C60 nucleotide (U60 in tRNA(Arg)) and the mRNA vector ($\vec{m}$) along the center of mass of the 5′ nucleotide to the 3′nucleotide. (B) Distribution of θ over the quadruplicate ensembles for each system. (C-D) Representative bent and straight tRNA conformations sampled with the corresponding ensemble-averaged θ values, $\langle\theta\rangle$ (standard deviations enclosed in parentheses), and occupancies for GUG (black) and IUG (cyan) in the A-site region. (Occ. = Percent occupancy for the conformations).

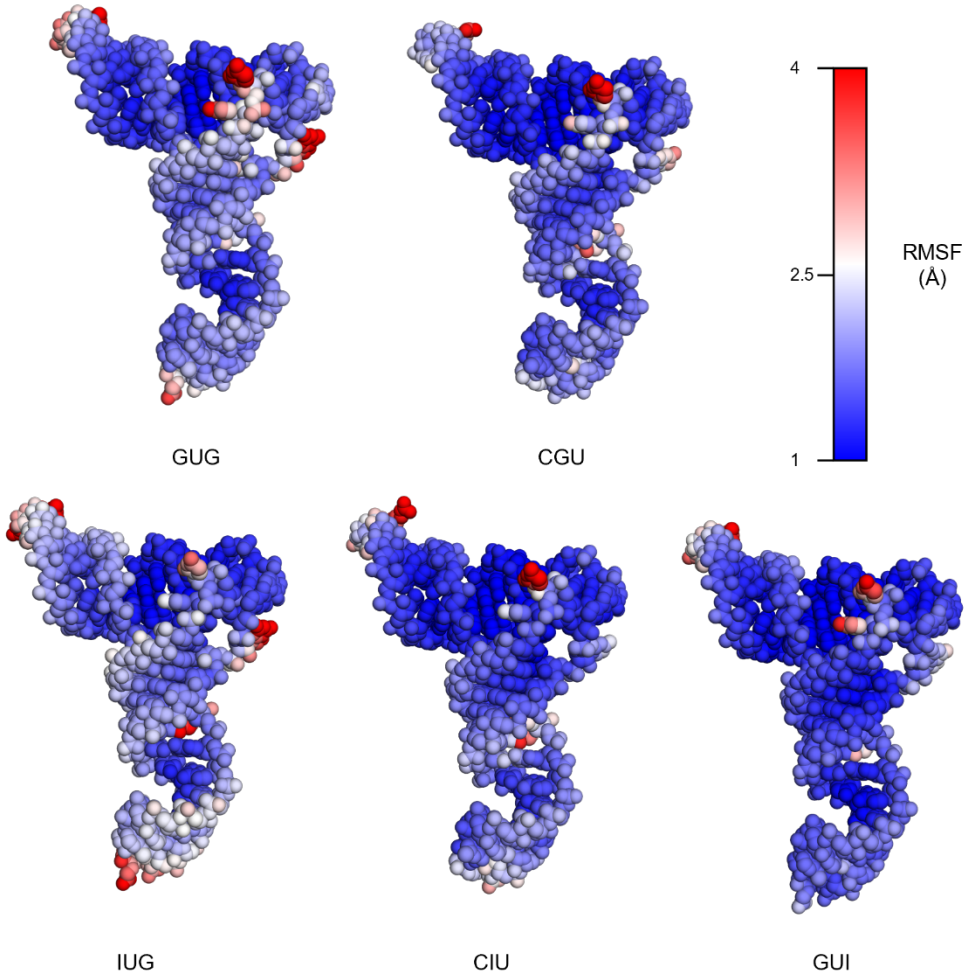

Figure 3.9. Flexibility of the tRNA over MD simulations as measured by root-mean-squared fluctuations (RMSFs). The residue of each tRNA is colored according to the blue-white-red spectrum denoting the RMSF value.

From a dynamical perspective, the localized flexibility of tRNA plays a crucial role in the selection process, where an increased flexibility has been observed in the C49–C72 nucleotides, TΨC-loop, and acceptor stem in simulations of non-cognate tRNAs bound to the A-site in the A/A conformation.[30] The A/T conformation transitions into the rigid A/A state stabilized by H89 and the PTC during accommodation.[31] Therefore, we expected that the flexibility trends would differ from those of fully accommodated A-site tRNAs positioned closer to the PTC after EF-Tu dissociation. Indeed, the mean RMSFs across all models spanned a wide range ~0.5–3.5 Å

(Figure 3.9) compared to the ~0.5–2.5 Å range observed in the accommodated tRNA simulations in previous work.[30] In the present work, across all models, individual nucleotides that were more solvent-exposed typically had high RMSFs. For example, the D-loop nucleotides DHU17 had an ensemble-averaged residue RMSF exceeding 2.3 Å in all models (GUG: 3.50(1.4), CGU: 3.23(0.5), IUG: 2.33(0.3), CIU: 2.97(0.8), and GUI: 2.47(0.4), all values in Å; Figure B.7). The G45 nucleotide, part of the variable loop, also had considerable flexibility in all models (GUG: 2.4(0.4), CGU: 2.5(0.6), IUG: 3.1(0.8), CIU: 2.8(0.9), and GUI: 2.2(0.8); Figure B.7). However, the trends for these individual nucleotides were not always consistent between models. For example, the flexibility of G20 present in the $tRNA^{Val}$ sequence was highly flexible in GUG and IUG, but not GUI (GUG: 3.43(1.0), IUG: 3.03(1.1), and GUI: 1.98(0.5); Figure B.7), while the flexibility of the corresponding D20 residue in $tRNA^{Arg}$ was lower (CGU: 2.20(0.7) and CIU: 1.80(0.5); Figure B.7). The RMSF of the ASL region (residues 27–43) and ACS region (residues 1–8 and 66–72) remained similar for GUG, CGU, CIU, and GUI, with ASL values clustering around 1.7 Å and ACS values between 1.2 and 1.3 Å (Table B.4). Among the GUG, CGU, CIU, and GUI models, GUG had the most flexible ASL (1.73(0.3) Å), while CGU and CIU showed the lowest ACS fluctuations at 1.24(0.2) Å and 1.26(0.2) Å, respectively (Table B.4). IUG exhibited the highest ASL and ACS flexibility (2.04(0.5) Å and 1.63(0.3) Å, respectively; Table B.4). The increased flexibility of both ribosome-contacting regions (the ASL and ACS) in the presence of the IUG codon (Figure. 3.9, Table B.4) suggests reduced stabilization by the A-site environment, consistent with impaired codon recognition.

Cluster analysis was performed using the eRMSD metric to classify dominant structural conformations at the tRNA–mRNA interface (see Chapter 2). In the most frequently sampled state across all systems (denoted ‘stacked’), all three nucleobases in both the codon and anticodon were optimally stacked for duplex formation (Figure 3.10A). In the second most-

commonly observed conformation ('wobble'), hydrogen bonding was disrupted at the wobble position. The base pair at the 5'-end of the minihelix is disrupted in the third conformation ('5'-disrupted') (Figure 3.10A). Importantly, the stacked, wobble, and 5'-disrupted maintain the minihelix structural alignment. However, in the final conformation ('rejected'), the proper WCF geometries of two or more of the base pairs were disrupted or the tRNA dissociated completely and moved far away (> 15.0 A C1'–C1' distance) from the mRNA.

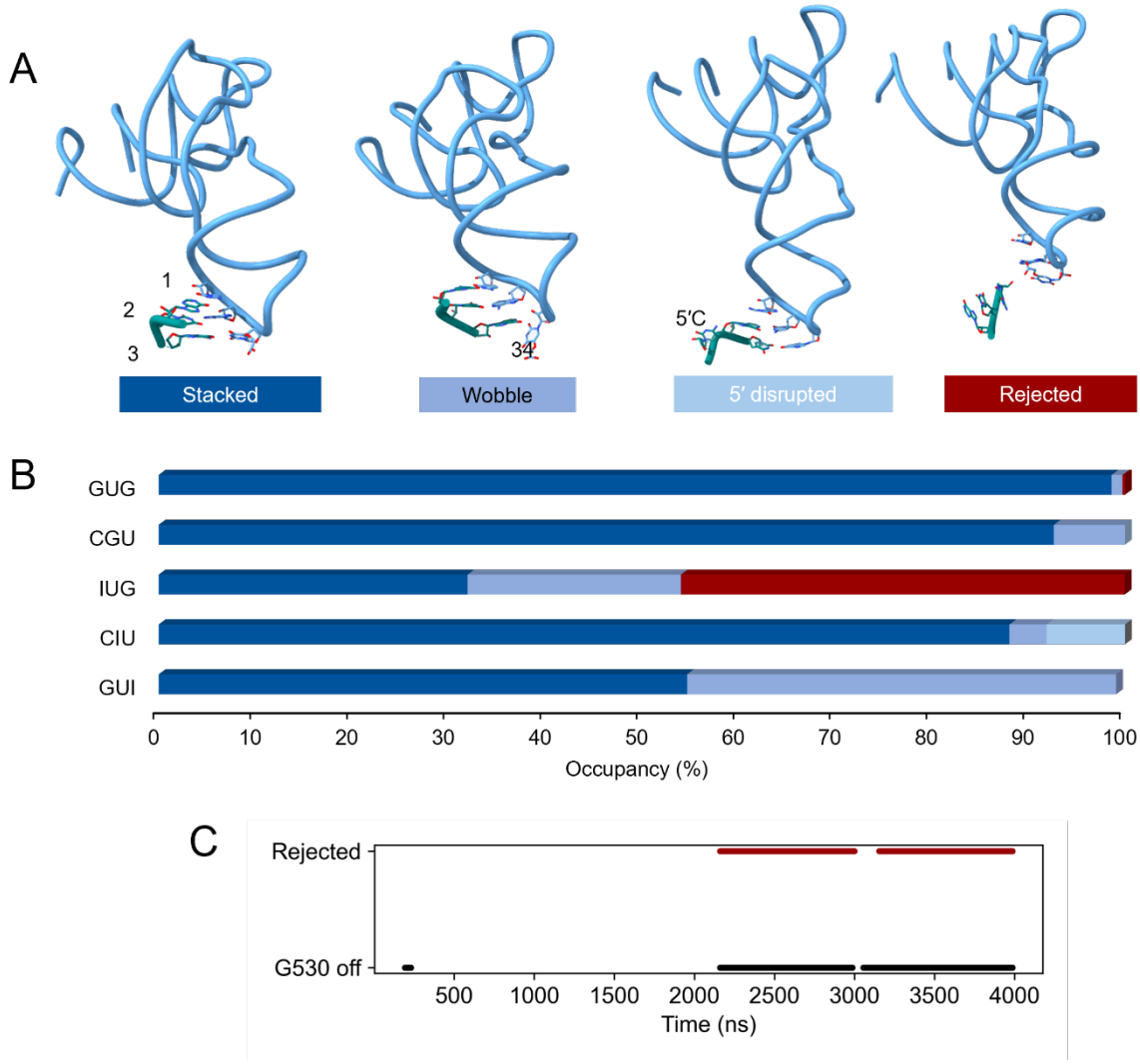

Figure 3.10. Representative conformations obtained by principal component analysis (PCA) of eRMSD and clustering over the MD simulations on ribosome subsystems. (A) Conformations sampled during simulations. (B) Occupancies of each conformation for each system. (C) Occupancy of the rejected and G530 off states over the simulation time.

For both models containing unmodified codons (GUG and CGU), the stacked state was the most dominant (99% and 93% for GUG and CGU, respectively; Figure 3.10B) across the quadruplicate replica ensemble. For CIU, the stacked state remained dominant (88%; Figure 3.10B). The 5'-disrupted state was only sampled for CIU as a minor conformation (8%; Figure 3.10B) and was associated with the lowered θ (Figure B.6E). While the wobble state was a minor conformation for GUG (1%), CGU (4%), and CIU (4%) (Figure 3.5B), GUI had an increased occupancy of the wobble state (44%) and adopted the stacked state for the remainder of the time (55%) (Figure 3.10B). Thus, all four systems maintain minihelix conformations conducive to productive selection. In stark contrast, IUG had a lower occupancy of the stacked (32%) and wobble (22%) conformations. Furthermore, IUG occupied the rejected state for nearly half (46%) of the simulation time (Figure 3.10A), indicating nonproductive selection for only this codon. Interestingly, the G530 off conformation was also adopted for a nearly identical percentage for IUG codon simulations (45%; Figure 3.6B). The G530 off state was further confirmed to be occupied at the same times as the rejected state, suggesting that G530 disengagement may exacerbate the loss of minihelix base pairs. In comparison, the A1492–3 off-off state occurred for a lower percentage (25%) of the time than G530 off. However, without considering A1493, A1492 was in the off state for 53% of the time in IUG simulations, much higher than any other model (GUG: 12%, CGU: 8%, CIU: 0%, GUI: 19%).

3.2.2 MD simulations of near-cognate tRNA

As mentioned in Section 3.1, it has been proposed that mRNA modifications can lead to the ribosome treating cognate tRNA in a fashion similar to near-cognate tRNAs. From the previous discussion, the cognate tRNA was more rejection-prone in the presence of an IUG mRNA codon, suggesting that IUG is treated as near-cognate by the ribosome. To examine this hypothesis, simulations were performed with near-cognate $tRNA^{Met}$, which bears a first position

mismatch (G:U) and a GUG codon. In addition, to examine whether inosine causes miscoding due to expanded base-pairing capabilities compared to G, simulations were performed on systems containing a near-cognate $tRNA^{Met}$ bound to the IUG codon (IUG^{Met}).

3.2.2.1 Structural convergence of ribosomal subsystem simulations

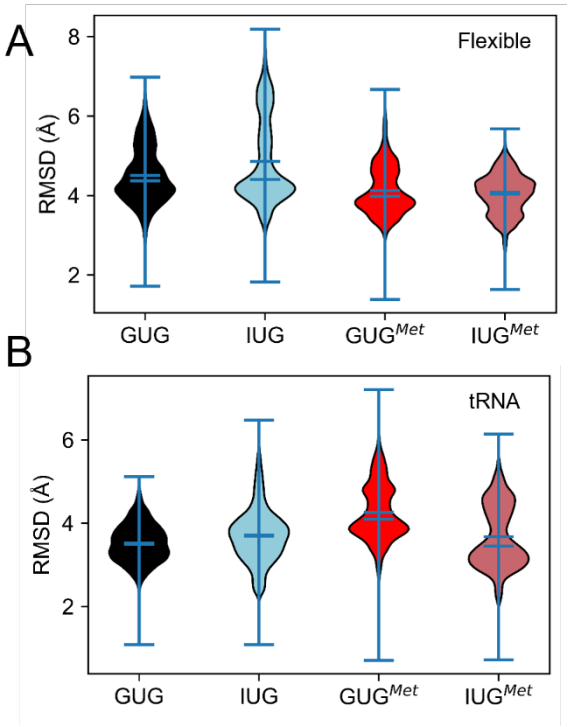

Figure 3.11. Structural convergence of the unrestrained region and A-site tRNA during MD simulations of the ribosomal A-site containing cognate $tRNA^{Val}$ or near-cognate $tRNA^{Met}$. (A) Distribution of backbone RMSD of the flexible region with respect to the experimental starting structure. (B) Distribution of backbone RMSD of the tRNA with respect to the experimental starting structure.

The convergence of the simulations was examined by computing the backbone RMSD of the flexible region of the ribosome subsystems (Figure B.8A) and the tRNA (Figure B.8B). The time series RMSD plots indicate convergence after 250-500 ns for each replica of the GUG and IUG-containing near-cognate systems for both the flexible region and tRNA. Furthermore, the RMSD distributions indicated similar ranges of RMSD with CVs of 0.150 and 0.128 for GUG^{Met} and IUG^{Met}, respectively (Figure 3.11A-B; Table B.1). The RMSD for GUG^{Met} and IUG^{Met} indicates that the systems did not undergo problematic or unrealistic structural distortions. The low

RMSD ranges occupied suggest that the dominant conformations exhibited by each system maintained the native structural folds of both the global structure and the tRNA.

3.2.2.2 Near-cognate tRNA^{Met} systems alter monitoring by A1492, A1493 and G530

The monitoring angles of A1492 and A1493 exhibited correlated behaviour over the microsecond simulations for the near-cognate systems, with occasional independent flipping of A1492 towards the off-state for GUG^{Met} and IUG^{Met} (Figure B.9). The on-on state occupancy was lowered by about two-thirds from GUG (62%) to GUG^{Met} (39%; Figure 3.12A-D). Moreover, GUG^{Met} sampled the off-off state for 5% of the simulation compared to 0.1% in GUG (Figure 3.12A-B). The changes in monitoring from cognate to near-cognate tRNA were not unexpected given that the U:G mispair should result in a degree of disengagement of the monitoring bases. However, the IUG model impacted A1492–3 monitoring in the GUG model more drastically (increased off-off by 25% and decreased on-on by 51%) than the GUG^{Met} model (increased occupancy of the off-off state by 5% and decreased on-on by 23%) despite the latter containing a mispair in the first position (Figure 3.12B-C).

Interestingly, when comparing IUG and IUG^{Met}, the on-on state increased from 11% to 64% and the off-off state was eliminated (Figure 3.12B,D) suggesting that the IUG codon completely offsets the monitoring disengagement when in the presence of near-cognate tRNA. In fact, the offset resulted in agreement between the IUG^{Met} and GUG monitoring conformation occupancies, where on-on was dominant, off-on was minor, and off-off was not significantly sampled (on-on: 64% and 62%, respectively; off-on: 1% and 6%, respectively; off-off: 0.1% and 0.1%, respectively; Figure 3.12B,D). These results suggest that substituting the first base pair (G1:C36) to a mismatch (G1:U36) causes a decrease in engagement of A1492–3 that is less pronounced than inosine substitution (I1:C36). These effects were also confirmed upon investigating the A1492–3 MGDs, for which GUG^{Met} exhibited modest broadening compared to

GUG, but for IUG^{Met} the MGDs narrowed and were most densely occupied at short distances for IUG^{Met} (Figure B.10).

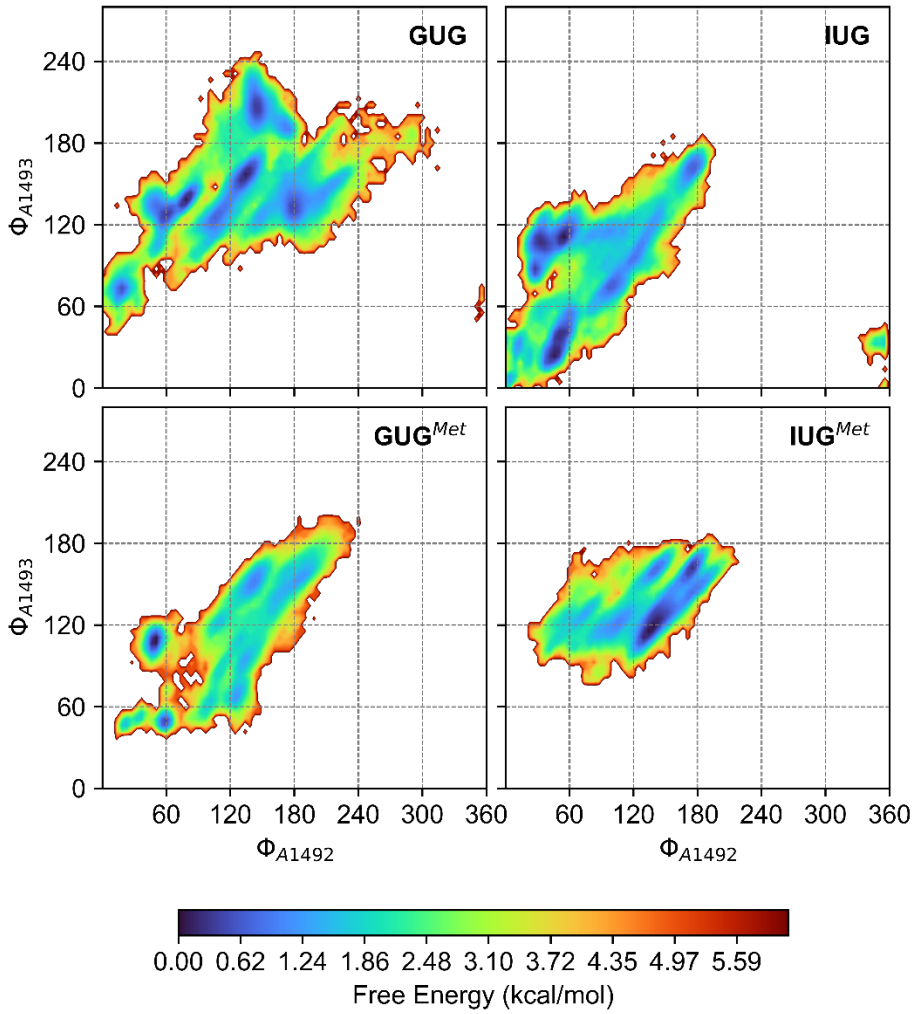

Figure 3.12. The influence of near-cognate tRNA binding on the 2D Free Energy Landscapes (FELs) versus the monitoring angles (Φ). FELs for quadruplicate ensemble MD simulations of each GUG or IUG systems containing cognate tRNA^{Val} or near-cognate tRNA^{Met} in the A-site. The color bar at the bottom indicates the free energy scale used in the FELs (refer to Chapter 2 for full details about the generation of the FEL plots).

G530 adopted the on state for GUG^{Met} (occ.=41%; Figure 3.13A) and two not previously observed conformations where G530 stacks with the 3rd codon base (denoted G530-G3 stacked; occ. 49%; Figure B.11A), and where the G530 base engages with an out-of-frame minihelix (denoted “pseudo-on”; 9%; Figure B.11A). For GUG^{Met}, the G530–G3 stacked conformation is

structurally related to the G530 semi-on state, as the wobble base pair is often dynamically broken and reformed, allowing G3 to flip out of the minihelix and stack with G530 (Figure B.11A). However, the G530–G3 stacking interaction precludes proper positioning of G530, implying that the conformation disfavours successful codon recognition by near-cognate tRNA. In the pseudo-on state, the tRNA anticodon is shifted such that A35 pairs with the first codon base G1 instead of U2, leaving U36 unpaired (interacting with A1492) and G3 without an anticodon partner, resulting in an unconventional (and likely unproductive) codon recognition configuration (Figure B.11A). The dominant conformation for IUG^{Met} corresponded to the G530 on state (82%), but the off state also occurred as a minor conformation (11%; Figure B.11B). Over the remaining simulation time (7%), the G530 base stacked with the A35 of tRNA (denoted "G530–A35 stacked"; Figure B.11B).

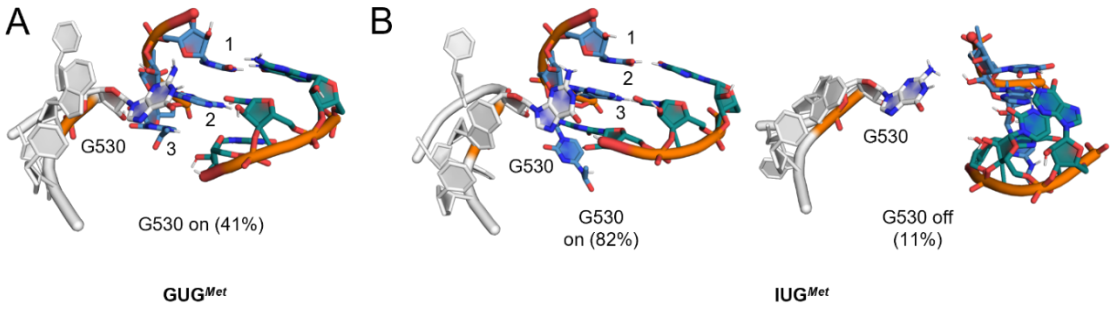

Figure 3.13. G530 conformations and occupancies during the MD simulations of ribosome subsystems containing or near-cognate tRNA^{Met} in the A-site. (A-B) Conformation occupancies obtained by cluster analysis applied to the heavy atoms of G530, the tRNA anticodon (B34-36; colored in blue), and the A-site mRNA codon (B1-3; colored in teal) for the quadruplicate ensemble of the GUG and IUG systems with near-cognate tRNA bound in the A-site. See Figure B.9 for all G530 conformations observed for GUG^{Met} and IUG^{Met}.

Moreover, G530 monitoring disruption manifested in different ways for GUG^{Met} and IUG^{Met}. The G530 off state was absent for GUG^{Met}, but was highly sampled for IUG, suggesting that G530 more readily disengaged from the minor groove in the presence of a modified pair compared to the mispair. While G530-off appeared for IUG^{Met} (11%), it was less frequently observed than for IUG (45%). GUG^{Met} and IUG^{Met} also exhibited unconventional decoding center

configurations (pseudo-on and G530–G3 stacked in GUG^{Met} and G530–A35 stacked in IUG^{Met}) in which G530 is associated with the minihelix, but its conformation blocks it from properly stabilizing the minihelix minor groove. The G530 on state, which was never sampled for IUG, became the dominant conformation (82%) for IUG^{Met} and the second-most occupied conformation (41%) for GUG^{Met}. These findings suggest that while monitoring is impaired in both near-cognate systems, G530 retains partial functionality through continued sampling of the G530 on state. IUG^{Met} displays a more binary response to the minihelix, alternating between fully engaged (G530 on; 82%) and disengaged (G530 off; 11%) conformations. In contrast, GUG^{Met} elicits a more intermediate behavior, with G530 remaining associated with the minihelix throughout the simulations, but occupying non-productive configurations for the majority (59%) of the time.

Both near-cognate systems exhibited compromised G530 latching compared to GUG, though the extent of disruption was substantially less pronounced for both near-cognate systems than for IUG. In addition to the modestly disrupted monitoring activity by A1492–3 for both near-cognate systems, these results suggest that minor groove solvent shielding by G530 and A1492–3 should be reduced for GUG^{Met} and IUG^{Met} relative to GUG. However, for both GUG^{Met} and IUG^{Met}, the average number of water molecules within the vicinity of the minihelix minor groove unexpectedly decreased compared to GUG (6 and 5 waters vs. 8 waters in GUG; Figure B.12). This result suggests that solvent shielding of the minihelix minor groove is improved for both near-cognate systems. However, given the previous findings for the near-cognate systems where G530 and A1492–3 monitoring was impaired to some degree for GUG^{Met} and IUG^{Met} relative to GUG, the enhanced minihelix solvent shielding could not have been solely due to the G530 and A1492–3 behaviour. Alternatively, the solvent shielding was likely due to

some change in rRNA or protein conformation uniquely occurring in the presence of near-cognate tRNA that occludes water molecules from interacting with the minihelix minor groove.

3.2.2.3 The minihelix geometry is disrupted in presence of near-cognate tRNAs but the near-cognate tRNA does not dissociate from the mRNA codon

The A1492–3 and G530 monitoring function was impaired for both near-cognate systems with respect to GUG. However, the milder disruption of G530 monitoring in GUG^{Met} and IUG^{Met} compared to IUG suggests a less pronounced structural destabilization of the minihelix in the near-cognate systems. Indeed, the magnitude of the standard deviation of the glycosidic distances of all three base pairs for GUG^{Met} and IUG^{Met} increased with respect to GUG, but the increase was less drastic than that observed for IUG (Figure 3.14A). However, the interplanar angles between opposing nucleobases in the minihelix revealed similar broadening for both GUG^{Met} and IUG^{Met} as observed for IUG for all three base pairs, suggesting significant distortions from WCF geometry (Figure 3.14B). Moreover, hydrogen-bonding interactions were severely decreased for both GUG^{Met} and IUG^{Met} with respect to GUG. The first base pair (B1:B36) for both GUG^{Met} and IUG^{Met} was decreased from 97% occupancy in GUG to 66% and 78%, respectively, comparable to IUG (decreased to 74%; Table B.3). The hydrogen-bonding occupancies in the second and third base pairs (B2:B35, B3:B34) were also decreased with respect to the GUG system (90%, 20%), in GUG^{Met} (67%, 7%), and IUG^{Met} (81% and 7%), with a similar decrease for IUG (76% and 6%; Table B.3).

The lower standard deviations in the glycosidic distances for all three base pairs in the near-cognate systems compared to IUG suggests that the codon and anticodon are not pulled apart as far. Indeed, the mean distances observed for the near-cognate systems between the glycosidic carbons of the codon and anticodon nucleotides in the second base pair (GUG^{Met}:10.3(0.7) Å; IUG^{Met}: 10.8(0.7) Å) were comparable to GUG (10.4(0.5) Å) and significantly lower than for IUG (11.7(4.0) Å; Figure 3.14A). The maintained engagement of A1492–3 and

G530 may have aided in attempting to enforce base-pairing interactions by forcing proximity between the codon and anticodon in the near-cognate systems. However, despite the proximity between base pairs, the minihelix structure itself was severely impaired for both GUG^{Met} and IUG^{Met} as indicated by the similar trends in coplanar angles between opposing nucleobases and the comparable loss of WCF hydrogen-bonding interactions to IUG. The enforcement of this proximity between the codon and anticodon implies that the ribosome is still attempting to recognize the tRNA, rather than rejecting the tRNA outright, as was observed for IUG.

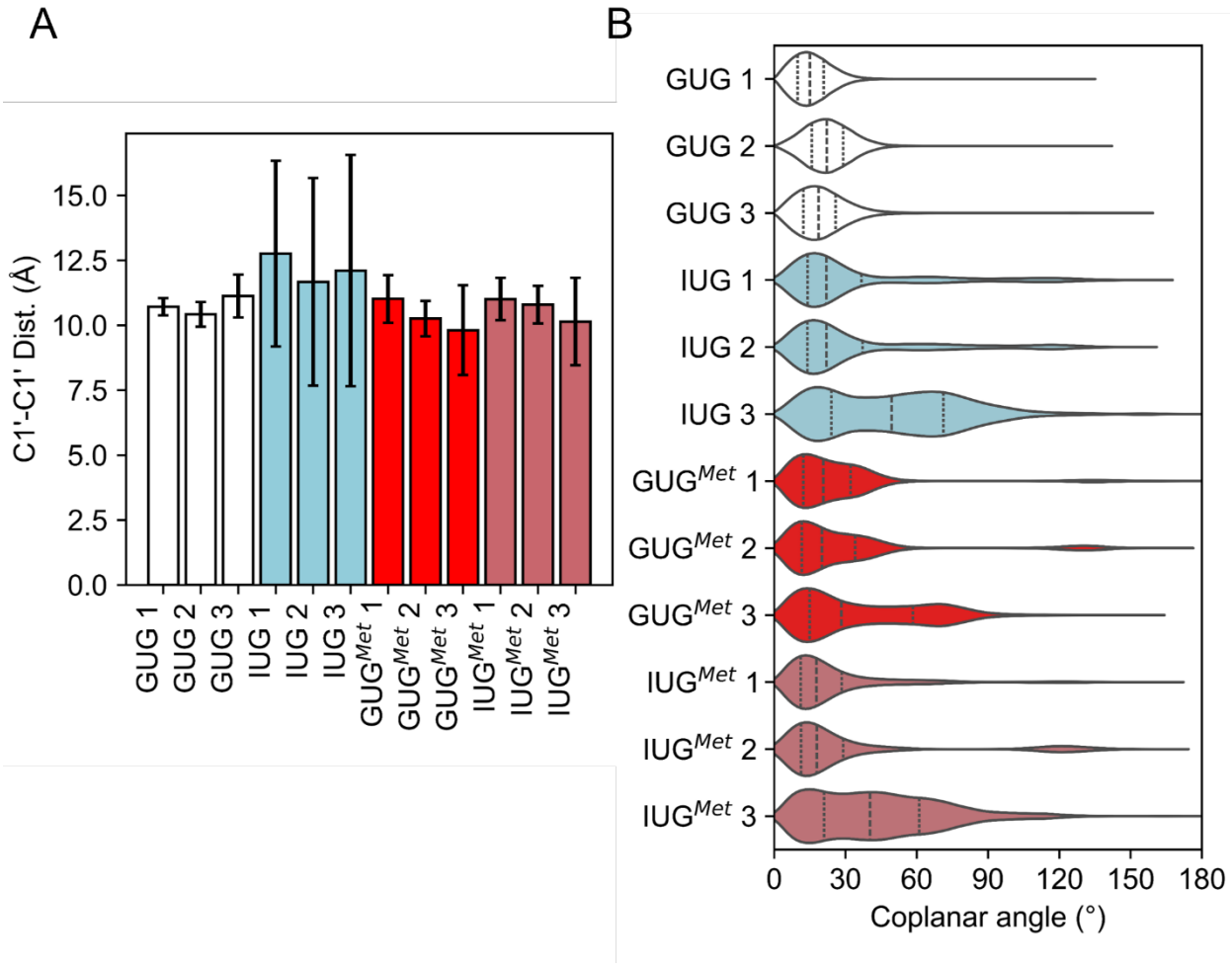

Figure 3.14. Geometric alignment and distance between the codon-anticodon minihelix during the MD simulations containing near-cognate tRNAs in the A-site. (A) Glycosidic distances between opposing nucleobases in the minihelix. (B) Coplanar angles between opposing nucleobase aromatic rings in the minihelix.

3.2.2.4 Near-cognate tRNA exhibit increased flexibility and premature straightening

The alignment of tRNA in the A-site was measured with the θ variable (Figure 3.8A). Relative to GUG, GUG^{Met} exhibited a broader θ distribution, while IUG^{Met} showed a leftward shift in the distribution (Figure. S3.11A). However, neither GUG^{Met} nor IUG^{Met} significantly sampled populations at the low range of θ (Figure B.11A). The GUG^{Met} system sampled two distinct tRNA conformations, denoted 'A/T-I' and 'A/T-II', (Figure B.11B), corresponding to the upper (120–180°) and middle (90–120°) ranges in the θ distributions, respectively. The A/T-II state represents an ∼9 Å shift of the ASL and mRNA codon distal to EF-Tu (i.e., towards the P-site) with negligible movement in EF-Tu or the acceptor arm of the tRNA, suggesting tRNA straightening (Figure B.11C). Despite the predominantly large θ (115(9)°) sampled in IUG^{Met}, the dominant conformation was also a straight conformation (Figure B.13C). Therefore, while the complete dissociation from the mRNA codon in IUG caused a distinguishable shift in θ, the θ angle cannot adequately ascertain straightened and bent conformations for tRNAs that remained close to the mRNA codon such as GUG^{Met} and IUG^{Met} (Figure 3.14B).

To better estimate the relative populations of the bent and straight conformations during the simulations for the near-cognate systems, the deviation angle of the acceptor stem (ACS) relative to the long axis of the tRNA, Δ^{ACS}, was computed. Specifically, the vector formed by the COM of the central junction of the tRNA (base pair 10–25 of the D-arm and residue 44 of the variable loop) and the COM of the ACS was computed for the reference experimental structure, and the dot product angle was computed for each subsequent frame during the simulation to measure Δ^{ACS} (Figure 3.15A). Larger Δ^{ACS} angles therefore indicate that the tRNA ACS aligns along the axis of the tRNA body and straightens. The COM distance of the ASL to the tRNA elbow were also calculated, where larger distances suggest straightening (Figure 3.15A). Full calculation details for Δ^{ACS}, and the ASL-elbow distance are discussed in Chapter 2.

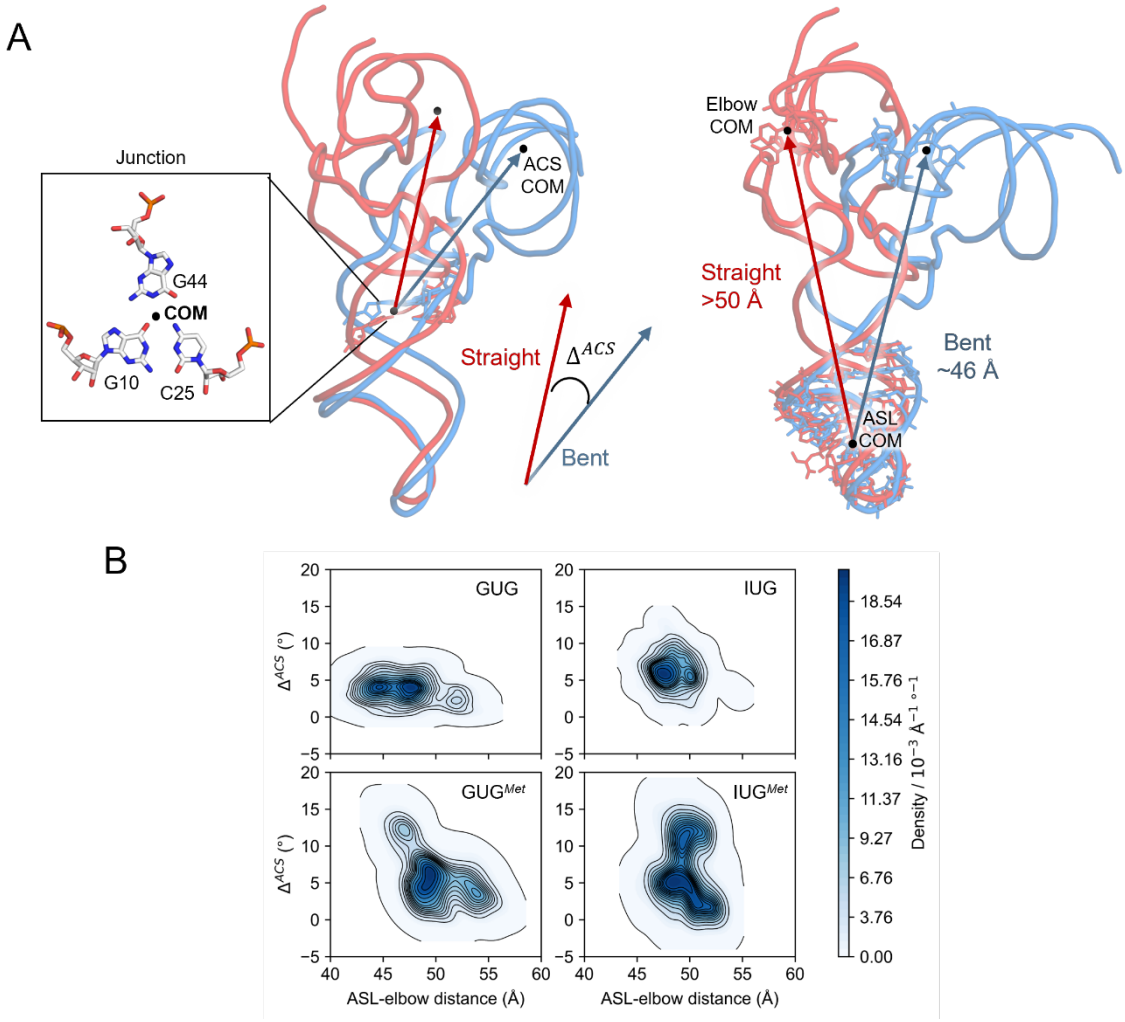

Figure 3.15. Internal conformations of cognate and near-cognate tRNA systems. (A) Schematic diagram of the Δ^{ACS} angle and ASL-elbow distances for straight (red) and bent (blue) conformations. The Δ^{ACS} angle is measured with respect to the experimental starting structure vector formed from the center of mass (COM) of the junction (base pair 10–25 of the D-arm and residue 44 of the variable loop) to the COM of the acceptor arm (ACS; residues 1–8 and 58–76) perpendicular to the tRNA principle axis. The ASL–elbow distance is measured between the COM of the ASL (residues 27–43) and the elbow on the acceptor domain (residues 55–57). (B) Kernel Density Estimate (KDE) plot of ASL–elbow distance and Δ^{ACS}. Darker blue regions represent higher occupation probabilities over simulation ensembles. Black contours show increments of ~1/15 of the estimated probability density range.

With respect to GUG, the Δ^{ACS} density distributions were broadened significantly for IUG, GUG^{Met}, and IUG^{Met} (Figure 3.15B), suggesting sampling of straightened conformations at higher Δ^{ACS} angles. Both near-cognate systems sampled Δ^{ACS} angles in the upper range (> 10°) more frequently than IUG (Figure 3.15A). IUG^{Met} had the most significant density in the upper

range of Δ^{ACS}, suggesting that IUG had the highest degree of tRNA straightening. The ASL–tRNA elbow distance was also significantly increased for IUG, GUG^{Met} and IUG^{Met} with respect to GUG, with distances of ~46 Å for GUG to distances > 50 Å for IUG, GUG^{Met}, and IUG^{Met}. Both GUG^{Met} and IUG^{Met} also had increased ASL–elbow distances compared to IUG, suggesting that tRNA lengthens more significantly in the near-cognate systems. Both the increased Δ^{ACS} and ASL–elbow distances suggest that premature straightening occurred for IUG, GUG^{Met}, and IUG^{Met}, with the most pronounced effects for IUG^{Met}. The premature straightening of tRNA was more prominent in the near-cognate systems than either cognate tRNA system, suggesting that even when the minihelix remains close to the near-cognate anticodons, the tRNA fails to maintain the bent state.

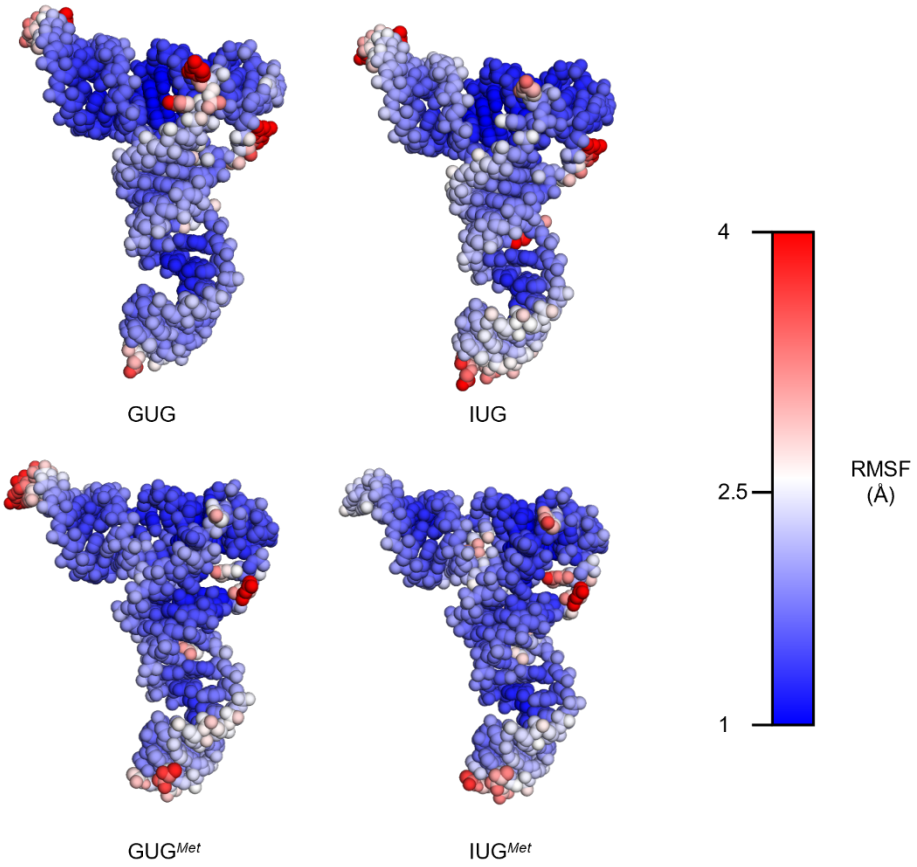

Figure 3.16. Flexibility of the tRNA over MD simulations as measured by root-mean-squared fluctuations (RMSFs). The residue of each tRNA is colored according to the blue-white-red spectrum denoting the RMSF value.

The mean per-residue RMSF values for both GUG^{Met} and IUG^{Met} tRNAs were highly consistent (Figure 3.16; Figure B.12). The similarities were confirmed by examining a detailed breakdown of the RMSF of each tRNA domain. In the ASL domain, the RMSF for GUG^{Met} (1.88(0.4) Å) was only slightly lower than IUG^{Met} (1.93(0.4) Å; Table B.4). Similarly, the TΨC-arm (GUG^{Met}: 1.30(0.2) Å; IUG^{Met}: 1.37(0.3) Å) fell within a consistent range of RMSF values for the near-cognate models. Comparing the cognate and near-cognate models, the ASL had increased fluctuation in the order of GUG (1.73(0.3)) < IUG^{Met} (1.88(0.4)) < GUG^{Met} (1.93(0.4)) < IUG (2.04(0.5) Å). On the other hand, the ACS fluctuation trend followed in the order of GUG (1.46(0.2)) < GUG^{Met} (1.63(0.3)) ≈ IUG (1.63(0.3)) < IUG^{Met} (1.77(0.4) Å) (Table B.4). The contribution to the highest flexibility of the ACS observed in IUG^{Met} was due to the 5'-end of the tRNA (residues 1–7) rather than the 3'-end residues, which had comparable RMSFs to GUG (Figure B.12). In contrast, GUG^{Met} had the most flexible 3'-terminal adenosine (3.84(1.5) Å) of any systems (GUG: 3.00(0.6), IUG: 3.55(1.2), and IUG^{Met}: 2.38(0.4) Å), suggesting that the aminoacylated terminal nucleoside is not effectively held in place by domain II of EF-Tu. While after GTP hydrolysis the aa-tRNA dissociates from EF-TU:GDP, [32] strong aa-tRNA:EF-Tu interactions are meant to be maintained during codon recognition and GTPase activation. [33, 34] In the proper progression of mRNA decoding, dissociation of domain 2 of EF-Tu from the CCA tail of aa-tRNA occurs after GTPase activation and irreversible GTP hydrolysis or after Pi release. [35, 36] Therefore, the near-cognate aa-tRNA encountering a GUG codon may lead to faulty interactions between EF-Tu and the aa-tRNA. Overall, the RMSF results show that flexibility of the tRNA is increased for both near-cognate systems with respect to GUG with similar behavior to IUG. The localized flexibility increases in the ribosome-contacting regions (ACS and ASL) suggest that A-site binding is destabilization for the GUG^{Met} and IUG^{Met} systems is comparable to IUG.

In the eRMSD cluster analysis, GUG^{Met} and IUG^{Met} both displayed significantly decreased occupancies of the stacked state (GUG^{Met}: 33%; IUG^{Met}: 26%; Figure 3.17A-B) compared to GUG (100%) and were slightly decreased with respect to IUG (41%). The wobble conformation was occupied for a larger percent of the quadruplicate ensemble for IUG^{Met} (49%) than GUG^{Met} (23%), with IUG in the middle (37%). Lastly, the rejected state was sampled for just under half the total simulation time in GUG^{Met} (45%), but was slightly lower in IUG^{Met} (25%), which marginally exceeded the occupancy in IUG (22%).

The analysis of aa-tRNA structural dynamics revealed several unique features for the near-cognate systems. Although the θ angle distribution was broader for GUG^{Met} and shifted to lower values for IUG^{Met}, the θ metric could not distinguish between the bent and straight conformations when the ASL remained near the codon. In contrast, both the Δ^{ACS} and ASL-elbow distances indicated tRNA straightening for near-cognate GUG^{Met} and IUG^{Met}, with broader distributions and a higher frequencies of large values. The near-cognate tRNAs, like IUG, also exhibited increased flexibility in the ASL and ACS relative to the unmodified systems. Rejected conformations were common in GUG^{Met} (45%) and IUG^{Met} (25%), which was comparable to IUG (22%). For GUG^{Met} and IUG^{Met}, these findings indicate increased instability in the codon-anticodon minihelix and loss of the tRNA bent conformation, for GUG^{Met} and IUG^{Met}, without tRNA dissociation from the codon. While for IUG, tRNA was rejected outright due to overtly compromised G530 and A1492–3 monitoring, the near-cognate tRNAs exhibited a relatively minor perturbation to monitoring and solvent shielding was enhanced. These results suggest that the near-cognate tRNAs were less prone to immediate ribosomal rejection than IUG.

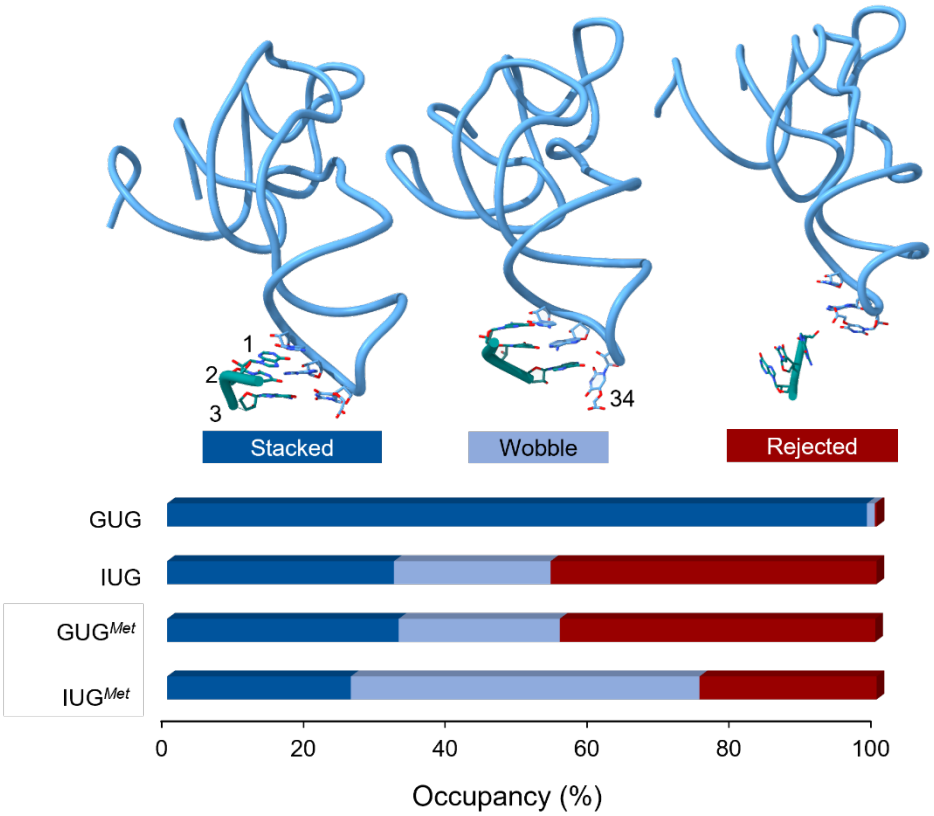

Figure 3.17. Representative conformations obtained by principal component analysis (PCA) of eRMSD and clustering over the MD simulations on ribosome subsystems containing cognate and near-cognate tRNAs. (A) Conformations sampled during simulations. (B) Occupancies of each conformation for each system.

3.3 Conclusions

The MD simulations presented in this chapter offer insight into the structural and dynamical consequences of inosine incorporation within mRNA codons during translation. Specifically, the simulations demonstrated structural dynamics conducive to productive tRNA selection for the GUG, CGU, CIU, and GUI codons. This compatibility stems from three key structural features: (1) active engagement of the ribosomal monitoring nucleotides A1492 and A1493, and partial to full G530 engagement, (2) stability of the minihelix formed between the tRNA anticodon and mRNA codon, and (3) ribosome-mediated suppression of the tRNA ASL and acceptor stem dynamics coupled with preservation of the bent conformation of A-site tRNA. Each of these features cumulatively suggest efficient codon recognition and that inosine

modifications at B2 or B3 do not impair codon recognition. In contrast, the presence of inosine in the first position of the mRNA codon (IUG) results in significant structural deviations that likely compromise decoding efficiency. The most striking features observed in the simulations include increased flexibility and distortion of the minihelix, premature straightening of the tRNA, and disengagement of ribosomal monitoring nucleotides. The monitoring adenines A1492 and A1493, which normally facilitate correct codon-anticodon recognition, exhibit a higher propensity for the 'off-off' conformation in IUG, significantly reducing their ability to monitor base pairing, while G530 fails to engage in a stable latched conformation and completely disengages for nearly half of the sampled simulation time (45%). These alterations collectively contribute to rapid tRNA rejection in the presence of the IUG codon. The simulations therefore provide a molecular rationale for the differences observed in elongation rates for inosine-modified mRNAs, where IUG had a greater-than 8-fold reduction in rates of peptide bond formation compared to GUG, but second and third position inosines had negligible impacts.[15]

The GUG^{Met} simulations revealed how the first position G:U mismatch may impair productive tRNA selection for GUG^{Met} relative to GUG. A1492–3 and G530 monitoring was suppressed in the presence of the mismatch, geometric distortions were induced in the minihelix at all three base pairs, and the tRNA exhibited significant premature straightening. However, GUG^{Met} impairment of selection appeared less severe than for IUG. A1492–3 occupied disengaged states for only 5% of the time during simulations, while G530 alternated between engaged and perturbed states, including a fully-latched G530 conformation ("pseudo on") despite minihelix distortion. Solvent shielding of the minor groove was increased compared to both IUG and GUG, suggesting the ribosome may not immediately reject the near-cognate tRNA, like for IUG. Nevertheless, the tRNA exhibited premature straightening and high flexibility, indicating that GUG^{Met} may be able to undergo successful codon recognition, but minihelix

distortions and tRNA misalignment recognition may compound to trigger rejection during later steps (GTPase activation or proofreading). The first position modified pair (I:U) in IUG^{Met} restored A1492–3 engagement, suppressed G530 disengagement, and enhanced solvent shielding relative to IUG, indicating that the ribosome tolerated inosine in the first codon position better with near-cognate tRNA. However, the minihelix remained geometrically perturbed despite the codon remaining close to the anticodon, similar to GUG^{Met}. IUG^{Met} also induced premature tRNA straightening and flexibility, suggesting that both the I:U and G:U pairs may lead to rejection during GTPase activation or proofreading, which is consistent with the reduced observed rate constants of amino acid addition measured by the Koutmou lab.[15]

The simulations and analysis performed in this chapter enhance our mechanistic understanding of how inosine mRNA modifications influence decoding at the atomistic level. Depending on the position of inosine in the mRNA codon and the complementarity of the anticodon, molecular mechanisms during initial selection can be drastically altered. Overall, the insights gained from this chapter enhance our mechanistic understanding of how inosine mRNA modifications influence translation at the atomistic level. The results provide a foundation for future investigations into the broader regulatory consequences of inosine or other mRNA modifications.

3.4 References

(1) Keegan, L. P.; Hajji, K.; O'Connell, M. A. Adenosine Deaminase Acting on RNA (ADAR) Enzymes: A Journey from Weird to Wondrous. *Acc. Chem. Res.* **2023**, *56* (22), 3165-3174. DOI: 10.1021/acs.accounts.3c00433.

(2) Nishikura, K. A-to-I editing of coding and non-coding RNAs by ADARs. *Nat. Rev. Mol. Cell Biol.* **2016**, *17* (2), 83-96. DOI: 10.1038/nrm.2015.4.

(3) Mendoza, H. G.; Beal, P. A. Structural and functional effects of inosine modification in mRNA. *RNA* **2024**, *30* (5), 512-520. DOI: 10.1261/rna.079977.124.

(4) Hosaka, T.; Tsuji, H.; Kwak, S. RNA Editing: A New Therapeutic Target in Amyotrophic Lateral Sclerosis and Other Neurological Diseases. *Int. J. Mol. Sci.* **2021**, *22* (20), 10958.

(5) Singh, M. Dysregulated A to I RNA editing and non-coding RNAs in neurodegeneration. *Front. Genet.* **2013**, *3*, 326.

(6) Costa Cruz, P. H.; Kawahara, Y. RNA editing in neurological and neurodegenerative disorders. *REMP* **2021**, 309-330.

(7) Zhu, X.; Zhang, Y.; Yang, X.; Hao, C.; Duan, H. Gene therapy for neurodegenerative disease: clinical potential and directions. *Front. Mol. Neurosci.* **2021**, *14*, 618171.

(8) Chan, T. H. M.; Lin, C. H.; Qi, L.; Fei, J.; Li, Y.; Yong, K. J.; Liu, M.; Song, Y.; Chow, R. K. K.; Ng, V. H. E. A disrupted RNA editing balance mediated by ADARs (Adenosine DeAminases that act on RNA) in human hepatocellular carcinoma. *Gut* **2014**, *63* (5), 832-843.

(9) Qin, Y.-R.; Qiao, J.-J.; Chan, T. H. M.; Zhu, Y.-H.; Li, F.-F.; Liu, H.; Fei, J.; Li, Y.; Guan, X.-Y.; Chen, L. Adenosine-to-inosine RNA editing mediated by ADARs in esophageal squamous cell carcinoma. *Cancer Res.* **2014**, *74* (3), 840-851.

(10) Chan, T. H.; Qamra, A.; Tan, K. T.; Guo, J.; Yang, H.; Qi, L.; Lin, J. S.; Ng, V. H.; Song, Y.; Hong, H.; et al. ADAR-Mediated RNA Editing Predicts Progression and Prognosis of Gastric Cancer. *Gastroenterology* **2016**, *151* (4), 637-650.e610. DOI: 10.1053/j.gastro.2016.06.043.

(11) Giraulo, C.; De Palma, G.; Plaitano, P.; Cicala, C.; Morello, S. Insight into adenosine pathway in psoriasis: Elucidating its role and the potential therapeutical applications. *Life Sci.* **2024**, *357*, 123071. DOI: https://doi.org/10.1016/j.lfs.2024.123071.

(12) Guo, X.; Wiley, C. A.; Steinman, R. A.; Sheng, Y.; Ji, B.; Wang, J.; Zhang, L.; Wang, T.; Zenatai, M.; Billiar, T. R.; et al. Aicardi-Goutières syndrome-associated mutation at ADAR1 gene locus activates innate immune response in mouse brain. *J. Neuroinflammation* **2021**, *18* (1), 169. DOI: 10.1186/s12974-021-02217-9.

(13) Licht, K.; Hartl, M.; Amman, F.; Anrather, D.; Janisiw, M. P.; Jantsch, M. F. Inosine induces context-dependent recoding and translational stalling. *Nucleic Acids Res.* **2019**, *47* (1), 3-14. DOI: 10.1093/nar/gky1163.

(14) Hoernes, T. P.; Faserl, K.; Juen, M. A.; Kremser, J.; Gasser, C.; Fuchs, E.; Shi, X.; Siewert, A.; Lindner, H.; Kreutz, C.; et al. Translation of non-standard codon nucleotides reveals minimal requirements for codon-anticodon interactions. *Nat. Commun.* **2018**, *9* (1), 4865. DOI: 10.1038/s41467-018-07321-8.

(15) Koutmou, K.; Giles, R. Private Communication. 2025.

(16) Monroe, J.; Eyler, D. E.; Mitchell, L.; Deb, I.; Bojanowski, A.; Srinivas, P.; Dunham, C. M.; Roy, B.; Frank, A. T.; Koutmou, K. S. N1-Methylpseudouridine and pseudouridine modifications modulate mRNA decoding during translation. *Nat. Commun.* **2024**, *15* (1), 8119. DOI: 10.1038/s41467-024-51301-0.

(17) Ieong, K.-W.; Indrisiunaite, G.; Prabhakar, A.; Puglisi, J. D.; Ehrenberg, M. N6-Methyladenosines in mRNAs reduce the accuracy of codon reading by transfer RNAs and peptide release factors. *Nucleic Acids Res.* **2021**, *49* (5), 2684-2699. DOI: 10.1093/nar/gkab033.

(18) Blanchet, S.; Cornu, D.; Hatin, I.; Grosjean, H.; Bertin, P.; Namy, O. Deciphering the reading of the genetic code by near-cognate tRNA. *Proc. Natl. Acad. Sci. U.S.A.* **2018**, *115* (12), 3018-3023. DOI: doi:10.1073/pnas.1715578115.

(19) Satpati, P.; Sund, J.; Åqvist, J. Structure-Based Energetics of mRNA Decoding on the Ribosome. *Biochem.* **2014**, *53* (10), 1714-1722. DOI: 10.1021/bi5000355.

(20) Kondo, J.; Urzhumtsev, A.; Westhof, E. Two conformational states in the crystal structure of the Homo sapiens cytoplasmic ribosomal decoding A site. *Nucleic Acids Res.* **2006**, *34* (2), 676-685. DOI: 10.1093/nar/gkj467 (acccessed 1/3/2025).

(21) Zeng, X.; Chugh, J.; Casiano-Negroni, A.; Al-Hashimi, H. M.; Brooks, C. L., 3rd. Flipping of the ribosomal A-site adenines provides a basis for tRNA selection. *J Mol Biol* **2014**, *426* (19), 3201-3213. DOI: 10.1016/j.jmb.2014.04.029.

(22) Brodersen, D. E.; Clemons, W. M.; Carter, A. P.; Morgan-Warren, R. J.; Wimberly, B. T.; Ramakrishnan, V. The Structural Basis for the Action of the Antibiotics Tetracycline, Pactamycin, and Hygromycin B on the 30S Ribosomal Subunit. *Cell* **2000**, *103* (7), 1143-1154. DOI: 10.1016/s0092-8674(00)00216-6.

(23) Petry, S.; Brodersen, D. E.; Murphy, F. V.; Dunham, C. M.; Selmer, M.; Tarry, M. J.; Kelley, A. C.; Ramakrishnan, V. Crystal Structures of the Ribosome in Complex with Release Factors RF1 and RF2 Bound to a Cognate Stop Codon. *Cell* **2005**, *123* (7), 1255-1266. DOI: 10.1016/j.cell.2005.09.039.

(24) Wimberly, B. T.; Brodersen, D. E.; Clemons, W. M.; Morgan-Warren, R. J.; Carter, A. P.; Vonrhein, C.; Hartsch, T.; Ramakrishnan, V. Structure of the 30S ribosomal subunit. *Nature* **2000**, *407* (6802), 327-339. DOI: 10.1038/35030006.

(25) Fislage, M.; Zhang, J.; Brown, Z. P.; Mandava, C. S.; Sanyal, S.; Ehrenberg, M.; Frank, J. Cryo-EM shows stages of initial codon selection on the ribosome by aa-tRNA in ternary complex with GTP and the GTPase-deficient EF-TuH84A. *Nucleic Acids Res* **2018**, *46* (11), 5861-5874. DOI: 10.1093/nar/gky346.

(26) Loveland, A. B.; Demo, G.; Grigorieff, N.; Korostelev, A. A. Ensemble cryo-EM elucidates the mechanism of translation fidelity. *Nature* **2017**, *546* (7656), 113-117. DOI: 10.1038/nature22397.

(27) Agris, P. F.; Eruysal, E. R.; Narendran, A.; Väre, V. Y. P.; Vangaveti, S.; Ranganathan, S. V. Celebrating wobble decoding: Half a century and still much is new. *RNA Biology* **2018**, *15* (4-5), 537-553. DOI: 10.1080/15476286.2017.1356562.

(28) Rozov, A.; Westhof, E.; Yusupov, M.; Yusupova, G. The ribosome prohibits the G•U wobble geometry at the first position of the codon–anticodon helix. *Nucleic Acids Res.* **2016**, gkw431. DOI: 10.1093/nar/gkw431.

(29) Pape, T.; Wintermeyer, W.; Rodnina, M. Induced-fit in initial selection and proofreading of aminoacyl-tRNA on the ribosome. *EMJO J.* **1999**, *18* (13), 3800-3807. DOI: 10.1093/emboj/18.13.3800.

(30) Girodat, D.; Wieden, H. J.; Blanchard, S. C.; Sanbonmatsu, K. Y. Geometric alignment of aminoacyl-tRNA relative to catalytic centers of the ribosome underpins accurate mRNA decoding. *Nat. Commun.* **2023**, *14* (1), 5582. DOI: 10.1038/s41467-023-40404-9.

(31) Fislage, M.; Zhang, J.; Brown, Z. P.; Mandava, C. S.; Sanyal, S.; Ehrenberg, M.; Frank, J. Cryo-EM shows stages of initial codon selection on the ribosome by aa-tRNA in ternary complex with GTP and the GTPase-deficient EF-TuH84A. *Nucleic Acids Res.* **2018**, *46* (11), 5861-5874. DOI: 10.1093/nar/gky346.

(32) Warias, M.; Grubmüller, H.; Bock, L. V. tRNA Dissociation from EF-Tu after GTP Hydrolysis: Primary Steps and Antibiotic Inhibition. *Biophys. J.* **2020**, *118* (1), 151-161. DOI: https://doi.org/10.1016/j.bpj.2019.10.028.

(33) Ott, G.; Schiesswohl, M.; Kiesewetter, S.; Förster, C.; Arnold, L.; Erdmann, V. A.; Sprinzl, M. Ternary complexes of Escherichia coli aminoacyl-tRNAs with the elongation factor Tu and GTP: Thermodynamic and structural studies. *Biochimica et Biophysica Acta (BBA) - Gene Structure and Expression* **1990**, *1050* (1), 222-225. DOI: https://doi.org/10.1016/0167-4781(90)90170-7.

(34) Nissen, P.; Kjeldgaard, M.; Thirup, S.; Polekhina, G.; Reshetnikova, L.; Clark, B. F. C.; Nyborg, J. Crystal Structure of the Ternary Complex of Phe-tRNA^{Phe}, EF-Tu, and a GTP Analog. *Science* **1995**, *270* (5241), 1464-1472. DOI: doi:10.1126/science.270.5241.1464.

(35) Yang, H.; Perrier, J.; Whitford, P. C. Disorder guides domain rearrangement in elongation factor Tu. *PSFB* **2018**, *86* (10), 1037-1046. DOI: https://doi.org/10.1002/prot.25575.

(36) Loveland, A. B.; Demo, G.; Korostelev, A. A. Cryo-EM of elongating ribosome with EF-Tu•GTP elucidates tRNA proofreading. *Nature* **2020**, *584* (7822), 640-645. DOI: 10.1038/s41586-020-2447-x.

CHAPTER 4: METHYLGUANOSINE DAMAGE TO mRNA CODONS MODULATES THE STRUCTURAL DYNAMICS OF RIBOSOMAL DECODING

4.1 Objectives

As discussed in Section 1.3.3.2, mRNA is susceptible to chemical damage from UV light, reactive oxygen species (ROS), and alkylating agents.[1-8] The integrity of the cellular proteome relies on preserving accurate mRNA translation, and ribosomal surveillance mechanisms such as NGD (no go decay; occurring in eukaryotes only) or *trans* translation (prokaryotes) are activated when the ribosome encounters defective mRNA transcripts.[3, 9] The activation of degradation indicates that mRNA damage can have severe deleterious impacts on translation, such as ribosome stalling or miscoding, if left unchecked.[5, 8, 10, 11]

The recently identified alkylation-induced lesions, m^1G and m^2G, were found to impact the efficiency of dipeptide formation differentially depending on their position in the mRNA codon. [12, 13] Specifically, m^1G abolishes peptide bond formation when present in the first and second codon positions, but has a negligible impact when present in the third position.[14] In contrast, m^2G slows peptide bond formation moderately when present in the first (~2-fold decrease in k_{obs}) and second (~1.6-fold) positions, but causes drastic slowing when in the third (>2100-fold) position. [14] To induce these effects, m^1G and m^2G (among other damage modifications) are hypothesized to influence codon-anticodon interactions or ribosomal monitoring in the A-site.[1-3, 7, 12, 13, 15] However, due to the lack of structural characterization, the influence of damaged mRNA on ribosomal dynamics during codon recognition are not currently known.

MD simulations provide a powerful tool for investigating the structural and functional consequences of mRNA modifications at atomic resolution. This chapter aims to rationalize the experimental results and clarify the molecular consequences of m^1G and m^2G incorporation into the A-site codon using MD simulations of A-site ribosome subsystem models.

4.2 Results and discussion

4.2.1 MD simulations of systems containing m^1G codon modifications

This section investigates the impacts of the m^1G modification on ribosomal decoding. As discussed in Chapter 1, the m^1G modification is situated such that it directly interferes with the central G:C hydrogen bond formed between the hydrogen bond donor N1–H1 of G and the acceptor N3 of C. For the first and second position modified codons, m^1GUG and Cm^1GU, it has been proposed that the compromised hydrogen-bonding interactions substantially impaired elongation, whereas the relative flexibility afforded to wobble base pairs accounts for the negligible impact for GUm^1G.[12, 13] While hydrogen-bonding may play a role, these explanations ignore other mechanistically-important details such whether or not m^1G impacts ribosomal monitoring, codon-anticodon geometry, or tRNA dynamics. The MD simulations performed in this section seek to uncover these context-dependent effects on these mechanistic details.

4.2.1.1 Simulations of A-site ribosome codon systems containing m^1G codon modifications converge within 1 microsecond

Backbone RMSD of the unrestrained region for each ribosome subsystem was calculated to evaluate global convergence over the MD simulations. The RMSD time series for the m^1G systems converged to stable average values within 500 ns for all replicas of Cm^1GU and GUm^1G, and for replicas 1, 3, and 4 of m^1GUG (Figure C.1A). For replica 2 of m^1GUG, the RMSD converged after ~100 ns and remained stable for ~775 ns before rapidly increasing during the final ~125 ns (Figure C.1A). The increase in RMSD was confirmed to result from a rotation of EF-Tu relative to the tRNA (Figure C.1C) rather than any large-scale structural distortions in the rRNA or ribosomal proteins that would reflect unrealistic deviation from the starting experimental structure. The RMSD of the tRNA backbone relative to the experimental starting structure for replica 2 of m^1GUG converged within 500 ns (Figure C.1B). The tRNA backbone

RMSDs converged within 500 ns for nearly all replicas across all models, with the RMSDs of replica 4 of m^1GUG and Cm^1GU converging within 750 ns (Figure C.1B).

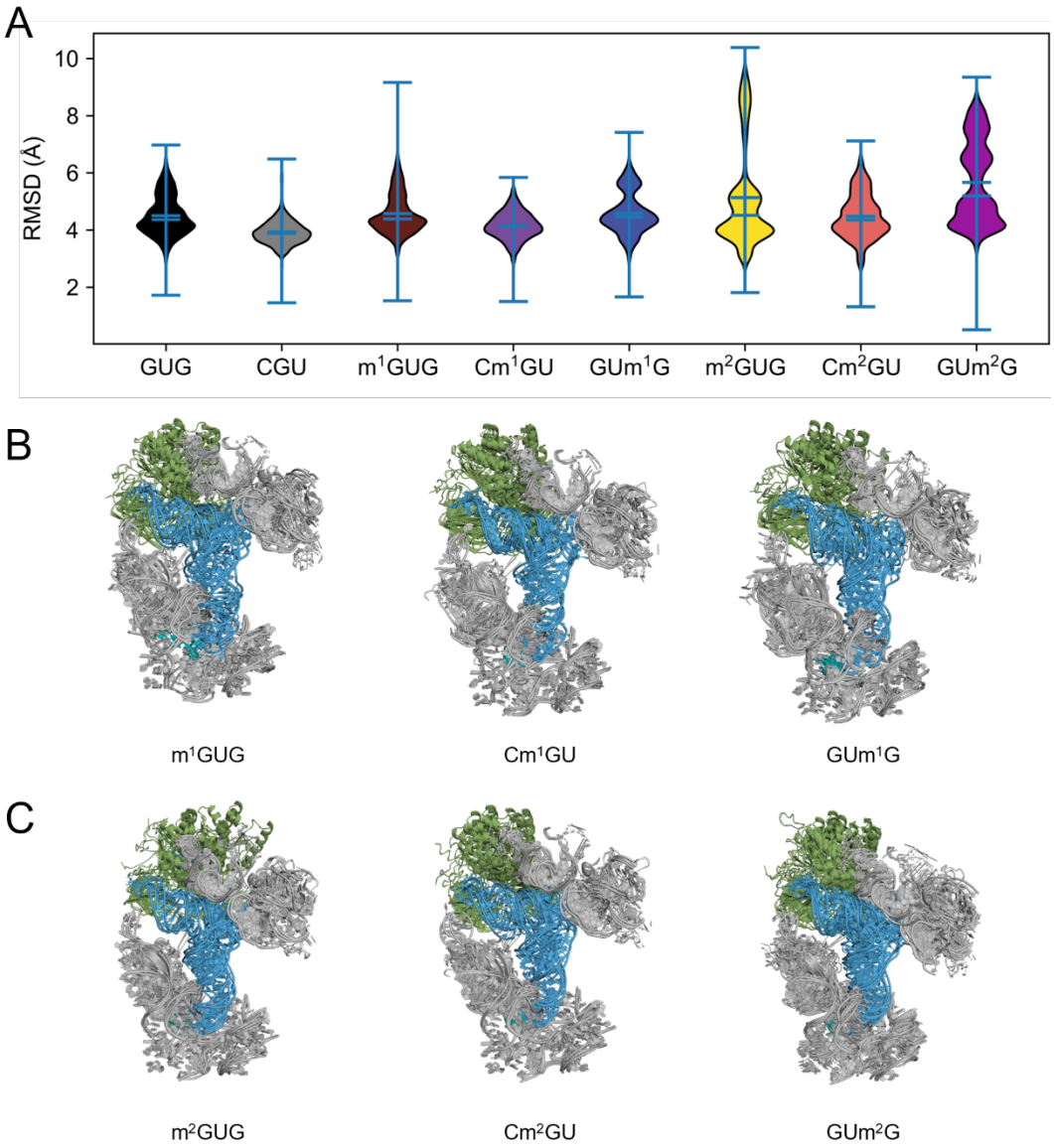

Figure 4.1. Structural convergence of MD simulations of the ribosomal A-site subsystem model with m^1G and m^2G modifications. (A) Violin plot of the backbone RMSD distributions with respect to the starting structures for m^1G and m^2G-modified compared to unmodified systems. (B-C) Overlays of the last frame of each replica simulation for each model.

For each m^1G system, there was substantial overlap in the distributions of backbone RMSD for the unrestrained regions (Figure 4.1A). The CVs confirmed high consistency (<4% difference) between GUG (0.158), m^1GUG (0.162), and GUm^1G (0.164), and identical values to

the third decimal place for CGU (0.121) and Cm^{1}GU (0.121) (Table C.1). The representative structures of each replica for each m^{1}G model showed that the tertiary folds of the unrestrained system were maintained in the simulations (Figure 4.1B). The CVs for the backbone RMSD distributions of the tRNAs increased for the first (33% difference) and second (62%) position m^{1}G modifications compared to the corresponding unmodified systems. However, for GUm^{1}G, the CV for the tRNA backbone RMSD decreased by 7% relative to GUG. Moreover, while the ensemble-averaged tRNA RMSD was higher for m^{1}GUG and Cm^{1}GU (4.01(0.7) and 3.17(0.8) Å, respectively) than for GUG and CGU (3.52(0.5) and 3.05(0.4) Å), it was lower for GUm^{1}G (3.00(0.4) Å). The backbone RMSDs of the unrestrained region suggest that m^{1}G modifications do not significantly affect fluctuation of the global structure, but there is an increase in the tRNA fluctuations for first, second, but not third, position m^{1}G codon modifications.

4.2.1.2 16S rRNA monitoring is impacted for m^{1}G modified codons

Within individual replica simulations for codons containing m^{1}G, the A1492–3 monitoring angles (Φ) closely overlapped throughout the simulations, indicating strongly synchronized behaviour and shared metastable states (Figure 4.2). Within each replica for the m^{1}G simulations, metastable Φ states had similar dwell times and transitions between states for A1492 and A1493 occurred concurrently (Figure 4.2). To quantify the degree of correlation between the A1492–3 Φ angles, the average linear correlation coefficient (r_c) was computed for each system (Table C.3; see Chapter 2 for full computational details). For all systems, r_c was greater than 0 (Table C.3), indicating a positive correlation between the Φ of A1492 and A1493 (i.e., the angles concurrently increase or decrease). The r_c was consistently greater than or approximately equal to 0.8 across all replicas for m^{1}GUG, GUm^{1}G, and Cm^{1}GU, suggesting strong coupling of A1492–3 motions and consistency across the ensemble. Interestingly, the ensemble-averaged r_c values were higher in the m^{1}G-modified systems (m^{1}GUG: 0.91(0.05), Cm^{1}GU

0.89(0.07), and GUm^{1}G 0.89(0.05)) than the unmodified systems (GUG: 0.68(0.17) and CGU: 0.84(0.15)).

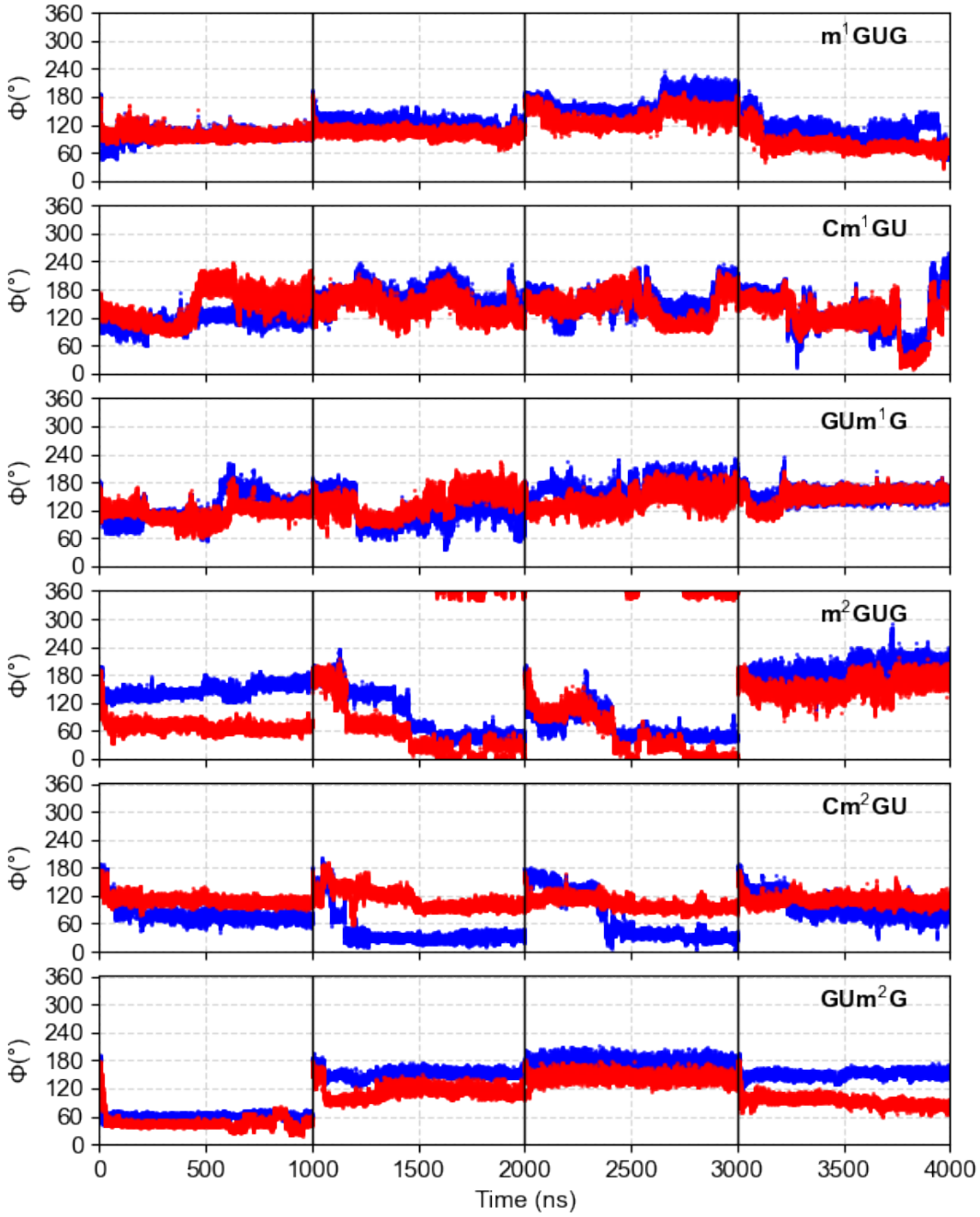

Figure 4.2. Motions of the A1492–3 residues of ribosome subsystem models containing m^{1}G or m^{2}G codon modifications during MD simulations as a function of time. Each of the four replica trajectories are enclosed by black lines. The blue and red colored lines represent the monitoring angle of A1492 and A1493, respectively. The graphs for GUG and CGU can be found in Figure 3.5.

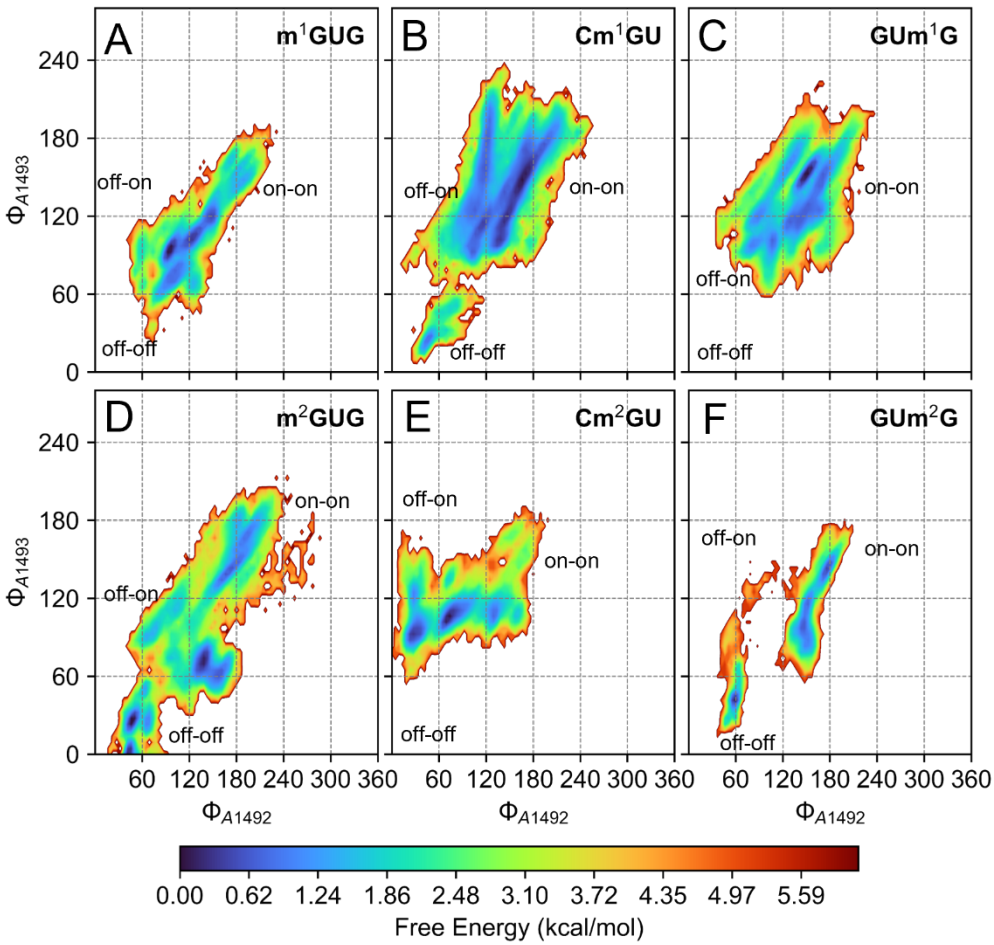

Figure 4.3. 2D Free energy landscapes (FEL) as a function of the monitoring angles (Φ) over MD simulations of ribosomal subsystems containing m^1G or m^2G codon modifications. (A-F) FELs for quadruplicate ensemble MD simulations of each codon system. The color bar at the bottom indicates the free energy scale used in the FELs (refer to Chapter 2 for full details about the generation of the FEL plots).

While the time-resolved analysis of A1492–3 captures the difference in monitoring base dynamics, it does not reveal how m^1G affected the relative energetic preferences of conformational states. Time-independent FELs were constructed to examine the distribution of A1492–3 conformations and their energetic preferences across the quadruplicate ensembles (Figure 4.3A–F). For the m^1G-modified systems, the strong correlation between A1492–3 led to the majority of measured monitoring angles to cluster along the $\Phi_{A1492} = \Phi_{A1493}$ diagonal. For m^1GUG, occupancy of the on-on (23%; Figure 4.3A) state was reduced significantly compared to

GUG (62%). Cm^{1}GU increased the on-on state occupancy relative to CGU (60% vs. 33%), while rarely sampling the off-off state (2%). The GUm^{1}G system adopted the on-on state for a similar percent occupancy (62%) to GUG (61%), but did not significantly sample the off-on state (0.1%).

Given that both first and second position m^{1}G modifications entirely abolished elongation based on kinetics experiments, impaired A1492–3 monitoring was anticipated. However, the off-off state was not sampled in m^{1}GUG, and was minimally observed for Cm^{1}GU (2%). While m^{1}GUG did lead to a significant reduction in the on-on state occupancy compared to GUG, Cm^{1}GU unexpectedly increased the on-on state occupancy (60%) relative to CGU (33%). In conjunction with the strong correlated motions between A1492–3 observed for first, second, and third position m^{1}G modified codons, these results alone do not suggest significantly impaired A1492–3 monitoring.

As discussed in Section 3.2.1.2, the Φ angles provide an indirect measure of A1492–3 monitoring by describing solely the intramolecular orientation of the monitoring residues with respect to the 16S rRNA. This measurement may be misleading in cases where A1492–3 adopt monitoring-like conformations relative to the 16S rRNA, but do not meaningfully engage with the codon-anticodon minor groove. Therefore, metrics to assess how A1492–3 interacts with the codon-anticodon minor groove were sought for a more comprehensive appreciation of the effects of m^{1}G on A1492–3 monitoring. To further analyze how the m^{1}G modification affects A1492–3 monitoring of the codon-anticodon minihelix, minor groove distances (MGDs) between A1492 and B2:B35, and between A1493 and B1:B36, were computed (Figure 4.4). The MGD distributions for A1492 and A1493 were broader for m^{1}GUG and Cm^{1}GU compared to the unmodified systems (Figure 4.4).

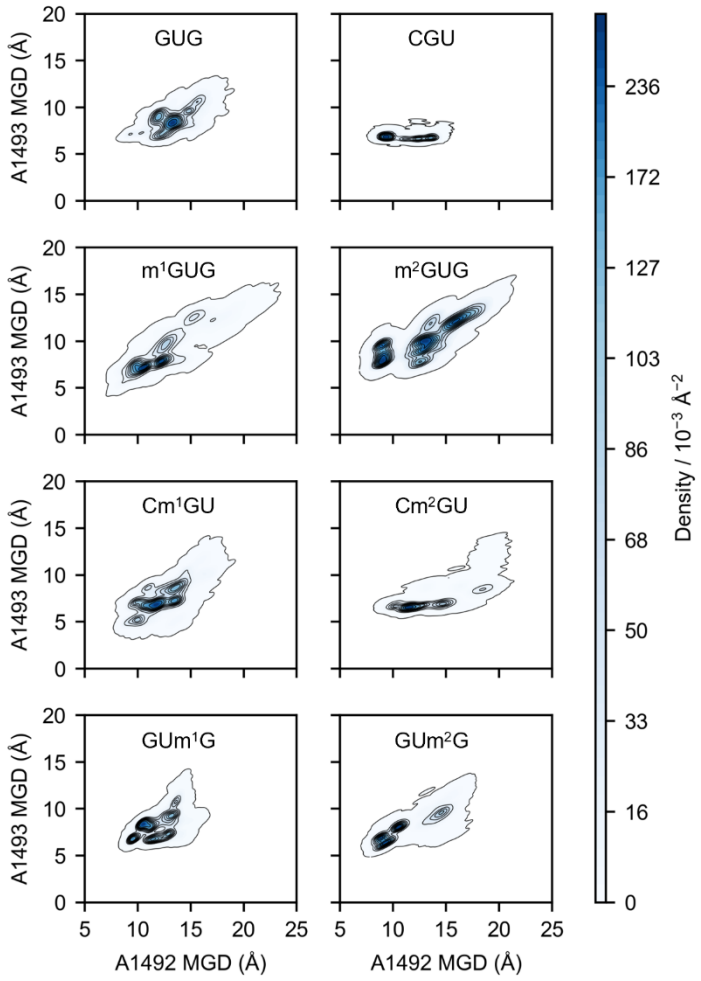

Figure 4.4. 2D Kernel density estimate (KDE) distribution of the A1492–3 minor groove distances (MGDs) for ribosomal subsystems containing unmodified codons, m^1G, or m^2G codon modifications. The MGDs are defined as the distance between center of mass (COM) of the A1492 or A1493 nucleotide from the COM of the B2:B35 or B1:B36 base pair nucleotides, respectively. Darker blue regions represent higher occupation probabilities over each simulation ensemble and black contours show increments of ~1/15 of the estimated probability density range.

For m^1GUG, the highest density MGD contours remained concentrated within the same range observed for GUG (~7.5–12.5 Å for A1492 and ~5–12.5 Å for A1493; Figure 4.4). In contrast, the low- to mid-density contours for m^1GUG extended toward higher values (>17.5 Å for A1492 and >12.5 Å for A1493; Figure 4.4) relative to GUG, confirming that A1492–3 disengaged from the minihelix minor groove for m^1GUG despite not adopting the off-off state. For Cm^1GU, the highest density contours for A1493 were notably broader, spanning ~7.5–10 Å, in contrast to the narrow peak at ~7.5 Å for CGU (Figure 4.4). Cm^1GU also extended the low- to

mid-density contours toward higher MGDs relative to CGU, suggesting increased sampling of A1492–3 disengaged states by A1492–3 (Figure 4.4). In contrast, the MGD distribution for GUm^{1}G closely matched that of GUG, with no appreciable broadening or extension towards higher values observed across any contour level (Figure 4.4). The MGD broadening suggests increased disengagement of A1492–3 from the minihelix minor groove for m^{1}GUG and Cm^{1}GU, but maintained engagement for GUm^{1}G. These findings imply that despite A1492–3 residues primarily adopting on-on states for all m^{1}G-modified systems, both residues disengaged from the minihelix minor groove more frequently for m^{1}GUG and Cm^{1}GU, but not for GUm^{1}G.

While A1492–3 monitoring is crucial during codon recognition, G530 latching is required for SSU domain closure to occur and permit GTP hydrolysis. [16] To examine how m^{1}G-modified codons influence G530 latching, the conformations G530 adopted during the trajectory ensembles were determined using cluster analysis (see Chapter 2 for computational details). For all m^{1}G-modified codon systems, G530 sampled three conformations, including the “on”, “semi-on”, “pseudo semi-on”, and “off” states (as defined in Chapter 3). The m^{1}GUG system exhibited both the pseudo semi-on (64% occupancy; Figure 4.5A) and the off (36%) states. In the m^{1}GUG semi-on conformation, the codon base B1 intercalated between the anticodon bases B36 and B37, and G530 was positioned in the minor groove between a shifted B2:B34 base pair below B36 (Figure 4.5A). For Cm^{1}GU, both the pseudo semi-on (82%) and off (7%) conformations were observed (Figure 4.5B), where the pseudo semi-on conformation for Cm^{1}GU also exhibited a perturbed minihelix structure (Figure 4.5B). In the Cm^{1}GU pseudo semi-on state, the B2 nucleobase intercalates with the B1:B36 base pair and B35 of the anticodon due to the steric bulk of the methyl group at the WCF binding face (Figure 4.5B). For GUm^{1}G, G530 remained engaged for 100% of the simulation time across the quadruplicate ensemble, occupying the on (83%) and semi-on (17%; Figure 4.5C) states.

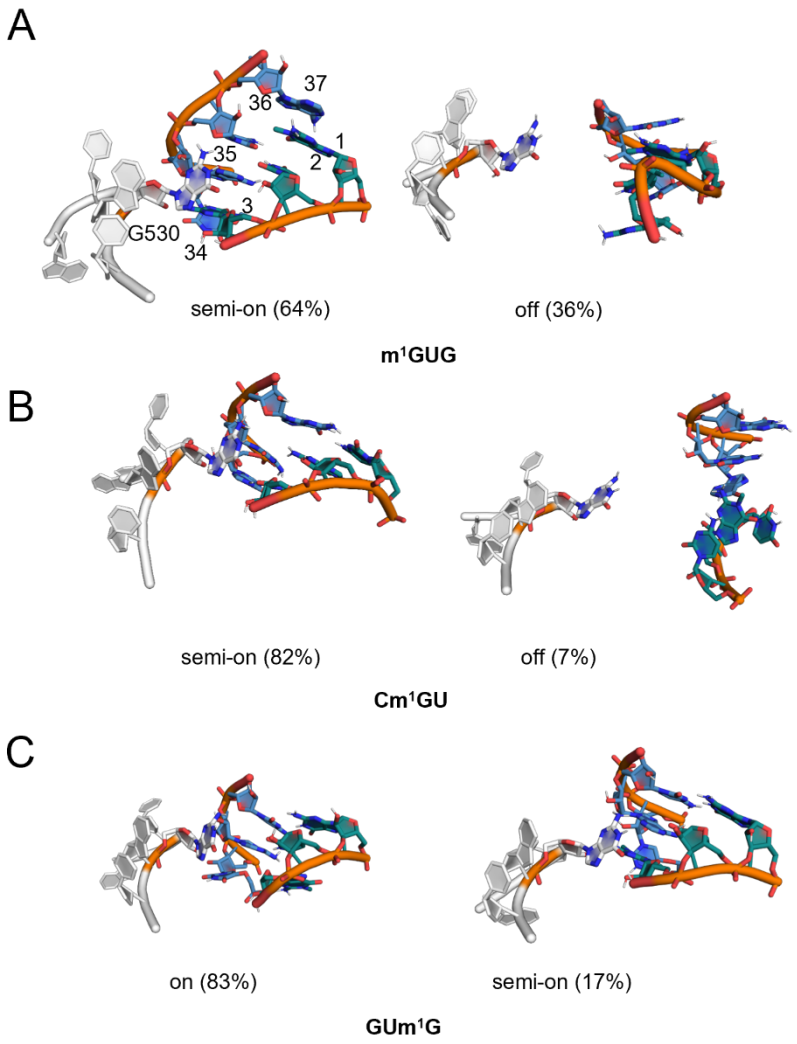

Figure 4.5. G530 conformations and occupancies during the MD simulations of ribosomal A-site models with the m^{1}G modification in the codon. (A-C) Conformation occupancies obtained by cluster analysis applied to the heavy atoms of G530, the tRNA anticodon (B34-36; colored in blue), and the A-site mRNA codon (B1-3; colored in teal) for the quadruplicate ensembles of m^{1}G-modified mRNA codon systems.

The appearance of the G530 off state for m^{1}GUG indicates that the first position m^{1}G drove significant disengagement of G530 for a substantial portion of the simulation ensemble. In addition, the pseudo semi-on state sampled for m^{1}GUG is not ideal for successful codon recognition as the codon-anticodon minihelix geometry is compromised. Similarly, for the Cm^{1}GU system, G530 also sampled the off state (7%). Although the pseudo semi-on conformation occupancy was lower (82%) than the semi-on for CGU (92%), the codon-anticodon

minihelix geometry being disrupted from the WCF geometry suggests that the second position m^1G also interferes with minor groove engagement by G530. Therefore, the simulations reveal that both first and second position m^1G promote misaligned conformations between G530 and the minihelix, thereby prohibiting codon recognition. Furthermore, the reduced engagement of the A1492–3 nucleobases suggests that all three monitoring residues actively reject the m^1GUG and Cm^1GU codons in the A-site. In contrast, the effects of the third position m^1G were less pronounced. Although G530 exhibited a moderate decrease in the on state occupancy relative to GUG (93% vs. 83%), and the appearance of the semi-on state (17%), the minihelix stayed intact. This suggests that the semi-on state exhibited by G530 for GUm^1G was a true intermediate along the G530 latching pathway and does not substantially impair codon recognition. These results indicate that m^1G modifications at the first and second codon positions disrupt G530 latching, whereas the third position modification does not. Therefore, A1492–3 and G530 exhibited a greater tendency to disengage from the cognate tRNA when m^1G was present at the first or second codon positions, but not the third.

Given the crucial combined role of all three monitoring bases in shielding the minihelix minor groove from solvent, [17, 18] these observations prompted further investigation into whether this function was compromised for m^1GUG and Cm^1GU, but preserved for GUm^1G. The ensemble-averaged number of water molecules contained within 5 Å of the minor groove for the first and second base-pairing positions was calculated for all m^1G systems (Figure 4.6**;** See Chapter 2 for calculation details).

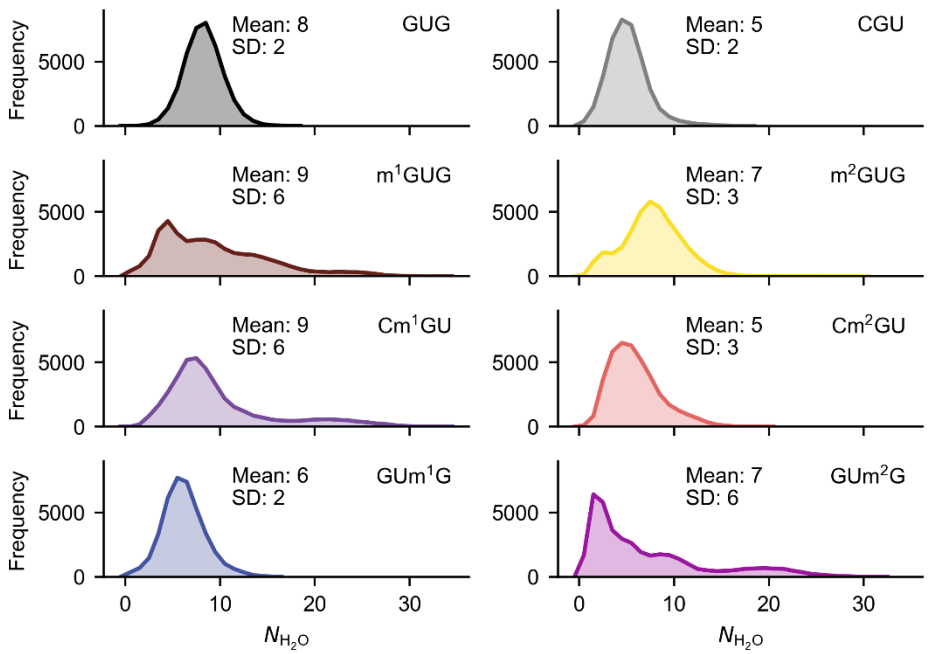

Figure 4.6. Water molecule distribution for the unmodified systems and systems containing m^{1}G or m^{2}G codon modifications. Histogram of the number of water molecules (N_{H_2O}) located within 5 Å of the minor groove for the first and second base-pairing positions of the codon-anticodon minihelix.

Compared to GUG, the water histogram distribution shifted rightward and broadened substantially for m^{1}GUG (Figure 4.6A), indicating a higher average count of waters and greater S.D. (N_{H_2O} of 10(6)) than for GUG (8(2); Table C.4). At the second position, the mean number of waters between m^{1}GUG and GUG was the same (8) but the S.D. was noticeably higher for m^{1}GUG (5 vs. 2; Table C.4). For the Cm^{1}GU system, the water histogram distribution was skewed rightward relative to CGU, indicating that a higher quantity of waters was more frequently found in the minor groove throughout the simulation ensemble (Figure 4.6). Moreover, the number of water molecules present in the minor groove region was higher for the first and second base pairs in Cm^{1}GU (10(7) and 8(5)) compared to CGU (4(2) and 9(4); Table C.4). For GUm^{1}G, there were minimal changes in the water distribution compared to GUG aside from a leftward shift (6 waters for GUm^{1}G vs. 8 waters for GUG; Figure 4.6). The increased abundance of water molecules at both the first and second positions for the m^{1}GUG and Cm^{1}GU suggests that

solvent shielding of the minor groove was reduced relative to the unmodified codon systems. In contrast, solvent shielding was enhanced for GUm^{1}G compared to GUG. Together with the increased disengagement of A1492–3 and G530 observed for m^{1}GUG and Cm^{1}GU, but not GUm^{1}G, these findings suggest that decoding center organization is selectively perturbed for the first and second position-modified systems in a manner that interferes with the monitoring base solvent shielding mechanism.

Compared to the unmodified systems, both m^{1}GUG and Cm^{1}GU systems exhibited disengagement of A1492–3, disrupted G530 latching, and increased the number of water molecules within the minor groove, indicating a reorganization of the decoding center that prevents productive codon recognition. In contrast, GUm^{1}G maintained A1492–3 and G530 engagement to reduce water accessibility in the minor groove, which collectively suggests that the initial selection pathway was not impeded. Collectively, these findings are in agreement with the Koutmou lab experiments that found abolished amino acid addition for m^{1}GUG and Cm^{1}GU, but no significant influence for GUm^{1}G, compared to unmodified systems.

4.2.1.3 Distortion of minihelix structure and tRNA misalignment induced by m^{1}G modifications

The detailed investigation of 16S rRNA monitoring revealed mechanisms through which m^{1}G modifications impact codon recognition. Monitoring is central to the productive induced-fit kinetic mechanism during tRNA selection, as it helps stabilize the codon-anticodon minihelix structure. [19] Although several representative structures from the G530 cluster analysis adopted non-WCF minihelix geometries (Figure 4.6), a systematic investigation of these geometrical perturbations was required. To assess the effects of m^{1}G on the geometric stability of the minihelix, two structural parameters were analyzed over the trajectory ensembles: the average glycosidic distances between each base pair in the minihelix and the magnitude of coplanar angles between opposing nucleobases (Figure 4.7; see Chapter 2 for detailed definitions of these

metrics). In addition, to measure the impacts of m^1G modifications on the discrete codon-anticodon interactions, the occupancies of hydrogen-bonding interactions between the WCF edges of opposing nucleobases were calculated.

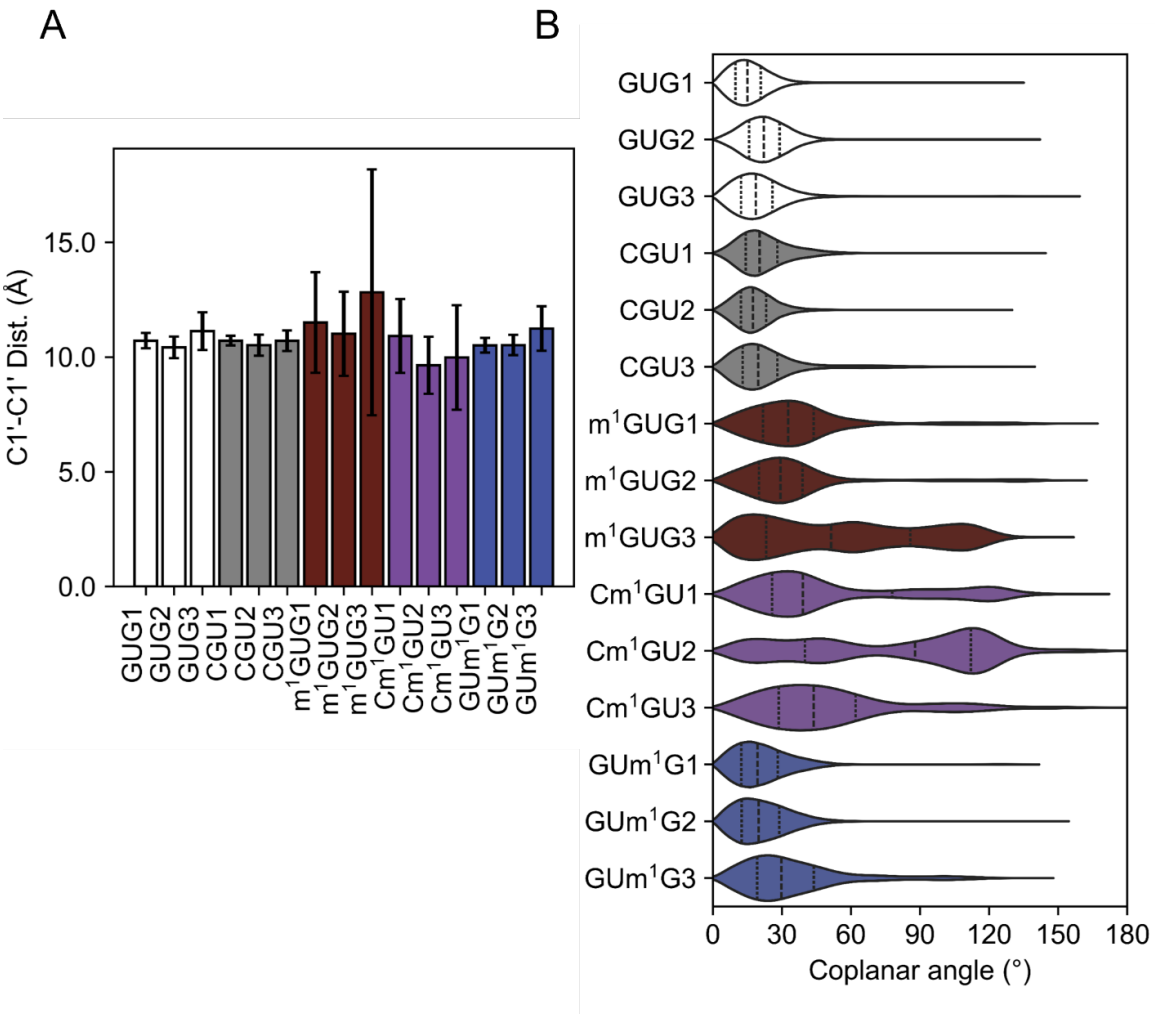

Figure 4.7. Analysis of the minihelix geometry for the m^1G modified codon-anticodon minihelix during the MD simulations. (A) Glycosidic distances between opposing nucleobases in the minihelix. (B) Interplanar angles between opposing nucleobase aromatic rings in the minihelix.

Higher standard deviations in the glycosidic distances and broad coplanar angle distributions were observed for the m^1GUG and Cm^1GU systems compared to GUG and CGU, respectively (Figure 4.7A-B). In addition, the concurrent broadening of the distributions of both structural variables for the first and second position m^1G-modified systems suggests the minihelix geometry was perturbed and the tRNA was dissociating from the mRNA (Figure 4.7A-

B). In contrast, the GUm^{1}G system was relatively unaffected compared to GUG, both exhibiting similar glycosidic distance and coplanar angle ranges (Figure 4.7A-B). The occupancies of WCF hydrogen bonds were significantly perturbed across all three base-pairing positions for m^{1}GUG, with 0% occupancy for any interactions between m^{1}G1···C36 and low occupancies of WCF interactions between the U2···A35 and G3···cmo^{5}U34 base pairs (26% and 6%, respectively; Table C.5). Hydrogen-bonding occupancies were also decreased for Cm^{1}GU in the first (29%) and third (9%) base-pairing positions, with the most severe impact on the m^{1}G2···C35 base pair (5%; Table C.5). In contrast, the first and second base pair hydrogen-bonding interactions were maintained at high occupancies (94% and 92%, respectively) for the GUm^{1}G system, with the third base pair occupancy moderately decreasing from 47% in GUG (Table C.5) to 25% in GUm^{1}G (Table C.5).

The simulation results were in agreement with the simple hypothesis proposed in the heading of Section 4.2.1, where hydrogen-bonding interaction occupancies were severely reduced or eliminated in all three base-pairing positions for m^{1}GUG and Cm^{1}GU. The glycosidic distances and coplanar angles additionally showed that the minihelix is geometrically perturbed and the codon dissociates from the anticodon for m^{1}GUG and Cm^{1}GU. The third position m^{1}G modification caused a moderate decrease in hydrogen-bonding interaction occupancy as well as slight broadening in the coplanar angle distribution for the third base pair. However, GUm^{1}G did not perturb the geometry of the first or second base pair or exhibit dissociation of the anticodon from the codon. These simulations indicate that the minihelix structure is disrupted for m^{1}GUG and Cm^{1}GU, but preserved for GUm^{1}G, which is consistent with experimental results showing impaired amino acid addition for m^{1}GUG and Cm^{1}GU, but not for GUm^{1}G.

4.2.1.4 m^1G codon modifications influence tRNA dynamics in the A-site

The alignment of the tRNA in the A-site of the ribosome was assessed by measuring the θ variable (see Chapter 2). m^1GUG exhibited a conformation in the low-θ region (0-90°) separated from a bimodal distribution in the high-θ region (90-150°; Figure 4.8A). The straight conformation exhibited by m^1GUG included a conformationally twisted state of the m^1G nucleotide in conjunction with the misaligned minihelix (Figure 4.8B). The second position m^1G modification caused a widening and leftward shift of the θ distribution relative to GUG distribution. Moreover, Cm^1GU exhibited a population with a modal peak of $\theta \sim 71°$, which corresponded to a straightened tRNA conformation (Figure 4.8A-B). The GUm^1G system exhibited a bimodal distribution in the middle-upper range of θ, but the structure maintained contact with both the mRNA and EF-Tu in the bent conformation for 100% of the simulation time (Figure 4.8B).

The Δ^{ACS} and ASL-elbow distances were measured to further confirm that straightening occurred for m^1GUG and Cm^1GU. m^1GUG favoured higher Δ^{ACS} angles and caused a significant broadening of the Δ^{ACS} distribution compared to GUG, indicating that the ACS region relaxed with respect to the central axis of the tRNA upon first position modification (Figure C.8). The preference for the higher Δ^{ACS} values was also exhibited by Cm^1GU, but the ASL-elbow distance was shortened, suggesting that straightening was accompanied by a significant compression, rather than elongation, of the tRNA body along the principal axis (Figure C.8). tRNA body compression also occurred for m^1GUG as the increased Δ^{ACS} was not accompanied by increased sampling of larger ASL-elbow distances (Figure C.8). The GUm^1G system Δ^{ACS} and the ASL-elbow distributions overlapped significantly with the corresponding distributions in GUG (Figure C.8), confirming that straightening did not occur.

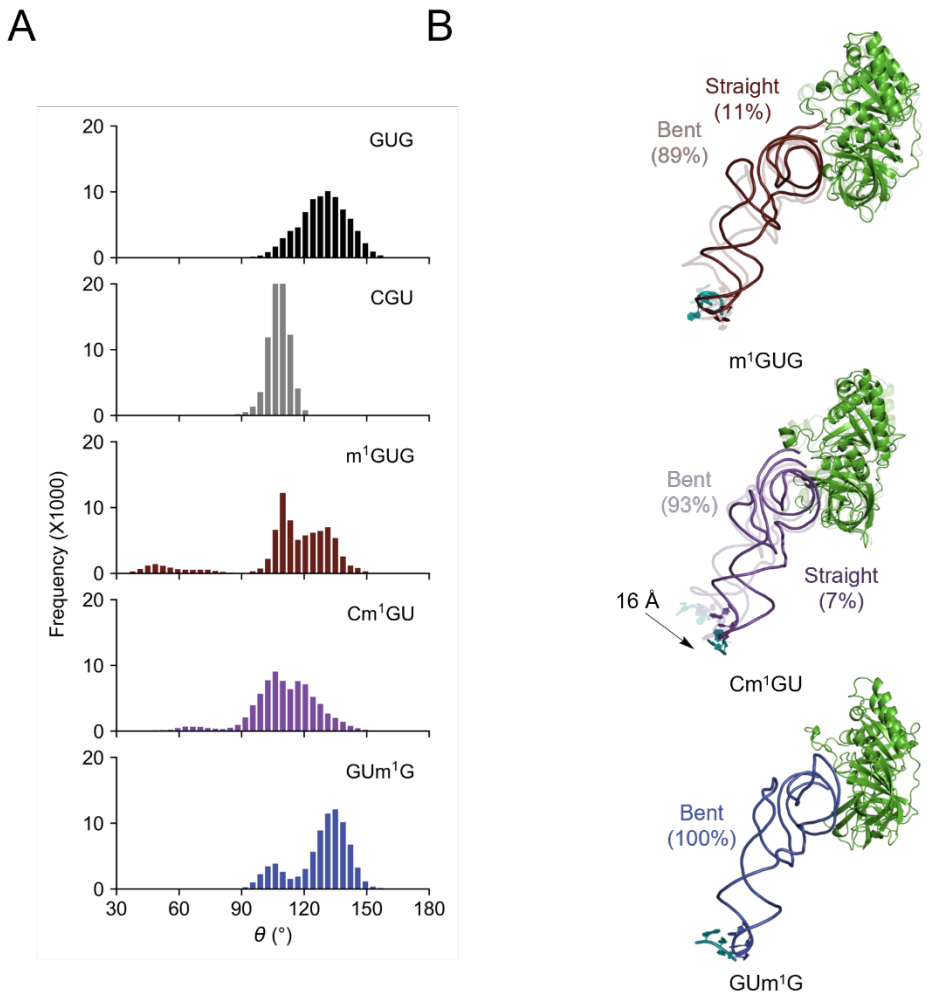

Figure 4.8. Alignment and conformation of tRNA in the A-site containing the m^{1}G modification in the codon during MD simulations. (A) Distribution of θ over the quadruplicate ensembles for each system. (B) Representative bent and straight tRNA conformations sampled. The parentheses show the percent occupancy of the corresponding conformations.

The flexibility of various regions of the tRNA was examined by computing the per-residue RMSF. m^{1}GUG exhibited high flexibility in all regions of the tRNA, with the most dramatic fluctuations in the ASL (2.00(0.5) Å, Table C.6; Figure 4.9). Cm^{1}GU also exhibited high flexibility in the ASL (2.29(0.5) Å) but maintained a relatively inflexible ACS region (1.19(0.2) Å; Table C.6). The lower RMSF in the ACS region for Cm^{1}GU suggests that EF-Tu maintained stronger engagement with Cm^{1}GU than for m^{1}GUG. Although both first and second position m^{1}G modifications led to minihelix distortions and tRNA misalignment, the effects on tRNA flexibility

were distributed differently: for m^1GUG, flexibility was more delocalized across the tRNA body, whereas for Cm^1GU, flexibility was concentrated in the ASL.

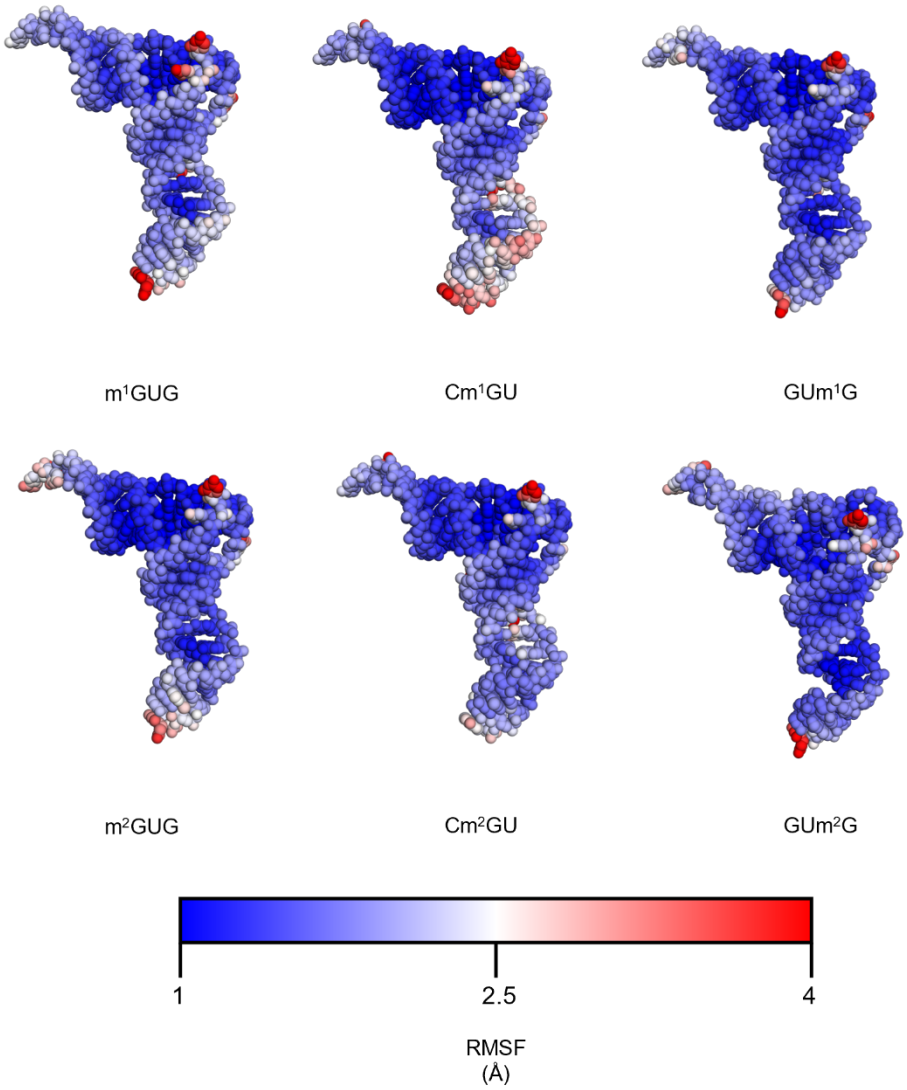

Figure 4.9. Flexibility of the tRNA sampled in MD simulations as measured by root-mean-squared fluctuations (RMSFs). The residue of each tRNA is colored according to the blue-white-red spectrum coloring denoting the RMSF value.

The conformation of the A-site minihelix was assessed using cluster analysis with Barnaba, which revealed three distinct conformations sampled across the simulations for the m^1G -modified ribosome subsystems: denoted “stacked”, “wobble”, and “rejected”, respectively (defined in Chapter 3). All three m^1G modified systems sampled the stacked (m^1GUG: 6% occupied, Cm^1GU: 12%, and GUm^1G: 67%) and wobble (14%, 12%, and 33%) states.

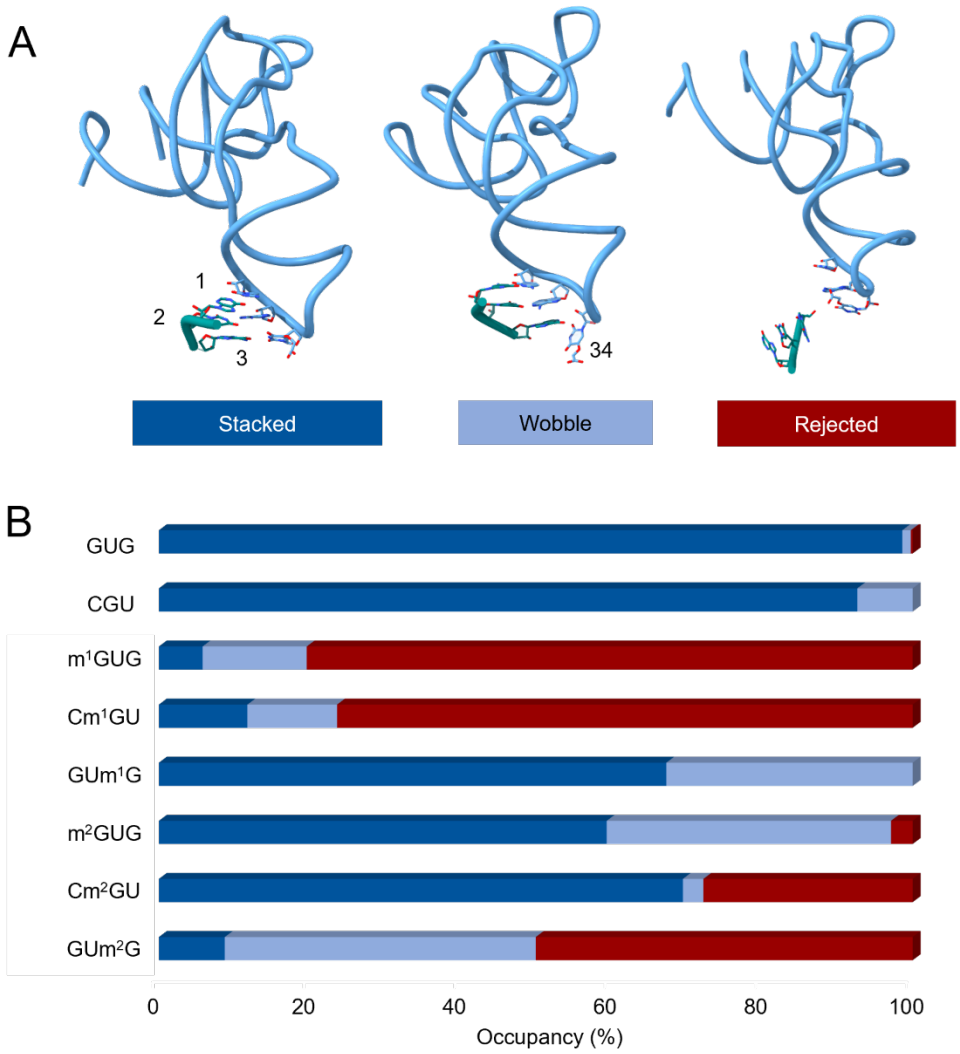

Figure 4.10. Representative conformations obtained by principal component analysis (PCA) of eRMSD and clustering over the MD simulations on ribosome subsystems containing m^1G or m^2G modifications. (A) Conformations sampled during simulations. (B) Occupancies of each conformation for each system.

Although the third position m^1G modification caused a significant increase in the occupancy of the wobble state (1% in GUG to 33% in GUm^1G; Figure 4.10B), it sampled the stacked state for the majority of the time (67%; Figure 4.10B). Both the first and second position m^1G-modified systems favoured the rejected state, occupying this state for 80% and 76% occupancies for m^1GUG and Cm^1GU, respectively, while the rejected state was not sampled for GUm^1G (Figure 4.10B). The substantial increase in occupancy of the rejected state occupancies for first and

second position m^1G modifications is consistent with the total abolishment of amino acid addition observed in the kinetics experiments by the Koutmou group. [14]

In summary, for the m^1G systems, the significant premature straightening, increase in tRNA flexibility, and high occupancy of rejected conformations for the first and second position codon modifications suggest that the cognate aa-tRNA fails to pass the codon recognition checkpoint in the ribosomal A-site. In contrast, for GUm^1G, tRNA straightening did not occur, the tRNA flexibility decreased with respect to GUG, and the tRNA did not sample the rejected state. These results are in good agreement with the observed slowed amino acid addition for m^1GUG and Cm^1GU, but not GUm^1G.

4.2.2 MD simulations of systems containing m^2G codon modifications

The kinetics measurements for the m^2G-modified systems suggest that the modification causes impairment of amino acid addition rates when placed in any of the three codon positions, but that the rate reduction is most substantial for GUm^2G. [14] It is difficult to justify these patterns using hydrogen bonding alone. The m^2G modification is positioned on the exocyclic amine N2 hydrogen bond donor, which allows it to preserve all three canonical G:C base pairs. However, the wobble base pair, as mentioned, is less strictly monitored by the ribosome, which allows non-WCF geometries at the third base pair. It is therefore unclear why GUm^2G impairs amino acid addition so drastically. The simulations in this section offer structural insights to rationalize these observed patterns.

4.2.2.1 Simulations of A-site ribosome codon systems containing m^2G codon modifications converge within 1 microsecond

For the m^2G systems, convergence plateaus in the backbone RMSD for the flexible region (Figure C.2A) and the tRNA (Figure C.2B) were reached within 500 ns for most replicas, except for tRNA backbone RMSDs of replicas 2 and 4 for Cm^2GU, which both converged after around 750 ns (Figure C.2A). Although the backbone RMSD of the unrestrained regions

converged across all replicas for each system, several replicas stabilized at high RMSD values (>6 Å), including replica 3 of m^2GUG, and replicas 1 and 2 of GUm^2G (Figure C.2). As previously observed for m^1GUG, the spikes in RMSD values for replica 3 of m^2GUG and replica 1 of GUm^2G were found to also arise from the motions of EF-Tu relative to the tRNA (Figure C.2).

The RMSD distributions for the unrestrained region of all m^2G models were significantly broadened relative to the unmodified systems (Figure 4.1A), with increases in CVs of 116% for m^2GUG (0.342), 45% for Cm^2GU (0.176), and 61% for GUm^2G (0.255; Table C.1). Moreover, high RMS deviations were observed for the unrestrained region RMSDs: 21% of m^2GUG and 43% of GUm^2G exceeded an RMSD of 6 Å, while 25% of Cm^2GU exceeded 5 Å (Figure 4.1A). The CVs of the tRNA backbone RMSD distributions were increased relative to unmodified systems for m^2GUG, Cm^2GU, and GUm^2G by 26%, 28%, and 62%, respectively (Table C.2). Although the CV of the backbone tRNA RMSD for GUm^2G increased significantly relative to GUG, the ensemble-averaged RMSD was slightly lower for GUm^2G (3.36 Å) than for GUG (3.52 Å). The higher variability in the tRNA backbone RMSD is attributed to replica 1 of GUm^2G, which stabilized at a higher average RMSD value than replicas 2–4 (Figure C.2).

4.2.2.2 16S rRNA monitoring is impacted for m^2G modified codons

For the m^2G systems, the monitoring angles exhibited substantial variability in r_c values across replicas. Some replicas showed high correlation between A1492 and A1493 (>0.8; replicas 2,3,4 of m^2GUG, 1 and 4 of Cm^2GU, and 1 and 3 of GUm^2G), while others showed moderate (from 0.5-0.8; replicas 3 of Cm^2GU; 2 and 4 of GUm^2G) or low (<0.55 in replicas 1 of m^2GUG, 2 of Cm^2GU, and 4 of GUm^2G) correlation. Despite this heterogeneity in the ensemble statistics, r_c values for the m^2G-modified systems (m^2GUG: 0.69(0.29), Cm^2GU: 0.69(0.22), and GUm^2G: 0.77(0.16)) were comparable with the unmodified systems (GUG: 0.68(0.17) and CGU:

0.84(0.15); Table C.3). These findings prompted further investigations into the favoured conformations of the monitoring bases and their interactions with the minihelix minor groove.

In the FEL distribution of A1492–3 monitoring angles, m^2GUG exhibited a significant reduction in on-on state occupancy (29%) from GUG, along with increased sampling of the off-off state (24%; Figure 4.3D–F). Cm^2GU showed a reduction in the on-on occupancy from CGU (33% to 5%) and a modest increased sampling of the off-on state (from 1% to 6%). For GUm^2G, on-on state occupancy decreased by nearly half (62% to 33%), while the off-off state appeared with 8% occupancy. Notably, for both m^2GUG and GUm^2G, A1493 adopted the off state (32% and 24%) more frequently than A1492 (23% and 8%), indicating that A1493 was disengaged while A1492 remained in either the intermediate or on states. This finding is unusual because, while experimental ribosome structures have captured A1492 independently adopting the off state in intermediate codon recognition states (see, for example, PDB IDs 4V4Q, 1N34, and 1N36), [20, 21] no experimental structure to date has shown A1493 adopting the off state independent of A1492. Therefore, first and third position m^2G modifications may drive aberrant decoupling of A1492–3 to slow the progression of codon recognition.

For m^2GUG, the MGDs sampled large A1492 and A1493 distances within the highest-density contours, indicating significant disengagement of both A1492–3 from the minor groove (Figure 4.4). For Cm^2GU, broadening of the MGD distribution was observed in the low- to moderate-density levels, but the narrow density observed for CGU was maintained in the high density contours for Cm^2GU (Figure 4.4). For GUm^2G, the highest density contours were all concentrated at lower A1493 distances than for GUG. However, the A1492 distances displayed slightly higher MGDs than GUG within the lowest 5 contour levels (Figure 4.4). The overall MGD shifts support the interpretation that A1492–3 are significantly disengaged from the minor groove of m^2GUG, while Cm^2GU, and GUm^2G exhibit more moderate disengagement. To

examine how effective the monitoring by A1492–3 and G530 was, the number of waters contained within the minor groove were measured.

The water distribution near the minor groove was not significantly affected when comparing GUG to m^2GUG or CGU to Cm^2GU (Figure 4.6). The average and standard deviation of water molecules within 5 Å of the minor groove for the first and second base-pairing positions were comparable between GUG (8(2) and 8(2)) and m^2GUG (9(3) and 6(3); Table C.4). Similarly, the number of water molecules for Cm^2GU (5(3) and 6(3)) were comparable to CGU (4(2) and 5(3)). In contrast, for GUm^2G, the histogram distribution broadened substantially, with distinct populations in the low range (<5 water molecules) and high range (>15 water molecules; Figure 4.6). While the mean number of water molecules at the first position was similar between GUm^2G and GUG (9 vs. 8), the shape of the distributions differed significantly (Figure 4.6). The distribution for GUm^2G is markedly broader and skewed to the right, causing the mode to shift to the left with respect to GUG. These aspects of the distribution reflect increased sampling of both highly solvent-shielded and solvent-exposed states for GUm^2G compared to the other systems. Together, the water distribution and MGD analysis results suggest that solvent shielding was not substantially affected for first and second position m^2G codon modifications. Moreover, GUm^2G leads to the presence of both highly shielded and poorly shielded states whereas shielding was unaffected for m^2GUG and Cm^2GU relative to the unmodified systems. However, the A1492–3 analyses alone were not sufficient to explain the trends observed in solvent shielding. For example, the high degree of A1492–3 disengagement for m^2GUG does not explain how the solvent accessibility of the minor groove was decreased relative to GUG. Therefore, the conformational occupancies of G530 were measured to examine whether G530 engagement was enhanced for m^2GUG.

The sole G530 conformation sampled for m^2GUG was the on state (occ.=99%; Figure 4.11A), explaining why solvent was excluded from the minor groove despite the disengagement of A1492–3 from the minihelix. In contrast, the semi-on state was dominant for Cm^2GU and GUm^2G, at 73% and 76% occupancy, respectively (Figure 4.11B-C). Additionally, both Cm^2GU and GUm^2G exhibited unconventional G530 conformations similar to those observed in the GUG^{Met} and IUG^{Met} trajectories described in Chapter 3. In Cm^2GU, a conformation in which B34 of the anticodon flips out of the ASL and stacks with G530 (denoted "G530–B34 stacked") was observed with 10% occupancy (Figure C.7A). A similar conformation was observed for GUm^2G (8%), in which G530 stacks with B3 of the codon instead of stacking with B34 ("G530–B3 stacked"; Figure C.7B). GUm^2G also sampled the pseudo semi-on state (11%), in which the WCF geometry between the first and second base pairs is completely disrupted (Figure C.7B).

The G530 monitoring conformation analysis provides a clear rationale for how solvent shielding was maintained for m^2GUG despite compromised A1492–3 engagement. Compared to GUG, the occupancy of the G530 on state for m^2GUG was increased from 93% to 99%, suggesting that G530 latching was enhanced in the presence of a first position m^2G codon modification. This G530 behaviour likely compensates for the decreased hydrophobic stabilization by A1492–3, thereby maintaining solvent exclusion. This observation explains why the water distribution for m^2GUG was not significantly different from GUG, despite the larger MGDs and increased sampling of the A1492–3 off-off states (Figure 4.3D and 4.4). Similarly, for Cm^2GU, the number of water molecules in the first base pair position remained comparable (CGU: 4(2) and Cm^2GU 5(2); Table C.4), consistent with the absence of the G530 off state in both systems. However, the reduced occupancy of the semi-on conformation compared to CGU (73% vs. 92%) likely accounts for the increased water at the third codon position from 9(3) for CGU to 13(3) for Cm^2GU (Figure 4.11B and Table C.4). Although none of the m^2G systems sampled the

G530 off state, G530 monitoring was disrupted for GUm^{2}G, where the G530 on state was entirely lost (0%) and the semi-on state dominated (76%; Figure 4.11C). The loss of complete G530 latching explains the increased variability in the solvent exposure observed for GUm^{2}G in the first two base pairing positions. However, it was unclear whether the monitoring bases engagement or lack thereof contributed to structural deviations in the codon-anticodon minihelix for the m^{2}G-modified systems. In particular for GUm^{2}G, the lack of full disengagement by G530 was unexpected due to its greater degree of impaired amino acid addition relative to m^{2}GUG and Cm^{2}GU in the corresponding experiments by the Koutmou lab. [14] To assess the structural consequences of m^{2}G incorporation, Section 4.2.2.3 examines geometric distortions within the codon-anticodon minihelix.

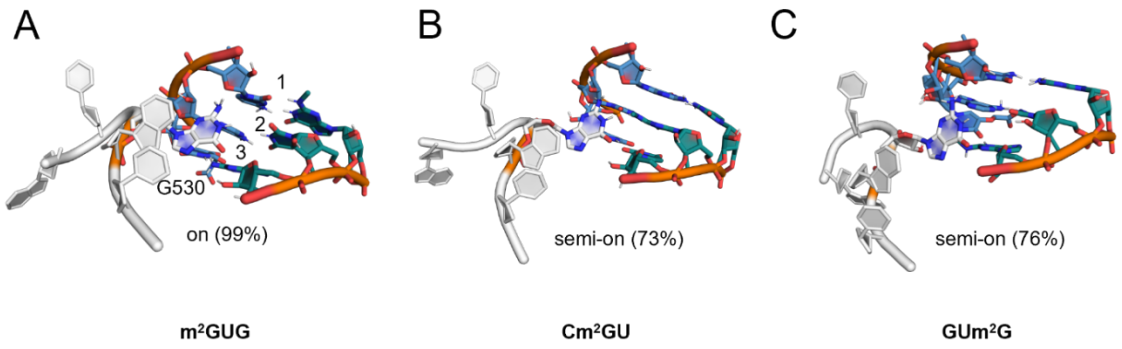

Figure 4.11. G530 conformations and occupancies during the MD simulations of ribosomal A-site models with the m^{2}G modification in the codon. (A-C) Conformation occupancies obtained by cluster analysis applied to the heavy atoms of G530, the tRNA anticodon (B34-36; colored in blue), and the A-site mRNA codon (B1-3; colored in teal) for the quadruplicate ensemble of m^{2}G-modified mRNA codon systems.

4.2.2.3 Distortion of minihelix structure induced by m^{2}G modifications

For m^{2}GUG, the glycosidic distances and coplanar angles were not significantly impacted at the first and second base-pairing positions. The third position base pair of m^{2}GUG was perturbed slightly as indicated by the increased standard deviation of the glycosidic distance and adoption of a population of higher coplanar angles (Figure 4.12A-B). For Cm^{2}GU, the second base pair exhibited a broader glycosidic distance distribution, while the first and third base pairs

were less affected (Figure 4.12A). The coplanar angle distribution for Cm^2GU was modestly broadened at the first and third base pairs, with a second distinct population emerging, in which most of the fourth quartile of data points exceeded 90° (Figure 4.12B). In contrast, for GUm^2G, the glycosidic distances showed marked increases in variability across all three base pairs, suggesting the anticodon dissociated from the codon (Figure 4.12A). Additionally, GUm^2G exhibited a substantial increase in the variability of the coplanar angles for all three base pairs (Figure 4.12A-B), indicating that proper WCF geometry of the minihelix was lost.

The WCF hydrogen bonds were maintained at high occupancies in the first and second positions for m^2GUG (97% and 90%, respectively) with a moderate decrease in the third position compared to GUG (47% to 24%; Table B.3 and Table C.5). The Cm^2GU system maintained high occupancies for the three canonical WCF G:C base pairing interactions between the nucleobases of the first base pair, with the lowest occupied GC interaction between the N4–H of C1 with O6 of G36 (90%), a negligible decrease from CGU (94%; Table B.3). Although both CGU and Cm^2GU maintained canonical G:C interactions (Figure C.8A-B), the occupancies of all three G:C hydrogen-bonding interactions in the B2:B35 were decreased for Cm^2GU (Figure C.8A-B and Table C.4). In addition, both CGU and Cm^2GU exhibited a shifted hydrogen-bonding interaction in which the N1 of G2 forms a contact with the O2 of C35, which decreased in occupancy from CGU (53%) to Cm^2GU (43%). This shifted interaction was accompanied by distortion in the minihelix Cm^2GU (Figure C.8D), but not CGU (Figure C.8C), consistent with the broader coplanar angle distribution for Cm^2GU at the second position (Figure 4.12B). Moreover, Cm^2GU reduced the occupancy of the third position hydrogen bond to 64% (Table C.5) compared to CGU (85%; Table B.3). Although the methyl group moiety did not fully disrupt the second base pair for Cm^2GU at it did for Cm^1GU, m^2G led to reduced hydrogen-bonding occupancies and coplanarity, as well as slightly increased distance between B2 and B35.

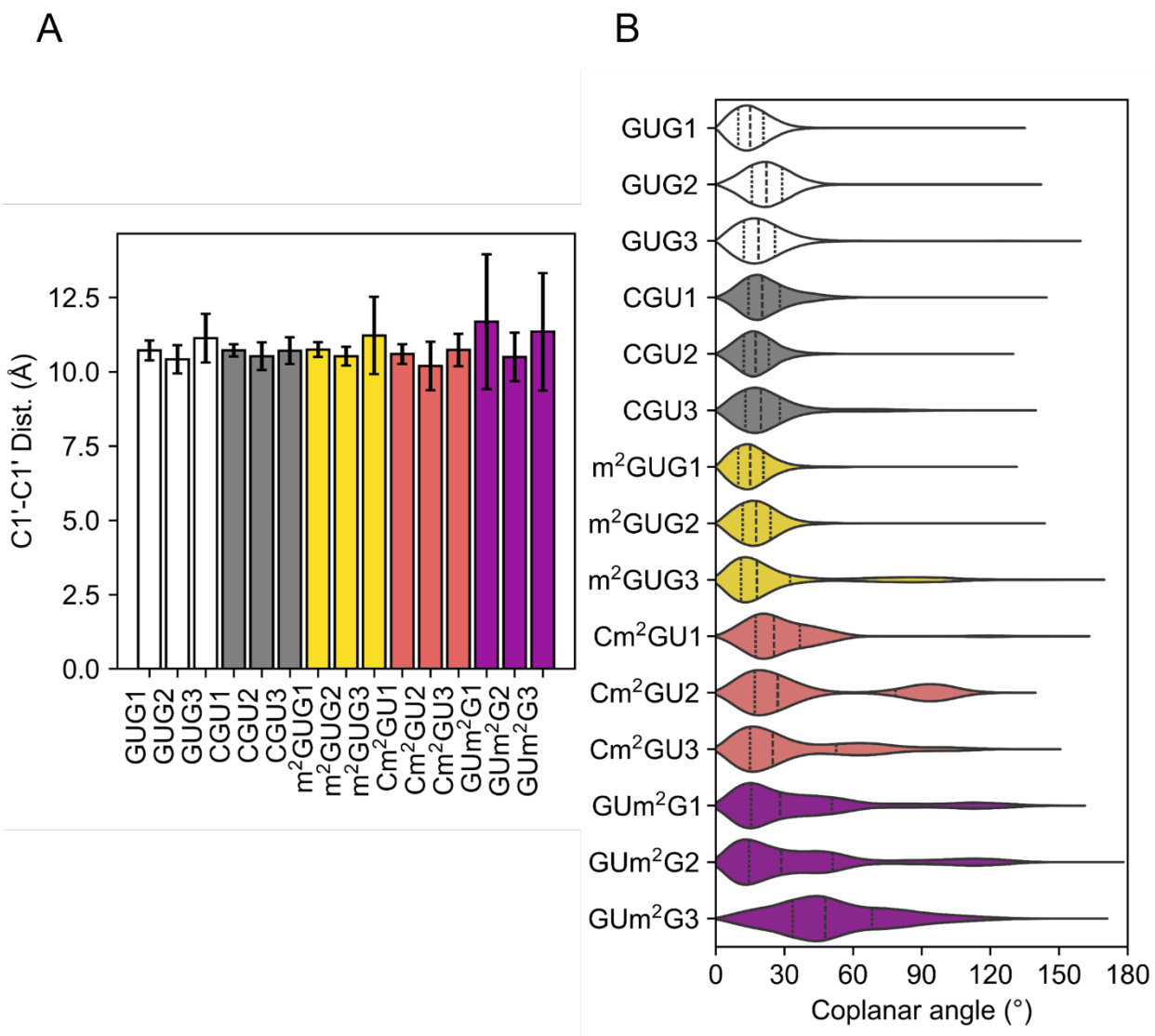

Figure 4.12. Analysis of the minihelix geometry for the m^{2}G modified codon-anticodon minihelix during the MD simulations.(A) Glycosidic distances between opposing nucleobases in the minihelix. (B) Interplanar angles between opposing nucleobase aromatic rings in the minihelix.

The GUm^{2}G system caused a significant decrease in the occupancy of the hydrogen-bonding interactions associated with the unshifted base pairing interaction in the first position G:C pair (98% in GUG to 42% in GUm^{2}G). Conversely, the shifted base pair between N1 of G1 and O2 of C36 increased modestly, from 23% in GUG to 35% in GUm^{2}G. The occupancy of second and third base pair hydrogen bonds were disrupted for GUm^{2}G (36% and 16%) compared to GUG (98% and 20%). Therefore, while Cm^{2}GU perturbed minihelix hydrogen bonding, its impact

on the first base pair was less severe than for GUm^{2}G. The simulation results indicating that the most pronounced minihelix distortions occurred for GUm^{2}G were in good agreement with the Koutmou lab group findings that the most severe impairment of amino acid addition occurred for GUm^{2}G. To examine whether these distortions to the minihelix affected the tRNA dynamics, Section 4.2.2.4 explores the structural features of tRNA bending and dissociation from mRNA.

4.2.2.4 m^{2}G codon modifications influence tRNA dynamics in the A-site

The unimodal θ distribution observed for GUG became bimodal for m^{2}GUG, yet the range of values (90–120°) suggested retention of the bent conformation for 100% of the simulation time (Figure 4.13A-B). The θ distribution for Cm^{2}GU closely matched that of CGU, suggesting negligible impact on the overall tRNA conformation when m^{2}G was incorporated at the second codon position. In contrast, GUm^{2}G exhibited a multimodal θ distribution, where θ angles were sampled in the low range (0–90°), as well as a leftward shift of the primary population from high (120–150°) to moderate (90–120°) range θ angles, suggesting premature tRNA straightening (Figure 4.13A-B). Moreover, for GUm^{2}G, the θ angles corresponded to a straight conformation with an occupancy of 16% (Figure 4.13B). The Δ^{ACS} and ASL-elbow distance measures confirmed that m^{2}GUG and Cm^{2}GU did not lose the bent conformation (Figure C.8). There was only a slight increase (~3°) of Δ^{ACS} for m^{2}GUG and Cm^{2}GU (Figure C.8) in the most populated contour, no discernable influence on the ASL–elbow distance for m^{2}GUG, and a decrease and narrowing of the ASL–elbow distance for Cm^{2}GU. The straightening was confirmed for GUm^{2}G, which exhibited a significant increase in the densities at high (>10°) $\Delta^{ACS}$and ASL-elbow distances with respect to GUG (Figure C.8).

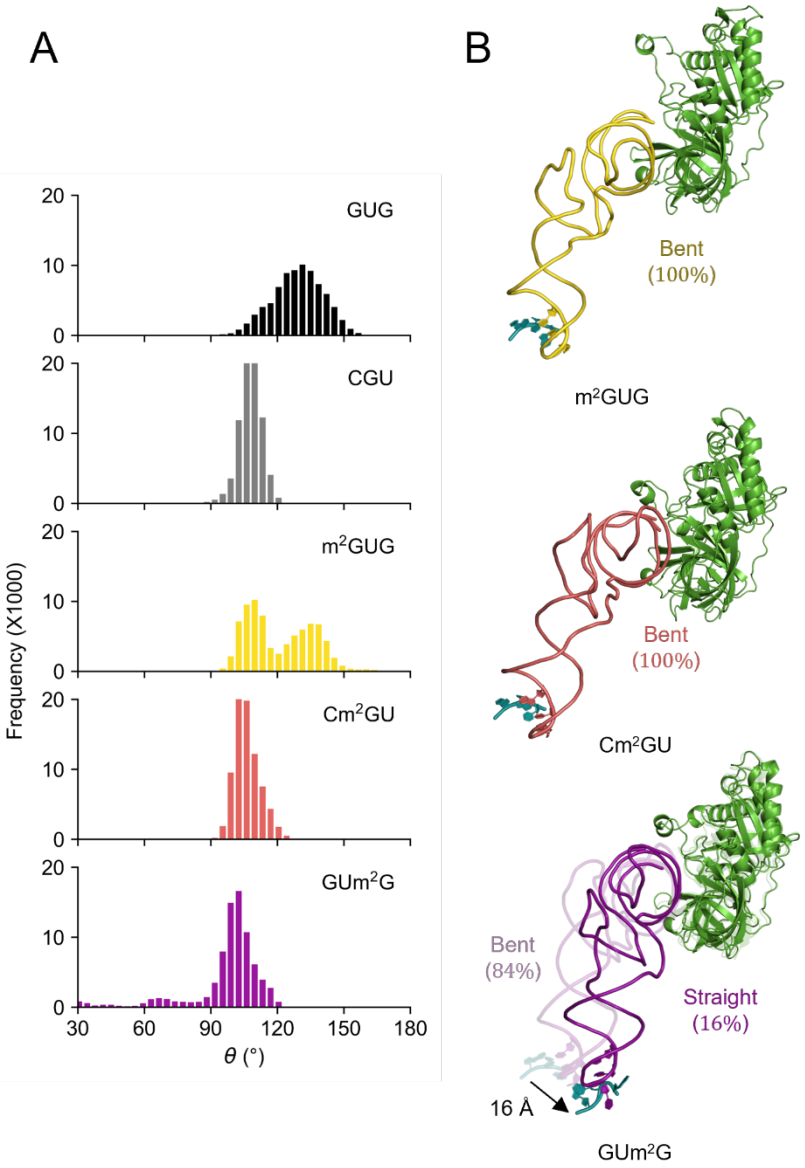

Figure 4.13. Alignment and conformation of tRNA in the A-site containing the m^{2}G modification in the codon during MD simulations. (A) Distribution of the θ over the quadruplicate ensembles for each system. (B) Representative bent and straight tRNA conformations sampled. Parenthesis correspond to the percent occupancy of the identified conformation.

The tRNA of the m^{2}GUG and Cm^{2}GU systems exhibited comparable overall flexibility to GUG (Figure 4.9). Aside from the ASL, which had a consistent mean RMSF for m^{2}GUG and Cm^{2}GU (1.85(0.5) and 1.89(0.3) Å, respectively) compared to GUG (1.73(0.3)), the D-arm, TΨC-arm, and ACS had decreased RMSFs (Table C.6). Interestingly, the V-loop had remarkably high flexibility in Cm^{2}GU (2.00(1.2)), but not in m^{2}GUG (1.42(0.4)), while GUG was intermediate

between the two (1.76(0.6)). For GUm^{2}G, the ASL, D-arm, and V-loop flexibility were reduced, while the flexibility of the backbone of the TΨC-arm and ACS were slightly increased compared to GUG (Table C.6; Figure C.9A-B). However, local regions of both the ASL and ACS were more flexible for the GUm^{2}G system compared to GUG; including the cmo^{5}U34 nucleotide and 5'–end of the ACS (Figure C.9A-B). The increased residue fluctuations at the anticodon and ACS suggest poor induced-fit of the tRNA in the ribosomal A-site for GUm^{2}G compared to GUG, as these regions are closest to the SSU and LSU contact points. To assess the overall fit of the tRNA at the A-site for the m^{2}G-modified models, the conformational occupancies for the tRNA:mRNA interaction were calculated using Barnaba (see Chapter 2 for full calculation details).

For m^{2}GUG, the occupancy of the wobble conformation increased with respect to GUG, from 1% to 38%, and the rejected state was sampled for 3% of the simulation ensemble (Figure 4.10B). In contrast, for Cm^{2}GU, the rejected state occupancy (28%) was higher than for m^{2}GUG, but the stacked state remained the dominant conformation (70%; Figure 4.10B). GUm^{2}G sampled the rejected state for half (50%) the simulation time and reduced the sampling of the stacked state from 99% in GUG to 9% (Figure 4.10B). The distribution of tRNA conformations in the A-site aligns with the Koutmou lab observations that amino acid addition is most impaired most for GUm^{2}G, and less severely impacted for m^{2}GUG and Cm^{2}GU. In the simulations, GUm^{2}G exhibited the highest occupancy of the rejected state and the most pronounced reduction of the stacked conformation compared to m^{2}GUG and Cm^{2}GU.

In summary, for the m^{2}G-modified systems, GUm^{2}G exhibited the most severe impairment of the ability of cognate tRNA to recognize the mRNA codon by causing significant tRNA straightening and sampling the greatest occupancy of the rejected state, increasing localized residue flexibility in the ASL and ACS, and severely decreasing the stacked state occupancy. In contrast, the effects of first and second position m^{2}G modifications to the codon

were less pronounced than the third position modification, with little to no tRNA straightening, smaller changes in the stacked state occupancies, and lower rejected state occupancies.

4.3 Conclusions

The MD data presented in this chapter revealed that m^1G and m^2G alkylative damage products can modulate decoding in drastically different ways depending on their position in the mRNA codon. Moreover, the simulations rationalize the observed alterations in k_{obs} for peptide bond formation due to m^1G and m^2G incorporation into each of the three mRNA codon positions.

The extreme impacts of m^1G modifications on rates of peptide bond formation when placed in the first and second positions can be explained by perturbed monitoring by all three monitoring nucleobases, A1492–3 and G530, which fail to shield the minihelix minor groove from solvent and adopt a high proportion of disengaged conformations. The lack of monitoring engagement led to aberrant premature straightening of the tRNA, high variability in the glycosidic distances, and disrupted coplanarity and hydrogen bonding for all three base pairs in the codon-anticodon minihelix, which resulted in substantially increased sampling of the rejected conformation. The simulations also revealed that more nuanced structural mechanisms can potentially interfere with codon recognition. For example, m^1G at the first and second positions may lead to overly correlated A1492–3 motions that stabilize incorrect minihelix geometries which would presumably decrease the rate of codon recognition. These structural features rationalize the trends in the kinetics data collected by the Koutmou group, wherein the first and second position m^1G modification substantially reduced the observed rate constants of amino acid addition, while the third position did not.

In the case of m^2G, the simulations indicate that A1493 flips into the intrahelical off conformation independently of A1492 for m^2GUG and GUm^2G, which is not an experimentally

reported conformation and may signify impaired codon recognition. The A1492–3 and G530 monitoring were most significantly impaired for GUm^{2}G. Additionally, while the codon-anticodon minihelix was disrupted for the second and third position m^{2}G variants, GUm^{2}G led to an even greater disruption to the minihelix (broader distributions of the glycosidic distances for all three base pairs). Moreover, premature straightening of the tRNA was substantial for GUm^{2}G, while m^{2}GUG and Cm^{2}GU largely maintained the bent conformation. Although each of the three m^{2}G-modified systems sampled the rejected state, GUm^{2}G nearly eliminated the stacked state and had the highest occupancy (50%) of the rejected state. Thus, the simulations suggest that while impairments to codon recognition were observed for m^{2}GUG and Cm^{2}GU, they were most severe for GUm^{2}G. The results for m^{2}G modified systems were also in line with the Koutmou group experiments which showed that the observed rates of amino acid addition were slowed for all three m^{2}G modification positions in the codon, but most drastically in the third.

Overall, this chapter provided the first structural evidence for the impacts of mRNA damage during ribosomal decoding. The simulations revealed detailed mechanisms occurring during early tRNA selection that can explain the growing associations between mRNA alkylative damage and defective translation.

4.3 References

(1) Hudson, B. H.; Zaher, H. S. O6-Methylguanosine leads to position-dependent effects on ribosome speed and fidelity. *RNA* **2015**, *21* (9), 1648-1659. DOI: 10.1261/rna.052464.115.

(2) Simms, C. L.; Zaher, H. S. Quality control of chemically damaged RNA. *CMLS.* **2016**, *73* (19), 3639-3653. DOI: 10.1007/s00018-016-2261-7.

(3) Thomas, E. N.; Kim, K. Q.; McHugh, E. P.; Marcinkiewicz, T.; Zaher, H. S. Alkylative damage of mRNA leads to ribosome stalling and rescue by trans translation in bacteria. *eLife* **2020**, *9*, e61984. DOI: 10.7554/eLife.61984.

(4) Wurtmann, E. J.; and Wolin, S. L. RNA under attack: Cellular handling of RNA damage. *Crit. Rev. Biochem. Mol. Biol.* **2009**, *44* (1), 34-49. DOI: 10.1080/10409230802594043.

(5) Zaher, H. S.; Mosammaparast, N. RNA Damage Responses in Cellular Homeostasis, Genome Stability, and Disease. *Annu. Rev. Pathol.* **2025**, *20* (Volume 20, 2025), 433-457. DOI: https://doi.org/10.1146/annurev-pathmechdis-111523-023516.

(6) Simms, C. L.; Hudson, B. H.; Mosior, J. W.; Rangwala, A. S.; Zaher, H. S. An active role for the ribosome in determining the fate of oxidized mRNA. *Cell Rep.* **2014**, *9* (4), 1256-1264. DOI: 10.1016/j.celrep.2014.10.042.

(7) Thomas, E. N.; Simms, C. L.; Keedy, H. E.; Zaher, H. S. Insights into the base-pairing preferences of 8-oxoguanosine on the ribosome. *Nucleic Acids Res.* **2019**, *47* (18), 9857-9870. DOI: 10.1093/nar/gkz701.

(8) Yan, L.; Simms, C.; McLoughlin, F.; Vierstra, R.; Zaher, H. Oxidation and alkylation stresses activate ribosome-quality control. *Nat. Commun.* **2019**, *10*, 5611. DOI: 10.1038/s41467-019-13579-3.

(9) Simms, C. L.; Thomas, E. N.; Zaher, H. S. Ribosome-based quality control of mRNA and nascent peptides. *WIREs RNA* **2017**, *8* (1), e1366. DOI: https://doi.org/10.1002/wrna.1366.

(10) Simms, C.; Yan, L.; Qiu, J.; Zaher, H. Ribosome Collisions Result in +1 Frameshifting in the Absence of No-Go Decay. *Cell Rep.* **2019**, *28*, 1679-1689.e1674. DOI: 10.1016/j.celrep.2019.07.046.

(11) Yan, L. L.; Zaher, H. S. Ribosome quality control antagonizes the activation of the integrated stress response on colliding ribosomes. *Mol. Cell.* **2021**, *81* (3), 614-628.e614. DOI: https://doi.org/10.1016/j.molcel.2020.11.033.

(12) Jones, J. D.; Franco, M. K.; Smith, T. J.; Snyder, L. R.; Anders, A. G.; Ruotolo, B. T.; Kennedy, R. T.; Koutmou, K. S. Methylated guanosine and uridine modifications in S. cerevisiae mRNAs modulate translation elongation. *RSC Chem. Biol.* **2023**, *4* (5), 363-378. DOI: 10.1039/d2cb00229a.

(13) You, C.; Dai, X.; Wang, Y. Position-dependent effects of regioisomeric methylated adenine and guanine ribonucleosides on translation. *Nucleic Acids Res.* **2017**, *45* (15), 9059-9067. DOI: 10.1093/nar/gkx515.

(14) Koutmou, K.; Giles, R. Private Communication. 2025.

(15) Hoernes, Thomas P.; Clementi, N.; Faserl, K.; Glasner, H.; Breuker, K.; Lindner, H.; Hüttenhofer, A.; Erlacher, Matthias D. Nucleotide modifications within bacterial messenger RNAs regulate their translation and are able to rewire the genetic code. *Nucleic Acids Res.* **2015**, *44* (2), 852-862. DOI: 10.1093/nar/gkv1182 (acccessed 9/5/2024).

(16) Loveland, A. B.; Demo, G.; Grigorieff, N.; Korostelev, A. A. Ensemble cryo-EM elucidates the mechanism of translation fidelity. *Nature* **2017**, *546* (7656), 113-117. DOI: 10.1038/nature22397.

(17) Satpati, P.; Sund, J.; Åqvist, J. Structure-Based Energetics of mRNA Decoding on the Ribosome. *Biochem.* **2014**, *53* (10), 1714-1722. DOI: 10.1021/bi5000355.

(18) Sanbonmatsu, K. Y.; Joseph, S. Understanding discrimination by the ribosome: stability testing and groove measurement of codon-anticodon pairs. *J. Mol. Biol.* **2003**, *328* (1), 33-47. DOI: 10.1016/s0022-2836(03)00236-5.

(19) Pape, T.; Wintermeyer, W.; Rodnina, M. Induced-fit in initial selection and proofreading of aminoacyl-tRNA on the ribosome. *EMBO J.* **1999**, *18* (13), 3800-3807. DOI: https://doi.org/10.1093/emboj/18.13.3800.

(20) Schuwirth, B. S.; Borovinskaya, M. A.; Hau, C. W.; Zhang, W.; Vila-Sanjurjo, A.; Holton, J. M.; Cate, J. H. D. Structures of the Bacterial Ribosome at 3.5 Å Resolution. *Science* **2005**, *310* (5749), 827-834. DOI: doi:10.1126/science.1117230.

(21) Ogle, J. M.; Murphy, F. V.; Tarry, M. J.; Ramakrishnan, V. Selection of tRNA by the Ribosome Requires a Transition from an Open to a Closed Form. *Cell* **2002**, *111* (5), 721-732. DOI: https://doi.org/10.1016/S0092-8674(02)01086-3.

CHAPTER 5: GLOBAL CONCLUSIONS

5.1 Thesis review

RNA is indispensable to translation because of its dual role as an information carrier and a catalyst.[1] Every known organism relies on rRNA, tRNA, and mRNA to convert genetic information into protein, making translation stand out as one of the most universally essential processes in biology. Although protein synthesis is regulated by numerous complex cellular mechanisms,[2-5] RNA modification stands out as a ubiquitous, high-order regulatory strategy.[6-10] The chemical diversification of RNA via modification crucially fine-tunes the accuracy and efficiency of translation. The heart of translation, ribosomal decoding, is fundamentally driven by choreographed structural dynamics among tRNA, mRNA, and rRNA.[3,11-16] It is therefore increasingly important to situate RNA modifications within the evolving mechanistic and regulatory framework of ribosomal decoding. While the abundance and chemical diversity of tRNA and rRNA modifications have attracted considerable research attention, the roles of mRNA codon modifications remain poorly understood at the mechanistic level. However, systems-level studies are continuously identifying potential roles of mRNA modifications in disease prevention.[6, 7, 17-21 22, 19, 23-34 35 36, 37] While it has been suggested that mRNA modifications modulate decoding during early tRNA selection (i.e., before proofreading),[38-44] this hypothesis has not been thoroughly examined.

As discussed in Chapter 1, it is increasingly recognized that stochastic structural fluctuations on the nanosecond to microsecond timescale underlies the discrete transitions between intermediates during ribosomal decoding.[16] However, these motions are often difficult to measure directly using available experimental techniques. The objective of this thesis was to establish a robust computational model and utilize MD simulations to characterize how various

mRNA modifications impact codon recognition and modulate the structural dynamics of ribosomal decoding.

5.1.1 Inosine, m^1G, and m^2G mRNA modifications influence codon recognition

Chapter 3 used a ribosomal A-site model to study how the inosine mRNA modification affects decoding by cognate aa-tRNA. Inosine plays established roles in decoding, being commonly introduced into tRNA at the wobble position (B34) and B37 (adjacent to the anticodon). Inosine is also present in mRNA, with approximately 1500 A-to-I editing sites located in the CDS in humans. Despite their presence, the majority of these sites do not have assigned biological roles nor mechanistic characterization. The Koutmou group measured the apparent rate of peptide synthesis in reconstituted translation systems when inosine was placed in the first, second, or third codon position (k_{obs}). The first position inosine codon modification substantially reduced the rate, whereas the second and third had no significant impacts.

MD simulations performed for this thesis (Section 3.2.1) indicated that productive initial tRNA selection was favoured among the unmodified (GUG and CGU) and second (CIU) or third (GUI) position modified systems. Specifically, though A1492, A1493, and G530 ribosomal monitoring nucleotides exhibited conformational flexibility, each remained engaged with the minor groove of the codon-anticodon minihelix. Consequently, the minihelix preserved an optimal WCF geometry, in line with the induced-fit kinetic mechanism, and the aa-tRNA maintained a bent conformation aligned with both the mRNA codon and EF-Tu in the A-site. Productive initial selection indicates that these systems would proceed to the second selection stage and likely contribute to dipeptide formation. In contrast, these structural features were disrupted for the first position (IUG) inosine-modified codon. A1492–3 and G530 exhibited fully disengaged conformations, the minihelix WCF geometry was perturbed, and the aa-tRNA exhibited premature straightening and complete dissociation from the mRNA codon. The

simulations provide a structural explanation for the slowed rate of dipeptide formation observed experimentally for IUG (but not I in the other codon positions),[45] implicating disrupted monitoring, minihelix instability, and tRNA dissociation during decoding.

Simulations with near-cognate aa-tRNA (Section 3.2.2) were then performed, motivated by two observations. First, the IUG simulations with cognate tRNA exhibited conformational rearrangements commonly associated with near-cognate tRNA,[11, 46] prompting the question of whether the IUG codon can induce near-cognate-like behaviour in cognate tRNA. This was supported by the Koutmou group who found that the k_{obs} for near-cognate $tRNA^{Met}$, which exhibits a G:U mismatch at the first codon position (GUG^{Met}), was impaired to a similar extent as for IUG. Second, because inosine can expand base-pairing potential,[25] it was hypothesized that the IUG codon might permit miscoding by near-cognate tRNAs. To directly assess these hypotheses, the Koutmou group measured k_{obs} for GUG^{Met} and IUG^{Met} systems, revealing similar impairments in dipeptide formation across IUG, GUG^{Met}, and IUG^{Met}. However, the mechanisms of differential impaired decoding for cognate or near-cognate systems in the presence of the GUG or IUG codon was unclear.

Simulations on the near-cognate systems (GUG^{Met} and IUG^{Met}) revealed that ribosomal monitoring was less disrupted than for IUG. For GUG^{Met}, A1492–3 engagement was moderately perturbed, while G530 remained engaged, but adopted noncanonical conformations and a low occupancy of the G530 on state. In contrast, IUG^{Met} retained the G530 on state as the dominant conformation but also sampled the off state (11% occupancy) and nonproductive conformations, while A1492–3 engagement was largely preserved. Despite milder monitoring defects relative to IUG, both near-cognate systems exhibited distortions in the minihelix geometry and induced premature tRNA straightening. However, unlike IUG, the tRNAs remained closely associated with the codon despite misalignment. Thus simulation data for near-cognate

tRNA (Section 3.2.2) suggest that disrupted monitoring is not the sole cause of impaired decoding. Instead, local instability in the codon–anticodon helix can be sufficient to induce tRNA misalignment and straightening, even while monitoring bases do not fully disengage from the minihelix.

Chapter 4 investigated how damage-induced mRNA modifications affect elongation, given their emerging relevance to translational stalling. *In vivo*, mRNA damage can trigger ribosome-mediated decay pathways typically associated with obstructive elements in the coding sequence, such as stable hairpins or rare codons.[36, 47-49] These decay signals can be harmful if left unchecked, suggesting that damage lesions within mRNA coding regions may have serious pathological consequences.[36, 47-49] The Koutmou group performed kinetic assays on two alkylative lesions, m^1G and m^2G, and found distinct position-dependent effects on k_{obs} for dipeptide formation.[45] Specifically, m^1GUG and Cm^1GU modifications abolished elongation, while the GUm^1G had no measurable effect. In contrast, although both m^2GUG and Cm^2GU reduced k_{obs}, the strongest impairment was observed for GUm^2G.[45]

For both m^1GUG and Cm^1GU, MD simulations (Section 4.2.1) revealed that all three monitoring bases exhibit impaired function, the codon-anticodon minihelix is disrupted, and the tRNA straightens prematurely and dissociates from the mRNA. However, GUm^1G did not induce any of these structural effects that are detrimental to initial selection. The MD data for the m^1G systems are therefore in alignment with the kinetics data collected by the Koutmou group where m^1GUG and Cm^1GU, but not GUm^1G led to significant impairment of dipeptide formation by reducing k_{obs}.[45] For the m^2G systems, A1492–3 and G530 monitoring dynamics were perturbed for all three systems, but most significantly for GUm^2G. Distortions in the minihelix geometry were observed for Cm^2GU and GUm^2G, but the codon only dissociates from the anticodon when the modification is at the third position. Premature straightening was modest in

m^2GUG and Cm^2GU, but substantial in GUm^2G. These results were also in agreement with the position-dependent impairments observed in the Koutmou lab experiments,[45] in which all three m^2G-modified codons reduced k_{obs}, with GUm^2G causing the most pronounced effect. Overall, these results provide a structural basis for the position-dependent impairments observed in the Koutmou lab experiments and suggest that decoding disruption can arise through distinct mechanisms depending on the modification and its position in the codon.

5.1.2. MD simulations reveal novel insights into A-site dynamics during decoding

The simulations performed in this thesis revealed previously unreported features of decoding dynamics that expand the current mechanistic framework for tRNA selection and help contextualize the regulatory role of mRNA modifications. Notably, this thesis presents the first observations of spontaneous transitions in A1492–3 and G530 from fully engaged to intermediate and disengaged conformations without the use of enhanced sampling methods. Intrahelical and extrahelical motions of A1492–3 occurred repeatedly on the microsecond timescale, with A1492 often, but not always, behaving independently of A1493. The conformational preferences observed were consistent with those captured in 116 high-resolution X-ray and cryo-EM structures (Table A.3 and Section 3.2.1.2).[50-85] Moreover, these simulations directly sampled rapid rejection and full dissociation of aa-tRNA during codon recognition. This process has been observed in structure-based model (SBM) simulations,[46] where codon recognition failure occurs via a motion in which the aa-tRNA loses contact with the mRNA codon and orients perpendicular to the body of the tRNA (observed in Chapter 3 in this thesis). However, this thesis did not impose the biasing restraints to artificially direct progression of the tRNA to the A-site as implemented in SBM simulations, showing that the unbiased microsecond aaMD simulations of the ribosome subsystem developed and applied in this thesis can sample spontaneous aa-tRNA rejection. Moreover, this thesis is the first to report

the rejection for a cognate tRNA in the presence of a chemically modified mRNA codon (as observed for IUG, m^1GUG, and Cm^1GU), showing that modifications can alter the capability of the ribosome to select cognate tRNAs.

The detailed analysis of the simulations further refined existing models of ribosomal monitoring. While the results support the prevailing hypothesis that A1492–3 and G530 contribute to codon recognition via solvent shielding of the minihelix minor groove,[86, 87] additional subtle effects were sampled in the simulation trajectories that provide additional context to the experiments. For GUG, CGU, CIU, GUI, and GUm^1G, shielding enhanced the optimal codon-anticodon WCF geometries. In disrupted systems (e.g., IUG, m^1GUG, and Cm^1GU), solvent exposure led to destabilizing water-mediated interactions. However, a subset of perturbed systems (GUG^{Met}, IUG^{Met}, and GUm^2G) revealed the unexpected finding that the minor groove could become dehydrated, yet still stabilize a perturbed codon-anticodon minihelix structure. This finding suggests that solvent shielding of the minihelix minor groove may serve as a critical feature to allow ambiguous substrates to enter proofreading, where structural misalignment or instability during accommodation ultimately prevents successful decoding.

5.1.3 MD simulations suggest two alternative aa-tRNA rejection pathways

Together, the insights from this thesis can be integrated into the existing mechanistic framework of tRNA selection. The simulations performed in this thesis suggest that mRNA modifications modulate tRNA rejection pathways and can be organized into two different tRNA rejection pathways.

Pathway 1: Immediate rejection

The first pathway is characterized by early, geometry-driven discrimination that occurs following codon recognition. Prior work has shown that near-cognate aa-tRNAs enter the codon recognition state with rates similar to those of cognate tRNAs, implying that discrimination

occurs only after this initial engagement. [16] The simulations in this thesis support a model in which improper codon-anticodon geometry prevents the formation of a productive decoding center conformation. As a result, the dissociation rate is accelerated, and all three ribosomal monitoring bases (A1492, A1493, and G530) disengage within tens to hundreds of nanoseconds. This disengagement is accompanied by distortion of the codon-anticodon minihelix, loss of the bent tRNA conformation, and full aa-tRNA dissociation from the mRNA codon. As mentioned in Section 5.1.2, the rejected tRNA typically adopts an orientation nearly perpendicular to the P-site tRNA, indicating failed codon recognition, as observed in previous SBM simulations of near-cognate aa-tRNAs.[46] This rejection pathway was most prominent for the IUG, m^1GUG, and Cm^1GU systems in the simulations performed for this thesis. Immediate rejection likely also occurs for multiple mismatch-containing (i.e., non-cognate) aa-tRNAs, as they have identical forward rates of codon recognition (k_2 in Figure 1.2A) to cognate and near-cognate aa-tRNAs, but never undergo GTPase activation (k_3 in Figure 1.2A).[3, 12, 13] The simulations revealed that the structural features characteristic of immediate rejection can be fully captured using the ribosomal A-site model.

Pathway 2: Delayed or conditional rejection

The second pathway appears to represent cases in which the ribosome is more permissive, allowing ambiguous or near-cognate TCs to persist in the A-site despite subtle geometric incompatibilities between the codon and anticodon. In this pathway, the monitoring bases remain at least partially engaged, and G530 may still latch onto the minor groove, hypothetically enabling SSU domain closure. This could, in principle, trigger GTP hydrolysis by EF-Tu even if the codon-anticodon geometry is imperfect. However, minor misalignments in the A-site may interfere with downstream steps, such as tRNA accommodation. Indeed, previous simulation studies have shown that misalignment of aa-tRNA perturbs the trajectory of motion

of aa-tRNA along the accommodation corridor,[46] in agreement with the drastically slowed accommodation rates for near-cognate aa-tRNA relative to cognate aa-tRNA.[3, 46] While the simulations in this thesis do not model chemical reactions and thus do not purport to predict post-GTP hydrolysis outcomes, the reduced tendency for outright rejection by the lack of full aa-tRNA dissociation for the GUG^{Met}, IUG^{Met}, and GUm^{2}G systems suggests that these TCs may follow the second pathway.

The MD simulations performed in this thesis provide novel structural insights into how select naturally-occurring mRNA modifications may cause the ribosome to utilize multiple strategies to reject different tRNA substrates at the A-site. However, the structural roles of numerous other RNA modifications remain unknown. Section 5.2 discusses how the ribosome A-site model developed in this thesis can be used to better characterize the structural and functional roles of other RNA modifications

5.2 Future directions

The highly conserved three-dimensional architectures of A-site ribosomal components, along with the consistent conformations observed in trapped intermediate states, reflect evolutionary pressure to maintain a universal mechanism for decoding. This conservation supports the general applicability of the A-site truncation model developed in this thesis for studying diverse RNA modifications during initial selection. As detailed in Chapter 2, a single template ribosome structure was used throughout Chapters 3 and 4, with the tRNA sequence substituted to match tRNA^{Val}, tRNA^{Arg}, and tRNA^{Met}, and the A-site codon sequence and chemical composition modified to the GUG and CGU codons and their corresponding modified variants. Given the established versatility of the A-site model, it can reasonably be applied in future work to investigate a wide range of modification contexts.

Further applications of the model developed in this thesis may include exploring the roles of many of the mRNA modifications covered in Chapter 1 that have postulated roles during initial selection. For example, the Koutmou group has collected data for the position-dependent effects of various artificial mRNA modifications on the rate of dipeptide formation.[45] This includes data for the locked nucleic acid modification (LNA; Figure 5.1), the unlocked modification (UNA; Figure 5.1), and the 2'-fluoro modification (FNA; Figure 5.1) in all three codon positions. The collected data all show remarkable differences in position-dependent impacts as were observed for the inosine and methylguanosine modifications explored in this thesis. MD simulations would be able to clarify the observed experimental measurements in a similar manner. As artificial mRNAs gain recognition as powerful therapeutics, [18] these simulations may offer mechanistic insight into the roles of synthetic modifications during translation before clinical application.

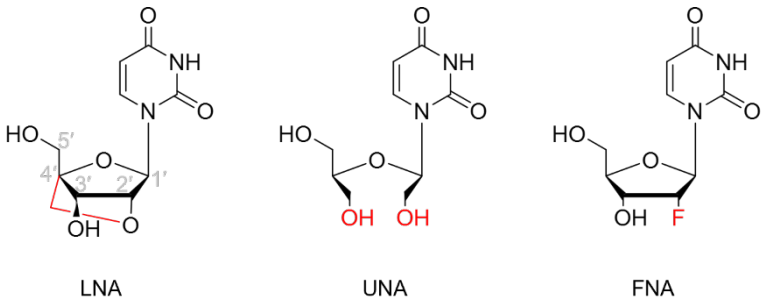

Figure 5.1. Representative artificial mRNA modifications with potential therapeutic use. Abbreviations: LNA=locked nucleic acid, UNA=unlocked nucleic acid, and FNA=2'-fluorinated nucleic acid.

Although the model used in this thesis was scientifically robust and significant work was undertaken to optimize simulation speeds (approximately 50-130 ns per day, see Chapter 2), the simulations required substantial hardware utilization per replica (2–6 V100l, P100, A100, A40, A4000, or A4500 GPUs along with 8–16 AMD EPYC 7413, Intel Gold 6148 Skylake, Intel 5-2650 v4 Broadwell, or Intel Silver 4216 Cascade Lake CPUs). The use of virtual sites was excluded to preserve accuracy in hydrogen bonding, but the actual impact of this decision should be further

evaluated. If virtual sites can be incorporated without significant loss of accuracy, then simulation speeds could nearly double using the same resources. This would enable the simulations to be performed with less computational burden.

To expand on the hypotheses proposed in Section 5.1.3 regarding the second rejection pathway, SBM simulation approaches could provide complementary insights into how position-dependent modifications influence accommodation trajectories, which occur on millisecond timescales.[12] Software like SMOG (discussed in Chapter 2) supports the inclusion of chemical modifications and is well suited for modeling these broader motions. [88-95]

Finally, although not implemented in this thesis, FEP methods offer valuable potential for quantitatively linking simulation outputs to experimental kinetics, as discussed in Chapter 2.[87, 96, 97] FEP simulations can be performed on models containing structural intermediates during decoding, which makes them useful for understanding how modifications alter the free energy landscape during codon recognition, GTPase activation, and accommodation. These simulations could therefore complement the aaMD A-site ribosomal model simulations to understand the impact of mRNA modifications on the structure-based energetics of tRNA selection.

5.3 Final remarks

Overall, this thesis provided novel mechanistic insights into the context-dependent roles of the inosine, m^1G, and m^2G mRNA modifications in ribosomal decoding. The ribosomal A-site model developed herein proved highly effective in rationalizing experimental kinetic data and offered a level of mechanistic detail not accessible through current experimental techniques. The simulations demonstrated how dynamics within the decoding center play a central role in directing aa-tRNA selection. The strength of the computational approach developed in this thesis suggests that a similar protocol can be applied to investigate a wide range of rRNA, tRNA, and mRNA modifications to uncover their roles during translation.

5.4 References

(1) Alberts, B.; Johnson, A.; Lewis, J.; Raff, M.; Roberts, K.; Walter, P. The RNA World and the Origins of Life. *MBoC* 4th ed.; Garland Science, 2002.

(2) Knight, J. R. P.; Garland, G.; Pöyry, T.; Mead, E.; Vlahov, N.; Sfakianos, A.; Grosso, S.; De-Lima-Hedayioglu, F.; Mallucci, G. R.; von der Haar, T.; et al. Control of translation elongation in health and disease. *Dis. Model. Mech.* **2020**, *13* (3). DOI: 10.1242/dmm.043208.

(3) Rodnina, M. V. Translation in Prokaryotes. *Cold Spring Harb Perspect Biol* **2018**, *10* (9). DOI: 10.1101/cshperspect.a032664.

(4) Brito Querido, J.; Díaz-López, I.; Ramakrishnan, V. The molecular basis of translation initiation and its regulation in eukaryotes. *Nat. Rev. Mol. Cell Biol.* **2024**, *25* (3), 168-186. DOI: 10.1038/s41580-023-00624-9.

(5) Dunkle, J. A.; Dunham, C. M. Mechanisms of mRNA frame maintenance and its subversion during translation of the genetic code. *Biochimie* **2015**, *114*, 90-96. DOI: 10.1016/j.biochi.2015.02.007.

(6) Boo, S. H.; Kim, Y. K. The emerging role of RNA modifications in the regulation of mRNA stability. *Exp. Mol. Med.* **2020**, *52* (3), 400-408. DOI: 10.1038/s12276-020-0407-z.

(7) Hoernes, T. P.; Hüttenhofer, A.; Erlacher, M. D. mRNA modifications: Dynamic regulators of gene expression? *RNA Biol.* **2016**, *13* (9), 760-765. DOI: 10.1080/15476286.2016.1203504.

(8) López, J.; Blanco, S. Exploring the role of ribosomal RNA modifications in cancer. *Curr. Opin. Genet. Dev.* **2024**, *86*, 102204. DOI: https://doi.org/10.1016/j.gde.2024.102204.

(9) Wang, L.; Lin, S. Emerging functions of tRNA modifications in mRNA translation and diseases. *J. Genet. Genom.* **2023**, *50* (4), 223-232. DOI: https://doi.org/10.1016/j.jgg.2022.10.002.

(10) Zhao, Y.; Rai, J.; Li, H. Regulation of translation by ribosomal RNA pseudouridylation. *Sci. Adv.* **2023**, *9* (33), eadg8190. DOI: doi:10.1126/sciadv.adg8190.

(11) Daviter, T.; Gromadski, K. B.; Rodnina, M. V. The ribosome's response to codon–anticodon mismatches. *Biochimie* **2006**, *88* (8), 1001-1011. DOI: https://doi.org/10.1016/j.biochi.2006.04.013.

(12) Gromadski, K. B.; Rodnina, M. V. Kinetic Determinants of High-Fidelity tRNA Discrimination on the Ribosome. *Mol. Cell* **2004**, *13* (2), 191-200. DOI: 10.1016/S1097-2765(04)00005-X (acccessed 2025/03/19).

(13) Pape, T.; Wintermeyer, W.; Rodnina, M. Induced-fit in initial selection and proofreading of aminoacyl-tRNA on the ribosome. *EMBO J.* **1999**, *18* (13), 3800-3807. DOI: https://doi.org/10.1093/emboj/18.13.3800.

(14) Peske, F.; Savelsbergh, A.; Katunin, V. I.; Rodnina, M. V.; Wintermeyer, W. Conformational changes of the small ribosomal subunit during elongation factor G-dependent tRNA–mRNA translocation. *J. Mol. Biol.* **2004**, *343* (5), 1183-1194.

(15) Petrychenko, V.; Peng, B. Z.; de, A. P. S. A. C.; Peske, F.; Rodnina, M. V.; Fischer, N. Structural mechanism of GTPase-powered ribosome-tRNA movement. *Nat. Commun.* **2021**, *12* (1), 5933. DOI: 10.1038/s41467-021-26133-x.

(16) Rodnina, M. V.; Fischer, N.; Maracci, C.; Stark, H. Ribosome dynamics during decoding. *Philosophical Transactions of the Royal Society B: Biological Sciences* **2017**, *372* (1716), 20160182. DOI: doi:10.1098/rstb.2016.0182.

(17) Franco, M. K.; Koutmou, K. S. Chemical modifications to mRNA nucleobases impact translation elongation and termination. *Biophys. Chem.* **2022**, *285*, 106780. DOI: 10.1016/j.bpc.2022.106780.

(18) Liu, A.; Wang, X. The Pivotal Role of Chemical Modifications in mRNA Therapeutics. *Front. Cell Dev. Biol.* **2022**, *10*, Review. DOI: 10.3389/fcell.2022.901510.

(19) Mendoza, H. G.; Beal, P. A. Structural and functional effects of inosine modification in mRNA. *RNA* **2024**, *30* (5), 512-520. DOI: 10.1261/rna.079977.124.

(20) Nunomura, A.; Lee, H.-g.; Zhu, X.; Perry, G. Consequences of RNA oxidation on protein synthesis rate and fidelity: implications for the pathophysiology of neuropsychiatric disorders. *Biochem. Soc. Trans.* **2017**, *45* (5), 1053-1066.

(21) Poulsen, H. E.; Specht, E.; Broedbaek, K.; Henriksen, T.; Ellervik, C.; Mandrup-Poulsen, T.; Tonnesen, M.; Nielsen, P. E.; Andersen, H. U.; Weimann, A. RNA modifications by oxidation: a novel disease mechanism? *Free Radic. Biol. Med.* **2012**, *52* (8), 1353-1361.

(22) Chen, X.-Y.; Zhang, J.; Zhu, J.-S. The role of m^6A RNA methylation in human cancer. *Mol. Cancer* **2019**, *18* (1), 103. DOI: 10.1186/s12943-019-1033-z.

(23) Huang, H.; Weng, H.; Chen, J. The biogenesis and precise control of RNA m^6A methylation. *Trends Genet.* **2020**, *36* (1), 44-52.

(24) Jain, S.; Koziej, L.; Poulis, P.; Kaczmarczyk, I.; Gaik, M.; Rawski, M.; Ranjan, N.; Glatt, S.; Rodnina, M. V. Modulation of translational decoding by m^6A modification of mRNA. *Nat. Commun.* **2023**, *14* (1), 4784. DOI: 10.1038/s41467-023-40422-7.

(25) Licht, K.; Hartl, M.; Amman, F.; Anrather, D.; Janisiw, M. P.; Jantsch, M. F. Inosine induces context-dependent recoding and translational stalling. *Nucleic Acids Res.* **2019**, *47* (1), 3-14. DOI: 10.1093/nar/gky1163.

(26) Hosaka, T.; Tsuji, H.; Kwak, S. RNA Editing: A New Therapeutic Target in Amyotrophic Lateral Sclerosis and Other Neurological Diseases. *Int. J. Mol. Sci.* **2021**, *22* (20). DOI: 10.3390/ijms222010958.

(27) Singh, M. Dysregulated A to I RNA editing and non-coding RNAs in neurodegeneration. *Front. Genet.* **2013**, *3*, 326.

(28) Costa Cruz, P. H.; Kawahara, Y. RNA editing in neurological and neurodegenerative disorders. *REMP* **2021**, 309-330.

(29) Zhu, X.; Zhang, Y.; Yang, X.; Hao, C.; Duan, H. Gene therapy for neurodegenerative disease: clinical potential and directions. *Front. Mol. Neurosci.* **2021**, *14*, 618171.

(30) Chan, T. H. M.; Lin, C. H.; Qi, L.; Fei, J.; Li, Y.; Yong, K. J.; Liu, M.; Song, Y.; Chow, R. K. K.; Ng, V. H. E. A disrupted RNA editing balance mediated by ADARs (Adenosine DeAminases that act on RNA) in human hepatocellular carcinoma. *Gut* **2014**, *63* (5), 832-843.

(31) Qin, Y.-R.; Qiao, J.-J.; Chan, T. H. M.; Zhu, Y.-H.; Li, F.-F.; Liu, H.; Fei, J.; Li, Y.; Guan, X.-Y.; Chen, L. Adenosine-to-inosine RNA editing mediated by ADARs in esophageal squamous cell carcinoma. *Cancer Res.* **2014**, *74* (3), 840-851.

(32) Chan, T. H.; Qamra, A.; Tan, K. T.; Guo, J.; Yang, H.; Qi, L.; Lin, J. S.; Ng, V. H.; Song, Y.; Hong, H.; et al. ADAR-Mediated RNA Editing Predicts Progression and Prognosis of Gastric Cancer. *Gastroenterology* **2016**, *151* (4), 637-650.e610. DOI: 10.1053/j.gastro.2016.06.043.

(33) Giraulo, C.; De Palma, G.; Plaitano, P.; Cicala, C.; Morello, S. Insight into adenosine pathway in psoriasis: Elucidating its role and the potential therapeutical applications. *Life Sci.* **2024**, *357*, 123071. DOI: https://doi.org/10.1016/j.lfs.2024.123071.

(34) Guo, X.; Wiley, C. A.; Steinman, R. A.; Sheng, Y.; Ji, B.; Wang, J.; Zhang, L.; Wang, T.; Zenatai, M.; Billiar, T. R.; et al. Aicardi-Goutières syndrome-associated mutation at ADAR1 gene locus activates innate immune response in mouse brain. *J. Neuroinflammation* **2021**, *18* (1), 169. DOI: 10.1186/s12974-021-02217-9.

(35) Picardi, E.; Manzari, C.; Mastropasqua, F.; Aiello, I.; D'Erchia, A. M.; Pesole, G. Profiling RNA editing in human tissues: towards the inosinome Atlas. *Sci. Rep.* **2015**, *5* (1), 14941.

(36) Doma, M. K.; Parker, R. Endonucleolytic cleavage of eukaryotic mRNAs with stalls in translation elongation. *Nature* **2006**, *440* (7083), 561-564. DOI: 10.1038/nature04530.

(37) Zaher, H. S.; Mosammaparast, N. RNA Damage Responses in Cellular Homeostasis, Genome Stability, and Disease. *Annu. Rev. Pathol.* **2025**, *20* (Volume 20, 2025), 433-457. DOI: https://doi.org/10.1146/annurev-pathmechdis-111523-023516.

(38) Thomas, E. N.; Simms, C. L.; Keedy, H. E.; Zaher, H. S. Insights into the base-pairing preferences of 8-oxoguanosine on the ribosome. *Nucleic Acids Res.* **2019**, *47* (18), 9857-9870. DOI: 10.1093/nar/gkz701 (acccessed 4/1/2025).

(39) Hoernes, Thomas P.; Clementi, N.; Faserl, K.; Glasner, H.; Breuker, K.; Lindner, H.; Hüttenhofer, A.; Erlacher, Matthias D. Nucleotide modifications within bacterial messenger RNAs regulate their translation and are able to rewire the genetic code. *Nucleic Acids Res.* **2015**, *44* (2), 852-862. DOI: 10.1093/nar/gkv1182 (acccessed 9/5/2024).

(40) You, C.; Dai, X.; Wang, Y. Position-dependent effects of regioisomeric methylated adenine and guanine ribonucleosides on translation. *Nucleic Acids Res.* **2017**, *45* (15), 9059-9067. DOI: 10.1093/nar/gkx515 (acccessed 9/5/2024).

(41) Hudson, B. H.; Zaher, H. S. O6-Methylguanosine leads to position-dependent effects on ribosome speed and fidelity. *RNA* **2015**, *21* (9), 1648-1659. DOI: 10.1261/rna.052464.115.

(42) Thomas, E. N.; Kim, K. Q.; McHugh, E. P.; Marcinkiewicz, T.; Zaher, H. S. Alkylative damage of mRNA leads to ribosome stalling and rescue by trans translation in bacteria. *eLife* **2020**, *9*, e61984. DOI: 10.7554/eLife.61984.

(43) Simms, C. L.; Zaher, H. S. Quality control of chemically damaged RNA. Cell. Mol. *Life Sci.* **2016**, *73* (19), 3639-3653. DOI: 10.1007/s00018-016-2261-7.

(44) Jones, J. D.; Franco, M. K.; Smith, T. J.; Snyder, L. R.; Anders, A. G.; Ruotolo, B. T.; Kennedy, R. T.; Koutmou, K. S. Methylated guanosine and uridine modifications in S. cerevisiae mRNAs modulate translation elongation. *RSC Chem. Biol.* **2023**, *4* (5), 363-378. DOI: 10.1039/d2cb00229a.

(45) Koutmou, K.; Giles, R. Private Communication. 2025.

(46) Girodat, D.; Wieden, H.-J.; Blanchard, S. C.; Sanbonmatsu, K. Y. Geometric alignment of aminoacyl-tRNA relative to catalytic centers of the ribosome underpins accurate mRNA decoding. *Nat. Commun.* **2023**, *14* (1), 5582. DOI: 10.1038/s41467-023-40404-9.

(47) Simms, C.; Yan, L.; Qiu, J.; Zaher, H. Ribosome Collisions Result in +1 Frameshifting in the Absence of No-Go Decay. *Cell Rep.* **2019**, *28*, 1679-1689.e1674. DOI: 10.1016/j.celrep.2019.07.046.

(48) Simms, C. L.; Hudson, B. H.; Mosior, J. W.; Rangwala, A. S.; Zaher, H. S. An active role for the ribosome in determining the fate of oxidized mRNA. *Cell Rep.* **2014**, *9* (4), 1256-1264. DOI: 10.1016/j.celrep.2014.10.042.

(49) Simms, C. L.; Thomas, E. N.; Zaher, H. S. Ribosome-based quality control of mRNA and nascent peptides. *WIREs RNA* **2017**, *8* (1), e1366. DOI: https://doi.org/10.1002/wrna.1366.

(50) Zhao, X.; Ma, D.; Ishiguro, K.; Saito, H.; Akichika, S.; Matsuzawa, I.; Mito, M.; Irie, T.; Ishibashi, K.; Wakabayashi, K.; et al. Glycosylated queuosines in tRNAs optimize translational rate and post-embryonic growth. *Cell* **2023**, *186* (25), 5517-5535.e5524. DOI: https://doi.org/10.1016/j.cell.2023.10.026.

(51) Tomono, J.; Asano, K.; Chiashi, T.; Suzuki, M.; Igarashi, M.; Takahashi, Y.; Tanaka, Y.; Yokoyama, T. Direct visualization of ribosomes in the cell-free system revealed the functional evolution of aminoglycoside. *J. Biochem.* **2024**, *175* (6), 587-598. DOI: 10.1093/jb/mvae002.

(52) McMullan, G.; Naydenova, K.; Mihaylov, D.; Yamashita, K.; Peet, M. J.; Wilson, H.; Dickerson, J. L.; Chen, S.; Cannone, G.; Lee, Y.; et al. Structure determination by cryoEM at 100 keV. *Proc. Natl. Acad. Sci. U.S.A.* **2023**, *120* (49), e2312905120. DOI: doi:10.1073/pnas.2312905120.

(53) Akiyama, N.; Ishiguro, K.; Yokoyama, T.; Miyauchi, K.; Nagao, A.; Shirouzu, M.; Suzuki, T. Structural insights into the decoding capability of isoleucine tRNAs with lysidine and agmatidine. *Nat. Struct. Mol. Biol.* **2024**, *31* (5), 817-825. DOI: 10.1038/s41594-024-01238-1.

(54) Watson, Z. L.; Knudson, I. J.; Ward, F. R.; Miller, S. J.; Cate, J. H. D.; Schepartz, A.; Abramyan, A. M. Atomistic simulations of the Escherichia coli ribosome provide selection criteria for translationally active substrates. *Nat. Chem.* **2023**, *15* (7), 913-921. DOI: 10.1038/s41557-023-01226-w.

(55) Watson, Z. L.; Ward, F. R.; Méheust, R.; Ad, O.; Schepartz, A.; Banfield, J. F.; Cate, J. H. Structure of the bacterial ribosome at 2 Å resolution. *eLife* **2020**, *9*, e60482.

(56) Agirrezabala, X.; Schreiner, E.; Trabuco, L. G.; Lei, J.; Ortiz-Meoz, R. F.; Schulten, K.; Green, R.; Frank, J. Structural insights into cognate versus near-cognate discrimination during decoding. *EMBO J.* **2011**, *30* (8), 1497-1507. DOI: https://doi.org/10.1038/emboj.2011.58.

(57) Loveland, A. B.; Demo, G.; Grigorieff, N.; Korostelev, A. A. Ensemble cryo-EM elucidates the mechanism of translation fidelity. *Nature* **2017**, *546* (7656), 113-117. DOI: 10.1038/nature22397.

(58) Nissley, Amos J.; Penev, Petar I.; Watson, Zoe L.; Banfield, Jillian F.; Cate, Jamie H. D. Rare ribosomal RNA sequences from archaea stabilize the bacterial ribosome. *Nucleic Acids Res.* **2023**, *51* (4), 1880-1894. DOI: 10.1093/nar/gkac1273 (acccessed 4/21/2025).

(59) Gersteuer, F.; Morici, M.; Gabrielli, S.; Fujiwara, K.; Safdari, H. A.; Paternoga, H.; Bock, L. V.; Chiba, S.; Wilson, D. N. The SecM arrest peptide traps a pre-peptide bond formation state of the ribosome. *Nat. Commun.* **2024**, *15* (1), 2431. DOI: 10.1038/s41467-024-46762-2.

(60) Majumdar, C.; Walker, J. A.; Francis, M. B.; Schepartz, A.; Cate, J. H. D. Aminobenzoic Acid Derivatives Obstruct Induced-fit in the Catalytic Center of the Ribosome. *ACS Cent. Sci.* **2023**, *9* (6), 1160-1169. DOI: 10.1021/acscentsci.3c00153.

(61) Rozov, A.; Demeshkina, N.; Khusainov, I.; Westhof, E.; Yusupov, M.; Yusupova, G. Novel base-pairing interactions at the tRNA wobble position crucial for accurate reading of the genetic code. *Nat. Commun.* **2016**, *7* (1), 10457. DOI: 10.1038/ncomms10457.

(62) Murphy, F. V.; Ramakrishnan, V.; Malkiewicz, A.; Agris, P. F. The role of modifications in codon discrimination by tRNALysUUU. *Nat. Struct. Mol. Biol.* **2004**, *11* (12), 1186-1191. DOI: 10.1038/nsmb861.

(63) Murphy, F. V.; Ramakrishnan, V. Structure of a purine-purine wobble base pair in the decoding center of the ribosome. *Nat. Struct. Mol. Biol.* **2004**, *11* (12), 1251-1252. DOI: 10.1038/nsmb866.

(64) DeMirci, H.; Destan, E. Crystal structure of the Thermus thermophilus (HB8) 30S ribosomal subunit with mRNA and cognate transfer RNA anticodon stem-loop and sisomicin derivative N1,3''Bz bound. **2022**. DOI: 10.2210/pdb7duj/pdb.

(65) Hoffer, E. D.; Hong, S.; Sunita, S.; Maehigashi, T.; Gonzalez, R. L. J.; Whitford, P. C.; Dunham, C. M. Structural insights into mRNA reading frame regulation by tRNA modification and slippery codon-anticodon pairing. *eLife* **2020**, *9*. DOI: 10.7554/eLife.51898.

(66) Dunham, C. M.; Selmer, M.; Phelps, S. S.; Kelley, A. C.; Suzuki, T.; Joseph, S.; Ramakrishnan, V. Structures of tRNAs with an expanded anticodon loop in the decoding center of the 30S ribosomal subunit. *RNA* **2007**, *13* (6), 817-823. DOI: 10.1261/rna.367307.

(67) Ogle, J. M.; Brodersen, D. E.; Clemons, W. M.; Tarry, M. J.; Carter, A. P.; Ramakrishnan, V. Recognition of Cognate Transfer RNA by the 30S Ribosomal Subunit. *Science* **2001**, *292* (5518), 897-902. DOI: doi:10.1126/science.1060612.

(68) Rozov, A.; Wolff, P.; Grosjean, H.; Yusupov, M.; Yusupova, G.; Westhof, E. Tautomeric G•U pairs within the molecular ribosomal grip and fidelity of decoding in bacteria. *Nucleic Acids Res.* **2018**, *46* (14), 7425-7435. DOI: 10.1093/nar/gky547.

(69) Demeshkina, N.; Jenner, L.; Westhof, E.; Yusupov, M.; Yusupova, G. A new understanding of the decoding principle on the ribosome. *Nature* **2012**, *484* (7393), 256-259. DOI: 10.1038/nature10913.

(70) Rozov, A.; Westhof, E.; Yusupov, M.; Yusupova, G. The ribosome prohibits the G•U wobble geometry at the first position of the codon–anticodon helix. *Nucleic Acids Res.* **2016**, *44* (13), 6434-6441. DOI: 10.1093/nar/gkw431.

(71) Rybak, M. Y.; Gagnon, M. G. Structures of the ribosome bound to EF-Tu–isoleucine tRNA elucidate the mechanism of AUG avoidance. *Nat. Struct. Mol. Biol.* **2024**, *31* (5), 810-816. DOI: 10.1038/s41594-024-01236-3.

(72) Voorhees, R. M.; Schmeing, T. M.; Kelley, A. C.; Ramakrishnan, V. The Mechanism for Activation of GTP Hydrolysis on the Ribosome. *Science* **2010**, *330* (6005), 835-838. DOI: doi:10.1126/science.1194460.

(73) Weixlbaumer, A.; Murphy, F. V.; Dziergowska, A.; Malkiewicz, A.; Vendeix, F. A. P.; Agris, P. F.; Ramakrishnan, V. Mechanism for expanding the decoding capacity of transfer RNAs by modification of uridines. *Nat. Struct. Mol. Biol.* **2007**, *14* (6), 498-502. DOI: 10.1038/nsmb1242.

(74) Kurata, S.; Weixlbaumer, A.; Ohtsuki, T.; Shimazaki, T.; Wada, T.; Kirino, Y.; Takai, K.; Watanabe, K.; Ramakrishnan, V.; Suzuki, T. Modified Uridines with C5-methylene Substituents at the First Position of the tRNA Anticodon Stabilize U·G Wobble Pairing during Decoding*. *Journal of Biological Chemistry* **2008**, *283* (27), 18801-18811. DOI: https://doi.org/10.1074/jbc.M800233200.

(75) Voorhees, R. M.; Mandal, D.; Neubauer, C.; Köhrer, C.; RajBhandary, U. L.; Ramakrishnan, V. The structural basis for specific decoding of AUA by isoleucine tRNA on the ribosome. *Nat. Struct. Mol. Biol.* **2013**, *20* (5), 641-643. DOI: 10.1038/nsmb.2545.

(76) Arenz, S.; Juette, M. F.; Graf, M.; Nguyen, F.; Huter, P.; Polikanov, Y. S.; Blanchard, S. C.; Wilson, D. N. Structures of the orthosomycin antibiotics avilamycin and evernimicin in complex

with the bacterial 70S ribosome. *Proc. Natl. Acad. Sci. U.S.A.* **2016**, *113* (27), 7527-7532. DOI: doi:10.1073/pnas.1604790113.

(77) Borovinskaya, M. A.; Pai, R. D.; Zhang, W.; Schuwirth, B. S.; Holton, J. M.; Hirokawa, G.; Kaji, H.; Kaji, A.; Cate, J. H. D. Structural basis for aminoglycoside inhibition of bacterial ribosome recycling. *Nat. Struct. Mol. Biol.* **2007**, *14* (8), 727-732. DOI: 10.1038/nsmb1271.

(78) Carter, A. P.; Clemons, W. M.; Brodersen, D. E.; Morgan-Warren, R. J.; Wimberly, B. T.; Ramakrishnan, V. Functional insights from the structure of the 30S ribosomal subunit and its interactions with antibiotics. *Nature* **2000**, *407* (6802), 340-348. DOI: 10.1038/35030019.

(79) James, N. R.; Brown, A.; Gordiyenko, Y.; Ramakrishnan, V. Translational termination without a stop codon. *Science* **2016**, *354* (6318), 1437-1440. DOI: doi:10.1126/science.aai9127.

(80) Brodersen, D. E.; Clemons, W. M.; Carter, A. P.; Morgan-Warren, R. J.; Wimberly, B. T.; Ramakrishnan, V. The Structural Basis for the Action of the Antibiotics Tetracycline, Pactamycin, and Hygromycin B on the 30S Ribosomal Subunit. *Cell* **2000**, *103* (7), 1143-1154. DOI: https://doi.org/10.1016/S0092-8674(00)00216-6.

(81) Wimberly, B. T.; Brodersen, D. E.; Clemons, W. M.; Morgan-Warren, R. J.; Carter, A. P.; Vonrhein, C.; Hartsch, T.; Ramakrishnan, V. Structure of the 30S ribosomal subunit. *Nature* **2000**, *407* (6802), 327-339. DOI: 10.1038/35030006.

(82) Petry, S.; Brodersen, D. E.; Murphy, F. V.; Dunham, C. M.; Selmer, M.; Tarry, M. J.; Kelley, A. C.; Ramakrishnan, V. Crystal Structures of the Ribosome in Complex with Release Factors RF1 and RF2 Bound to a Cognate Stop Codon. *Cell* **2005**, *123* (7), 1255-1266. DOI: https://doi.org/10.1016/j.cell.2005.09.039.

(83) Hoffer, E. D.; Maehigashi, T.; Fredrick, K.; Dunham, C. M. Ribosomal ambiguity (ram) mutations promote the open (off) to closed (on) transition and thereby increase miscoding. *Nucleic Acids Res.* **2019**, *47* (3), 1557-1563. DOI: 10.1093/nar/gky1178.

(84) Fislage, M.; Zhang, J.; Brown, Z. P.; Mandava, C. S.; Sanyal, S.; Ehrenberg, M.; Frank, J. Cryo-EM shows stages of initial codon selection on the ribosome by aa-tRNA in ternary complex with GTP and the GTPase-deficient EF-TuH84A. *Nucleic Acids Res.* **2018**, *46* (11), 5861-5874. DOI: 10.1093/nar/gky346.

(85) Ogle, J. M.; Murphy, F. V.; Tarry, M. J.; Ramakrishnan, V. Selection of tRNA by the Ribosome Requires a Transition from an Open to a Closed Form. *Cell* **2002**, *111* (5), 721-732. DOI: https://doi.org/10.1016/S0092-8674(02)01086-3.

(86) Sanbonmatsu, K. Y.; Joseph, S. Understanding Discrimination by the Ribosome: Stability Testing and Groove Measurement of Codon–Anticodon Pairs. *J. Mol. Biol.* **2003**, *328* (1), 33-47. DOI: 10.1016/s0022-2836(03)00236-5.

(87) Satpati, P.; Sund, J.; Åqvist, J. Structure-Based Energetics of mRNA Decoding on the Ribosome. *Biochemistry* **2014**, *53* (10), 1714-1722. DOI: 10.1021/bi5000355.

(88) Noel, J. K.; Whitford, P. C. How EF-Tu can contribute to efficient proofreading of aa-tRNA by the ribosome. *Nat. Commun.* **2016**, *7* (1), 13314. DOI: 10.1038/ncomms13314.

(89) Noel, Jeffrey K.; Chahine, J.; Leite, Vitor B. P.; Whitford, Paul C. Capturing Transition Paths and Transition States for Conformational Rearrangements in the Ribosome. *Biophys. J.* **2014**, *107* (12), 2881-2890. DOI: https://doi.org/10.1016/j.bpj.2014.10.022.

(90) Yang, H.; Noel, J. K.; Whitford, P. C. Anisotropic Fluctuations in the Ribosome Determine tRNA Kinetics. *J. Phys. Chem. B.* **2017**, *121* (47), 10593-10601. DOI: 10.1021/acs.jpcb.7b06828.

(91) Bui, P. T.; Hoang, T. X. Protein escape at the ribosomal exit tunnel: Effect of the tunnel shape. *J. Chem. Phys.* **2020**, *153* (4), 045105. DOI: 10.1063/5.0008292.

(92) Bui, P. T.; Hoang, T. X. Protein escape at the ribosomal exit tunnel: Effects of native interactions, tunnel length, and macromolecular crowding. *J. Chem. Phys.* **2018**, *149* (4).

(93) Nissley, D. A.; Vu, Q. V.; Trovato, F.; Ahmed, N.; Jiang, Y.; Li, M. S.; O'Brien, E. P. Electrostatic Interactions Govern Extreme Nascent Protein Ejection Times from Ribosomes and Can Delay Ribosome Recycling. *J. Amer. Chem. Soc.* **2020**, *142* (13), 6103-6110. DOI: 10.1021/jacs.9b12264.

(94) Takada, S. Gō model revisited. *Biophys. Physicobiol.* **2019**, *16*, 248-255. DOI: 10.2142/biophysico.16.0_248.

(95) de Oliveira, A. B., Jr.; Contessoto, V. G.; Hassan, A.; Byju, S.; Wang, A.; Wang, Y.; Dodero-Rojas, E.; Mohanty, U.; Noel, J. K.; Onuchic, J. N.; et al. SMOG 2 and OpenSMOG: Extending the limits of structure-based models. *Protein Sci.* **2022**, *31* (1), 158-172. DOI: 10.1002/pro.4209.

(96) Aqvist, J.; Lind, C.; Sund, J.; Wallin, G. Bridging the gap between ribosome structure and biochemistry by mechanistic computations. *Curr. Opin. Struct. Biol.* **2012**, *22* (6), 815-823. DOI: 10.1016/j.sbi.2012.07.008.

(97) Lind, C.; Esguerra, M.; Jespers, W.; Satpati, P.; Gutierrez-de-Terán, H.; Åqvist, J. Free energy calculations of RNA interactions. *Methods* **2019**, *162-163*, 85-95. DOI: https://doi.org/10.1016/j.ymeth.2019.02.014.

APPENDIX I: SUPPLEMENTARY INFORMATION FOR CHAPTER 2

Figures A.1 and Tables A.1 – 3

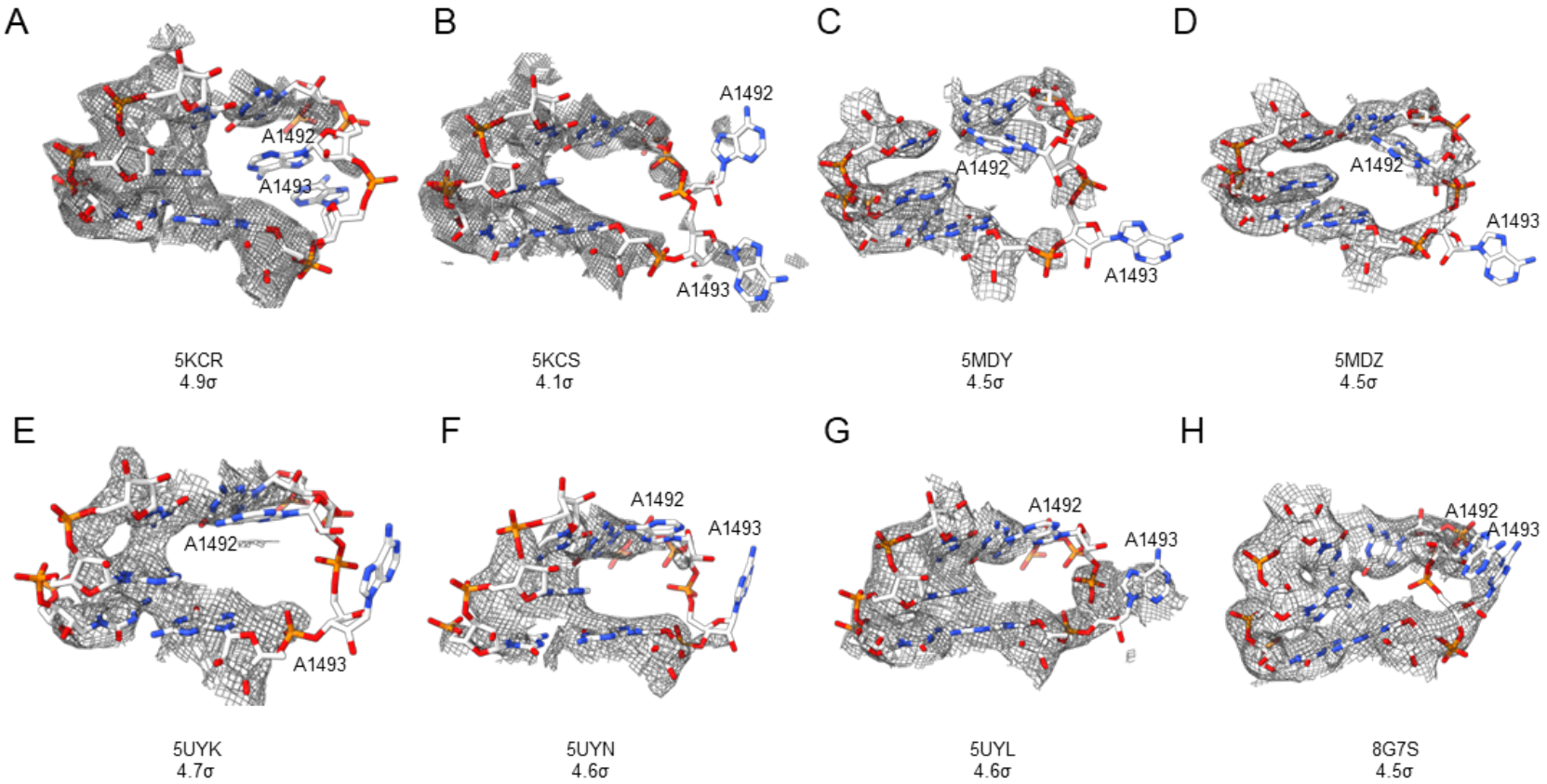

Figure A.1. (A-H) Map-model fits for various cryo-EM structures of 16S rRNA. The contour levels for the map density depictions are reported below each PDB ID code.

Table A.1. The counts for each component of each ribosomal A-site model.

tRNA	mRNA	Total atoms	Water	Mg^{2+}	K^{+}	Cl^{-}
Val	GUG	373,759	113,778	43	844	378
Val	IUG	373,757	113,778	43	844	378
Val	GUI	373,593	113,696	43	885	419
Arg	CGU	373,776	113,780	43	842	378
Arg	CIU	373,774	113,780	43	842	378
Met	GUG	373,815	113,777	43	845	378
Met	IUG	373,813	113,777	43	845	378
Val	m^1GUG	373,762	113,778	43	844	378
Val	Cm^1GU	373,779	113,780	43	842	378
Arg	GUm^1G	373,762	113,778	43	844	378
Val	m^2GUG	373,762	113,778	43	844	378
Val	Cm^2GU	373,779	113,780	43	842	378
Arg	GUm^2G	373,762	113,778	43	844	378

Table A.2. Simulation performance for the A-site ribosome model for a variety of hardware configurations.[a,b]

GPU count	GPU type	MPI tasks	CPU cores	CPU type	OpenMP threads	Performance (ns/day)
2	A100SXM4	2	4	AMD EPYC 7413 (Zen 3)	2	56.6
2	A100SXM4	2	8	AMD EPYC 7413 (Zen 3)	4	55.0
2	A100SXM4	2	16	AMD EPYC 7413 (Zen 3)	8	57.9
2	A100SXM4	2	24	AMD EPYC 7413 (Zen 3)	12	56.7
2	A100SXM4	2	32	AMD EPYC 7413 (Zen 3)	16	54.1
3	A100SXM4	3	6	AMD EPYC 7413 (Zen 3)	2	80.8
3	A100SXM4	3	6	AMD EPYC 7413 (Zen 3)	2	95.6
3	A100SXM4	3	12	AMD EPYC 7413 (Zen 3)	4	67.2
3	A100SXM4	3	24	AMD EPYC 7413 (Zen 3)	8	93.4
3	A100SXM4	3	36	AMD EPYC 7413 (Zen 3)	12	85.2
3	A100SXM4	3	48	AMD EPYC 7413 (Zen 3)	16	95.1
4	A100SXM4	4	8	AMD EPYC 7413 (Zen 3)	2	114.6
4	A100SXM4	4	16	AMD EPYC 7413 (Zen 3)	4	122.6
4	A100SXM4	4	32	AMD EPYC 7413 (Zen 3)	8	80.6
4	A100SXM4	4	48	AMD EPYC 7413 (Zen 3)	12	128.3

[a]The $tRNA^{Val}$ ribosome with a GUG codon model was used for these tests.

[b]All simulations enabled GPU offload and interconnect settings.

Table A.3. Monitoring angles (Φ) and conformations of the A1492–3 residues measured in 126 unique experimental ribosome structures along with the identity of the A-site tRNA, or "None" if not bound.[a,b]

PDB ID	Φ_{A1492}	Φ_{A1493}	A1492–3 Conformation	A-site tRNA
7Y7G	173.7	165.4	on-on	Cognate
8IFC	163.9	159.3	on-on	Cognate
7Y7E	173.8	164.8	on-on	Cognate
8PVA	172.6	164.6	on-on	Cognate
8HU1	177.1	170.1	on-on	Cognate
8EMM	165.0	157.3	on-on	Cognate
7Y7C	174.7	166.1	on-on	Cognate
7K00	169.4	161.6	on-on	Cognate
4V6K	173.5	158.7	on-on	Cognate
8HTZ	175.6	166.4	on-on	Cognate
7Y7H	174.4	167.5	on-on	Cognate
8HSP	174.8	165.2	on-on	Cognate
5UYM	171.0	160.3	on-on	Cognate
8EIU	169.0	161.7	on-on	Cognate
8QOA	174.7	160.3	on-on	Cognate
8G6W	163.9	154.7	on-on	Cognate
7Y7D	176.3	166.7	on-on	Cognate
5UYL[b]	44.1	146.6	off-on	Cognate
7Y7F	174.1	165.9	on-on	Cognate
5E7K	170.7	159.0	on-on	Cognate
1XMQ	153.3	149.5	on-on	Cognate
7DUJ	169.0	157.3	on-on	Cognate
6NTA	51.0	113.2	off-on	Cognate
1XMO	156.8	148.8	on-on	Cognate
2UXC	156.8	148.0	on-on	Cognate
6O3M	48.7	115.0	off-on	Cognate
7DUL	170.9	160.3	on-on	Cognate
1IBL	155.9	149.5	on-on	Cognate
1IBM	172.6	162.1	on-on	Cognate
1IBK	147.4	135.2	on-on	Cognate
6NUO	45.7	145.8	off-on	Cognate
6GSJ	171.9	159.1	on-on	Cognate
4V8D	167.9	160.4	on-on	Cognate
4V5S	174.5	165.3	on-on	Cognate
5E7K	169.9	161.3	on-on	Cognate
6O3M	46.3	149.5	off-on	Cognate
2UXD	153.7	144.1	on-on	Cognate
5IBB	173.3	162.3	on-on	Cognate
6GSL	172.0	158.7	on-on	Cognate
6NTA	48.5	143.9	off-on	Cognate

4V5S	172.9	163.4	on-on	Cognate
7DUI	167.7	157.9	on-on	Cognate
4V5R	172.8	164.8	on-on	Cognate
6GSL	172.7	162.2	on-on	Cognate
2UXB	151.0	139.8	on-on	Cognate
7DUK	168.7	159.5	on-on	Cognate
1XNQ	156.6	146.6	on-on	Cognate
8G7P	170.9	162.7	on-on	Cognate
6NUO	49.0	115.7	off-on	Cognate
4V5L	154.7	147.0	on-on	Cognate
5IBB	175.2	164.4	on-on	Cognate
7DUG	168.7	157.7	on-on	Cognate
7DUH	165.5	156.8	on-on	Cognate
4V8D	172.8	166.2	on-on	Cognate
6GSJ	173.9	163.7	on-on	Cognate
2UUC	157.2	149.4	on-on	Cognate
2VQF	154.4	145.8	on-on	Cognate
1XNR	155.1	144.5	on-on	Cognate
4V8N	154.1	147.4	on-on	Cognate
2VQE	156.0	145.7	on-on	Cognate
4V8N	148.8	148.2	on-on	Cognate
2UUA	157.2	148.0	on-on	Cognate
2UU9	157.1	149.6	on-on	Cognate
2UUB	156.9	148.8	on-on	Cognate
8G7S[b]	111.2	160.8	on-on	None
5KCR[b]	346.3	293.7	off-on	None
4V5Y	156.2	130.8	on-on	None
4V5Y	144.8	120.2	on-on	None
5KCS	159.4	179.1	on-on	None
5KCS	159.4	179.1	on-on	None
1FJG	155.4	134.1	on-on	None
5MDY[b]	40.1	192.6	off-on	None
1HNW	50.3	36.2	off-off	None
1J5E	28.4	359.4	off-off	None
4V4S	52.5	4.8	off-off	None
4V4R	52.5	4.8	off-off	None
5MDZ[b]	44.7	188.3	off-on	None
1HNX	49.3	35.3	off-off	None
6BUW	59.7	116.0	off-on	None
5MDW	45.2	185.9	off-on	None
4V4T	52.5	4.8	off-off	None
6BUW	46.7	97.2	off-on	None
1HNZ	48.0	26.7	off-off	None
5UYK[b]	38.2	126.0	off-on	Near-Cognate

5UYP	166.5	138.5	on-on	Near-Cognate
5UYN[b]	45.3	130.8	off-on	Near-Cognate
4V6L	171.3	152.3	on-on	Near-Cognate
5WFS	174.2	163.4	off-on	Near-Cognate
5UYQ	172.5	158.1	on-on	Near-Cognate
5WF0	62.6	32.5	on-on	Near-Cognate
5WFK	113.8	151.1	off-off	Near-Cognate
5IB7	159.7	151.0	on-on	Near-Cognate
6BZ7	170.0	163.9	on-on	Near-Cognate
1N32	157.7	148.4	on-on	Near-Cognate
5IB7B	155.3	145.8	on-on	Near-Cognate
6OSI	57.8	118.0	on-on	Near-Cognate
6OPE	154.9	144.3	off-on	Near-Cognate
6BZ7	174.7	166.2	on-on	Near-Cognate
1N34	46.2	136.8	on-on	Near-Cognate
6NWY	124.5	113.6	off-on	Near-Cognate
5IB8	19.0	90.1	on-on	Near-Cognate
4V5Q	171.0	161.9	off-on	Near-Cognate
4V5P	174.2	166.2	on-on	Near-Cognate
4V8B	173.3	160.1	on-on	Near-Cognate
6OSI	136.2	118.1	on-on	Near-Cognate
1N33	158.5	147.3	on-on	Near-Cognate
6OJ2	154.1	142.7	on-on	Near-Cognate
6BZ8	171.0	167.2	on-on	Near-Cognate
6OJ2	153.9	145.2	on-on	Near-Cognate
6NSH	51.3	118.7	on-on	Near-Cognate
5IB8	176.0	163.5	off-on	Near-Cognate
6OPE	153.1	145.0	on-on	Near-Cognate
6NWY	65.5	120.8	on-on	Near-Cognate
6NSH	49.6	141.1	off-on	Near-Cognate
4V5PB	168.9	162.2	off-on	Near-Cognate
6GSK	174.5	161.4	on-on	Near-Cognate
6GSK	178.3	150.8	on-on	Near-Cognate
1N36	52.3	130.4	on-on	Near-Cognate
4V5Q	175.9	165.9	off-on	Near-Cognate
4V8B	170.7	160.3	on-on	Near-Cognate
6BZ8	171.4	162.7	on-on	Near-Cognate
4V8C	156.1	146.7	on-on	Near-Cognate
4V8C	156.5	148.3	on-on	Near-Cognate
8G7Q	158.4	151.9	on-on	Near-Cognate

[a]For PDB IDs with multiple molecules in the asymmetric unit, both sets of A1492–3 were measured and tabulated separately.

[b]Structures with poor A1492–3 map-model fit that were not included in the final dataset.

APPENDIX II: SUPPLEMENTARY INFORMATION FOR CHAPTER 3

Figures B.1–14 and Tables B.1–4

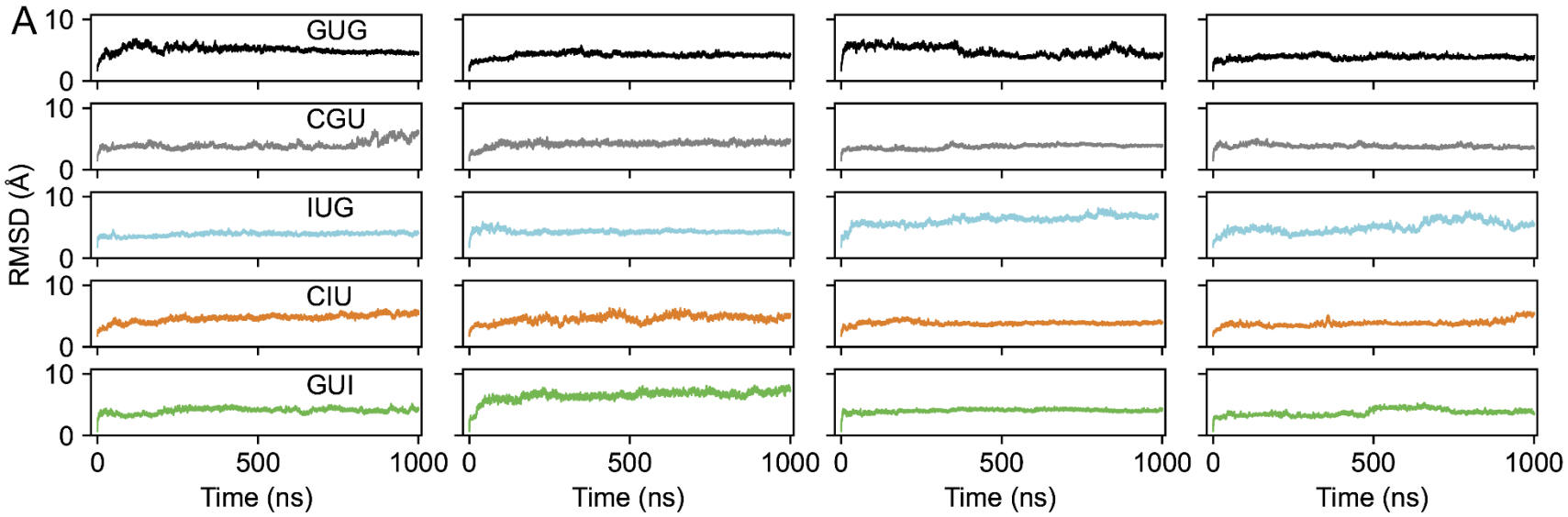

Figure B.1. Root-mean-squared deviation (RMSD) from the experimental structure during of MD simulations of the ribosomal A-site subsystem models. Backbone RMSD of the unrestrained residues of the ribosome system with respect to the starting structure coordinates as a function of simulation time for each model containing cognate $tRNA^{Val}$ or $tRNA^{Arg}$.

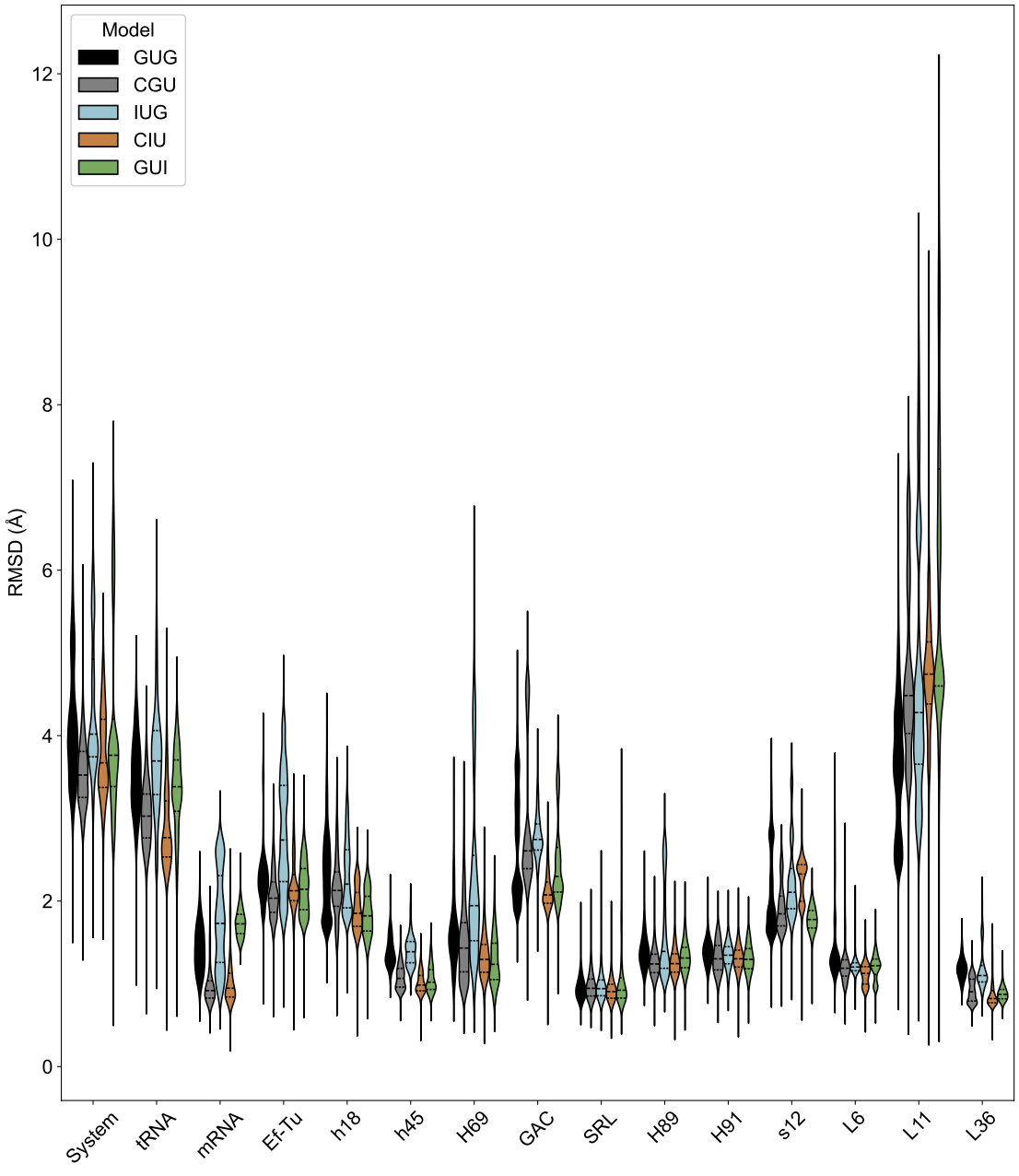

Figure B.2. Backbone structural deviation of system components from the experimental structure. Backbone RMSDs for each model containing cognate $tRNA^{Val}$ or $tRNA^{Arg}$ were computed over the entire quadruplicate ensemble. "System" includes the entire model with all unrestrained and restrained residues. The individual components include the tRNA, mRNA, elongation factor Tu (EF-Tu), helical domains of the 16S rRNA (h18 and h45), the 23S rRNA (H69, H89, and H91), rRNA domains such as the GTPase activating center (GAC) and Sarcin-ricin loop (SRL), and ribosomal proteins (s12, L11, and L36).

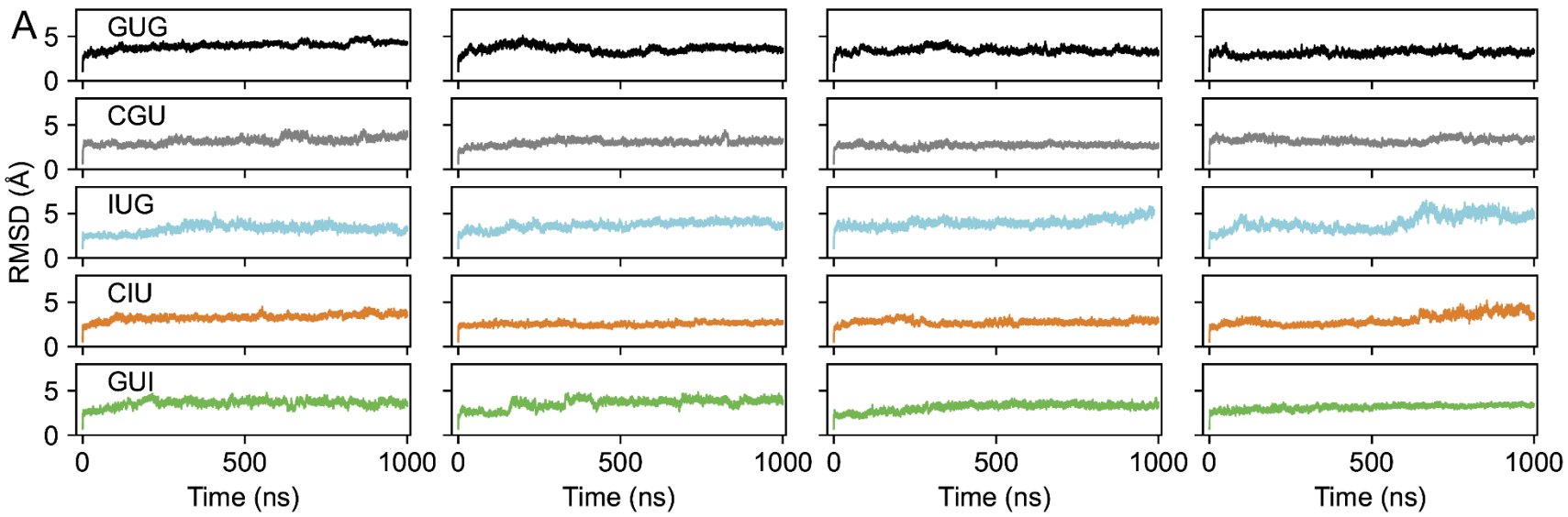

Figure B.3. Structural convergence of MD simulations of the ribosomal A-site tRNA. Backbone RMSD of the tRNA with respect to the starting coordinates as a function of simulation time for each model containing cognate $tRNA^{Val}$ or $tRNA^{Arg}$ where each column indicates an independent 1000 ns replica simulation.

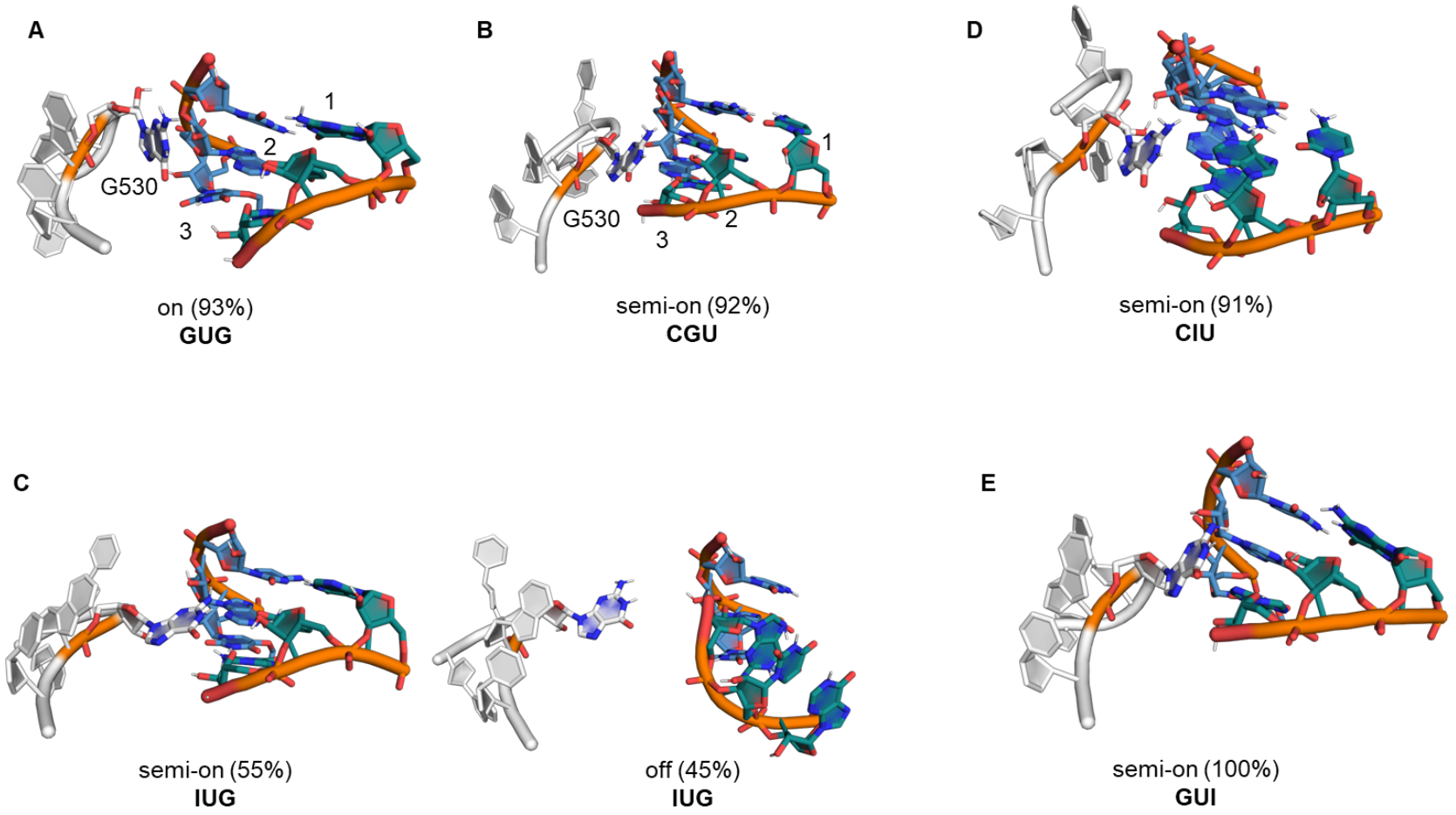

Figure B.4. G530 latching conformations and occupancies during the MD simulations across all models (see Figure 3.6A for definitions of "on", "semi-on" and "off" conformations). Conformation occupancies were obtained by cluster analysis applied to the heavy atoms of G530, the tRNA anticodon (B34-36; colored in blue), and the A-site mRNA codon (B1-3; colored in teal) for the quadruplicate ensemble of the GUG, CGU, IUG, CIU and GUI systems.

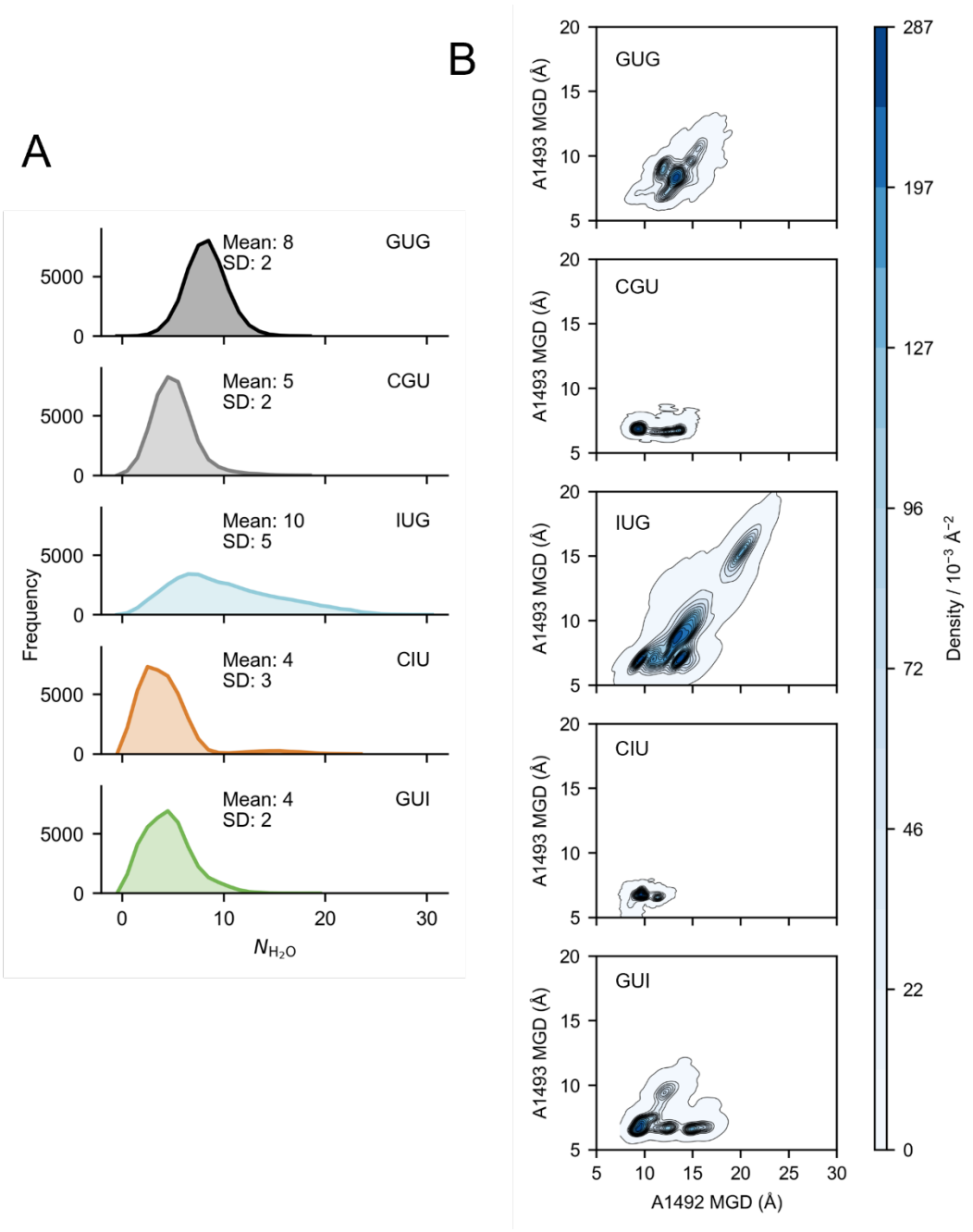

Figure B.5. Monitoring of the codon-anticodon minihelix by G530 and A1492–3 for cognate tRNA. (A) Histogram plot of the number of water molecules (N_{H_2O}) located within 5 Å of the minor groove for the first and second base-pairing positions of the codon-anticodon minihelix for the GUG, CGU, IUG, CIU, and GUI codons. (B) 2D Kernel density estimate plot of the A1492–3 minor groove distances (MGDs) for GUG, CGU, IUG, CIU, and GUI codons. The MGDs are defined as the distance between center of mass (COM) of the A1492 or A1493 nucleotide from the COM of the B2:B35 or B1:B36 base pair nucleotides, respectively. Darker blue regions represent higher occupation probabilities over each simulation ensemble and black contours show increments of ~1/15 of the estimated probability density range.

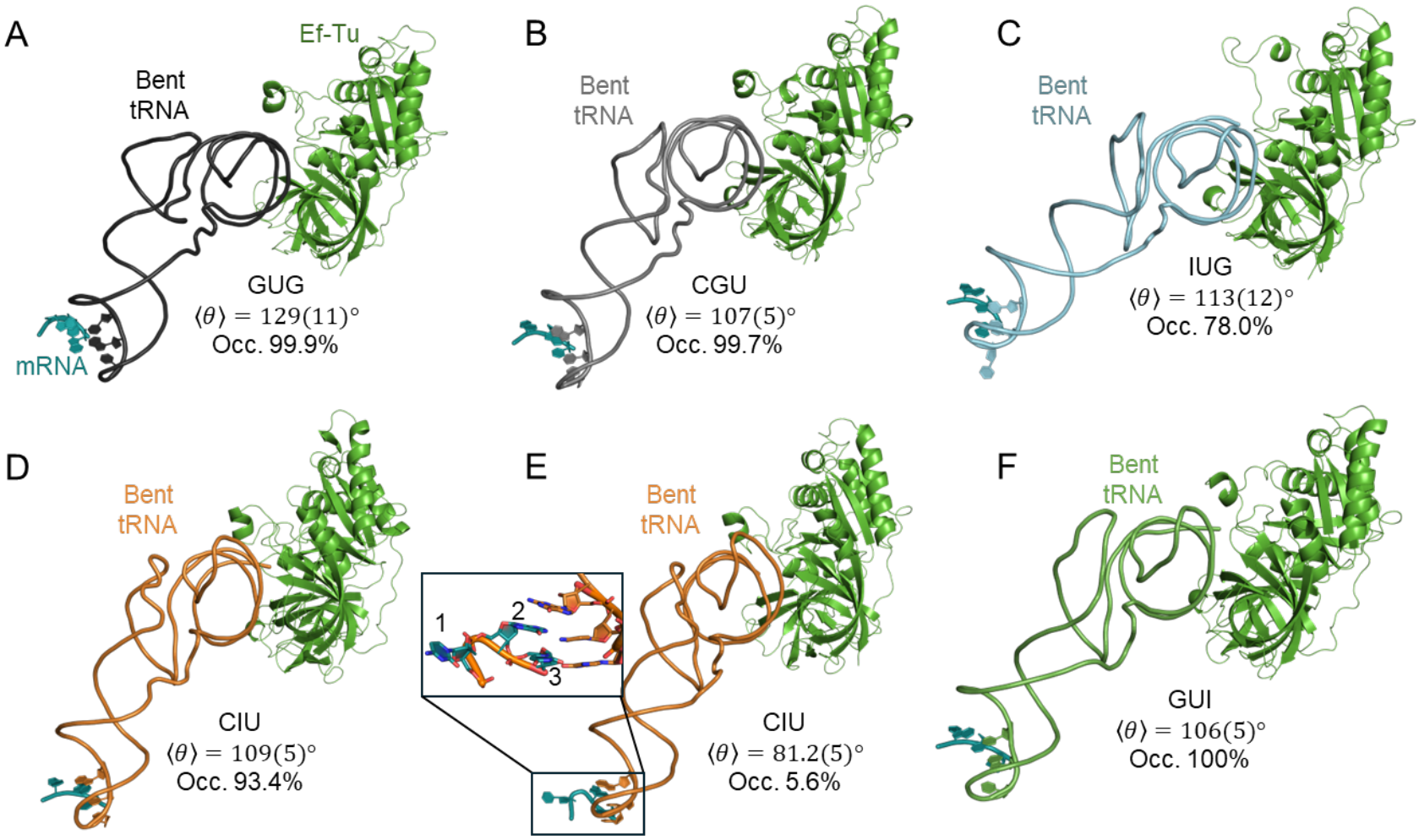

Figure B.6. Conformations of cognate aa-tRNAs in the A-site during MD simulations of the ribosomal subsystem. (A-F) Representative bent and straight tRNA conformations sampled with the corresponding ensemble-averaged θ values, $\langle\theta\rangle$ (standard deviations enclosed in parentheses), and occupancies for GUG (black), CGU (gray), IUG (cyan), CIU (orange), and GUI (green) in the A-site region. A zoomed-in view of the minihelix region is shown in (E) to visualize the 5′-disrupted minihelix conformation (see Figure 3.10) that was incorrectly assigned to the straightened region.

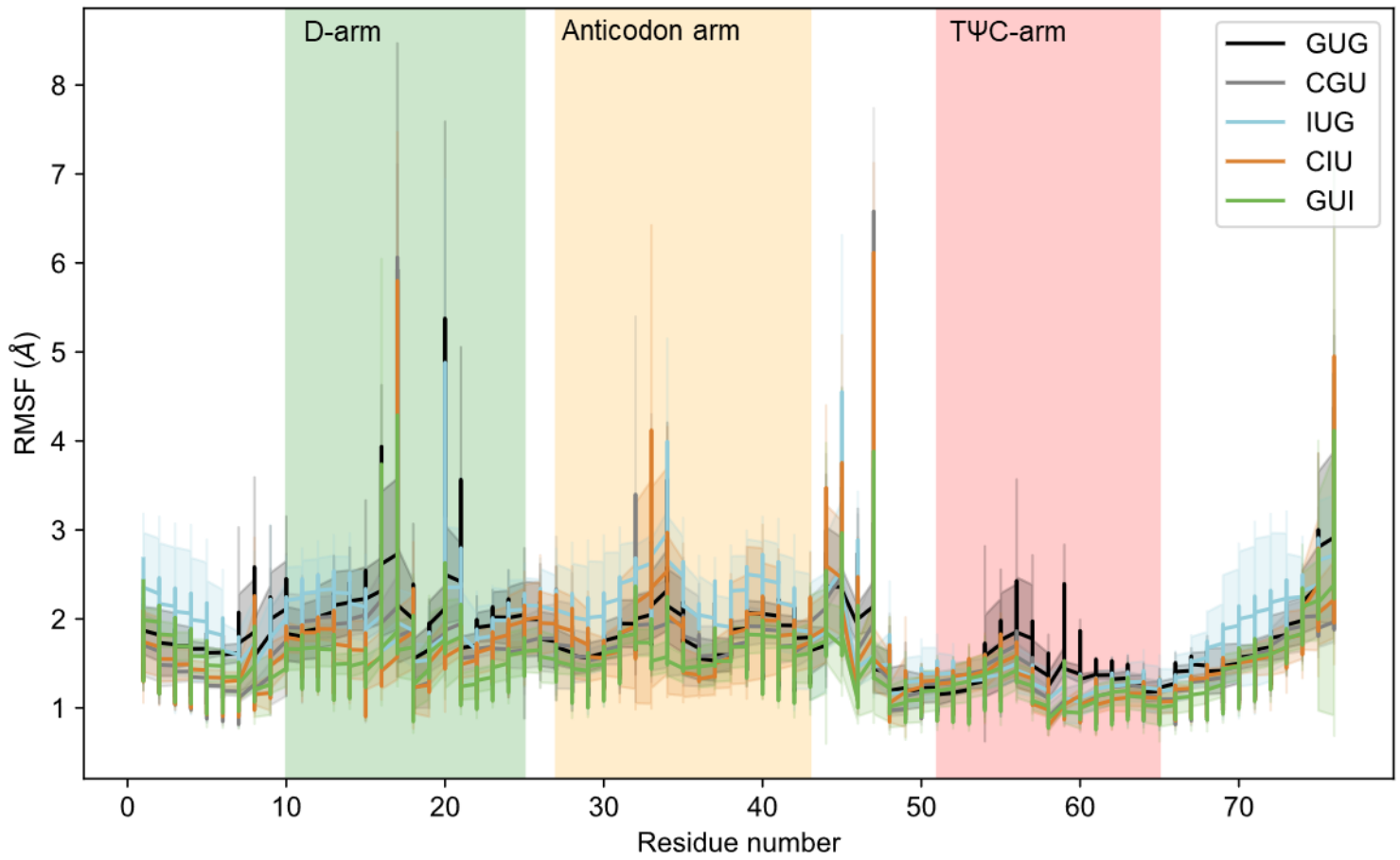

Figure B.7. Flexibility of the cognate aa-tRNAs over MD simulations as measured by root-mean-squared fluctuations (RMSFs). Ensemble-averaged per-residue RMSF line plot of each modified codon system with shaded tRNA domains (green: D-arm, yellow: anticodon arm, and red: TΨC arm). The standard deviations from the mean of each quadruplicate set of simulations is indicated by light shading centered on each line.

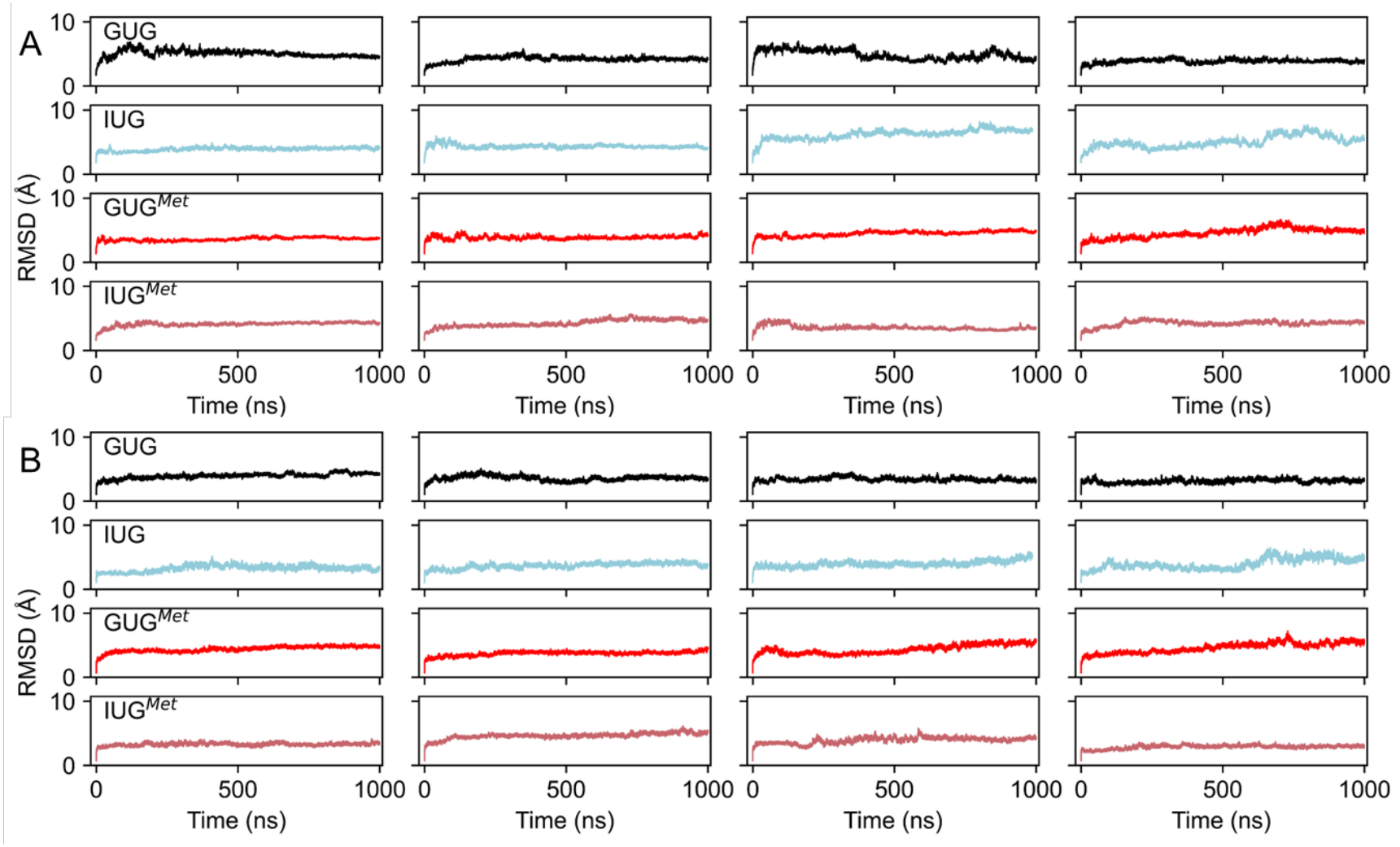

Figure B.8. Root-mean-squared deviation (RMSD) from the experimental structure during of MD simulations of the ribosomal A-site subsystem containing cognate tRNA^{Val} or near-cognate tRNA^{Met}. (A) Backbone RMSD of the unrestrained residues of the ribosome system with respect to the starting structure coordinates as a function of simulation time for each model. (B) Backbone RMSD of the tRNA with respect to the starting coordinates as a function of simulation time. Each column indicates an independent 1000 ns replica simulation.

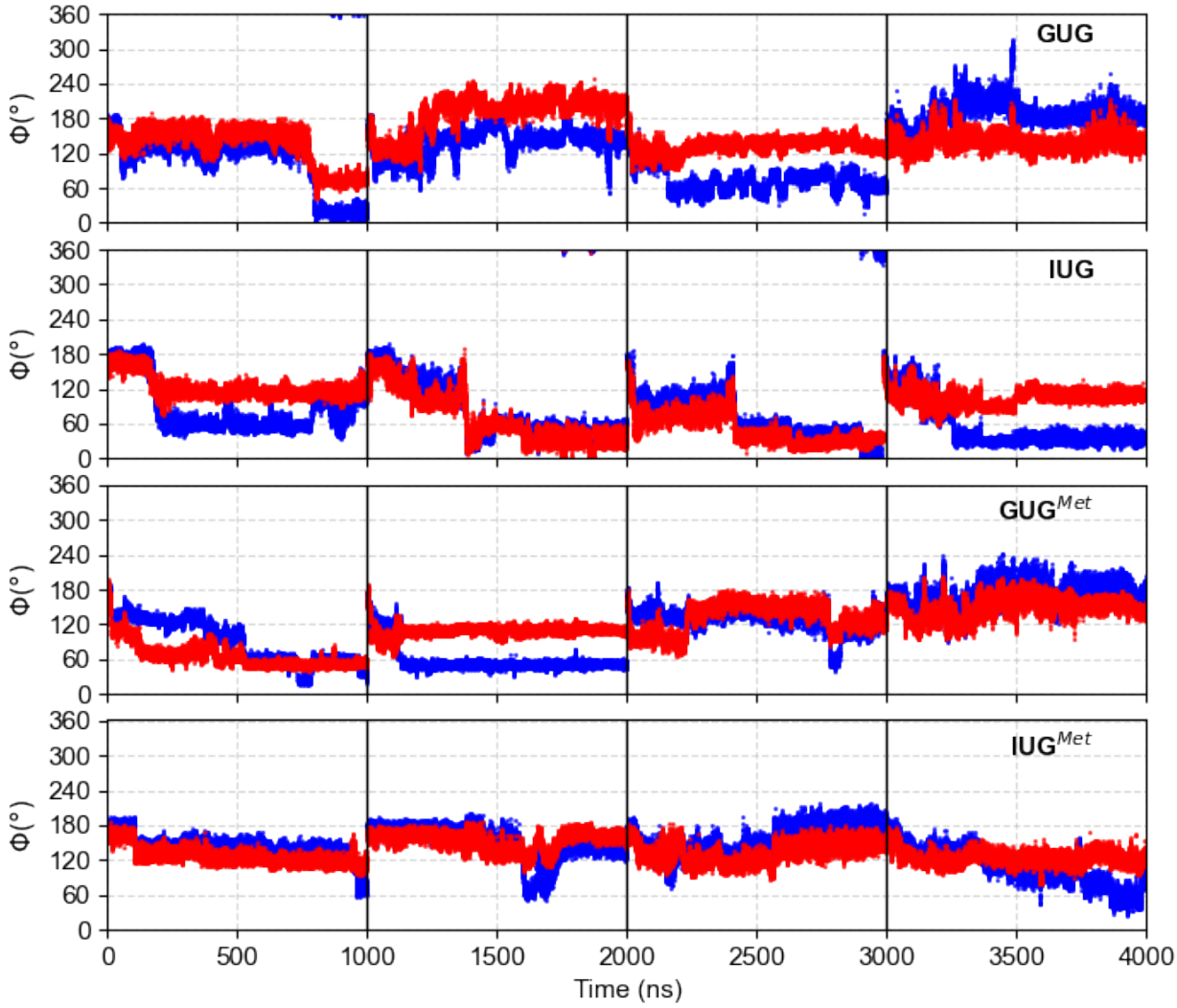

Figure B.9. Time series plots for the monitoring angles of A1492 (blue) and A1493 (red) over the simulations of the GUG and IUG codon ribosome subsystem model containing cognate tRNA^{Val} or near-cognate tRNA^{Met}. The independent replica simulations are separated by black lines in the order of replica 1-4.

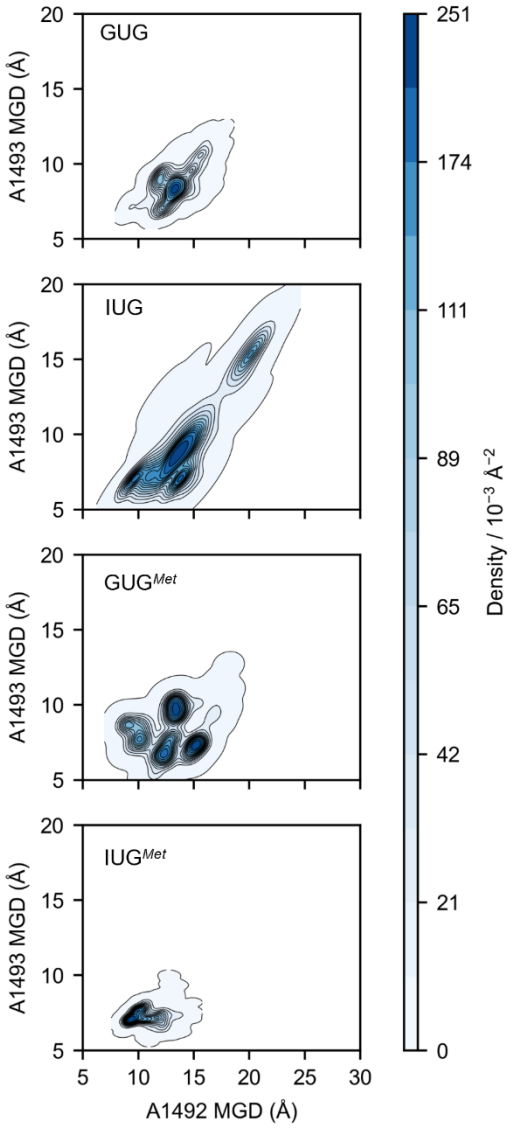

Figure B.10. 2D Kernel density estimate plot of the A1492–3 minor groove distances (MGDs) for ribosome subsystems containing cognate tRNA^{Val} or near-cognate tRNA^{Met}. The MGDs are defined as the distance between center of mass (COM) of the A1492 or A1493 nucleotide from the COM of the B2:B35 or B1:B36 base pair nucleotides, respectively. Darker blue regions represent higher occupation probabilities over each simulation ensemble and black contours show increments of ~1/15 of the estimated probability density range.

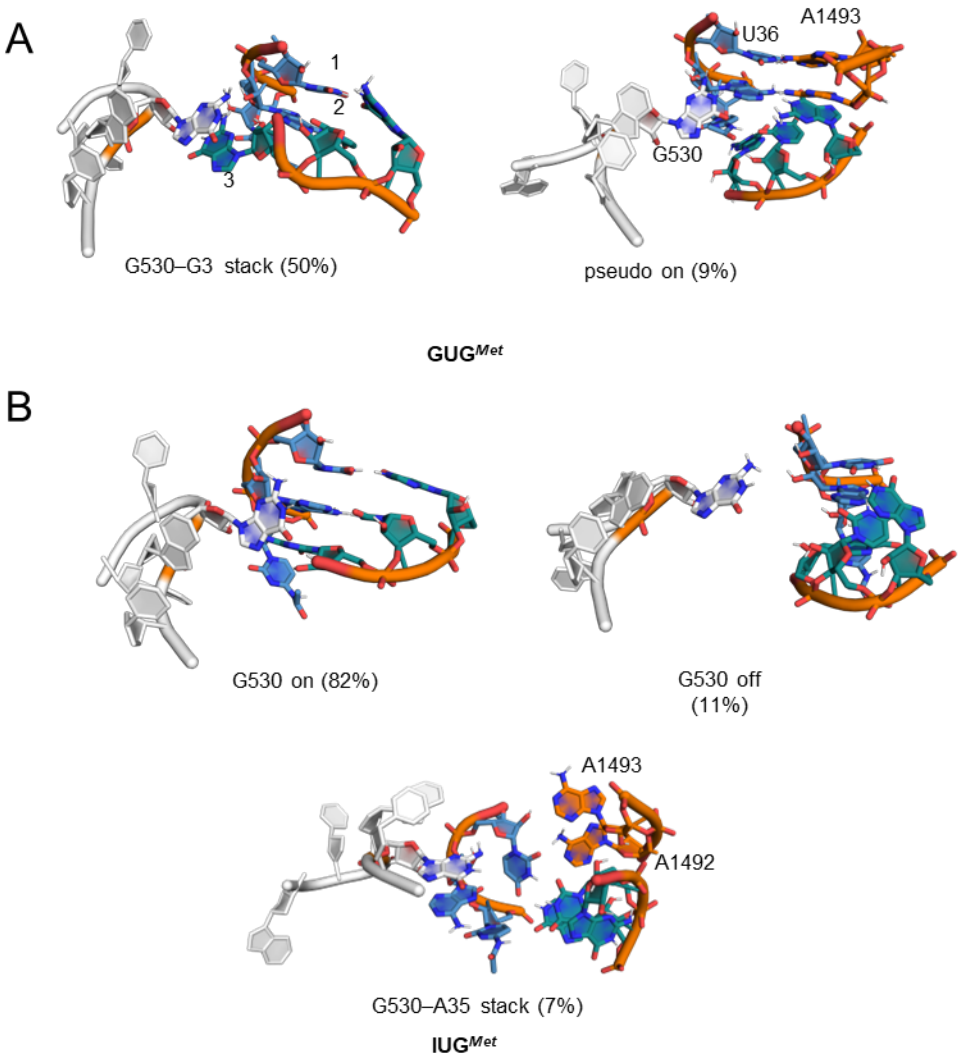

Figure B.11. G530 latching conformations in the presence of near-cognate tRNAs. Conformation occupancies were obtained by cluster analysis applied to the heavy atoms of G530, the tRNA anticodon (B34–36; colored in blue), and the A-site mRNA codon (B1–3; colored in teal) for the quadruplicate ensemble of the GUG^{Met} and IUG^{Met} systems

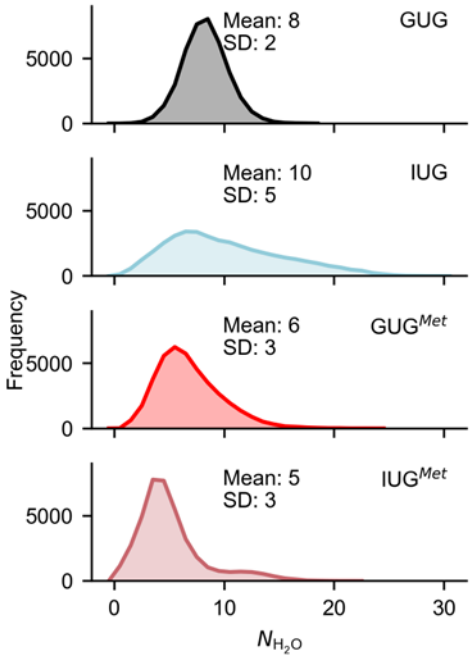

Figure B.12. Solvent shielding of the codon-anticodon minihelix by G530 and A1492–3 for near-cognate tRNA. Histogram plot of the number of water molecules (N_{H_2O}) located within 5 Å of the minor groove for the first and second base-pairing positions of the codon-anticodon minihelix for the GUG, IUG, GUG^{Met}, and IUG^{Met} codons.

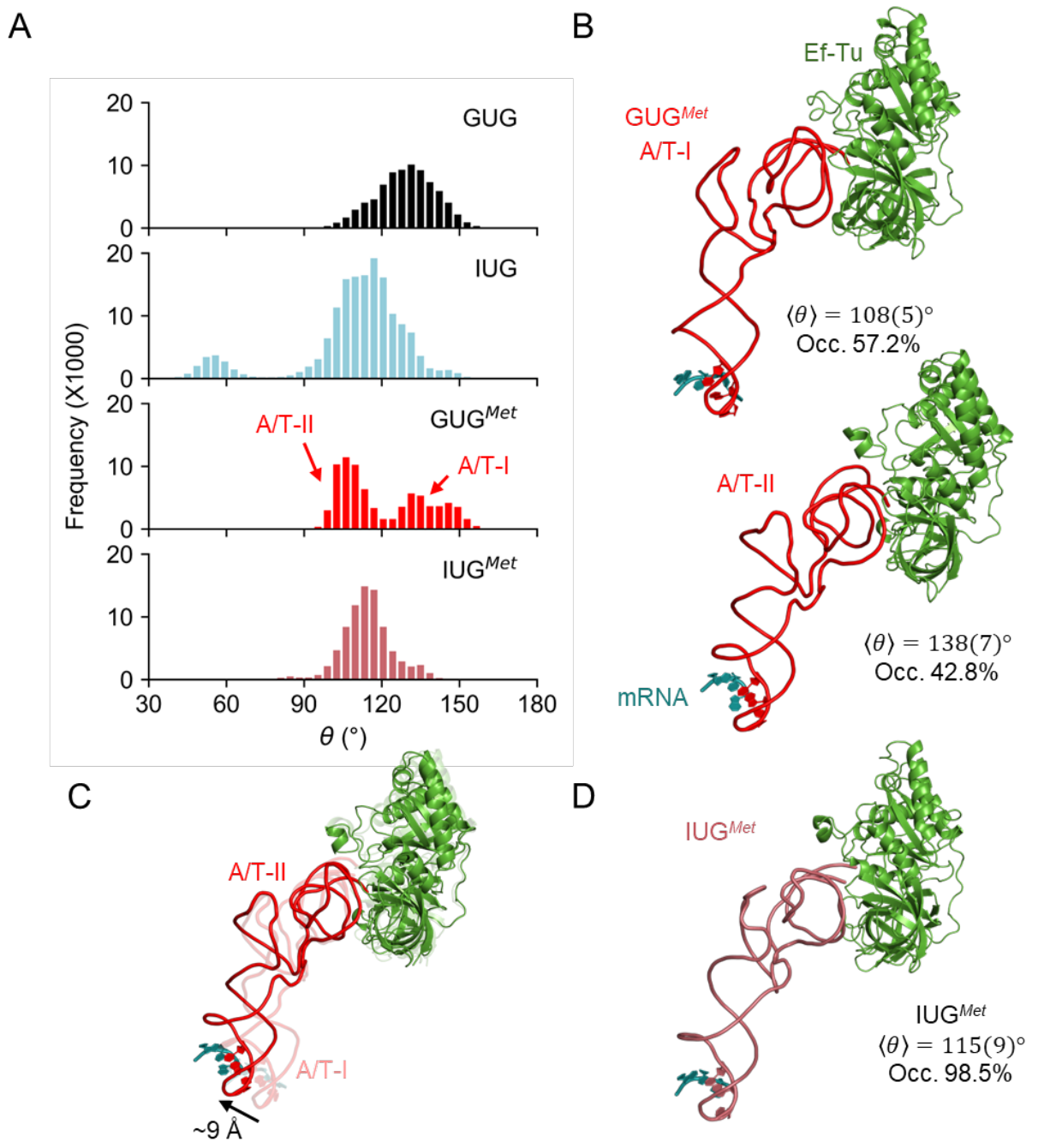

Figure B.13. Alignment and conformations of near-cognate tRNAs in the A-site. (A) Distribution of θ over the quadruplicate ensembles for each system. (B) Representative A/T tRNA conformations sampled during GUG^{Met} and IUG^{Met} simulations. (C) Overlay of the A/T-I and A/T-II states, where the A/T-I state is transparent. The corresponding ensemble-averaged θ values, $\langle\theta\rangle$, and occupancies for GUG^{Met} (red) and IUG^{Met} (pink) are next to each representative structure. (Occ. = Percent occupancy for the conformations).

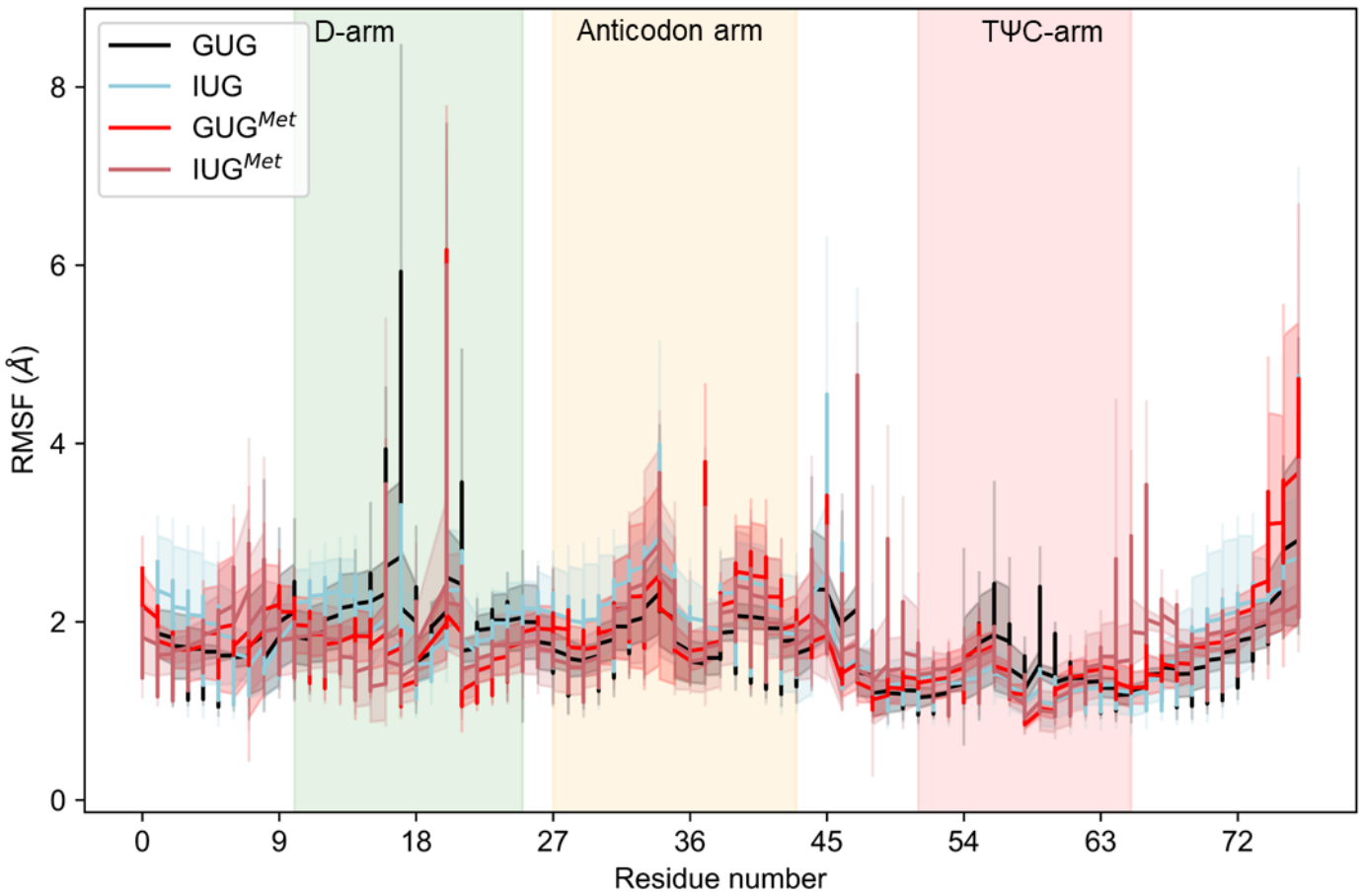

Figure B.14. Comparison between the per-residue root-mean-squared fluctuations (RMSFs) of cognate and near-cognate tRNA systems with GUG and IUG codons over MD simulations. Ensemble-averaged per-residue RMSF line plot of each modified codon system with shaded tRNA domains (green: D-arm, yellow: anticodon arm, and red: TΨC arm). The standard deviations from the mean of each quadruplicate set of simulations is indicated by light shading centered on each line.

Table B.1. Summary of mean RMSD and standard deviations for the backbone atoms of the flexible region of the ribosome subsystem model with respect to the experimental structure for each replica of 1000 ns MD simulations.

Model	Replica	Mean RMSD (Å)	Standard Deviation (Å)
GUG	1	5.07	0.5
	2	4.20	0.4
	3	4.87	0.7
	4	3.88	0.3
CGU	1	4.00	0.7
	2	4.19	0.4
	3	3.73	0.3
	4	3.82	0.3
IUG	1	3.89	0.3
	2	4.32	0.3
	3	6.21	0.7
	4	5.04	0.9
CIU	1	4.66	0.6
	2	4.56	0.6
	3	3.84	0.3
	4	3.81	0.5
GUI	1	4.03	0.4
	2	6.50	0.8
	3	4.04	0.2
	4	3.73	0.5
GUG^{Met}	1	3.60	0.3
	2	3.87	0.3
	3	4.47	0.4
	4	4.58	0.8
IUG^{Met}	1	4.10	0.3
	2	4.27	0.6
	3	3.56	0.4
	4	4.22	0.4

Table B.2. Summary of mean RMSD and standard deviations for the backbone atoms of the tRNA in the ribosome subsystem model with respect to experimental structure for each replica of 1000 ns MD simulations.

Model	Replica	Mean RMSD (Å)	Standard Deviation (Å)
GUG	1	3.94	0.4
	2	3.59	0.4
	3	3.42	0.3
	4	3.14	0.3
CGU	1	3.21	0.4
	2	3.02	0.3
	3	2.69	0.2
	4	3.26	0.3
IUG	1	3.25	0.5
	2	3.68	0.4
	3	3.96	0.5
	4	3.97	0.9
CIU	1	3.30	0.4
	2	2.54	0.2
	3	2.73	0.2
	4	3.02	0.6
GUI	1	3.59	0.4
	2	3.58	0.6
	3	3.14	0.4
	4	3.14	0.3
GUG^{Met}	1	4.40	0.4
	2	3.72	0.3
	3	4.32	0.7
	4	4.61	0.8
IUG^{Met}	1	3.27	0.2
	2	4.62	0.4
	3	3.91	0.5
	4	2.88	0.3

Table B.3. Average distance, angle and percent occupancy of hydrogen bonding interactions between the B1:B36, B2:B35 and B3:B34 base pairs for each model.[a]

Model	Base pair	Interaction	Occupancy (%)	Avg. Distance (Å)	Avg. Angle (°)
GUG	G1···C36	N3···H1-N1	98.93	2.97	162.8
	G1···C36	O2···H22-N2	51.74	2.87	162.2
	G1···C36	O2···H21-N2	46.74	2.87	162.3
	G1···C36	O2···H1-N1	22.56	3.26	134.1
	G1···C36	O6···H41-N4	74.82	2.91	162.5
	G1···C36	O6···H42-N4	23.36	2.90	161.3
	U2···A35	N1···H3-N3	98.03	2.97	162.7
	U2···A35	O4···H61-N6	45.68	2.99	158.7
	U2···A35	O4···H62-N6	44.03	2.99	158.8
	G3···OAU34	O4···H21-N2	24.18	2.94	153.1
	G3···OAU34	O4···H22-N2	23.18	2.93	153.2
	G3···OAU34	O4···H1-N1	19.66	2.93	153.3
	G3···OAU34	O32···H1-N1	9.18	2.95	148.9
	G3···OAU34	O30···H22-N2	9.16	2.98	138.1
	G3···OAU34	O31···H22-N2	9.09	2.96	155.2
	G3···OAU34	O31···H21-N2	9	2.95	155.8
	G3···OAU34	O32···H22-N2	8.71	2.95	154.9
	G3···OAU34	O32···H21-N2	8.66	2.95	155.1
	G3···OAU34	O30···H21-N2	8.47	2.98	138.1
	G3···OAU34	O31···H1-N1	7.97	2.95	149.1
	G3···OAU34	O32···HO2'-O2'	7.75	2.80	159.9
	G3···OAU34	O31···HO2'-O2'	5.45	2.81	159.2
CGU	C1···G36	O6···H42-N4	51.62	2.91	157.2
	C1···G36	O6···H41-N4	42.64	2.92	155.7
	C1···G36	N3···H1-N1	99.65	2.98	164.3
	C1···G36	O2···H21-N2	51.84	2.90	159.5
	C1···G36	O2···H22-N2	47.48	2.88	160.6
	C1···G36	O2···H1-N1	12.45	3.28	134.3
	C1···G36	N3···H21-N2	6.81	3.29	136.4
	C1···G36	N4···H1-N1	6.69	3.31	136.1
	C1···G36	N3···H22-N2	5.48	3.30	135.7
	G2···C35	N3···H1-N1	78.79	2.99	161.9
	G2···C35	O2···H1-N1	52.99	3.09	143.8
	G2···C35	O2···H21-N2	43.74	2.88	159.5
	G2···C35	O2···H22-N2	41.28	2.88	158.8
	G2···C35	O6···H41-N4	37.73	2.94	156.5
	G2···C35	O6···H42-N4	33.39	2.89	159.3
	U3···INO34	O6···H3-N3	86.28	2.90	155.8
	U3···INO34	O2···H1-N1	84.73	2.97	156.8

149 **Table B.3.** Continued.

IUG	INO1···C36	N3···H1-N1	74.62	3.00	159.2
	INO1···C36	O2···H1-N1	41.7	3.20	134.7
	INO1···C36	O6···H41-N4	57.08	2.94	161.6
	INO1···C36	O6···H42-N4	17.36	2.96	161.5
	U2···A35	N1···H3-N3	82.44	2.96	161.4
	U2···A35	O4···H61-N6	38.26	2.95	158.0
	U2···A35	O4···H62-N6	37.8	2.95	158.0
	G3···OAU34	O4···H1-N1	27.27	2.92	153.5
	G3···OAU34	O4···H21-N2	11.52	2.94	148.5
	G3···OAU34	O4···H22-N2	11.27	2.93	148.9
	G3···OAU34	O31···H1-N1	6.33	2.95	150.2
	G3···OAU34	O32···H1-N1	6.25	2.95	150.7
	G3···OAU34	N2···H3-N3	13.76	3.05	159.7
	G3···OAU34	O6···H3-N3	5.66	2.87	159.3
CIU	C1···G36	O6···H42-N4	48.12	2.91	156.7
	C1···G36	O6···H41-N4	38.16	2.92	155.5
	C1···G36	N3···H1-N1	91.63	2.99	164.7
	C1···G36	O2···H22-N2	54.04	2.89	160.0
	C1···G36	O2···H21-N2	37.36	2.90	159.5
	C1···G36	O2···H1-N1	10.04	3.29	134.8
	C1···G36	N4···H1-N1	5.36	3.30	136.2
	C1···G36	N3···H22-N2	5.05	3.31	136.0
	INO2···C35	N3···H1-N1	97.31	2.99	160.0
	INO2···C35	O2···H1-N1	73.67	3.15	136.5
	INO2···C35	O6···H41-N4	61.66	2.94	158.4
	INO2···C35	O6···H42-N4	30.61	2.93	159.1
	U3···INO34	O6···H3-N3	89.7	2.91	155.4
	U3···INO34	O2···H1-N1	82.68	2.95	155.0
GUI	G1···C36	N3···H1-N1	99.85	2.98	162.3
	G1···C36	O2···H22-N2	58.23	2.88	163.6
	G1···C36	O2···H21-N2	41.44	2.87	163.6
	G1···C36	O2···H1-N1	28.76	3.27	135.1
	G1···C36	O6···H41-N4	68.83	2.90	162.9
	G1···C36	O6···H42-N4	30.48	2.88	163.5
	U2···A35	N1···H3-N3	97.14	2.98	162.5
	U2···A35	O4···H61-N6	46.31	2.92	155.7
	U2···A35	O4···H62-N6	45.21	2.92	155.8
	INO3···OAU34	O2···H1-N1	57.85	2.99	156.0
	INO3···OAU34	O2'···H1-N1	37.82	2.98	153.9
	INO3···OAU34	O6···H3-N3	53.75	2.93	156.4

150

Table B.3. Continued.

GUG^{Met}	G1···U36	O2···H1-N1	66.17	2.94	154.0
	G1···U36	O6···H3-N3	76.51	2.91	157.4
	U2···A35	N1···H3-N3	78.70	2.985	158.4
	U2···A35	O4···H61-N6	34.24	2.976	158.2
	U2···A35	O4···H62-N6	33.16	2.976	158.4
	G3···4AC34	O2···H1-N1	7.12	2.970	154.3
	G3···4AC34	O30···H21-N2	6.21	2.962	157.4
	G3···4AC34	O30···H22-N2	5.69	2.963	157.8
	G3···4AC34	O30···HO2'-O2'	5.55	2.863	151.7
	G3···4AC34	O30···HO3'-O3'	5.49	2.904	148.5
	G3···4AC34	O2'···1H4-N4	12.56	3.042	153.5
	G3···4AC34	HO2'···1H4-N4	7.85	3.180	144.8
IUG^{Met}	INO1···U36	O2···H1-N1	78.36	2.995	161.0
	INO1···U36	O4···H1-N1	6.40	2.861	150.7
	INO1···U36	O6···H3-N3	83.49	2.871	158.8
	U2···A35	N1···H3-N3	81.06	2.982	160.3
	U2···A35	O4···H61-N6	42.51	2.920	159.0
	U2···A35	O4···H62-N6	42.07	2.920	159.2
	G3···4AC34	O2'···H1-N1	35.62	2.997	153.1
	G3···4AC34	N3···H1-N1	12.59	3.088	156.2
	G3···4AC34	O2···H22-N2	9.04	3.030	151.5
	G3···4AC34	O2···H21-N2	8.16	3.030	152.5
	G3···4AC34	O2···H1-N1	7.03	3.174	135.8
	G3···4AC34	O2'···H22-N2	6.64	3.103	142.8
	G3···4AC34	O2'···H21-N2	6.46	3.101	143.0
	G3···4AC34	O6···1H4-N4	17.94	2.891	154.9

[a]Acronyms, OAU = uridine-5-oxyacetic acid (cmo^{5}U), INO = inosine, 4AC = N^4-acetylcytidine.

Table B.4. Average RMSF values for domains of the tRNA in the ribosome subsystem models over the quadruplicate ensembles.[a]

Model	Domain	Mean RMSF (Å)	S.D.[b] (Å)
GUG	ASL	1.73	0.3
GUG	D-arm	2.11	0.7
GUG	TΨC-arm	1.34	0.3
GUG	V-loop	1.76	0.6
GUG	ACS	1.46	0.2
CGU	ASL	1.71	0.3
CGU	D-arm	1.75	0.6
CGU	TΨC-arm	1.17	0.2
CGU	V-loop	1.89	1.1
CGU	ACS	1.24	0.2
IUG	ASL	2.04	0.5
IUG	D-arm	1.93	0.5
IUG	TΨC-arm	1.21	0.2
IUG	V-loop	1.77	0.8
IUG	ACS	1.63	0.3
CIU	ASL	1.75	0.4
CIU	D-arm	1.61	0.5
CIU	TΨC-arm	1.12	0.2
CIU	V-loop	1.93	1.1
CIU	ACS	1.26	0.2
GUI	ASL	1.52	0.2
GUI	D-arm	1.53	0.5
GUI	TΨC-arm	1.08	0.2
GUI	V-loop	1.50	0.6
GUI	ACS	1.29	0.3
GUG^{Met}	ASL	1.93	0.4
GUG^{Met}	D-arm	1.72	0.6
GUG^{Met}	TΨC-arm	1.30	0.2
GUG^{Met}	V-loop	1.78	0.6
GUG^{Met}	ACS	1.63	0.3
IUG^{Met}	ASL	1.88	0.4
IUG^{Met}	D-arm	1.73	0.6
IUG^{Met}	TΨC-arm	1.37	0.3
IUG^{Met}	V-loop	1.97	0.6
IUG^{Met}	ACS	1.77	0.4

[a]ASL domain (anticodon stem loop, residues 27–43), D-arm (residues 10–25), TΨC-arm (residues 51–65), V-loop (variable loop, residues 44–50) and ACS (acceptor stem; residues 1–8 and 66–72)

[b]Standard deviation of the mean RMSF

APPENDIX III: SUPPLEMENTARY INFORMATION FOR CHAPTER 4

Figures C.1–9 and Tables C.1–6

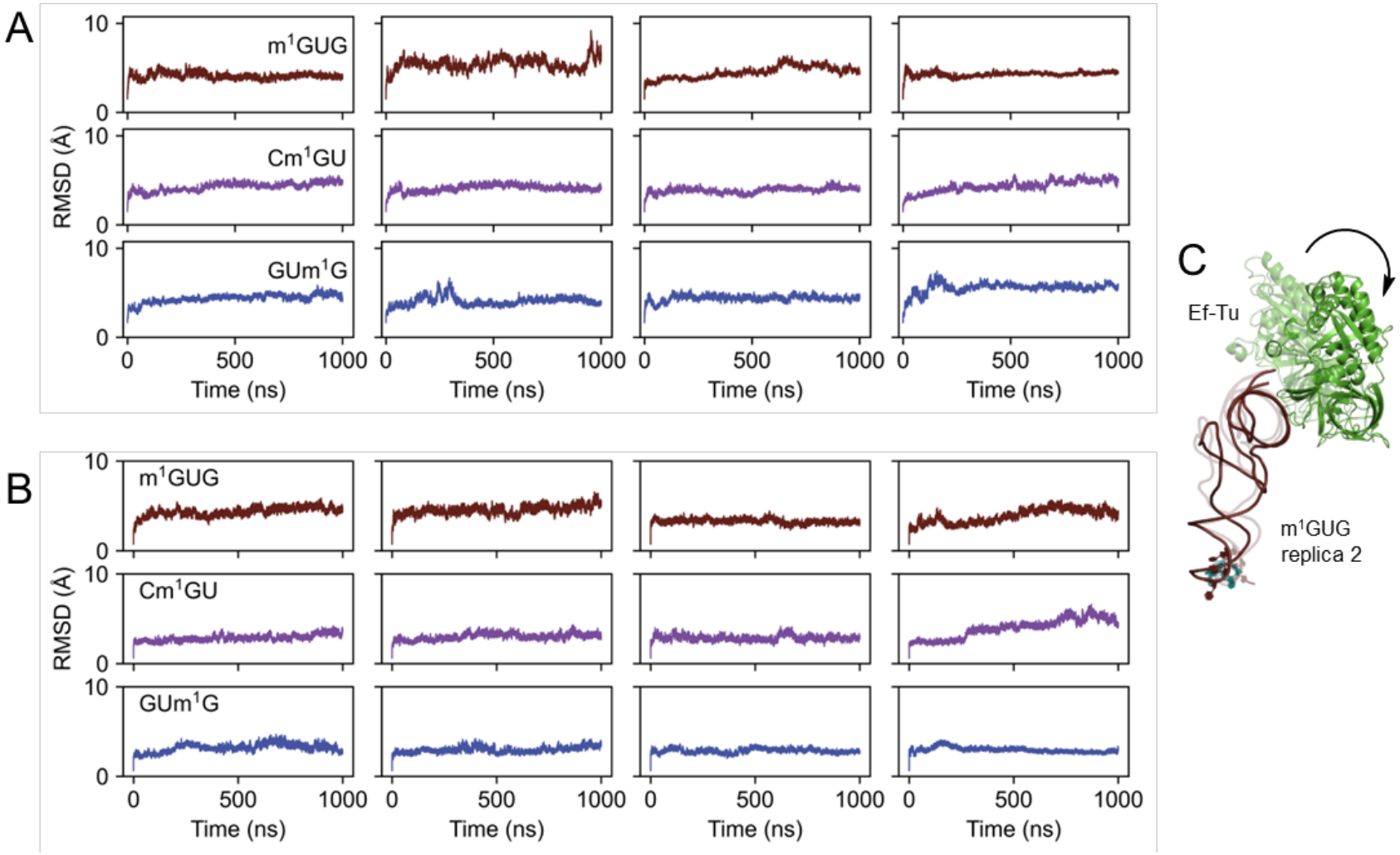

193

194 **Figure C.1. Backbone RMSD of the (A) flexible region and (B) tRNA over the MD simulations of m^1G-containing codon systems with respect to**
195 **the experimental starting structure.** (C) Overlay of the last frame structure (opaque) of the tRNA, mRNA, and EF-Tu for m^1GUG replica 2 at 500 ns
196 (transparent). Each column represents an independent replica trajectory.
197

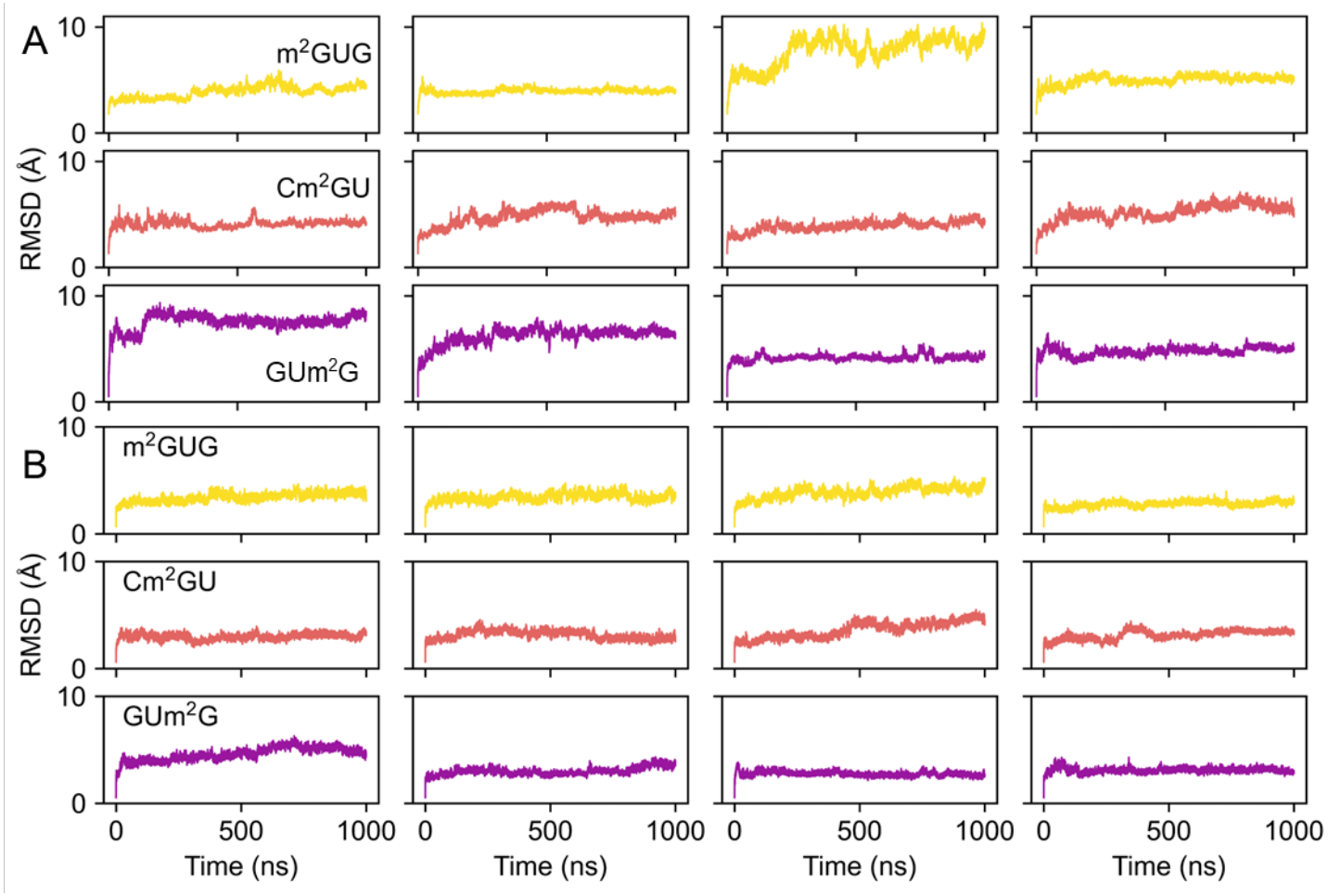

Figure C.2. Backbone RMSD of the (A) flexible region and (B) tRNA over the MD simulations of m^2G-containing codon systems with respect to the experimental starting structure. Each column represents an independent replica trajectory

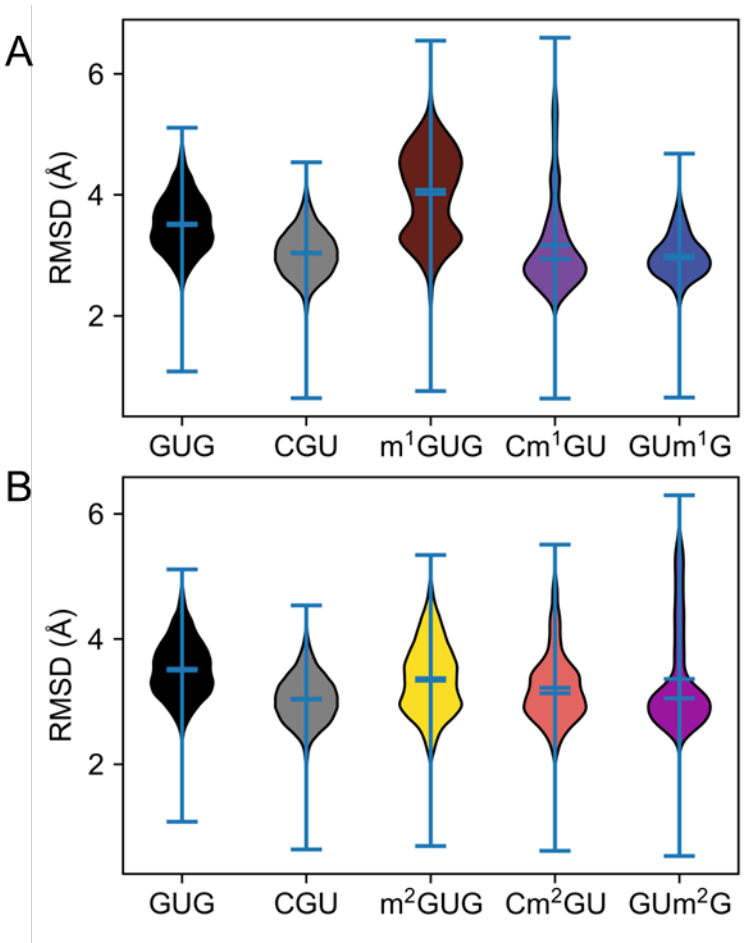

Figure C.3. Backbone RMSD distributions of the tRNA for MD simulations of models containing m^1G (A) and m^2G (B) codon modifications.

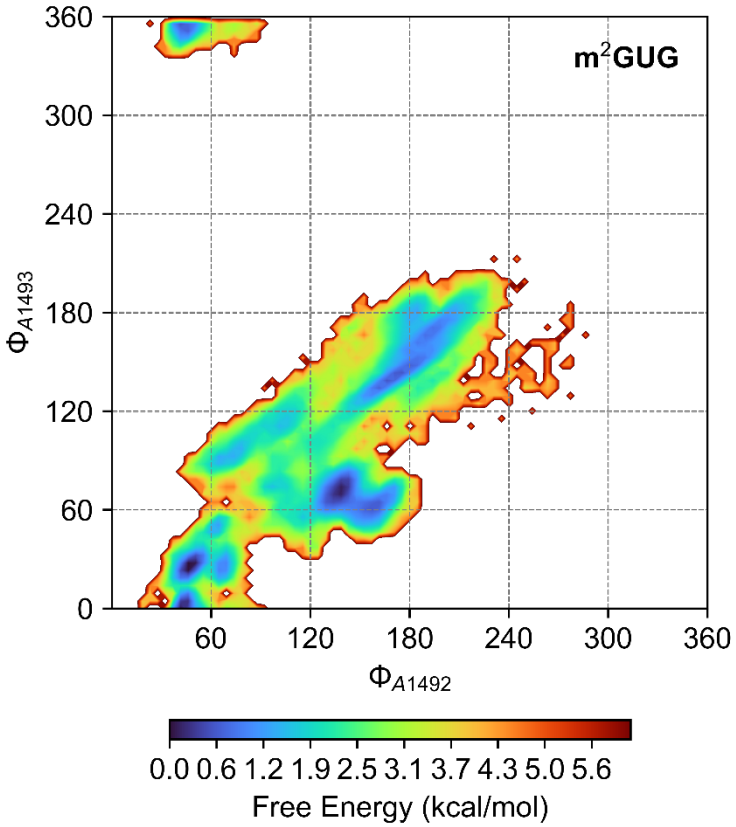

Figure C.5. The 2D Free Energy Landscapes (FEL) of monitoring angles (Φ; see Figure 3.3 its definition) in the m^{2}GUG system.
FELs for quadruplicate ensemble MD simulations of each codon system. The color bar at the bottom indicates the free energy scale used in the FELs (refer to Chapter 2 for full details about the generation of the FEL plots).

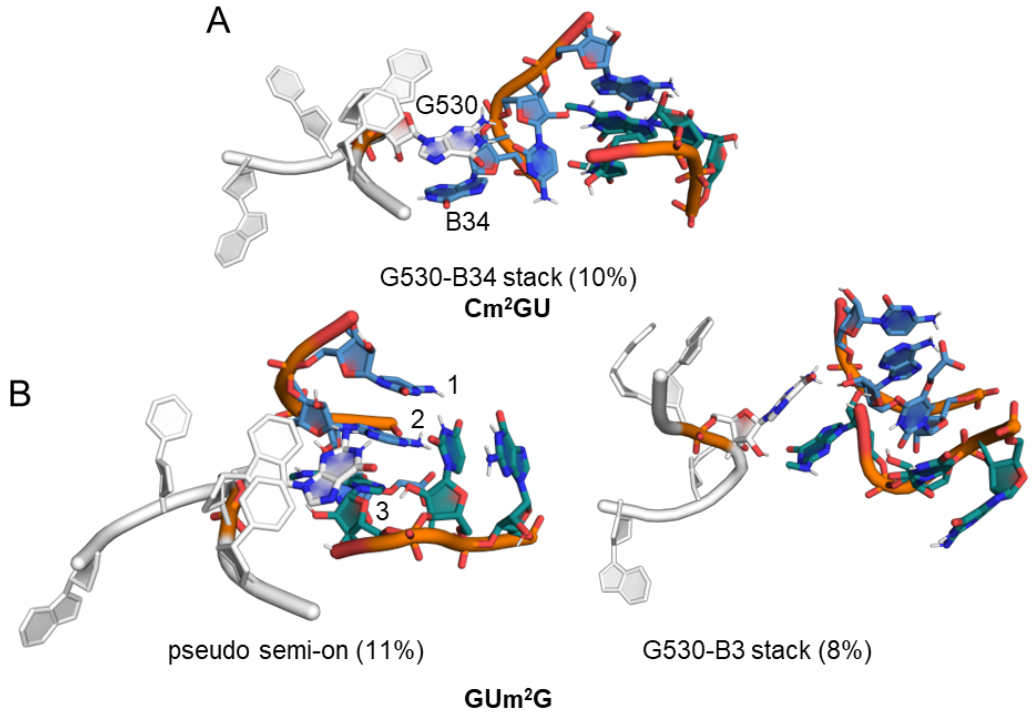

Figure C.6. Minor conformations of G530 sampled during the m^1G and m^2G modification containing mRNA codon systems. Conformation occupancies were obtained by cluster analysis applied to the heavy atoms of G530, the tRNA anticodon (B34-36; colored in blue), and the A-site mRNA codon (B1-3; colored in teal) for the quadruplicate ensemble of the m^1G and m^2G-modified systems

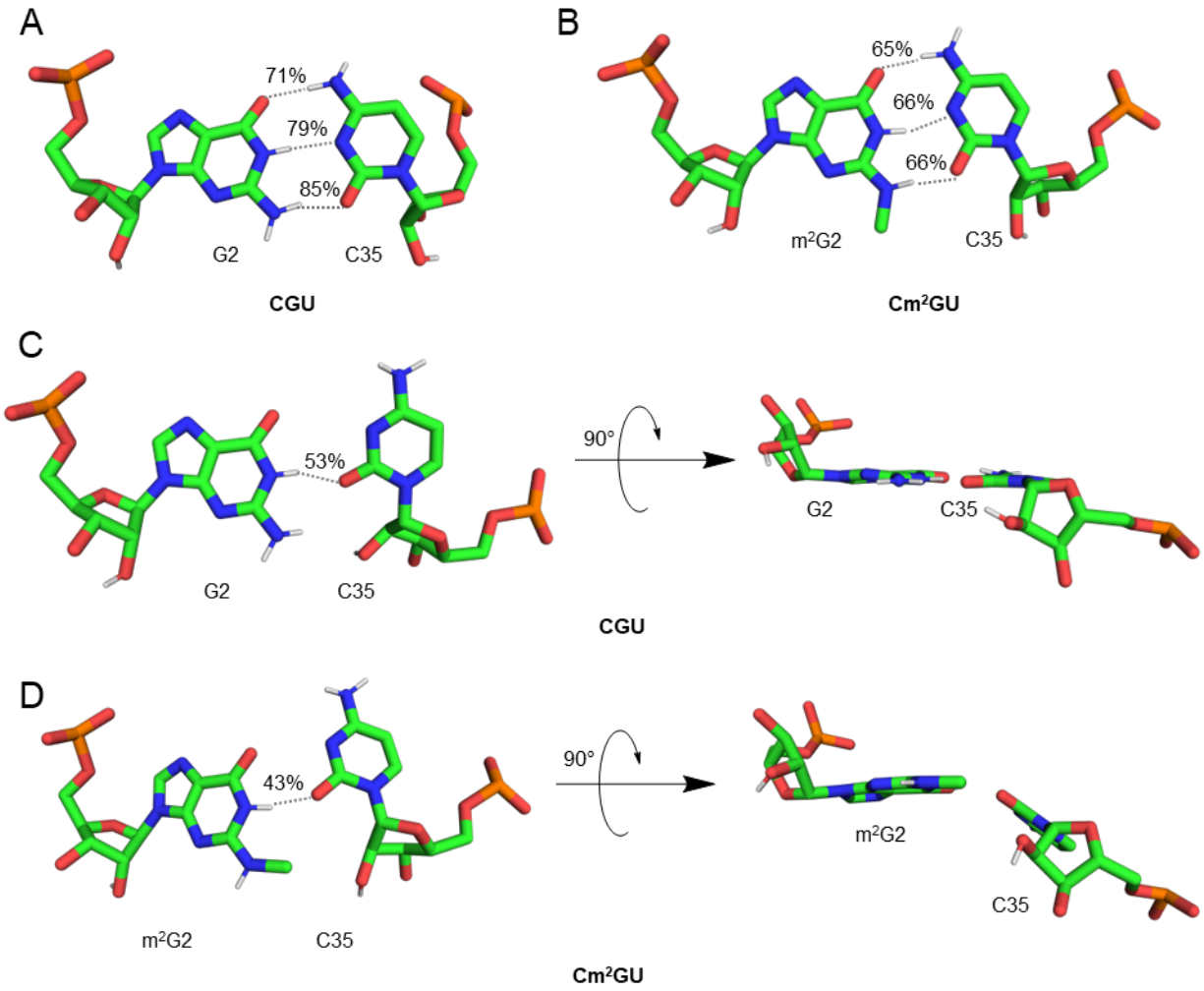

Figure C.7. Hydrogen-bonding interactions between the B2:B35 base pair in CGU and Cm²GU systems. (A-B) Standard GC pair hydrogen bond occupancies for CGU and Cm²GU systems. (C-D) Non-standard hydrogen-bonding orientations. The unrotated view (left) depicts the hydrogen-bonding interactions without considering the coplanarity between nucleobases while the 90° rotated view (right) shows the difference in coplanarity between nucleobases for B2:B35 in CGU and Cm²GU.

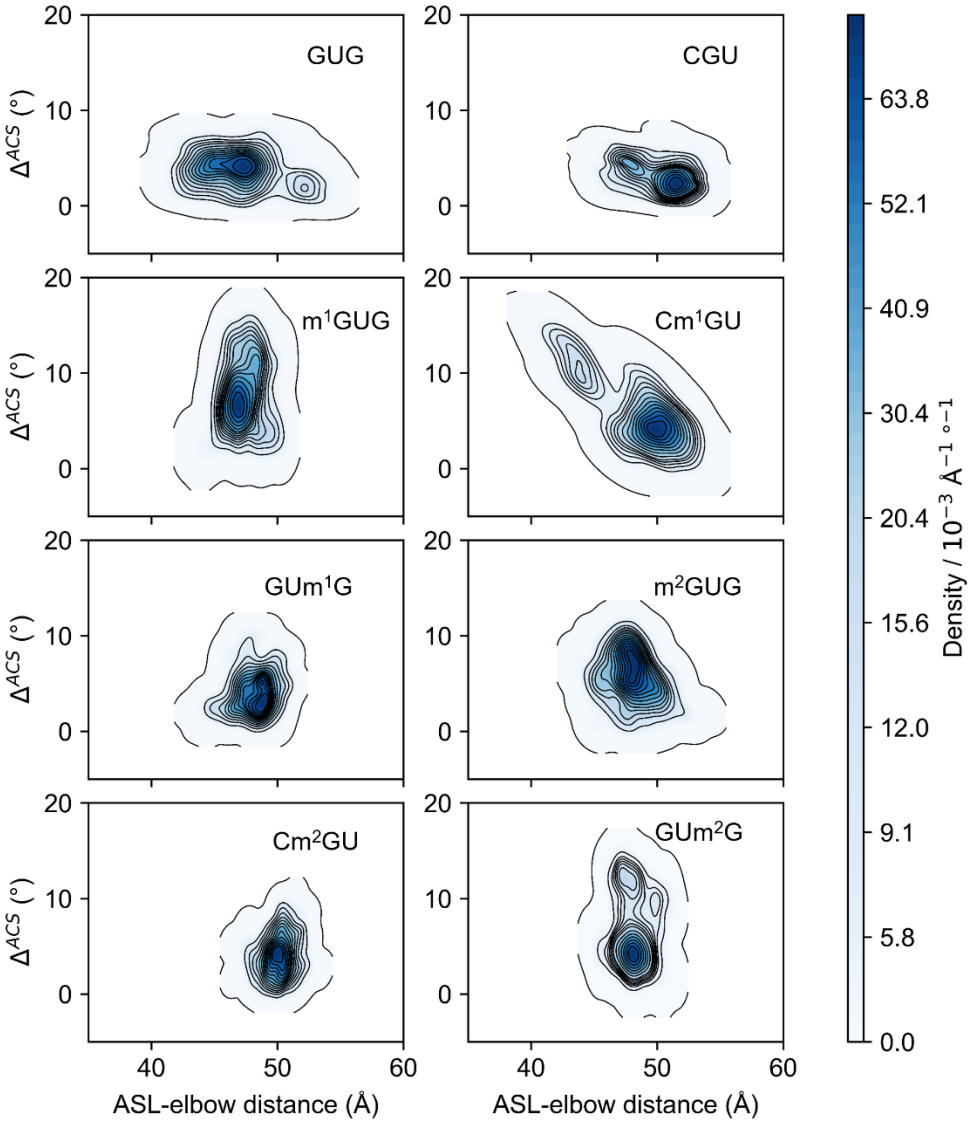

Figure C.8. Internal conformations of the A-site tRNA with m^{1}G- and m^{2}G-modified codons. Normalized 2D Kernel Density Estimate (KDE) plot of ASL–elbow distance and Δ^{ACS}. Darker blue regions represent higher occupation probabilities over simulation ensembles. Black contours show increments of ~1/15 of the estimated probability density range.

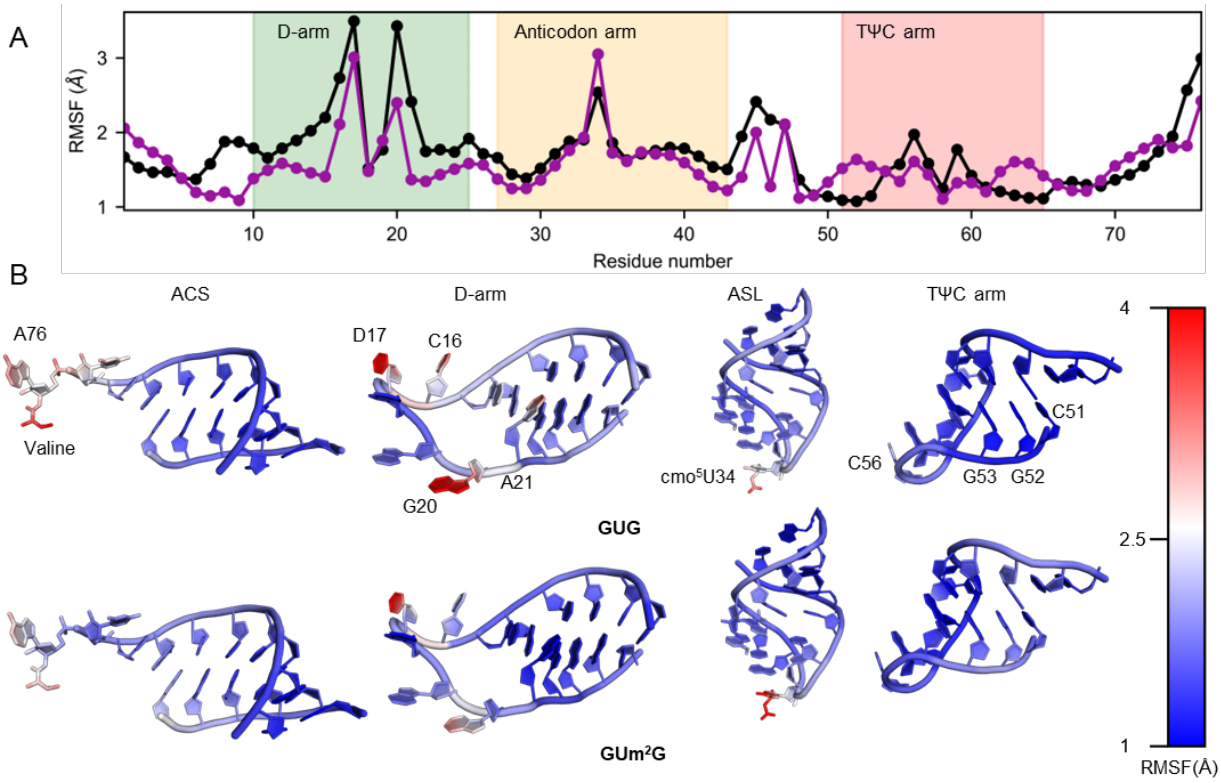

Figure C.9. Flexibility of tRNA domains for GUG and GUm^{2}G codon systems. (A) Ensemble-averaged per-residue RMSF line plot of each modified codon system with shaded tRNA domains (green: D-arm, yellow: anticodon arm, and red: TΨC arm). (B) Blue-white-red spectrum coloring of RMSF value for each of the tRNA domains compared between GUG (top) and GUm^{2}G (bottom).

Table C.1. Summary of mean RMSD and standard deviations for the backbone atoms of the flexible region of the ribosome subsystem model with respect to the experimental structure for each replica of 1000 ns MD simulations.

Model	Replica	Mean RMSD (Å)	Standard Deviation (Å)
m^1GUG	1	4.10	0.3
	2	5.45	0.7
	3	4.49	0.7
	4	4.29	0.3
Cm^1GU	1	4.27	0.5
	2	4.10	0.4
	3	3.87	0.3
	4	4.32	0.6
GUm^1G	1	4.36	0.5
	2	4.05	0.5
	3	4.38	0.3
	4	5.56	0.6
m^2GUG	1	3.88	0.6
	2	3.95	0.2
	3	7.73	1.4
	4	4.99	0.4
Cm^2Gu	1	4.11	0.4
	2	4.74	0.7
	3	3.89	0.5
	4	5.20	0.8
GUm^2G	1	7.56	0.7
	2	6.20	0.8
	3	4.15	0.3
	4	4.76	0.4

Table C.2. Summary of mean RMSD and standard deviations for the backbone atoms of the tRNA in the ribosome subsystem model with respect to experimental structure for each replica of 1000 ns MD simulations.

Model	Replica	Mean RMSD (Å)	Standard Deviation (Å)
m^1GUG	1	4.35	0.5
	2	4.55	0.5
	3	3.30	0.3
	4	3.86	0.8
Cm^1GU	1	2.86	0.4
	2	3.01	0.4
	3	2.86	0.3
	4	3.94	1.1
GUm^1G	1	3.20	0.5
	2	2.97	0.3
	3	2.85	0.2
	4	2.96	0.3
m^2GUG	1	3.41	0.4
	2	3.42	0.4
	3	3.88	0.5
	4	2.78	0.3
Cm^2Gu	1	2.98	0.3
	2	3.14	0.4
	3	3.61	0.8
	4	3.14	0.4
GUm^2G	1	4.60	0.6
	2	2.99	0.4
	3	2.75	0.2
	4	3.10	0.2

Table C.3. Circular correlation coefficients (r_c) computed between A1492–3 angle sets for each model.

Model	Replica	r_c
GUG	1	0.94
	2	0.63
	3	0.47
	4	0.66
CGU	1	0.94
	2	0.97
	3	0.59
	4	0.86
m^1GUG	1	0.97
	2	0.93
	3	0.88
	4	0.85
Cm^1GU	1	0.77
	2	0.94
	3	0.89
	4	0.94
GUm^1G	1	0.85
	2	0.86
	3	0.89
	4	0.97
m^2GUG	1	0.20
	2	0.80
	3	0.90
	4	0.86
Cm^2GU	1	0.84
	2	0.33
	3	0.72
	4	0.87
GUm^2G	1	0.95
	2	0.78
	3	0.83
	4	0.52

Table C.4. Average and standard deviation of the number of water molecules (N_{H_2O}) contained within a 5 Å distance from the minor groove of each base-pairing position in the codon-anticodon minihelix.

	Base pair					
	1		2		3	
Model	N_{H_2O}	S.D.	N_{H_2O}	S.D.	N_{H_2O}	S.D.
GUG	8	2	8	2	19	4
CGU	4	2	5	3	9	3
m^1GUG	10	6	8	5	21	8
Cm^1GU	10	7	9	4	15	4
GUm^1G	6	2	6	2	19	4
m^2GUG	9	3	6	3	18	6
Cm^2GU	5	2	6	3	13	3
GUm^2G	9	7	4	5	17	5

Table C.5. Average distance, angle and percent occupancy of hydrogen bonding interactions between the B1:B36, B2:B35 and B3:B34 base pairs for each ribosome A-site model with m^1G or m^2G modifications.[a]

Model	Base pair	Interaction	Occupancy (%)	Avg. Dist. (Å)	Avg. Angle (°)
m^1GUG	U2···A35	N1···H3-N3	25.69	3.04	157.8
	U2···A35	O4···H61-N6	16.20	2.99	154.1
	U2···A35	O4···H62-N6	16.20	2.99	154.2
	G3···OAU34	O2'···H1-N1	20.36	2.96	139.6
	G3···OAU34	O1P···H1-N1	10.36	2.89	158.6
	G3···OAU34	O2···H1-N1	9.45	3.12	149.9
	G3···OAU34	O30···H1-N1	6.23	3.03	157.8
	G3···OAU34	O4···H1-N1	5.52	2.91	151.6
	G3···OAU34	O6···H3-N3	5.91	2.90	159.3
Cm^1GU	C1···G36	O6···H41-N4	38.70	2.95	157.4
	C1···G36	O6···H42-N4	20.19	2.93	155.2
	C1···G36	N3···H1-N1	69.64	2.99	159.2
	C1···G36	O2···H21-N2	38.52	2.86	159.4
	C1···G36	O2···H22-N2	31.50	2.87	159.6
	C1···G36	O2···H1-N1	29.42	3.14	140.8
	m^1G2···C35	O2'···2H2-N2	13.34	2.92	155.9
	m^1G2···C35	O2'···1H2-N2	12.91	2.99	155.8
	m^1G2···C35	N3···2H2-N2	6.34	3.09	150.5
	m^1G2···C35	N3···1H2-N2	6.32	3.10	150.9
	m^1G2···C35	O2···1H2-N2	6.26	3.01	139.3
	m^1G2···C35	O2···2H2-N2	5.30	3.01	139.2
	U3···INO34	O6···H3-N3	9.37	2.97	149.0
	U3···INO34	O2···H1-N1	8.76	3.01	154.7
GUm^1G	G1···C36	N3···H1-N1	98.18	2.93	159.3
	G1···C36	O2···H22-N2	50.29	2.23	162.1
	G1···C36	O2···H21-N2	49.15	2.25	162.2
	G1···C36	O2···H1-N1	30.00	3.23	134.5
	G1···C36	O6···H41-N4	51.12	2.94	160.4
	G1···C36	O6···H42-N4	42.54	2.93	161.5
	U2···A35	N1···H3-N3	93.81	2.97	161.6
	U2···A35	O4···H62-N6	45.81	2.97	159.0
	U2···A35	O4···H61-N6	45.71	2.97	158.8
	m^1G3···OAU34	O32···HO'2-O2'	13.26	2.31	156.4
	m^1G3···OAU34	O4···H12-N2	12.39	2.96	151.2
	m^1G3···OAU34	O4···H22-N2	12.10	2.96	151.2
	m^1G3···OAU34	O30···H12-N2	10.11	3.07	143.5
	m^1G3···OAU34	O31···HO'2-O2'	9.97	2.89	153.9
	m^1G3···OAU34	O30···H22-N2	9.81	3.07	143.4
	m^1G3···OAU34	O31···H12-N2	8.30	3.03	152.7
	m^1G3···OAU34	O31···H22-N2	7.81	3.02	152.7
	m^1G3···OAU34	O32···HO3'-O3'	6.59	2.82	151.9
	m^1G3···OAU34	O32···H12-N2	6.26	3.03	153.3
	m^1G3···OAU34	O32···H22-N2	6.16	3.02	153.5

Table C.5. Continued

m^{2}GUG	m^{2}G1···C36	N3···H1-N1	98.11	3.01	162.0
	m^{2}G1···C36	O2···1H2-N2	97.25	2.88	160.9
	m^{2}G1···C36	O2···H1-N1	22.32	3.26	134.6
	m^{2}G1···C36	O6···H42-N4	67.77	2.91	162.1
	m^{2}G1···C36	O6···H41-N4	29.20	2.92	161.1
	U2···A35	N1···H3-N3	96.95	2.96	161.8
	U2···A35	O4···H61-N6	45.70	2.95	157.2
	U2···A35	O4···H62-N6	44.66	2.96	157.4
	G3···OAU34	O4···H1-N1	28.42	2.90	153.9
	G3···OAU34	O4···H22-N2	7.91	2.95	151.4
	G3···OAU34	O4···H21-N2	7.30	2.94	151.3
	G3···OAU34	O31···H1-N1	5.41	2.95	149.0
	G3···OAU34	O32···H1-N1	5.22	2.95	148.8
	G3···OAU34	N2···H3-N3	23.70	3.05	158.0
Cm^{2}GU	C1···G36	O6···H41-N4	51.02	2.93	155.2
	C1···G36	O6···H42-N4	39.12	2.91	155.2
	C1···G36	N3···H1-N1	99.24	2.98	162.9
	C1···G36	O2···H22-N2	56.51	2.88	159.2
	C1···G36	O2···H21-N2	42.82	2.89	160.1
	C1···G36	O2···H1-N1	17.19	3.25	13.1
	C1···G36	N4···H1-N1	6.82	3.30	134.8
	C1···G36	N3···H22-N2	5.94	3.29	136.0
	C1···G36	N3···H21-N2	5.65	3.30	136.3
	m^{2}G2···C35	O2···1H2-N2	66.24	2.91	161.0
	m^{2}G2···C35	N3···H1-N1	66.12	3.00	162.0
	m^{2}G2···C35	O2···H1-N1	43.43	3.12	149.2
	m^{2}G2···C35	O6···H41-N4	43.31	2.90	160.4
	m^{2}G2···C35	O6···H42-N4	21.60	2.88	160.3
	U3···INO34	O6···H3-N3	66.05	2.90	157.0
	U3···INO34	O2···H1-N1	63.55	2.94	159.0
GUm^{2}G	G1···C36	N3···H1-N1	72.74	3.00	161.4
	G1···C36	O2···H21-N2	39.29	2.89	159.4
	G1···C36	O2···H1-N1	34.55	3.20	137.0
	G1···C36	O2···H22-N2	3.10	2.89	160.2
	G1···C36	O6···H41-N4	42.17	2.94	160.4
	G1···C36	O6···H42-N4	16.41	2.91	161.3
	U2···A35	N1···H3-N3	79.56	2.94	161.8
	U2···A35	N6···H3-N3	5.57	3.30	13.3
	U2···A35	O4···H62-N6	3.09	2.95	157.0
	U2···A35	O4···H61-N6	32.63	2.95	156.7
	m^{2}G3···OAU34	O4···H1-N1	15.61	2.94	150.5
	m^{2}G3···OAU34	O2'···H1-N1	9.62	3.00	152.1
	m^{2}G3···OAU34	O2···H1-N1	8.44	3.02	157.1
	m^{2}G3···OAU34	O4···H12-N2	6.88	2.97	148.6
	m^{2}G3···OAU34	O6···H3-N3	9.32	2.94	158.2

[a]Acronyms, OAU = uridine-5-oxyacetic acid (cmo^{5}U), INO = inosine, m^{x}G = Nx-methylguanosine (x=1 or 2).

Table C.6. Average RMSF values for domains of the tRNA in the ribosome subsystem models over the quadruplicate ensembles.[a]

Model	Domain	Mean RMSF (Å)	S.D.[b] (Å)
m^1GUG	ASL	2.00	0.5
	D-arm	1.86	0.5
	TΨC-arm	1.28	0.2
	V-loop	1.94	0.9
	ACS	1.57	0.3
Cm^1GU	ASL	2.29	0.5
	D-arm	1.77	0.6
	TΨC-arm	1.22	0.3
	V-loop	1.71	1.0
	ACS	1.19	0.2
GUm^1G	ASL	1.66	0.4
	D-arm	1.56	0.5
	TΨC-arm	1.17	0.2
	V-loop	1.66	0.7
	ACS	1.40	0.3
m^2GUG	ASL	1.85	0.5
	D-arm	1.74	0.5
	TΨC-arm	1.12	0.2
	V-loop	1.42	0.4
	ACS	1.28	0.3
Cm^2GU	ASL	1.89	0.3
	D-arm	1.67	0.5
	TΨC-arm	1.15	0.2
	V-loop	2.00	1.2
	ACS	1.36	0.2
GUm^2G	ASL	1.64	0.5
	D-arm	1.68	0.5
	TΨC-arm	1.44	0.3
	V-loop	1.48	0.5
	ACS	1.49	0.4

[a]ASL domain (anticodon stem loop, residues 27–43), D-arm (residues 10–25), TΨC-arm (residues 51–65), V-loop (variable loop, residues 44–50) and ACS (acceptor stem; residues 1–8 and 66–72)
[b]Standard deviation of the mean RMSF